



Department of Physics

# **Bose – Einstein condensate manipulation and interferometry**

by

**Mateusz Zawadzki**

A thesis presented in fulfilment of the requirements for the degree  
of Doctor of Philosophy in Physics at the University of  
Strathclyde in Glasgow

2010

### **Copyright statement**

This thesis is the result of the author's original research. It has been composed by the author and has not been previously submitted for examination which has led to the award of a degree.

The copyright of this thesis belongs to the author under the terms of the United Kingdom Copyright Acts as qualified by University of Strathclyde Regulation 3.50. Due acknowledgement must always be made of the use of any material contained in, or derived from, this thesis.

Signed:

Date:

# Acknowledgements

My PhD has to be summarised as a great time with an even greater bunch of people. Experimental physics rocks! I am honored that I had the privilege of gaining an amazing experience in the last few years.

Dr. Aidan Arnold! First words have to be addressed to you, as you agreed to take me under your wings. Thank you for telling me about physics, supervising my work, and ‘straightening’ my thoughts with enormous patience. Lab conversations with you always put a different perspective on a topic – I really enjoyed that.

Professor Erling Riis, thank you for being such an organised and authoritative shining person. Your help, when ‘everything’ was failing was priceless. In moments when one might be puzzled you always took stock rightly - this encountered you as a person on whom I can rely on when making experimental decisions.

The photonics team has also contributed to the unique atmosphere that was in the office. I was extremely lucky to overlap with these guys during my PhD. The chief exporter of pain – Ian ‘Chuck’ Norris, who was not so scary as it sounds; no 2. squash player and no 1. prank maker – Kyle Gardner; Reblochon man – Matthieu Vangeleyn; electric ‘VECSEL’ car driver and Friday’s fun game master – Neal Radwell; photonics office bus driver - Kenneth ‘Kendo’ Hay, mattress hunter – Alessio Tierno; the next desk neighbour – Chris Burrows; the adornment of 3.08 office, female part – Stefanie and Aline who kept an eye on the ‘boys’. Finally, a huge thanks to ‘Irish Paul’, who always supported me and provided invaluable encouragement. I will have good memories of you folks, especially lunch time football playing and indoor baseball bat practicing, Donkey smash, office camping and Todd’s poisoning.

Dziękuję również moim rodzicom, którzy zawsze byli dla mnie ogromnym wsparciem. Od Was płynąca motywacja dodawała mi sił podczas ostatnich lat edukacji. Cieszę się, że mam takich wspinających rodziców.

Na koniec chciałbym podziękować, jednej z najważniejszych osób w moim życiu, mojej kochanej żonie – Magdalenie; za bycie przy moim boku, cierpliwość i wsparcie każdego dnia.

# Abstract

This thesis outlines the experimental realisation and manipulation of a Bose-Einstein condensate (BEC) towards a precise sensor based on atom interferometry.

A brief overview of the statistical and quantum mechanics used to describe the signature of BEC is given in the initial chapters, followed by computer simulations of the magnetic fields for coil configurations used.

Experimental chapters describe concepts and mechanisms leading to an experimental observation of matter wave interference fringes, where the fringe pattern was formed by releasing two Bose-Einstein condensates from traps generated by combining magnetic and optical fields. This is followed by a description of a scheme for producing two individual Bose condensates (or single multi-component BECs) using a new dual-frequency AOM scheme for an optical plug in conjunction with magnetic levitation. Experimental realisation of the interference pattern will be supported with theoretical analysis of the effect of the magnetic fields on the fringe spacing with and without atomic interactions. Additionally, an analysis of the matter wave interference data two methods of straightening the interference pattern, based on the Fourier processing, will be presented.

The thesis concludes with comments on potential improvements that can be done in the future, towards the experimental implementation of the Strathclyde giant storage ring for atom interferometry measurements.

# Contents

<b>Abstract</b>	<b>v</b>
<b>List of figures</b>	<b>xi</b>
<b>List of tables</b>	<b>xvi</b>
<b>Physical constants</b>	<b>xvii</b>
<b>1 Introduction</b>	<b>1</b>
1.1 Why go toward absolute zero? . . . . .	1
1.2 Quantum condensation . . . . .	2
1.2.1 Creating BEC . . . . .	5
1.3 Atom interferometry . . . . .	8
1.3.1 Ring geometry . . . . .	9
1.4 Thesis outline . . . . .	10
<b>2 Fundamental theory</b>	<b>12</b>
2.1 Quantum structure of Rubidium . . . . .	12
2.1.1 Repump beam . . . . .	13
2.1.2 Optical pumping . . . . .	14
2.2 Bose-Einstein statistics . . . . .	15
2.2.1 Non-interacting bosons . . . . .	15
2.3 Quantum mechanical description . . . . .	17

<b>3</b>	<b>How does it work?</b>	<b>21</b>
3.1	Laser cooling - Molasses and MOT . . . . .	21
3.1.1	Radiation pressure force . . . . .	22
3.1.2	Optical molasses . . . . .	24
3.1.3	Magneto-optical trap . . . . .	27
3.2	Magnetic influence on atoms . . . . .	30
3.2.1	Zeeman effect . . . . .	30
3.3	Magnetic fields - methodology . . . . .	32
3.3.1	Rectangular coil . . . . .	32
3.3.2	Magnetic field from circular coils . . . . .	33
3.3.3	Helmholtz and anti-Helmholtz configurations . . . . .	35
3.3.4	Quadrupole trap . . . . .	36
3.4	Ioffe-Prichard trap . . . . .	38
3.4.1	IP adiabatic compression . . . . .	40
3.5	Evaporation . . . . .	41
3.5.1	Evaporative cooling . . . . .	42
3.5.2	Runaway evaporation . . . . .	43
3.5.3	RF tool . . . . .	47
3.6	Light potential . . . . .	47
3.6.1	Two quantities - Interaction Potential and Scattering Rate . . . . .	48
3.6.2	Dipole potential beam characteristic . . . . .	49
3.7	Atom interferometers . . . . .	50
3.7.1	Atoms versus light - interferometry . . . . .	51
3.7.2	Five-step routine . . . . .	52
3.8	Type of interferometer . . . . .	53
3.8.1	Momentum space splitting . . . . .	53
3.8.2	Position space splitting . . . . .	54
3.8.3	Implementation of a confined BEC interferometer . . . . .	54
3.8.4	Geometry suited for atom interferometry . . . . .	55
<b>4</b>	<b>Experimental setup</b>	<b>58</b>
4.1	The laser system . . . . .	58
4.1.1	ECDL . . . . .	59
4.1.2	Temperature and current control . . . . .	60

4.1.3	Experimental upgrade . . . . .	61
4.1.4	Controlling the laser . . . . .	61
4.1.5	Locking . . . . .	64
4.1.6	Correction to the right frequency . . . . .	65
4.1.7	Dipole beam . . . . .	67
4.2	Low and High Pressure MOTs . . . . .	67
4.3	Hybrid trap . . . . .	71
4.3.1	Hybrid trap – MOT / IP and ring . . . . .	72
4.4	The toroidal magnetic storage ring . . . . .	76
4.4.1	Giant storage ring . . . . .	76
4.5	Current control . . . . .	77
4.5.1	Driving circuit . . . . .	78
4.5.2	DAC specification . . . . .	79
4.6	Dipole beam setup . . . . .	80
4.7	Cameras . . . . .	80
4.7.1	Absorption imaging . . . . .	82
4.7.2	Camera software development . . . . .	84
<b>5</b>	<b>BEC – selected methods</b>	<b>87</b>
5.1	Magneto-optical trap – loading sequence . . . . .	87
5.1.1	Push beam . . . . .	87
5.2	Optical pumping and magnetic trap . . . . .	89
5.2.1	Field synchronisation . . . . .	89
5.3	Magnetic trap . . . . .	91
5.3.1	Magnetic trap compression . . . . .	91
5.3.2	Measuring trap frequencies . . . . .	92
5.3.3	Current noise in the magnetic trap . . . . .	94
5.3.4	Spin flips . . . . .	96
5.4	Experimental evaporative cooling . . . . .	98
5.4.1	Magnetic noise and evaporation . . . . .	100
5.5	BEC . . . . .	101
5.5.1	Ballistic expansion dynamics . . . . .	102
<b>6</b>	<b>BEC – manipulation</b>	<b>106</b>
6.1	Optical dipole potential . . . . .	106

6.1.1	Dipole beam position . . . . .	106
6.1.2	Optical dipole force . . . . .	107
6.1.3	Impact . . . . .	108
6.1.4	Splitting in an adiabatic manner . . . . .	109
6.2	Controlling the dipole beam . . . . .	110
6.2.1	AOM drive . . . . .	110
6.2.2	Dipole beam displacement . . . . .	112
6.2.3	Single beam deflection . . . . .	114
6.2.4	Sideband BEC splitting . . . . .	116
6.2.5	Optical fork . . . . .	116
6.3	Levitation . . . . .	117
6.3.1	Magnetic levitation . . . . .	117
6.3.2	Application of the anti-gravity system . . . . .	118
6.3.3	Levitation field origin . . . . .	118
6.3.4	Triggering levitation . . . . .	120
6.3.5	Parameters of the levitation field . . . . .	121
6.3.6	Finding omega . . . . .	122
6.4	Interference . . . . .	124
6.4.1	Fringe spacing as a function of separation . . . . .	124
6.4.2	Levitation field correction . . . . .	127
6.5	Fringe pattern – Fourier processing . . . . .	128
6.5.1	Fourier transformation and fringe spacing . . . . .	130
6.5.2	Fringe tilt correction - methods . . . . .	131
6.6	Coherent properties of the BEC . . . . .	136
6.6.1	Quantum interference . . . . .	136
6.7	Magnetic ring experiments . . . . .	138
6.7.1	Ring transfer . . . . .	139
6.7.2	Comet . . . . .	141
<b>7</b>	<b>Conclusions</b>	<b>146</b>
7.1	Summary . . . . .	146
7.2	Improvements and future prospects . . . . .	147
<b>A</b>	<b>Appendix – Magnetic fields</b>	<b>150</b>
A.1	Magnetic field from square coils . . . . .	150

A.2	Magnetic field equations - current loops . . . . .	152
<b>B</b>	<b>Appendix – Time-averaged orbiting potential</b>	<b>155</b>
B.1	Time-averaged orbiting potential magnetic traps . . . . .	155
<b>C</b>	<b>Appendix – Article</b>	<b>158</b>
<b>D</b>	<b>Appendix – System noise</b>	<b>163</b>
D.1	Hot on the trail of the BEC fluctuation . . . . .	163
D.1.1	Spatial fluctuation . . . . .	163
D.1.2	System Noise . . . . .	164
D.1.3	Current irregularity . . . . .	165
<b>E</b>	<b>Appendix – Electronic circuits</b>	<b>168</b>
E.1	RF switch controlling circuit . . . . .	168
E.2	Proposed MOSFET bank driver . . . . .	169
E.3	MOSFET banks driver . . . . .	170
E.4	The coil-driver electronic circuit . . . . .	171

# List of Figures

1.1	The number of articles with the phrase ‘ <i>Bose-Einstein condensat*</i> ’ and ‘ <i>Atom interferomet*</i> ’ . . . . .	5
2.1	The energy level diagram for $^{87}\text{Rb}$ . . . . .	14
3.1	Doppler cooling in two counter-propagating laser beams setup . . . . .	24
3.2	Three dimensional optical molasses . . . . .	26
3.3	Transitions between Zeeman sublevels for a simple four-level atom . . . . .	28
3.4	Schematic of a 3D Magneto-optical trap . . . . .	29
3.5	The ground state Breit-Rabi diagram for $^{87}\text{Rb}$ . . . . .	32
3.6	Contour field plots and vector field plots from ‘pure’ circular Helmholtz and anti-Helmholtz coils configurations . . . . .	36
3.7	Geometry of the IP-type magnetic field coils . . . . .	39
3.8	Double well potential as a result of overcoming the pinch bias field $\mathbf{B}_p$ by the $\mathbf{B}_n$ field . . . . .	40
3.9	The magnetic field contours of the model IP trap in the compressed configuration . . . . .	41
3.10	The $\wp \equiv \tau_{\text{loss}}/\tau_{\text{el}}$ parameter as a function of truncation parameter $\eta$ . . . . .	45
3.11	The graphical presentation of the evaporative cooling efficiency as a function of truncation parameter . . . . .	46
3.12	Schematic of a double well potential with a dipole beam . . . . .	55
3.13	Examples of ring geometries for cold atoms or BECs . . . . .	56
4.1	Schematic diagram of the extended-cavity laser, viewed from above . . . . .	59

4.2	The trapping laser saturated absorption spectrometer . . . . .	62
4.3	Experimental Doppler-broadened absorption spectrum of the rubidium D2 line . . . . .	64
4.4	Experimental saturated absorption spectra of $^{87}\text{Rb}$ . . . . .	65
4.5	Experimental beam deflection after an acousto-optical modulator . . . . .	66
4.6	The double MOT optical bench layout . . . . .	69
4.7	Optical table setup at Strathclyde University (2009) . . . . .	70
4.8	Different views of the magnetic coil system of the Strathclyde magnetic storage ring . . . . .	73
4.9	The magnetic field contours of the Strathclyde MOT configuration gener- ated by the hybrid trap . . . . .	74
4.10	The magnetic field contours of the Strathclyde IP configuration gener- ated by the hybrid trap . . . . .	75
4.11	The magnetic field magnitude from the giant storage ring . . . . .	77
4.12	MOSFET bank system . . . . .	79
4.13	Dipole beam experimental setup . . . . .	81
4.14	Dipole beam experimental setup – a photograph of the actual setup . . . . .	81
4.15	Experimental sequence of absorption imaging . . . . .	83
4.16	A schematic of the Strathclyde absorption imaging set-up . . . . .	84
4.17	Ballistic expansion data for calibration of the magnification parameter . . . . .	84
4.18	CCD camera Labview structure of operation sequence . . . . .	86
5.1	The MOT loading sequence in representation of line triggers . . . . .	88
5.2	The MOT loading for different timing of the push beam . . . . .	88
5.3	Current monitor of the magnetic trap turn on . . . . .	90
5.4	The cold atoms in the magnetic trap after magnetic compression – effi- ciency of the optical pumping . . . . .	91
5.5	Clouds profiles and their optical depths – optical pumping efficiency . . . . .	91
5.6	The compression of the magnetic trap – current monitor . . . . .	92
5.7	The magnetic trap frequencies measurement . . . . .	94
5.8	The magnetic field monitored using sense resistor in the driving circuit for bias compensation coils from the ‘cold stage’ . . . . .	95
5.9	The magnetic field monitored using the sense resistor in the Hall effect sensor for the bias compensation coils after the ‘warm-up’ stage . . . . .	96

5.10	The magnetic field monitored using the sense resistor in the Hall effect sensor for the IP configuration coils . . . . .	97
5.11	Absorption images of atomic clouds distributed between the magnetic sublevels . . . . .	97
5.12	Experimental frequency ramp for evaporation cooling in the Strathclyde experiment . . . . .	98
5.13	Dynamics of the number of atoms and the temperature during the evaporation . . . . .	99
5.14	Atomic cloud density plots during the evaporation process . . . . .	100
5.15	The Fourier spectrum of axial magnetic noise . . . . .	101
5.16	The formation of the Strathclyde Bose-Einstein condensate . . . . .	103
5.17	The ballistic expansion of BEC in free fall . . . . .	104
6.1	Absorption images of the applied optical dipole beam potential on the atoms in the magnetic trap . . . . .	107
6.2	Rapid injection of the dipole beam . . . . .	109
6.3	Adiabatic splitting of the BEC . . . . .	110
6.4	RF spectrum sidebands . . . . .	111
6.5	The schematic diagram of the RF signal processing . . . . .	112
6.6	The 658 nm dipole beam optical path for splitting the BEC . . . . .	113
6.7	The output beam offset as a function of final lens focal distance for three chosen lenses . . . . .	114
6.8	The dipole beam dependence on the AOM driving frequency. . . . .	115
6.9	Macroscopic splitting of BEC with a double optical plug . . . . .	116
6.10	The BEC arrays in the ‘optical fork’ potential . . . . .	117
6.11	Illustration of the anti-gravity (levitation) field . . . . .	119
6.12	Contour field plots from four circular coils providing the levitation field	120
6.13	Time line of levitation . . . . .	121
6.14	Magnetic field levitation vertical ( $y$ ) magnitude . . . . .	121
6.15	Density plots of the BECs in the levitation field . . . . .	122
6.16	Temporal atom distribution in the levitation field . . . . .	123
6.17	Dipole beam optical power dependence on the computer controlled voltage	124
6.18	Fringe period versus power of the 658 nm dipole beam . . . . .	125

6.19	Absorption images of the fringe patterns for varied intensity of the dipole beam . . . . .	126
6.20	Interference patterns ( $850 \times 500 \mu\text{m}^2$ ) for $60 \mu\text{m}$ separated BECs . . . .	127
6.21	Fringe spacing as a function of levitation time . . . . .	129
6.22	Fourier spectra of the experimental interference patterns . . . . .	130
6.23	Interference pattern obtained by overlapping two BECs in the magnetic levitation field . . . . .	132
6.24	The selected ROI with the interference fringes and its Fourier representation . . . . .	132
6.25	The phases of the Fourier components describing the interference pattern	133
6.26	Interference pattern before and after the phase correction. . . . .	134
6.27	Density profile of the fringe pattern from the Fourier corrected image . .	134
6.28	Straightening interference patterns using the subpixel method . . . . .	135
6.29	Density profile of the fringe pattern from the subpixel processed image .	136
6.30	The theoretical spatio-temporal dynamics of two BECs in a free fall ballistic expansion . . . . .	138
6.31	Relative theoretical probability distributions – interference pattern . . .	139
6.32	The linear magnetic field dependance during the ring transfer . . . . .	140
6.33	The transfer of the BEC from the IP magnetic trap into the ring minimum	141
6.34	The comet-like cloud after one revolution in the giant storage ring . . .	142
6.35	The comet like cloud after two revolutions in the giant storage ring . . .	143
6.36	The recombination of two counter-rotating parts of the atomic cloud inside the giant storage ring . . . . .	144
7.1	A prospective option for simplifying the coils setup . . . . .	148
B.1	The effective time-averaged orbiting potential . . . . .	157
D.1	The spatial fluctuation of the final position of the BEC cloud in the levitation field . . . . .	164
D.2	The 50 Hz current noise as a reference signal for the spatial fluctuation correlation . . . . .	165
D.3	Polar plot representation of the 50 Hz noise phase shift dependence on BEC final position . . . . .	166
D.4	Current monitor showing a current surge into the toroidal coils . . . . .	166

E.1	The circuit diagram for the dipole beam RF switch controlling signal . .	168
E.2	The proposed coil-driver circuit diagram . . . . .	169
E.3	The Ioffe-Pritchard (IP) and MOT coil-driver circuit diagram . . . . .	170
E.4	The coil-driver electronic circuit diagram . . . . .	171

# List of Tables

1.1	The de Broglie wavelength for different atomic velocities of $^{87}\text{Rb}$ . . . . .	3
3.1	The D1 and D2 transition line recoil velocities for $^{85}\text{Rb}$ and $^{87}\text{Rb}$ . . . . .	23
3.2	$^{87}\text{Rb}$ field interaction parameters . . . . .	30
4.1	Dipole beam parameters . . . . .	67
5.1	State dependent magnetic field amplitude and related frequency shift of the atomic state . . . . .	101
5.2	Typical atomic parameters during the production of the Strathclyde BEC.	102
6.1	Computer controlled DAC voltage and corresponding visibility of the interference pattern . . . . .	128

# Physical constants

Planck's constant	$h = 6.626 \times 10^{-34} \text{ J s}$
Reduced Planck's constant	$\hbar = \frac{h}{2\pi} = 1.055 \times 10^{-34} \text{ J s}$
Boltzmann's constant	$k_B = 1.381 \times 10^{-23} \text{ J/K}$
Speed of light	$c = 2.998 \times 10^8 \text{ m/s}$
Permeability of free space	$\mu_0 = 4\pi \times 10^{-7} \text{ H/m}$
Permittivity of free space	$\epsilon_0 = 8.854 \times 10^{-12} \text{ F/m}$
Earth's surface gravitational acceleration	$g = 9.81 \text{ m/s}^2$
Electron charge	$e = 1.602 \times 10^{-19} \text{ C}$
Electron mass	$m_e = 9.109 \times 10^{-31} \text{ kg}$
Proton mass	$m_p = 1.673 \times 10^{-27} \text{ kg}$
Atomic mass unit	$m_{amu} = 1.661 \times 10^{-27} \text{ kg}$
Bohr radius	$a_0 = 5.292 \times 10^{-11} \text{ m}$
Bohr magneton	$\mu_B = \frac{e\hbar}{2m_e} = 9.274 \times 10^{-24} \text{ J/T}$
Nuclear magneton	$\mu_N = -\frac{e\hbar}{2m_p} = -5.051 \times 10^{-27} \text{ J/T}$
Proton magnetic moment	$\mu_p = 2.793 \mu_N$

## Rubidium atomic constants

Mass of $^{87}\text{Rb}$ , $^{85}\text{Rb}$	$m_{87} = 86.91 m_{amu}$ , $m_{85} = 84.91 m_{amu}$
$^{87}\text{Rb}$ , $^{85}\text{Rb}$ magnetic moment	$\mu_{87} = 2.751 \mu_N$ , $\mu_{85} = 1.353 \mu_N$
$^{87}\text{Rb}$ , $^{85}\text{Rb}$ nuclear spin	$I_{87} = 3/2$ , $I_{85} = 5/2$
Rb D2 linewidth	$\Gamma = 2\pi\Gamma_\nu = 2\pi \times (6.065(10) \text{ MHz})$
Rb D1 linewidth	$\Gamma = 2\pi\Gamma_\nu = 2\pi \times (5.745(10) \text{ MHz})$
Rb D2 frequency	$\nu_{D2} = 384.23 \text{ THz}$
Rb D1 frequency	$\nu_{D1} = 377.11 \text{ THz}$

# Introduction

## 1.1 Why go toward absolute zero?

In finding the answer to the above question it is worth using our imagination. Let's assume a few, in fact, unrealistic hypotheses that reveal a sense of reaching the temperatures much lower than people are used to, temperatures approaching absolute zero. If we consider ourselves born on the Sun which has a surface temperature of  $\approx 10^5\text{K}$  without knowledge of Earth's existence, some of the physical processes taking place on Earth would not be known to us. Having equipment allowing us to cool a part of the Sun and an eagerness to know what happens at lower temperatures we could discover unknown phenomena like phase transitions. An amazing change of vapour into liquid, liquid into solid and physical properties of these states would be something absolutely new and remarkable on the Sun.

Probably a similar point of view was familiar to some researchers on the Earth in cold physics experiments. Willingness to explore what really happens at low temperatures was richly rewarded. For example cold atomic samples at low temperatures reveal unintuitive properties like superfluidity and the related subject of superconductivity [1]. At low temperatures quantum effects related to the internal structure of the atoms are significant which results in the appearance of macroscopic quantum effects. Effects unseen for higher temperatures set a great motivation for pursuing cold physics phenomena. In this thesis we describe experiments based on the low temperature quantum condensation of a weakly interacting system. In order to understand the principle behind the phenomena at cold temperatures we first of all need to consider behaviour of particles in the cooled atomic sample.

## 1.2 Quantum condensation

A quantum mechanical description of particles divides them into two subcategories characterised by their spin; bosons with integer spin and fermions with half-integer spin. Each group exhibits different physical properties. Bosons are ‘friendly’ with other bosons and there is no restriction on the occupation numbers, whereas fermions obey the rule that at most one particle from the system can be in any certain state, which is known as the Pauli exclusion principle.

No restriction on the occupation number for bosons implies different low temperature properties of a perfect gas of bosons and gas of fermions. The first theoretical description of an ensemble of bosons in the same quantum state was studied by Bose and Einstein [2, 3]. In 1924 these two scientists provided the theoretical groundwork for a new area of physics. They predicted that if a collection of bosonic atoms were to be cooled to the lowest possible temperature resulting from kinetic energy, all atoms should collapse into the ground state. In consequence one may observe a macroscopic occupation of a single quantum (ground) state. This so-called condensation of bosonic particles into one quantum state is known today by the term, Bose-Einstein condensation (BEC) [1, 4].

Bose-Einstein condensation is a phase transition that occurs at a certain temperature and density. The Heisenberg uncertainty principle imposes balanced lack of knowledge between momentum  $p$  and position  $x$ . The uncertainty in the position of the particle refers to the thermal de Broglie wavelength ( $\Delta x \propto \Lambda_{\text{dB}}$ ). It follows that for high temperatures the momentum information is less accurate and  $\Lambda_{\text{dB}}$  is small ( $\Delta p \Lambda_{\text{dB}} \propto \hbar/2$ ). In contrast for low temperatures, with high momentum knowledge,  $\Lambda_{\text{dB}}$  is larger and can reach values comparable with the mean inter-particle spacing  $d_{\text{mips}}$ . When the bosonic atomic sample has very low temperature and high density it can be found in the regime

$$\Lambda_{\text{dB}} \approx n^{-1/3} = d_{\text{mips}} , \quad (1.1)$$

at which the Bose-Einstein condensation takes place. In Eq. 1.1  $n$  is the number density (spatial density). The commonly used unitless quantity that combines mean inter-particle spacing and de Broglie wavelength is the phase space density (PSD). With definition

$$\text{PSD} = n \Lambda_{\text{dB}}^3 = n \underbrace{(h/\sqrt{2\pi m k_B T})^3}_{\Lambda_{\text{dB}}^3} , \quad (1.2)$$

for an atom with mass  $m$  and where  $k_B$  is the Boltzmann constant. The definition of the thermal de Broglie wavelength from Eq. 1.2 can be found in many textbooks, e.g. in Ref. [5]. As the de Broglie wavelength is temperature dependent the phase space density is a combination of temperature and density. To get the best combination between these two, required for reaching the BEC transition, one has to maximise the phase-space density i.e. maximise density and minimise temperature. At the Bose-Einstein phase transition PSD is approximately equal to unity.<sup>1</sup>

Practically, when considering the size of the de Broglie wavelength it is useful to relate different velocities to  $\Lambda_{dB}$ . The de Broglie wavelength can be given, in meter units, as:

$$\Lambda_{dB} = 2\pi/k = h/(mv) \quad (1.3)$$

where  $v$  is the velocity in meters per second,  $m$  is the atomic mass and  $h$  is Planck's constant. For the general case when different species with different atomic masses are considered the de Broglie wavelength is approximately  $\frac{0.4}{Av} \mu\text{m}$ , where  $A$  is the atomic mass number. The large range in de Broglie wavelength depends mostly on velocities. A comparison between de Broglie wavelength and corresponding atomic velocities is presented in Tab. 1.1

$v$ (m/s)	$10^3$	$10^2$	$0.0589^*$	$10^{-3}$
$\Lambda_{dB}$ (m)	$4.59 \times 10^{-12}$	$4.59 \times 10^{-11}$	$7.80 \times 10^{-7}$	$4.59 \times 10^{-6}$
$n_{\text{PSD}=1.202}$ (atoms/cm <sup>3</sup> )	$1.24 \times 10^{28}$	$1.24 \times 10^{25}$	$2.53 \times 10^{12}$	$1.24 \times 10^{10}$

Table 1.1: The de Broglie wavelength for different atomic velocities of <sup>87</sup>Rb. \* corresponds to recoil velocity of <sup>87</sup>Rb for D2 line.

For atoms with velocities of hundreds of meters per second (like room temperature atoms) the de Broglie wavelength takes values of picometers, whereas for cold and ultra-cold atoms with velocities of a few millimetres per second the de Broglie wavelength is measured in micrometers. Tab. 1.1 also shows relevant densities required at the Bose-Einstein phase transition (PSD = 1.202), related to the de Broglie wavelengths.

The enormous gap between the room temperature phase space densities and the

---

<sup>1</sup>The value of phase space density is trapping potential dependent. In this thesis we use a three dimensional harmonic potential and hence  $\text{PSD} \approx \zeta(3) = 1.202$  at condensation [6], where  $\zeta$  stands for the Riemann Zeta function (See more in Sec. 2.2). In many textbooks the phase space density is equal to  $\zeta(3/2) = 2.612$  at condensation [5, 7], which is true for an ideal Bose gas in a three dimensional box potential.

phase space density in the quantum condensation regime  $\geq 1.202$  make the path to BEC very challenging. Many famous physicists who lived after 1924 did not believe the quantum statistics phenomenon of Bose-Einstein condensation, which required ultra-low temperatures at high densities would ever be possible to achieve in the laboratory [8].

A year before the experimental demonstration of BEC phenomena a research news article entitled “Hot on the trail of a cold mystery” quoted Steve Chu: “I am betting on Nature to hide Bose condensation from us. The last 15 years she’s been doing a great job” [9]. Against the frustration and general pessimism there was still a hope to experimentally obtain a BEC. Many technical issues in reaching condensation slowed the progress toward experimental realisation of BEC. The task was not easy. Scientists were trying to find an atomic system that would remain in its gaseous form even below the critical BEC transition temperature. The great breakthrough happened not long after. Nature showed her kind side and with scientific encouragement revealed new phenomena.

It took over 70 years to overcome many difficulties and obstacles in order to obtain quantum condensation. In June 5<sup>th</sup> 1995 for the first time in history gaseous condensate was produced by a team of researchers from University of Colorado at Boulder (JILA) [10]. Another group of researchers from the Massachusetts Institute of Technology (MIT) obtained a condensate which was about 1000 times larger four months later on September 13<sup>th</sup> [11]. This exotic state of matter played a great role in further research as quantum condensation is an interesting phenomena both from a theoretical and an experimental point of view.

This achievement opened a new era for cold atomic physics. The explosive growth of the field had an enormous impact on atomic physics resulting in many valuable scientific publications (see Fig. 1.1).

The experimental achievement of gaseous Bose-Einstein condensation started a new era when scientists undertook the challenge to reach the BEC transition with even more complex atomic systems. To date many different research groups worldwide succeeded in creating BECs in: stable alkali metal species - rubidium ( $^{87}\text{Rb}$ ) [10], sodium ( $^{23}\text{Na}$ ) [11], lithium ( $^7\text{Li}$ ) [12], rubidium ( $^{85}\text{Rb}$ ) [13], potassium ( $^{41}\text{K}$ ) [14] and ( $^{39}\text{K}$ ) [15], caesium ( $^{133}\text{Cs}$ ) [16]; along with non-metallic hydrogen (H) [17] and metastable helium ( $^4\text{He}$ ) [18]; chromium ( $^{52}\text{Cr}$ ) [19] from the transition metals group, two species of alkaline earth metals with two valence electrons calcium ( $^{40}\text{Ca}$ ) [20],

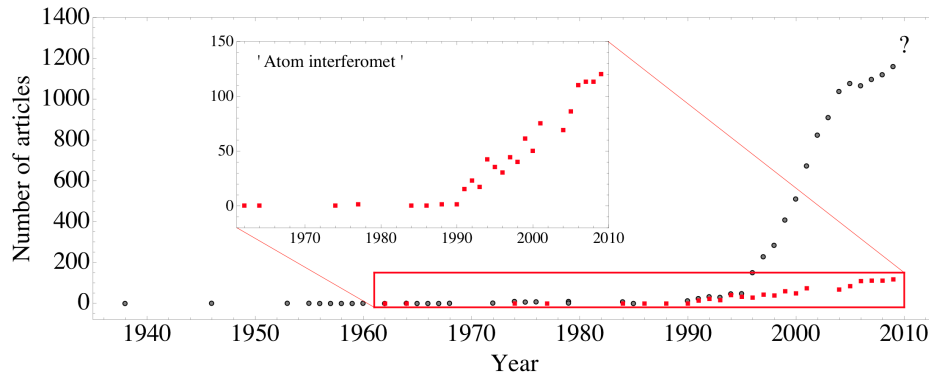


Figure 1.1: Trend represented by the number of articles with the phrase ‘*Bose-Einstein condensat\**’ title or abstract in each year (circles). The framed squares relate to the number of articles found with ‘*Atom interferomet\**’. The results were found using the ISI Web of Knowledge search engine.

strontium ( $^{84}\text{Sr}$ ) [21] and ytterbium ( $^{174}\text{Yb}$ ) [22], ( $^{170}\text{Yb}$ ) [23] from the lanthanides group.

### 1.2.1 Creating BEC

The complex processes performed on atoms leading to Bose-Einstein quantum condensation involve many different techniques. The way to reach BEC in an atomic vapour of  $^{87}\text{Rb}$  used in the Strathclyde experiment, not that different from most others, can be described by a three stage sequence based on the following steps:

- (1) Laser cooling and trapping  $\rightarrow$  (2) Magnetic trapping  $\rightarrow$  (3) Evaporative cooling
- Strathclyde BEC sequence

The temperature of atoms is in fact just a measure of their spread of velocities. The faster the atoms are the higher the kinetic energy, which is related to high temperature. Cooling down the atomic sample means slowing atoms down. The only thing one has to consider is how to change the atom’s momentum. The use of lasers as a coherent light source provides the momentum carriers as photons for slowing the motion of atomic particles.

#### Laser cooling and trapping

The idea of laser cooling was proposed in 1975 by two independent groups [24][25]. Not long afterward the first realisation of three-dimensional laser-cooling on neutral

atoms was performed at AT&T Bell Labs in 1985 [26]. This first three-dimensional laser cooling of sodium atoms reached temperatures as low as  $240 \mu\text{K}$ , related to an rms velocity of  $\approx 60 \text{ cm/s}$  with  $\approx 10^6 \text{ cm}^{-3}$  atomic density.

This laser cooling technique will be described in more detail in Sec. 3.1, as in this introduction we only present the idea behind laser cooling as a preparation stage on the way to Bose-Einstein condensation. Basically this technique exploits absorption and subsequent spontaneous emission of photons, which leads to so called light forces. These forces are velocity dependent through the Doppler effect. The three-dimensional laser-cooling setup used at Strathclyde utilises three pairs of counter-propagating beams and a vacuum chamber. The frequency of the laser light can be adjusted in such a way that as soon as atoms start moving towards one of these laser beams they experience a net force in the opposite direction. The viscous nature of the force in the red-detuned (laser light has a slightly lower frequency than an energy level transition within the atom) laser configuration led to the term *optical molasses*. In such a setup atoms can be decelerated by the light at accelerations of  $\approx 10^5 g$ . It means the atoms that start with velocities of  $100 \text{ m/s}$  can be stopped in a millisecond.

In order to increase phase space density, so important when trying to observe Bose-Einstein condensation, the combination of lasers was enriched with a spatially varying magnetic field. This particular configuration, lasers providing the velocity dependent force and a magnetic field resulting in a position dependent light force, results in a great increase in PSD. This setup is known as a magneto-optical trap (MOT) and was first suggested in 1986 by J. Dalibard [27]. Since then the magneto-optical trap played an enormous role in providing pre-cooled atomic samples. Simultaneous implementation of laser cooling and trapping using the MOT won the title of a ‘work horse’ in cold atom physics.

The MOT relies on the Zeeman effect and will be discussed in more detail in Sec. 3.2. The MOT combines circularly polarised, red-detuned laser beams to drive certain atomic transitions, and a quadrupole magnetic field. Magnetic field changes the position dependence of the absorption, i.e. it modifies the light force. The magnetic field is approximately proportional to the displacement from the centre of the trap local minimum ( $\mathbf{B} \propto (x, y, 2z)$ ). The Strathclyde experiment uses two magneto-optical traps separated by a distance of  $\approx 50 \text{ cm}$  and different operating pressures. Due to a pressure difference the MOT with a higher / lower pressure is called the High Pressure (HP) MOT / Low Pressure (LP) MOT respectively. The background pressure ratio of

the two chambers is about 100, and this is achieved by using a differential pumping technique. The pressure is  $10^{-9}$  Torr at the loading chamber and  $10^{-11}$  Torr at the collection chamber (where the BEC is generated). The double MOT setup is able to produce a high flux of cold atoms from the HP to LP MOT. The loading time, in the LP MOT, is shortened to a few seconds and still traps more than  $10^9$  atoms.

Cooling the atoms in the MOT can lead to a significant increase in the phase space density, but it is still not enough to reach the Bose-Einstein transition. The de Broglie wavelength for the recoil limit is too small for attainable densities (Tab. 1.1). The pursuit of higher phase space density resulted in the development of an alternative cooling technique – evaporative cooling (Sec. 3.5). The number of atoms one can collect in the LP MOT can be used as an indirect predictor of performing BEC through the evaporation cooling process. More atoms in the MOT provide more elastic collisions between the atoms, once loaded in a magnetic trap, and hence make the evaporation process more efficient (see Sec. 3.5).

### Magnetic trapping

The middle step towards quantum condensation solely involves magnetic fields. As a consequence of atoms possessing a magnetic dipole moment  $\boldsymbol{\mu}$  the magnetic field influence can not be omitted. An atom experiences a potential from the magnetic field  $U(\mathbf{r}) = -\boldsymbol{\mu} \cdot \mathbf{B}(\mathbf{r})$  and depending on its spin state the direction of the effective force from the potential is different. Some of the states occupied by atoms direct the atom into the local field minimum and other states place the atoms in the maximum local potential. For an atom in the hyperfine state described by quantum number  $m_F$  the energy related to the Zeeman effect

$$U(r) = g_F \mu_B m_F B(r) , \quad (1.4)$$

depends solely on the magnitude of the field,  $B$ . The  $\mu_B$  is the Bohr magneton and the rest of the parameters depend on a quantum state, namely the Landé g-factor  $g_F$ , and  $m_F$  the projection of the total atomic (electronic + nuclear) angular momentum  $F$  along  $\vec{B}$ . For the atom in the magnetic potential the magnetic force along the  $x$ -direction is  $F_\nabla = -g_F \mu_B m_F \frac{dB}{dx}$ . Depending on the spin state we can alter the sign of the acting magnetic force and we can differentiate atoms as low or high field seekers. The only state unaffected by the magnetic field potential is  $m_F = 0$ . Using combinations of magnetic field an effective trapping potential can be created (see Sec. 3.2). The wall-

free confinement of magnetic trapping was applied in many experiments with success. As an example, the compressed Ioffe-Prichard magnetic trap [28] offers the geometry and confinement in terms of trap frequency enabling the start of effective evaporation cooling which is the last step on the path to BEC. It will be shown in later section that IP-like traps impose a trap with a cigar-shape trapping potential. Usually in order to characterise the IP-like trap one needs to specify the trapping frequencies, namely axial frequency,  $\nu_z$ , along the long axis of the trap and radial frequency,  $\nu_r = \sqrt{\nu_x^2 + \nu_y^2}$ , with much tighter confinement ( $\frac{\nu_z}{\nu_r} \approx 10$ ).

### Evaporative cooling

After magnetic trapping further temperature reduction is achieved during the runaway evaporation process. Atom optics equips us with the tools that enable us to remove atoms from the trap by driving them to the anti-trapping states (which for us are the high-field-seeking states). Radio-frequency radiation, of frequency  $\nu_{\text{RF}}$  acts as a spatially-selective knife letting the atoms escape from the magnetic trap at positions  $r_0$ , where  $\nu_{\text{RF}} = \frac{g_{\text{F}}\mu_{\text{B}}}{h}B(r_0)$ . Every loss of atoms from the trap is followed by a thermalisation process in the atomic sample left in the trap. This continuous process effectively lowers the temperature down to the critical temperature,  $T_c$ , at which Bose-Einstein condensation occurs (see Sec. 2.2.1). During that process the PSD is increased by a factor of  $\approx 10^7$  and the temperature is lowered by a factor of  $\approx 10^3$ . Because evaporation is a lossy process (the number of trapped atoms typically drops by a factor of 1000), it is important to start with as large an atom number as possible in the magnetic trap in order to create large BECs.

With the great growth of interest in BEC itself one could hope to observe development of other research ideas employing this new quantum matter. One example of an application is the use of BECs as a source of coherent matter waves for implementation in the area of atom interferometry.

## 1.3 Atom interferometry

Four years before Bose-Einstein condensation was achieved experimentally another research area was considered for study. The development of atom interferometry as a field of research began to expand rapidly from 1991 when the first reports of applying atoms as a measurement tool appeared in press [29, 30, 31, 32]. Different experiments

based on ultra-precise atom interferometry have been realised for a variety of measurements, e.g. to sense accelerations [33, 34], rotations [35, 36], measure fundamental constants [37], observe quantum decoherence [38] or describe the distinctive nature of atoms and molecules [39]. The trend of interest in atom interferometry is represented by the increasing number of articles being published recently (see Fig. 1.1).

When considering atom interferometers one has to identify key differences and advantages when using matter waves instead of light. The relation between possible velocities of the light and the matter wave along with the wavelength,  $\frac{\lambda_{\text{ph}}}{\lambda_{\text{dB}}} \frac{c}{v_{\text{atom}}} = \frac{mc^2}{\hbar\omega}$ , leads to ratio of phase shift of order  $\propto 10^{10}$  showing that atom interferometers have a huge Sagnac response factor [40] compared to optical interferometers. It will be shown later on in this thesis (see Sec. 3.7.1) that slow atom interferometers result in high sensing performance.

### 1.3.1 Ring geometry

The ring geometry for cold atoms, where the atoms are guided around a closed path, is an interesting configuration for performing, for instance, ultra-sensitive atom interferometry. An application of particular interest is rotation sensing, where the potential sensitivity increases with the enclosed area. An electrostatic storage ring was first reported for molecules in 2001 [41]. However, for many interferometry experiments atoms are more suitable candidates as, in contrast to molecules, atoms are easily prepared in the same quantum state and they can be laser cooled to very low temperatures.

In 2001 researchers at the Georgia Institute of Technology have demonstrated the first storage ring for ultra-cold neutral atoms [42]. The first atomic storage ring made use of the interaction of a weak-field-seeking atom with the magnetic quadrupole field created by two concentric current carrying loops. The two-centimeter storage ring was operating using neutral  $^{87}\text{Rb}$  atoms. Since then the ring geometry was implemented in many experimental realisations in the field of cold atoms [41, 43, 44, 45, 46, 47, 48, 49].

For example, Gupta *et al.* have produced a Bose-Einstein condensate in a ring-shaped magnetic waveguide for the purpose of observing persistent quantized circulation and related propagation phenomena. The few-milimeter diameter non-zero bias ring was formed from a time-averaged (see Appendix B) quadrupole ring.

Additionally, one can find other arrangements based on a single current loop and an ac magnetic field perpendicular to the area confined by the current loop [49]. Depending on the ac magnetic field magnitude the radius of the ring for atoms can be alter

( $\sim 10$  mm). This geometry, where magnetic ring traps require no external wiring, simplifies the experimental setup and is very promising for atom interferometry.

In comparison, the Strathclyde storage ring [47] utilises the quadrupole field of a four-loop geometry (see Sec. 4.4), which has an effective diameter of  $\sim 10$  cm. To date, this is the biggest magnetic ring for cold atoms and BECs. Its large diameter and high level of optical access also facilitates the application of dipole force laser beams for manipulating the BEC. The Strathclyde storage ring can be used as an ultra-precise Sagnac interferometer,<sup>2</sup> which should yield even higher sensitivity and the flexibility to pursue other avenues of research. As our ring has a long lifetime, the atoms can complete tens of revolutions, further increasing our effective area and thus the interferometric sensitivity. Our ring contains more than  $5 \times 10^8$  atoms, has a lifetime of 50 s, and with an area of  $7200 \text{ mm}^2$ . This corresponds to a relative increase of 100, 60 and 23 in atom number, lifetime and area respectively, with respect to Ref. [42].

## 1.4 Thesis outline

This thesis contains a description of the Strathclyde BEC experiment and its progress towards an ultra-sensitive measuring tool, based on the atom interferometry.

Chapter 2 gives a brief description of the theoretical statistical and quantum mechanical properties of BECs.

In Chapter 3 the theory behind the techniques used to obtain Bose-Einstein condensation will be discussed. The primary areas that will be covered are laser cooling and trapping, magnetic trapping, and evaporative cooling. Additionally, in this chapter we will provide a brief theory for the optical dipole potential and a background for atom interferometry.

Chapter 4 details the experimental realisation of BEC. The outline of the experimental setup will be provided along with the main experimental parameters used during the realisation of the condensate. The novel features of the Strathclyde BEC will be discussed – particularly the implementation of the laser beam for optical dipole splitting of the BECs.

Chapter 5 focuses on optimisation of the procedure of reaching BEC. It narrates the selected experimental methods used in the Strathclyde BEC experiment. This chapter also mentions a few aspects that improve on the existing experimental setup.

---

<sup>2</sup>The Sagnac rotational effect is proportional to the enclosed area of the beams in an interferometer.

Details of the concepts and mechanisms leading to an experimental observation of matter wave interference fringes are given in Chapter 6. Additionally, this chapter provides a scheme for producing multi-component BEC using an AOM technique for a dual optical plug. Finally the experimental results and the analysis of the matter wave interference data, based on the Fourier processing, will be presented.

The thesis culminates in Chapter 7 with a summary of the thesis, and a discussion of improvements and future prospects.

# Fundamental theory

## 2.1 Quantum structure of Rubidium

The relatively simple energy level structure of rubidium made the element very well known and popular in the field of atom optics. Rubidium belongs to the ‘hydrogen-like’ group of atoms that can be well understood using a modified Hydrogen atom theory. The atomic structure based on a single valence electron has been readily used in trapping and cooling experiments.

Rubidium is a soft, silvery-white metallic element of the alkali metal group. In Nature one can find two isotopes of Rubidium ( $^{85}\text{Rb}$ ,  $^{87}\text{Rb}$ ). The  $^{85}\text{Rb}$  isotope occurs with an abundance of 72% whereas  $^{87}\text{Rb}$  has an abundance of 28% [50]. Each isotope possesses a different nuclear spin value. For  $^{85}\text{Rb}$  the nuclear spin is  $I = 5/2$  and for  $^{87}\text{Rb}$  the nuclear spin is  $I = 3/2$ .

In an alkali metal there are two groundstate  $F$  hyperfine levels. For both isotopes of Rubidium we have  $F(I_{85/87}, J_g = \frac{1}{2}) \rightarrow F = I_{85/87} \pm \frac{1}{2}$ , where  $J$  is the quantum number for total electronic angular momentum and  $I$  is the quantum number for nuclear angular momentum. In the presence of a magnetic field each  $F$  level is split into additional, non degenerate, magnetic sublevels. Each  $F$  level includes  $2F + 1$  magnetic sublevels  $m_F$ , which range over  $-F, -F + 1, \dots, F - 1, F$ . The excited states are defined depending on the atomic transition, hence we can distinguish two excited state  $F$  levels reached by the D1 transition and four excited state  $F$  levels for D2 transition. For D1 line:  $F'(I_{85/87}, J_e = \frac{1}{2}) \rightarrow F' = I_{85/87} \pm \frac{1}{2}$  and similarly for D2 line  $F'(I_{85/87}, J_e = \frac{3}{2}) \rightarrow F' = I_{85/87} \pm \frac{1}{2}, I_{85/87} \pm \frac{3}{2}$ . These states can be designated as  $5^2\text{P}_{1/2}$  and  $5^2\text{P}_{3/2}$  and the D1 and D2 lines correspond to transitions to these

respective states from the ground state  $5^2S_{1/2}$ . The specific states are designated in well known terms of the Russell-Saunders (R-S) notation [51] in the form  $^{2S+1}L_J$  where  $S$  represents the total spin quantum number,  $L$  is the total orbital quantum number and  $J$  is the total angular momentum quantum number<sup>1</sup>. For cooling and trapping purposes we will be interested in the D2 line that links  $5^2S_{1/2} \rightarrow 5^2P_{3/2}$  the ground and excited state. In the Strathclyde experiment we reach BEC with  $^{87}\text{Rb}$  therefore we present only the energy level diagram with frequency separations for this isotope with  $I = 3/2$  (see Fig. 2.1). The quantum level diagram helps us to understand and follow the mechanisms implemented between the atomic quantum states. The selection rules for light absorption on the D2 line follows:  $\Delta F = 0, \pm 1$  and  $\Delta m_F = 0, \pm 1$ . Transitions of the form  $\Delta F = \Delta m_F = m_F = 0$  are not allowed. In our laser cooling setup the laser that enables atomic transitions between the  $F = 2 \rightarrow F' = 3$  levels is referred to as the ‘trap laser’.

### 2.1.1 Repump beam

If the atom is placed in the excited state  $F' = 3$  it is governed by transition rules to decay to the  $F = 2$  state. This cycle creates a closed loop and enables effective laser cooling. However it is possible that the atoms escape from the trapping cycle. The trap laser is capable of driving transitions not only to the  $F' = 3$  state but also to the  $F' = 2$  and  $F' = 1$  atomic states. When an atom is excited to an  $F' \neq 3$  it can decay to the  $F = 1$  ground state and is lost from the cooling cycle. To avoid accumulation of atoms in the  $F = 1$  ground state an additional laser has to be introduced to pump atoms from the dark state to the cooling transition again. This laser is known as the hyperfine repumping laser and in this thesis we refer to that laser as the ‘repump laser’. This laser is tuned to the  $F = 1 \rightarrow F' = 2$  transition. In the experiment the repump beam is overlayed with the trap beams, however different directions are possible.

It is also possible to create BECs in the ground quantum state  $|F = 1, m_F = -1\rangle$ . In order to allow the collection of atoms in the lowest ground state the repump beam has to be switched off. Examples of BEC creation in this state can be found in many references, e.g. [53, 54, 55].

---

<sup>1</sup>According to R-S notation the total orbital quantum number of value 0, 1, 2, 3, 4, 5... is designated by letters S, P, D, F, G, H... respectively.

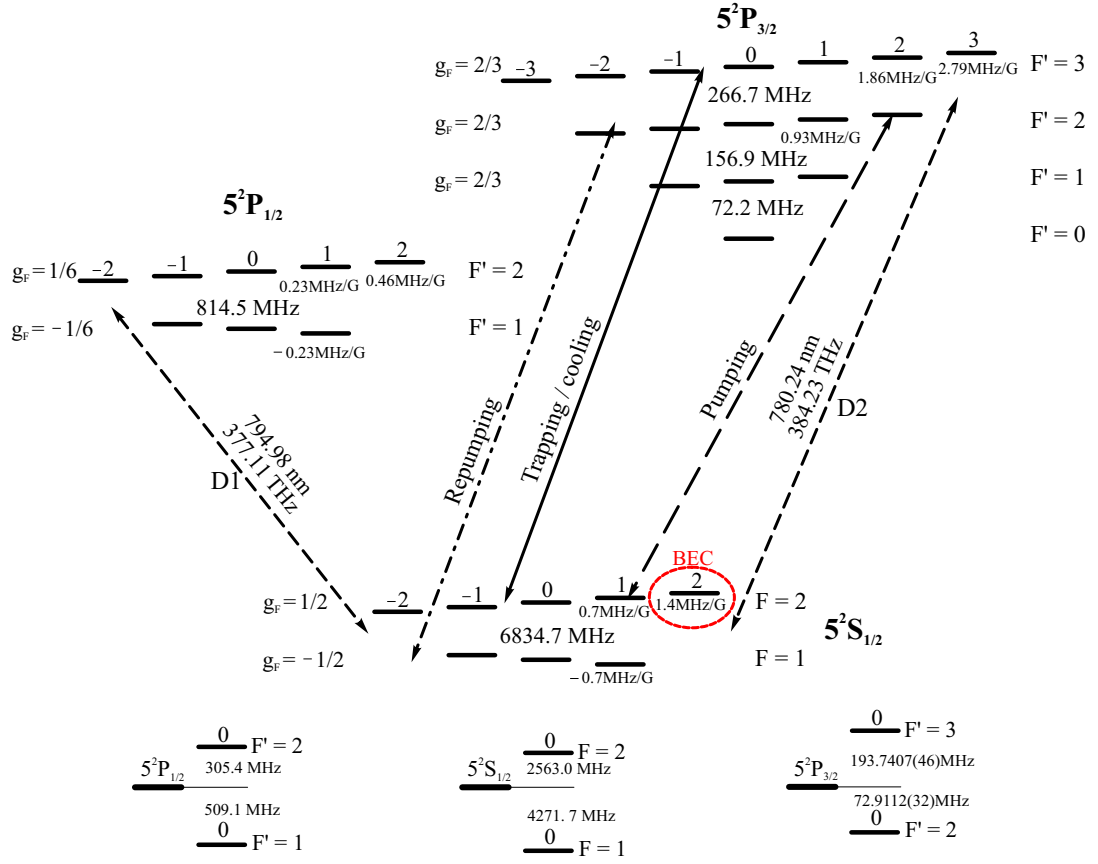


Figure 2.1: The energy level diagram for  $^{87}\text{Rb}$  (not to scale). The ground state for Rb is  $1s^2 2s^2 2p^6 3s^2 3p^6 3d^{10} 4s^2 4p^6 5s^1$ . Integers denote the  $m_F$  magnetic sublevels. The values for quantum level separations were taken from [52]. The quantum state  $|F = I + J = 2, m_F = 2\rangle$  (red circle) is the state where the Strathclyde BEC is generated.

### 2.1.2 Optical pumping

In the cooling cycle most of the atoms are expected to end up eventually in the ground state. Depending on the polarisation of the decaying transition atoms are distributed among the magnetic sublevels of the ground state. As is going to be explained in Sec. 3.2 atoms need to be reorganised to occupy the state where the further cooling and trapping process takes place. The  $|2, 2\rangle$  state is the ground quantum state utilised for BEC creation at Strathclyde. The process whereby one increases the population of atoms in particular quantum states is called optical pumping (OP) and in Sec. 3.2 we will present how to improve the efficiency of this mechanism.

## 2.2 Bose-Einstein statistics

A statistical description of an ensemble of bosons provides quantitative information about atoms, at temperature  $T$ . For indistinguishable particles Bose-Einstein statistics describe the population of the  $i$ -th energy state as

$$\langle N_i(E_i) \rangle = \frac{1}{e^{(E_i - \mu)\beta} - 1} \quad \text{for } \beta = (k_B T)^{-1}, \quad (2.1)$$

where  $N_i(E_i)$  is the population of atoms in the atomic state with energy  $E_i$  and  $\mu$  is the chemical potential. Similarly the population of the ground state with energy  $E_0$  can be written in form

$$\langle N_0(E_0) \rangle = \frac{1}{e^{(E_0 - \mu)\beta} - 1}. \quad (2.2)$$

Note that when  $\mu \rightarrow E_0$  there is a great increase in population in the ground state. In this section we will derive the critical temperature when the BEC transition occurs, allowing macroscopic occupation of the ground state to be observed. In order to derive this quantity we combine the theory from Refs. [5, 56].

### 2.2.1 Non-interacting bosons

We can define the total number of non-interacting bosonic particles and their energy as a sum over the discrete atomic states

$$N = \sum_{i=0}^{\infty} N_i(E_i), \quad E = \sum_{i=0}^{\infty} [E_i \cdot N_i(E_i)]. \quad (2.3)$$

For atoms that are trapped in a 3D harmonic trap the effective potential imposes the energy for each state as

$$E_i = \hbar(\omega_x i_x + \omega_y i_y + \omega_z i_z), \quad (i_{x,y,z} \geq 0), \quad (2.4)$$

where  $\omega_{x,y,z}$  are the trap frequencies in the  $x, y, z$  directions respectively, and  $i_{x,y,z}$  number the energy states in the trapping potential. For simplicity we assign the zero energy to the ground state,  $E_0 = 0 \mapsto i_x = i_y = i_z = 0$ .

The mean number of atoms in the trapping potential can be obtained by summing the atomic population over all the possible states, and hence, recalling Eq. 2.1 and Eq. 2.3, we get

$$\langle N \rangle = \sum_{i_{x,y,z}=0}^{\infty} \langle N_i(E_i) \rangle = \sum_{i_{x,y,z}=0}^{\infty} \frac{1}{e^{(E_i - \mu)\beta} - 1}. \quad (2.5)$$

Now we can introduce a coordinate system based on the space defined by perpendicular axes of  $i_{x,y,z}$ . With the assumption that  $\Delta E \ll k_B T$  in the given space the discrete

function from Eq. 2.5 can be replaced by the continuous function, and integration can take the place of the summation.

$$\iiint_{i_{x,y,z}=0}^{\infty} \frac{di_x di_y di_z}{e^{(E_i-\mu)\beta} - 1} \implies \left\{ \begin{array}{l} E_x = \hbar\omega_x i_x \\ E_y = \hbar\omega_y i_y \\ E_z = \hbar\omega_z i_z \end{array} \right\} \implies \frac{1}{\hbar^3\omega^3} \iiint_{E_{x,y,z}=0}^{\infty} \frac{dE_x dE_y dE_z}{e^{(E_i-\mu)\beta} - 1}. \quad (2.6)$$

In the above,  $\omega = \sqrt[3]{\prod_i \omega_i}$  for  $\{i = x, y, z\}$  is the geometric mean of the trapping frequencies. If the values  $E_{x,y,z}$  fulfill the condition  $E = E_x + E_y + E_z$ , and the function  $g(E)$  denotes the number of elements  $dE_x dE_y dE_z$  for an element  $dE$ , then the above equation can be transformed into

$$\frac{1}{\hbar^3\omega^3} \int_0^{\infty} \frac{g(E)dE}{e^{(E-\mu)\beta} - 1}. \quad (2.7)$$

The function  $g(E) = \frac{dG(E)}{dE}$  is also known as density of states function, where  $G(E)$  is the total number of states with energy less than  $E$ . In order to determine the number of all states with energy in the 0 to  $E$  we need to specify the function  $G(E)$ , that geometrically is represented by a four-sided triangular pyramid with corners at  $\{0, 0, 0\}, \{E, 0, 0\}, \{0, E, 0\}, \{0, 0, E\}$ , where the volume is defined as

$$G(E) = \frac{1}{3} \frac{E^2}{2} E = E^3/6. \quad (2.8)$$

From the above we get  $g(E) = \frac{dG(E)}{dE} = E^2/2$ , which when substituted in Eq. 2.7, results in

$$\langle N \rangle = \frac{1}{2\hbar^3\omega^3} \int_0^{\infty} \frac{E^2 dE}{e^{(E-\mu)\beta} - 1}. \quad (2.9)$$

Using a substitution  $\frac{1}{e^{(E-\mu)\beta} - 1} = \sum_{\xi=1}^{\infty} e^{\xi(\mu-E)\beta}$ , we obtain

$$\langle N \rangle = \frac{1}{2\hbar^3\omega^3} \sum_{\xi=1}^{\infty} e^{\xi\mu\beta} \int_0^{\infty} E^2 dE e^{-\xi E\beta}. \quad (2.10)$$

Using an additional substitution  $x = \xi E\beta$  and mathematical relation  $\int_0^{\infty} x^2 e^{-x} dx = \Gamma(3) = 2\Gamma(2) = 2$  leads to

$$\langle N \rangle = \frac{(k_B T)^3}{\hbar^3\omega^3} \sum_{\xi=1}^{\infty} e^{\xi\mu\beta} / \xi^3. \quad (2.11)$$

A consequence of Eq. 2.11 is that at a certain temperature, called the critical temperature,  $T_c$ , the chemical potential reaches the value  $\mu = 0$ , ( $\mu \mapsto E_0 = 0$ ). At that

---

<sup>2</sup>For a  $d$ -dimensional harmonic oscillator potential the density of states is given by:  $g(E) = \frac{E^{d-1}}{(d-1)!}$

stage a great increment in population of the ground atomic state occurs, known as Bose-Einstein condensation. When the chemical potential reaches 0, then Eq. 2.11, using the Riemann Zeta function  $\zeta(z) = \sum_{\xi=1}^{\infty} \xi^{-z}$ , takes the form

$$\langle N \rangle = \frac{(k_B T_c)^3}{\hbar^3 \omega^3} \sum_{\xi=1}^{\infty} 1/\xi^3 = \frac{(k_B T_c)^3}{\hbar^3 \omega^3} \zeta(3). \quad (2.12)$$

Rearranging Eq. 2.12 leads to an equation for the critical temperature,  $T_c = \frac{\hbar \omega}{k_B} \left( \frac{\langle N \rangle}{\zeta(3)} \right)^{1/3}$ , that depends on the number of atoms in the trap  $\langle N \rangle$  and the mean trapping frequency,  $\omega$ . The atoms that occupy the excited states are described by

$$\langle N_+ \rangle = \frac{(k_B T)^3}{\hbar^3 \omega^3} \zeta(3), \quad (2.13)$$

where we excluded atoms that are in the ground state. As the total number of atoms in the atomic trap is preserved,  $\langle N \rangle = \text{const.}$ , we can write

$$\langle N_0 \rangle = \langle N \rangle - \langle N_+ \rangle = \underbrace{\langle N \rangle \left( 1 - (T/T_c)^3 \right)}_{\text{CF}}, \quad (2.14)$$

for atoms that occupy the ground state of the atomic system. The CF term describes the relative fraction of condensed atoms with respect to the total atoms in the trap. This quantity is known as the condensate fraction. This relation is true for a three-dimensional harmonic oscillator potential, and with the assumption  $\langle N \rangle \rightarrow \infty$  and no interactions between particles. The description that includes interaction between atoms will be considered in the next section. The theory of quantum mechanical description follows Ref. [56].

## 2.3 Quantum mechanical description

The state of BEC, when all bosons are in the same single-particle state,  $\psi(\mathbf{r}, \mathbf{t})$ , can be written as a product state of  $N$  atoms

$$\Psi(\mathbf{r}_1, \mathbf{r}_2, \dots, \mathbf{r}_N, t) = \psi(\mathbf{r}_1, t) \cdot \psi(\mathbf{r}_2, t) \cdot \dots \cdot \psi(\mathbf{r}_N, t) = \bigotimes_{i=1 \rightarrow N} \Psi(\mathbf{r}_i, t), \quad (2.15)$$

with the single particle wave function  $\Psi(\mathbf{r}, t)$  normalised to unity  $\int d^3 \mathbf{r} |\Psi(\mathbf{r}, t)|^2 = 1$ . To describe the quantum mechanical behaviour of the single-particle wave-function we recall the fundamental equation for physical systems that evolve over time (time-dependent Schrödinger equation):

$$i\hbar \frac{\partial}{\partial t} \Psi(\mathbf{r}, t) = \left[ -\frac{\hbar^2 \nabla^2}{2m} + U(\mathbf{r}, t) \right] \Psi(\mathbf{r}, t) \equiv \hat{H} \Psi(\mathbf{r}, t), \quad (2.16)$$

where  $U(\mathbf{r}, t)$  is the potential the atom experiences. However, when the potential  $U$  becomes independent of time,  $U(\mathbf{r}, t) \rightarrow U(\mathbf{r})$ , one obtains the time-independent Schrödinger equation.

$$\left[ -\frac{\hbar^2 \nabla^2}{2m} + U(\mathbf{r}) \right] \psi(\mathbf{r}) = E\psi(\mathbf{r}), \quad (2.17)$$

where  $E$  stands for total atomic energy and  $\Psi(\mathbf{r}, t) \rightarrow \psi(\mathbf{r})e^{-i\omega t}$ . The above equations need to be considered in the case of an  $N$ -particle bosonic ensemble. For an accurate description of the bosonic ensemble the potential experienced by atoms has to be enriched by an additional effect. This additional contribution to the atomic potential energy  $U(\mathbf{r}, t)$  comes from the atomic interactions. Hence we may write the total potential in the form of two direct contributions:

$$U(\mathbf{r}, t) = \underbrace{U_{\text{ext}}(\mathbf{r}, t)}_{(1)} + \underbrace{U_{\text{int}}(\mathbf{r}, t)}_{(2)}. \quad (2.18)$$

In experiments term (1) represents the magnetic trapping potential. When defining the ratio of axial to radial trap frequencies of the external (magnetic) potential as  $\mathcal{R} := \frac{\omega_z}{\omega_\perp}$ , we get the typical cylindrically symmetric harmonic form:

$$U_{\text{ext}}(\mathbf{r}) = \frac{m}{2} \omega_\perp^2 (r_\perp^2 + \mathcal{R}^2 z^2) \quad (2.19)$$

Depending on the trap frequencies in axial and radial directions, one can obtain different trapping geometries: cigar-shaped trap for  $\mathcal{R} < 1$ , spherical trap for  $\mathcal{R} = 1$ , pancake shaped trap for  $\mathcal{R} > 1$ .

Term (2) in Eq. 2.18 represents the potential created by atomic interactions and refers to the internal contribution of the total potential. The internal potential is proportional to the number of particles in the ensemble. For  $N$  bosons described by a wave function the potential due to atomic interactions has the form:

$$U_{\text{int}}(\mathbf{r}, t) = N \int d^3 \mathbf{r}' \hat{\Psi}^\dagger(\mathbf{r}', t) V(\mathbf{r} - \mathbf{r}', t) \hat{\Psi}(\mathbf{r}', t), \quad (2.20)$$

where  $\hat{\Psi}(\mathbf{r}', t)$  and  $\hat{\Psi}^\dagger(\mathbf{r}', t)$  are the boson field operators that annihilate and create a particle at the position  $\mathbf{r}'$  and at time  $t$ , respectively; and term  $V(\mathbf{r} - \mathbf{r}', t)$  represents the two-body interaction potential on an atom at  $\mathbf{r}$  due to another atom at position  $\mathbf{r}'$  at time  $t$ . From the fact that the gas of bosons is in a dilute, weakly interacting sample we neglect the three- and many-body collisions. The many-body Hamiltonian

describing  $N$  interacting bosons confined by an external potential takes the form [4] :

$$\begin{aligned} \hat{H} = & \int d^3\mathbf{r} \hat{\Psi}^\dagger(\mathbf{r}, t) \left[ -\frac{\hbar^2 \nabla^2}{2m} + U_{\text{ext}}(\mathbf{r}, t) \right] \hat{\Psi}(\mathbf{r}, t) \\ & + \frac{1}{2} \iint d^3\mathbf{r} d^3\mathbf{r}' \hat{\Psi}^\dagger(\mathbf{r}, t) \hat{\Psi}^\dagger(\mathbf{r}', t) V(\mathbf{r} - \mathbf{r}', t) \hat{\Psi}(\mathbf{r}', t) \hat{\Psi}(\mathbf{r}, t) . \end{aligned} \quad (2.21)$$

Bose-Einstein condensation occurs when the atom number,  $N_0$ , in a particular state becomes very large,  $N_0 \gg 1$ . In this limit quantum fluctuation in the number of atoms become negligible. In the mean-field description of a dilute Bose gas formulated by Bogoliubov [57] the field operator can be generalised as

$$\hat{\Psi}(\mathbf{r}, t) = \Phi(\mathbf{r}, t) + \hat{\Psi}'(\mathbf{r}, t) , \quad (2.22)$$

where  $\Phi(\mathbf{r}, t)$  is the function that represents a classical field called *the wave function of the condensate* [4]. This complex function is defined as the expectation value of the field operator:  $\Phi(\mathbf{r}, t) \equiv \langle \hat{\Psi}(\mathbf{r}, t) \rangle$ . In Eq. 2.22 the field operator is decomposed into a ‘mean-field’ term  $\Phi(\mathbf{r}, t)$ , and a small fluctuating term which can be treated as a perturbation  $\hat{\Psi}'(\mathbf{r}, t)$ . In order to obtain the equation for the condensate wave function  $\Phi(\mathbf{r}, t)$ , we need to apply the field operator  $\hat{\Psi}(\mathbf{r}, t)$  using the Heisenberg equation with the many-body Hamiltonian (Eq. 2.21):

$$i\hbar \frac{\partial}{\partial t} \hat{\Psi}(\mathbf{r}, t) = [\hat{\Psi}, \hat{H}] = \left[ -\frac{\hbar^2 \nabla^2}{2m} + U_{\text{ext}}(\mathbf{r}, t) + \int d^3\mathbf{r}' \hat{\Psi}^\dagger(\mathbf{r}', t) V(\mathbf{r}' - \mathbf{r}, t) \hat{\Psi}(\mathbf{r}', t) \right] \hat{\Psi}(\mathbf{r}, t) . \quad (2.23)$$

In the dilute and cold gas approximation (when the free mean path of a travelling atom is greater than the range of interaction) the interacting term  $V(\mathbf{r} - \mathbf{r}', t)$  in the integral (Eq. 2.23) can be replaced by an effective interaction  $g \delta(\mathbf{r} - \mathbf{r}', t) = \frac{4\pi\hbar^2 a}{m} \delta(\mathbf{r} - \mathbf{r}', t)$ , where  $a$  is the scattering length. For  $^{87}\text{Rb}$  the scattering length  $a = 5.77 \text{ nm} = 109 a_0$ , where  $a_0$  is the Bohr radius [58]. As a consequence of applying an effective interaction into Eq. 2.23 ( $\hat{\Psi} \rightarrow \Phi$ ) we obtain a nonlinear Schrödinger equation, known as the time-dependent Gross-Pitaevskii equation:

$$i\hbar \frac{\partial}{\partial t} \Phi(\mathbf{r}, t) = \left[ -\frac{\hbar^2 \nabla^2}{2m} + U_{\text{ext}}(\mathbf{r}, t) + gN |\Phi(\mathbf{r}, t)|^2 \right] \Phi(\mathbf{r}, t), \quad (2.24)$$

and its equivalent, when the external potential does not depend on time (static potential), is

$$\mu \phi(\mathbf{r}) = \left[ -\frac{\hbar^2 \nabla^2}{2m} + U_{\text{ext}}(\mathbf{r}) + gN |\phi(\mathbf{r})|^2 \right] \phi(\mathbf{r}), \quad (2.25)$$

with the relation  $\Phi(\mathbf{r}, t) = \phi(\mathbf{r}) e^{-i\mu t/\hbar}$ , where  $\mu$  is the chemical potential of the condensate. In the regime of high atom number  $N$  the kinetic energy term in the

Gross-Pitaevskii equation becomes negligible [59] ( $\frac{\hbar^2 \nabla^2}{2m} \rightarrow 0$ ). This step, known as the *Thomas-Fermi* approximation, occurs when the kinetic energy term is dominated by the magnetic and interatomic potentials.

In this chapter we provided a brief theory of Bose-Einstein statistics. We also included a quantum mechanical description that will be used later on in this thesis to model the behaviour of atoms for given conditions. The general quantum mechanical description will be adapted to satisfy the conditions of the Strathclyde experimental setup in Sec. 6.6. However, before applying the content of this chapter to model possible solutions for the BEC we first introduce theoretically the main stages on the path to BEC. The next chapter will involve a description of laser cooling and trapping, magnetic trapping and evaporative cooling. Additionally, the end of the next chapter will provide a general characteristic of the optical dipole potential, and finally we will conclude with an introduction to atom interferometry and its applications.

## How does it work?

### 3.1 Laser cooling - Molasses and MOT

Discovering and understanding light's properties is an intriguing and extremely interesting topic. Many famous scientists have theoretically and experimentally pursued the nature of light phenomena. In 1873 Maxwell calculated the force exerted by electromagnetic waves on a solid body. The world had to wait 28 years for experimental demonstration and proof of Maxwell's theory. In 1901 Nichols and Hull verified experimentally the existence of light radiative pressure [60]. Frisch also showed that light could in fact exert force on matter [61]. In 1933 he demonstrated experimentally momentum transfer to an atom using the photon absorption mechanism with sodium atoms and a sodium resonance lamp. A revolution in our way of looking at light was made when Einstein applied quantum theory to the electromagnetic wave description. Light was no longer treated only classically (as waves) but its quantum nature (particle-like) was considered.

The next big step forward happened when tunable lasers were developed. Having such a useful tool in hand scientists could move forward in revealing previously undiscovered properties of light and its interaction with atoms. It was probably inevitable that after developing lasers and observing their effect on atoms researchers started to wonder about controllable momentum transfer from the light to the atoms. In 1975 the technique of laser cooling was proposed by two independent groups - Hänsch and Schawlow at Stanford University [24] and Wineland and Dehmelt at the University of Washington [62]. Two, complementary explanations saw laser cooling as a process of velocity dependent radiation pressure from the laser and alternatively as a Raman

process causing the reduction of energy of an atom. In the next section we will give a brief description of how the laser cooling mechanism works and show some widely used experimental setups.

### 3.1.1 Radiation pressure force

The first application of radiation pressure was to decelerate an atomic beam, where the deceleration was caused by absorption of counter-propagating resonant laser [63]. Not long after atoms slowing experiments the idea of laser cooling came to its experimental realisation. In 1985 cooling of neutral atoms by resonance radiation pressure was reported by Chu *et al.* in Ref. [64]. The setup used in Ref. [64] was not a trap itself, but as we will see in Sec. 3.1.3, it is a major component of the atomic trap.

When laser radiation is used for cooling the atoms we need to introduce a few important quantities. Consider an atom travelling within the cross section of the laser beam that is near a resonance line of the atom. The atom is bombarded with millions of photons in every second. The magnitude of the momentum from a single photon is given by:

$$p = \frac{h}{\lambda} = \hbar k , \quad (3.1)$$

where  $h$  is Plank's constant, ( $h = 2\pi\hbar$ ) and  $\lambda$  is the wavelength of the laser light. Close to the atomic resonance, the scattering rate of a two level atom, which is the rate of absorbing and spontaneously emitting photons, is in the form of the Lorentzian absorption profile [65]:

$$R(I, \Delta) = \frac{\Gamma}{2} \frac{I/I_{\text{sat}}}{1 + I/I_{\text{sat}} + (2\Delta/\Gamma)^2} , \quad (3.2)$$

where  $\tau = 1/\Gamma$  is the excited state lifetime ( $\tau = 26.2$  ns for rubidium natural linewidth  $\Gamma = 2\pi \times 6.07$  MHz),  $I/I_{\text{sat}}$  represents the ratio of the total light intensity to the saturation intensity,  $I_{\text{sat}}$ , and for the transition,  $\Delta$  is the detuning of the laser frequency from resonance. If  $\omega_0$  is the frequency interval between ground and excited state, and the laser beam has frequency  $\omega$  the detuning is defined as  $\Delta = \omega - \omega_0$ . In graphical representation  $\Gamma$  is the full width at half maximum, FWHM, of the Lorentzian function and also describes the rate at which the excited state population decays to the ground state. The saturation intensity characterises the strength of the laser induced coupling between atomic states ( $|g\rangle \rightarrow |e\rangle$ ). In many textbooks (e.g. Ref. [7]) the saturation intensity is found to be:

$$I_{\text{sat}} = \frac{h c \pi \Gamma}{3 \lambda^3} . \quad (3.3)$$

The saturation intensity for the D2 line of  $^{87}\text{Rb}$  atoms used in our experiment is  $I_{\text{sat}} = 1.67 \text{ mW/cm}^2$ , at which  $\frac{1}{4}$  of the population occupies the excited state.

In the case of low intensity laser fields, when  $I \ll I_{\text{sat}}$ , the effect of stimulated emission from the excited state in the atomic system can be neglected, and the population is mostly in the ground state. However when the light intensity increases and two level atom is found to be in the high intensity regime,  $I \gg I_{\text{sat}}$ , the stimulated emission rate can no longer be neglected. That leads to saturation. At high intensities the scattering rate (Eq. 3.2) saturates to  $\Gamma/2$ . We can rewrite the scattering rate equation as

$$R(I, \Delta) = \frac{\Gamma}{2} \left( \frac{I/I_{\text{sat}}}{1 + I/I_{\text{sat}}} \right) \left( \frac{1}{1 + (2\Delta/\Gamma')^2} \right), \quad (3.4)$$

where  $\Gamma' = \Gamma\sqrt{1 + I/I_{\text{sat}}}$  is known as the power-broadened linewidth of the transition. When the laser intensity  $I$  is equal to the saturation intensity we can observe power broadening of the linewidth of the transition by a factor of  $\sqrt{2}$ .

As an atom is absorbing photons with momenta  $\hbar\mathbf{k}$ , at a rate  $R$ , it will experience a force due to radiation pressure

$$\mathbf{F} = d\mathbf{p}/dt = \hbar\mathbf{k}R. \quad (3.5)$$

Every absorption and emission of a photon results in a change of momentum of an atom. The momentum involved in this effect is related to the atomic recoil velocity  $\mathbf{v}_{\text{rec}}$  as

$$\Delta\mathbf{p} = m\mathbf{v}_{\text{rec}} = \hbar\mathbf{k} \longrightarrow \mathbf{v}_{\text{rec}} = \frac{\hbar\mathbf{k}}{m}, \quad (3.6)$$

where  $m$  is the atomic mass,  $\mathbf{k} = \frac{2\pi}{\lambda}\hat{\mathbf{k}}$ ,  $\hat{\mathbf{k}}$  is the unit vector describing direction of incoming photon and  $\lambda$  is the wavelength of the light. The recoil velocity is a velocity that corresponds to single photon recoil momentum. The recoil velocities for  $^{85}\text{Rb}$  and  $^{87}\text{Rb}$  are presented in Table 3.1.

Species	D1 ( $5^2S_{1/2} \Rightarrow 5^2P_{1/2}$ )	D2 ( $5^2S_{1/2} \Rightarrow 5^2P_{3/2}$ )
$^{85}\text{Rb}$	$v_{\text{rec}} = 5.91 \text{ mm/s}$	$v_{\text{rec}} = 6.02 \text{ mm/s}$
$^{87}\text{Rb}$	$v_{\text{rec}} = 5.77 \text{ mm/s}$	$v_{\text{rec}} = 5.88 \text{ mm/s}$

Table 3.1: The D1 and D2 transition line recoil velocities for  $^{85}\text{Rb}$  and  $^{87}\text{Rb}$

Having the recoil velocity we can straight away define the recoil energy as

$$E_{\text{rec}} = \frac{mv_{\text{rec}}^2}{2} = \frac{\hbar^2 k^2}{2m}. \quad (3.7)$$

The above expression is also related to recoil temperature limit which corresponds to atoms with an average momentum of one photon recoil

$$k_{\text{B}}T_{\text{rec}} = \frac{\hbar^2 k^2}{m} \longrightarrow T_{\text{rec}} = \frac{2E_{\text{rec}}}{k_{\text{B}}} . \quad (3.8)$$

### 3.1.2 Optical molasses

In this section we explain how the radiation pressure force can be used for cooling atoms. To show the main idea behind laser cooling we start from a simple one-dimensional model which then can be extended to more dimensions.

Consider an atom travelling with velocity  $v$  exposed to two laser beams that are derived from the same source. The schematic of the beam alignment is shown in Fig. 3.1. When two counter-propagating beams are near an atomic resonance, but detuned to

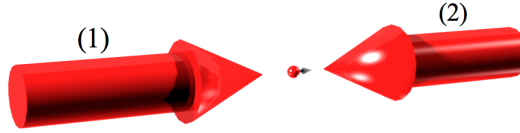


Figure 3.1: Two counter-propagating laser beams irradiate an atom possessing certain velocity  $v$ . For simplicity the velocity of the atom is aligned with the direction of propagation of one laser beam.

the red (*i.e.* low frequency side) there is always a force counteracting the motion of the atom. The photon-atom momentum transfer results in a change of momentum of the atom which causes a reduction of the kinetic energy related to lowering of the temperature [66, 67]. The reemission of the photon from the atom has no preferred direction, hence the direction of the recoil momentum is random – in analogy to Brownian motion [68], and atoms may drift away.

In the cooling mechanism the Doppler effect plays a key role. When two beams are detuned to the red the atom gets closer to resonance with the laser field opposing its motion, and at the same time gets further detuned from resonance with the other beam. The imbalance of these two forces exerted by two laser beams results in a net force opposite to  $v$ . The maximum average force is achieved when the light from the laser matches resonance with an atomic transition.

The radiation pressure force on the atom from two laser beams from Eq. 3.5 is:

$$\mathbf{F}(I, \Delta) = \sum_{i=1}^2 \hbar \mathbf{k}_i R(I, \Delta_i) , \quad (3.9)$$

where  $\Delta_i$  are the effective detunings of the two laser beams. When an atom has a velocity  $\mathbf{v}$  and is travelling in a laser beam containing photons with wave vector  $\mathbf{k}$  it will observe different detunings from two counter-propagating beams. The Doppler shifted angular frequency seen by an atom when travelling in the same direction, as the photons from the laser beam (1) is:

$$\Delta_1 = \Delta - kv, \quad (3.10)$$

for  $\Delta = \omega_1 - \omega_0$ . Similarly one can express the Doppler shifted angular frequency from the other laser :

$$\Delta_2 = \Delta + kv, \quad (3.11)$$

for  $\Delta = \omega_2 - \omega_0$ . In the pictured setup (Fig. 3.1) the frequency of the laser beam (1) is Doppler shifted to the red, while the frequency of the laser on the (2) is Doppler shifted to the blue.

Including the detunings from the two laser beams we can expand Eq. 3.9 as:

$$F(I, \Delta)_{1D} = \hbar k [R(I, \Delta - kv) - R(I, \Delta + kv)] . \quad (3.12)$$

From the definition of photon scattering rate the force  $F(I, \Delta)_{1D}$  is a difference of two Lorentzians. For small atomic velocities such that  $|kv| \ll \Gamma$  and  $|kv| \ll \Delta$  the cooling force has a linear response to all the atomic velocities ( $\Delta < 0$ ). This viscous damping force can be written as  $F = -\alpha v$  where  $\alpha$  is a damping coefficient in the form [65, 69]:

$$\alpha = -4\hbar k^2 \frac{I}{I_{\text{sat}}} \frac{(2\Delta/\Gamma)}{\left[1 + 2I/I_{\text{sat}} + (2\Delta/\Gamma)^2\right]^2}, \quad (3.13)$$

which is derived from Eq. 3.12. The term  $I/I_{\text{sat}}$  from the denominator can be neglected in the low intensity regime.

The damping force exists as a net effect of averaging many photon absorption/emission cycles. The two counter-propagating beams (one-dimensional) setup can be extended to three dimensions and hence Eq. 3.12 becomes:

$$\mathbf{F}(I, \Delta)_{3D} = \hbar k \sum_{c=x,y,z} [R_c(I, \Delta - kv_c) - R_c(I, \Delta + kv_c)] \hat{\mathbf{c}} . \quad (3.14)$$

The 3D setup incorporates three orthogonal pairs of counter-propagating laser beams (Fig. 3.2).

The 3D viscous field of photons from counter-propagating laser beams is commonly called *optical molasses*. The first demonstration of optical molasses was done by Chu



Figure 3.2: Three dimensional optical molasses. The setup of orthogonally orientated 3 pairs of red-detuned laser beams provide a syrup-like photon environment that interacts with atoms present in the cross section of all laser beams.

*et al.* [64] in 1985. Optical molasses introduced a notch on the temperature scale called the *Doppler temperature*. The Doppler cooling limit is imposed by the balance between the cooling force and heating from the cyclic process of random photon absorptions and emissions. A good approximation of Doppler temperature for low laser intensity is given as [65]:

$$T_D = \frac{\hbar\Gamma}{4k_B} \frac{1 + (2\Delta/\Gamma)^2}{2|\Delta|/\Gamma}. \quad (3.15)$$

This temperature reaches its minimum value when detuning  $\Delta$  is equal to half the value of the natural linewidth of the laser-driven transition  $-\Gamma/2$ . That results in

$$T_{D[\Delta=-\Gamma/2]} = \frac{\hbar\Gamma}{2k_B}. \quad (3.16)$$

The Doppler cooling limit differs for different species since they have different natural linewidths of the atomic transition. For example the Doppler temperature for both Rb isotopes of the D<sub>2</sub> line ( $5^2S_{1/2} \rightarrow 5^2P_{3/2}$ ) with natural linewidth (FWHM) of  $2\pi \times 6.07$  MHz is  $145 \mu\text{K}$ . Similarly for Na ( $\Gamma = 2\pi \times 10$  MHz)  $T_D$  nears  $240 \mu\text{K}$ .

Although this optical setup has an advantage of reducing all three atomic velocity components it does not confine the atoms into a spatial volume. To achieve spatial confinement for damped atoms in optical molasses a slight modification can be made by imposing an additional inhomogeneous magnetic field.

### 3.1.3 Magneto–optical trap

The first demonstration of a combined optical molasses and magnetic field for cooling and trapping atoms was demonstrated by Raab *et al.* in 1987. This arrangement is called the *magneto-optical trap* (MOT). The inhomogeneous magnetic field used in the first realisation of the magneto-optical trap was in the form of a spherical quadrupole magnetic field  $\mathbf{B} = B_1\{x, y, -2z\}$  and it originated from two opposed current loops in the anti-Helmholtz configuration. In this section only a brief outline on the magnetic field is presented whereas more details about the field used to form the MOT will be given in Sec. 3.3.2.

The magnetic field due to two coaxial current loops with opposite current flow provides a position–dependent Zeeman shift. The magnetic field is zero at the centre point of the trap. This place defines a point around which atoms in the MOT accumulate. From that point outwards the magnetic field changes linearly, changing sign at the origin. In the presence of a magnetic field the energy levels of the quantum states are altered and hence the frequencies of the atomic transitions. The Zeeman shift is proportional to the change in magnetic field. A transition frequency is shifted by  $\frac{\mu_B}{h} g_{F'} m_{F'} B$  as already introduced in Sec. 1.2.1. For clarity we use a prime when referring to the excited state in the following explanation.

For simplicity let's illustrate the working principle of the magneto-optical trap considering a hypothetical four-level atom with a ground state  $|F, m_F\rangle = |0, 0\rangle$  and non-degenerate excited states  $|F', m_{F'}\rangle \rightarrow |1, -1\rangle, |0, 0\rangle, |1, 1\rangle$ . The atomic transition between the ground  $F$  and excited  $F'$  energy level depends on the polarisation of the light used to excite an electron to the upper state. In the case of  $\sigma^+$  light polarisation the transition satisfies the magnetic sublevel relation as  $\Delta m_F = m_{F'} - m_F = +1$  whereas for  $\sigma^-$  light polarisation the transition obeys  $\Delta m_F = -1$ . We can also distinguish  $\pi$  polarisation that does not alter the magnetic sublevel when exciting an atom to the upper state. A simple diagram displays the relation between different transitions and the relevant change in the magnetic sublevels – see Fig. 3.3.

Let's for simplicity consider only one pair of counter-propagating beams. We will base our explanation on our previous 1D setup for optical molasses but with specified polarisation for the light. We will set the polarisation of the two beams to be  $\sigma^-$ . In the case of circularly polarised light the polarisation of a laser beam depends solely on the motion of the light's electric field vector around the local magnetic field. The laser polarisation may be altered from  $\sigma^-$  to  $\sigma^+$  by applying a  $\pi$  phase shift to one

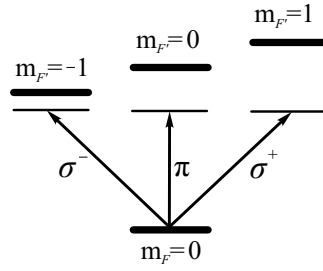


Figure 3.3: Transitions between Zeeman sublevels for a simple four-level atom where the excited state splits into 3 magnetic substates. Different polarisations of the light allows different transitions within the atom. Transitions marked as  $\sigma^+$  and  $\sigma^-$  drive the atoms with respect to the Zeeman sublevels as  $m_F \rightarrow m_{F'} + 1$  and  $m_F \rightarrow m_{F'} - 1$  respectively.

projection of the electric component of the electromagnetic laser field or reversing the orientation of the magnetic field. In the MOT configuration the magnetic field changes direction at the centre of the trap, hence when light with  $\sigma^-$  polarisation passes the centre point it becomes  $\sigma^+$  as it exits the MOT. For atoms with a small displacement from the origin of the trap ( $B > 0$ ) the (incoming) laser field with  $\sigma^-$  polarisation is close to resonance with state  $|1, 1\rangle$  and the radiation pressure force is strongest pointing towards the MOT centre. When the laser field polarisation becomes  $\sigma^+$  the detuning for the  $\Delta m_F = 1$  transition is larger and therefore the radiation pressure force become weaker. The same analogy applies for counter-propagating laser beams. When the atom is found to be at the point where the magnetic field cancels out the Zeeman splitting disappears. Also at that point a force from two counter-propagating beams vanishes due to the balance between two opposing laser fields. As a result any atom not located in the centre of the trap experiences a force pointing always to the centre of the MOT, which allows atomic confinement, i.e. trapping. The typical setup for a magneto-optical trap is presented in Fig. 3.4.

### Below the Doppler limit

For nearly ten years researchers had accepted  $T_D$ , the Doppler temperature, as the lowest possible temperature in laser cooling. This was soon to change. Although the Doppler temperature prediction for sodium is  $240 \mu\text{K}$  this theory was challenged in 1988 [70]. In this experiment sodium atoms were cooled in three-dimensional optical

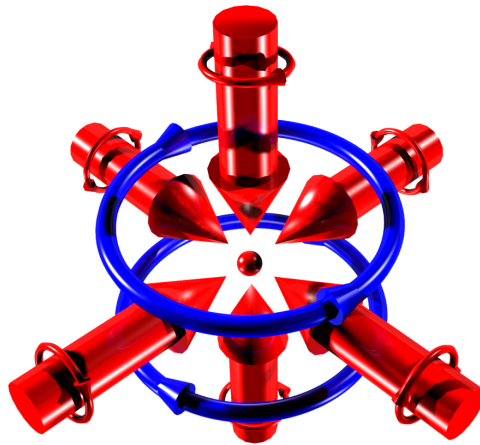


Figure 3.4: 3D magneto-optical trap. MOT configuration as stated by name combines magnetic and optical elements. Two coaxial coils (blue) with opposite current directions (arrows) provide the magnetic field effectively causing a restoring force towards the trap centre when combined with the laser beams (red). The circular arrows mark the  $\sigma_-$  polarisation for each ingoing laser beam.

molasses confinement [26]. The temperature of the atoms released from optical molasses was measured to be  $43 \pm 20 \mu\text{K}$  [70], which shattered the idea of the Doppler temperature limit by a factor of  $\approx 6$ . In addition, the temperatures achieved did not follow the frequency dependence assumed in the Doppler theory.

The simple two-level Doppler schematic model from Sec. 3.1.3 explaining operation of the magneto-optical trap fails with multilevel atoms. The hyperfine atomic states impose more complicated mechanisms on the cooling effect. The additional cooling processes also rely on the inhomogeneous radiation field produced by two counter-propagating laser beams. The description of these sub-Doppler cooling mechanisms, including the Sisyphus effect, can be found in Refs. [5, 71, 72, 73]

With laser cooling one can obtain temperatures of order  $\sim \mu\text{K}$ , which are still considerably far away from achieving BEC. There are limits to the temperature and density in laser cooling. To get better PSD one needs to improve temperature or density, or both. If the density of the atomic cloud becomes too large, light scattered by one atom is reabsorbed by others, causing a repulsion between them. The solution to this problem can be obtained using different confining techniques that make use of magnetic fields. In the next section we will consider the magnetic field influence on atoms and

typical magnetic field trap configurations.

## 3.2 Magnetic influence on atoms

An atom with a magnetic moment can be confined by an inhomogeneous magnetic field due to interaction of its magnetic moment and the field. The idea of using a non-uniform magnetic field to manipulate atoms was first employed in the realisation of Otto Stern and Walther Gerlach's experiment in 1921, where they proved the reality of spin quantisation [74]. The inhomogeneous field from magnetic poles made a thermal atomic beam of silver deflect in two quantised orientations. The deflection is proportional to the spin and to the magnitude of the magnetic field gradient.

### 3.2.1 Zeeman effect

In the absence of external magnetic fields all magnetic sublevels  $m_F$  for each hyperfine energy level  $F$  are degenerate. However, when an atom experiences a uniform external magnetic field  $\mathbf{B}$ , the energy levels are shifted. The effective Hamiltonian for an atom under the influence of a magnetic field, in the basis of the outer electron spin  $\mathbf{S}$ , orbital  $\mathbf{L}$  and the total nuclear  $\mathbf{I}$  angular momentum states  $|Sm_S; Lm_L; Im_I\rangle$  takes the form

$$\hat{H}_{(B)} = \mu_B(g_S\mathbf{S} + g_L\mathbf{L} + g_I\mathbf{I}) \cdot \mathbf{B} = \underbrace{\mu_B(g_S S_z + g_L L_z + g_I I_z)}_{\text{magnetic field aligned with the } z \text{ axis}} B_z, \quad (3.17)$$

where the quantities  $g_S, g_L, g_I$  are the electron spin, electron orbital, and nuclear  $g$ -factors, respectively. The corresponding values of these  $g$ -factors are presented in Tab. 3.2. If magnetic fields introduce an energy shift that is small compared to the

Electron spin $g$ -factor	$g_S$	2.0023193043622(15)*
Electron orbital $g$ -factor	$g_L = \frac{m_{\text{nuc}} - m_e}{m_{\text{nuc}}}$	0.999994
Nuclear spin $g$ -factor	$g_I$	-0.0009951414(10)**

Table 3.2:  $^{87}\text{Rb}$  field interaction parameters. \*/\*\* the values taken from Ref. [75] and [76] respectively. The values  $m_{\text{nuc}}/m_e$  stand for the nuclear / electron mass.

fine-structure splitting,  $J$  is a good quantum number which results in the interaction Hamiltonian

$$\hat{H}_{(B)\text{fs}} = \mu_B(g_J J_z + g_I I_z) B_z, \quad (3.18)$$

where  $J$  is the total electronic momentum ( $\mathbf{J} = \mathbf{S} + \mathbf{L}$ ) and the  $g_J$ -factor can be determined from the relation [7]:

$$g_J = g_L \frac{J(J+1) - S(S+1) + L(L+1)}{2J(J+1)} + g_S \frac{J(J+1) + S(S+1) - L(L+1)}{2J(J+1)} \quad (3.19)$$

$$\simeq \frac{3J(J+1) + S(S+1) - L(L+1)}{2J(J+1)} \implies \text{for } g_L \simeq 1 \text{ and } g_S \simeq 2. \quad (3.20)$$

We follow a similar approach for magnetic fields with a small energy shift compared to the hyperfine-structure splitting, when  $J$  is no longer a good quantum number, and has to be replaced with the  $F$  quantum number ( $\mathbf{F} = \mathbf{J} + \mathbf{I}$ ). In result the interaction Hamiltonian becomes

$$\hat{H}_{(B)\text{hfs}} = \mu_B g_F F_z B_z, \quad (3.21)$$

and accordingly the hyperfine  $g$ -factor is found to be [7]

$$g_F = g_J \frac{F(F+1) - I(I+1) + J(J+1)}{2F(F+1)} + g_I \frac{F(F+1) + I(I+1) - J(J+1)}{2F(F+1)} \quad (3.22)$$

$$\simeq g_J \frac{F(F+1) - I(I+1) + J(J+1)}{2F(F+1)} \implies \text{as } g_I \ll g_J \quad (3.23)$$

The corresponding Hamiltonian (Eq. 3.21) energy shift of atomic levels takes the form

$$\Delta E_{(B)\text{hfs}} = \mu_B g_F m_F B_z \quad (3.24)$$

For an alkali atom the two hyperfine levels of the ground state with energies  $E_{|F_-=I-1/2, m_F\rangle}(B)$  and  $E_{|F_+=I+1/2, m_F\rangle}(B)$ , which correspond to their state total angular momenta  $F_- = I - 1/2$  and  $F_+ = I + 1/2$  respectively, can be described using the well-known *Breit-Rabi* formula [52]:

$$E_{|J=1/2, m_J I m_I\rangle} = -\frac{\Delta E_{\text{hfs}}}{2(2I+1)} + g_I \mu_B m B \pm \frac{\Delta E_{\text{hfs}}}{2} \left(1 + \frac{4m}{2I+1} \mathcal{X} + \mathcal{X}^2\right)^{1/2}, \quad (3.25)$$

where  $\mathcal{X} = (g_J - g_I) \mu_B B / \Delta E_{\text{hfs}}$ ,  $\Delta E_{\text{hfs}} = A_{\text{hfs}}(I + 1/2)$  is the hyperfine splitting ( $A_{\text{hfs}}/h = 6835$  MHz for  $^{87}\text{Rb}$ ) and  $m = m_I \pm m_J$ . The result of implementing this formula for the ground state of  $^{87}\text{Rb}$  is presented in Fig. 3.5. The experimental magnetic fields used in the generation of the BEC are in the region of  $< 1$  mT.

The Zeeman effect results in the creation of two groups of atoms depending on their hyperfine state: (1) weak or low field seeking atoms which are attracted toward a local minimum  $B$  field and (2) strong or high field seeking atoms that are attracted toward a local maximum  $B$  field. The low (high) field seekers correspond to the hyperfine states with  $g_F m_F > 0$  ( $g_F m_F < 0$ ). These particular properties are used in magnetic trapping of atoms and we will discuss this in the next section.

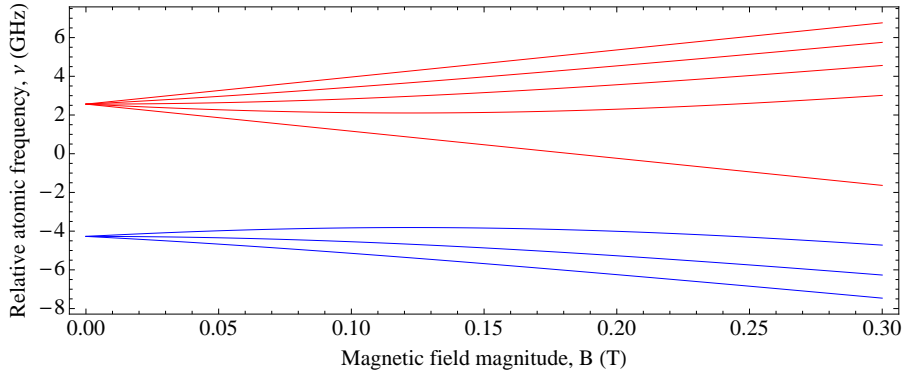


Figure 3.5: The ground state Breit-Rabi diagram for  $^{87}\text{Rb}$ . The frequency shift dependence on the magnetic field for each magnetic sublevel  $m_F$  of the ground state. Ground state energy levels  $|F, m_F\rangle$  are: (upper line)  $|2, 2\rangle, |2, 1\rangle, |2, 0\rangle, |2, -1\rangle, |2, -2\rangle, |1, -1\rangle, |1, 0\rangle, |1, 1\rangle$  (lower line), respectively. The hyperfine splitting between  $F = 1$  and  $F = 2$  ground states is 6835 MHz.

### 3.3 Magnetic fields - methodology

In this section we will deal with weak-field seeking atoms. Before considering the coil configurations for magnetic traps let us analyse a few concepts for determining the magnetic field and its magnitude. The well-known Biot-Savart law determines the magnetic field  $\mathbf{B}$  generated by an electric current in a wire:

$$d\mathbf{B} = \frac{\mu_0 I}{4\pi} \frac{d\mathbf{l} \times \hat{\mathbf{r}}}{|\mathbf{r}|^2}, \quad (3.26)$$

where the contribution of the magnetic field  $d\mathbf{B}$  is generated at a distance  $|\mathbf{r}|$  from the length of the current element of the wire  $I d\mathbf{l}$ ,  $\mu_0$  is the magnetic permeability of free space,  $\hat{\mathbf{r}} = \mathbf{r}/r$  is the unit vector to specify the direction of the vector distance  $|\mathbf{r}|$  from the current to the field point.

#### 3.3.1 Rectangular coil

Making theoretical magnetic field models enables us to precisely plan the setups used in the experiment. To obtain the formula for magnetic fields from rectangular coils we can simply divide the rectangular coil into four different straight wires. The magnetic field from each wire will contribute to the total magnetic field. In making this simplification one has to remember the direction of the current and position of each segment of the coil.

The magnetic field components for a single rectangular loop of wire of negligible wire cross section, with side dimensions  $2a$  by  $2b$ , in the  $xy$  plane can be expressed in form [77]:

$$B_x = \frac{\mu_0 I}{4\pi} \sum_{\alpha=i}^{iv} \left[ \frac{(-1)^{\alpha+1} z}{r_\alpha (r_\alpha + d_\alpha)} \right] \quad (3.27)$$

$$B_y = \frac{\mu_0 I}{4\pi} \sum_{\alpha=i}^{iv} \left[ \frac{(-1)^{\alpha+1} z}{r_\alpha [r_\alpha + (-1)^{\alpha+1} C_\alpha]} \right] \quad (3.28)$$

$$B_z = \frac{\mu_0 I}{4\pi} \sum_{\alpha=i}^{iv} \left[ \frac{(-1)^{\alpha+1} d_\alpha}{r_\alpha [r_\alpha + (-1)^{\alpha+1}]} - \frac{C_\alpha}{r_\alpha (r_\alpha + d_\alpha)} \right] \quad (3.29)$$

where

$$\begin{aligned} C_i &= -C_{iv} = a + x, & r_i &= \sqrt{(x-l)^2 + (y+b)^2 + z^2} \\ C_{ii} &= -C_{iii} = a - x, & r_{ii} &= \sqrt{(x-a)^2 + (y-l)^2 + z^2} \\ d_i &= d_{ii} = y + b, & r_{iii} &= \sqrt{(x-l)^2 + (y-b)^2 + z^2} \\ d_{iii} &= d_{iv} = y - b, & r_{iv} &= \sqrt{(x+a)^2 + (y-l)^2 + z^2}. \end{aligned} \quad (3.30)$$

To rotate obtained system by an angle in three dimension we use three basic rotation matrices:

$$R_x(\theta) = \begin{pmatrix} 1 & 0 & 0 \\ 0 & \cos \theta & -\sin \theta \\ 0 & \sin \theta & \cos \theta \end{pmatrix}, R_y(\theta) = \begin{pmatrix} \cos \theta & 0 & \sin \theta \\ 0 & 1 & 0 \\ -\sin \theta & 0 & \cos \theta \end{pmatrix}, R_z(\theta) = \begin{pmatrix} \cos \theta & -\sin \theta & 0 \\ \sin \theta & \cos \theta & 0 \\ 0 & 0 & 1 \end{pmatrix}. \quad (3.31)$$

These matrices represent counterclockwise rotations around the  $x, y$  and  $z$  axes respectively. For example applying simple transformation to  $\{x, y, z\}$  coordinates by  $90^\circ$  around  $x, y$  and  $z$  axes we get:  $R_x(\theta) \{x, y, z\} = \{x, z, -y\}$ ,  $R_y(\theta) \{x, y, z\} = \{-z, y, x\}$ ,  $R_z(\theta) \{x, y, z\} = \{y, -x, z\}$ .

### 3.3.2 Magnetic field from circular coils

A very useful geometry in magnetic field creation is a circular loop. Many specific magnetic fields can be generated from the composition of the current flowing in the wire loop. A well known configuration is the form of two parallel current loops that have a separation of one radius ( $a$  in Eqs. 3.34–3.40) and is named Helmholtz or anti-Helmholtz configuration depending on the direction of the current flow in one coil

with respect to the other. In the next section these configurations will be described. Here we want to present a general approach of strict magnetic field generation from a current loop. Knowledge of the basic, but not trivial, recipe enables the creation of complicated and more sophisticated wire structures where the current loops are used. For convenience the formulae for different coordinate systems are specified. It is necessary to introduce a concept of elliptic integrals.

Elliptic integrals are considered as the next step in complexity above elementary integrals [78]. The elliptic integrals frequently arise in the calculations of relatively simple geometries in physics applications but nevertheless they cannot be expressed using algebraic, trig and inverse trig, log or exponential elementary functions. The most common set of elliptic integrals can be found in Ref. [78]. Here we limit ourselves to present only two essential complete elliptic integrals which will be used when the magnetic field from a current loop will be defined. Let us identify complete elliptic integrals before they appear in a magnetic field formulae.

$$K(m) = \int_0^{\frac{\pi}{2}} \frac{d\theta}{\sqrt{1 - m \sin^2 \theta}}, \quad E(m) = \int_0^{\frac{\pi}{2}} d\theta \sqrt{1 - m \sin^2 \theta}. \quad (3.32)$$

Equivalently, using an alternate notation (if we let  $t = \sin \theta$  and  $dt = \cos \theta d\theta = \sqrt{1 - t^2} d\theta$ )

$$K(m) = \int_0^1 \frac{dt}{\sqrt{(1 - t^2)(1 - mt^2)}}, \quad E(m) = \int_0^1 \frac{\sqrt{1 - mt^2}}{\sqrt{1 - t^2}}, \quad (3.33)$$

where  $K(m)$  and  $E(m)$  are complete elliptic integrals of the first and second kind respectively, and  $m$  is the elliptic integral argument (sometimes written as  $k^2$ ). We use the same notation as in Ref. [79]. The field from circular coils can be expressed in elliptic integrals in the following way [80]:

In order to simplify the relations the following substitutions are used:  $r^2 \equiv x^2 + y^2 + z^2$ ,  $\rho^2 \equiv x^2 + y^2$ ,  $\alpha^2 \equiv a^2 + \rho^2 + z^2 - 2a\rho$ ,  $\beta^2 \equiv a^2 + \rho^2 + z^2 + 2a\rho$ ,  $m = 1 - \alpha^2/\beta^2$ .

- In Cartesian coordinates

$$B_x = \frac{\mu_0 I x z}{2\pi \alpha^2 \beta \rho^2} [(a^2 + r^2) E(m) - \alpha^2 K(m)] \quad (3.34)$$

$$B_y = \frac{\mu_0 I y z}{2\pi \alpha^2 \beta \rho^2} [(a^2 + r^2) E(m) - \alpha^2 K(m)] = \frac{y}{x} B_x \quad (3.35)$$

$$B_z = \frac{\mu_0 I x z}{2\pi \alpha^2 \beta} [(a^2 - r^2) E(m) + \alpha^2 K(m)] \quad (3.36)$$

- In spherical coordinates

$$B_r = \frac{\mu_0 I a^2 \cos \theta}{\pi \alpha^2 \beta} E(m) \quad (3.37)$$

$$B_\theta = \frac{\mu_0 I}{2\pi \alpha^2 \beta \sin \theta} [(r^2 + a^2 \cos^2 \theta) E(m) - \alpha^2 K(m)] \quad (3.38)$$

- In cylindrical coordinates

$$B_\rho = \frac{\mu_0 I z}{\pi \alpha^2 \beta \rho} [(a^2 + \rho^2 + z^2) E(m) - \alpha^2 K(m)] \quad (3.39)$$

$$B_z = \frac{\mu_0 I}{2\pi \alpha^2 \beta} [(a^2 - \rho^2 - z^2) E(m) + \alpha^2 K(m)] \quad (3.40)$$

A measure of how a magnetic field generated by a coil changes can be obtained by finding the spatial derivatives of the above field components. The explicit formulae of spatial derivatives for Cartesian coordinates can be found in Appendix A. Having a model ready to form useful configurations of the coils lets us consider a few basic experimental structures.

### 3.3.3 Helmholtz and anti-Helmholtz configurations

A handy technique for generating an adequately uniform magnetic field is the use of a pair of circular or rectangular coils with a common axis and equal currents flowing in them (for convenience in most cases the coils are connected in series and fed from the same power supply). For two circular coils of radius  $a$ , separated also by the radius  $a$  (see Fig. 3.6) there are two forms of the magnetic field. Firstly, for creating uniform magnetic field when the coils carry current in the same sense – called Helmholtz configuration. Secondly, when a pair of coils produce the inhomogeneous magnetic field caused by current flowing in opposite sense in each coil – which is called anti-Helmholtz configuration.

The primary purpose of Helmholtz coils is to provide a uniform magnetic field at the centre between the coils. The magnetic field from the Helmholtz coils is directly proportional to the number of turns in the coils and the current applied to them. On the other hand the anti-Helmholtz configuration is most useful when the creation of a local magnetic field minimum is needed. The magnetic field gradient from the anti-Helmholtz coils finds a useful application in the generation of the spherical quadruple magnetic field for optical traps [81] (see also Sec. 3.1.3). In Fig. 3.6 we present a model of ‘pure’ Helmholtz and anti-Helmholtz coils. However, the most linear quadrupole field is

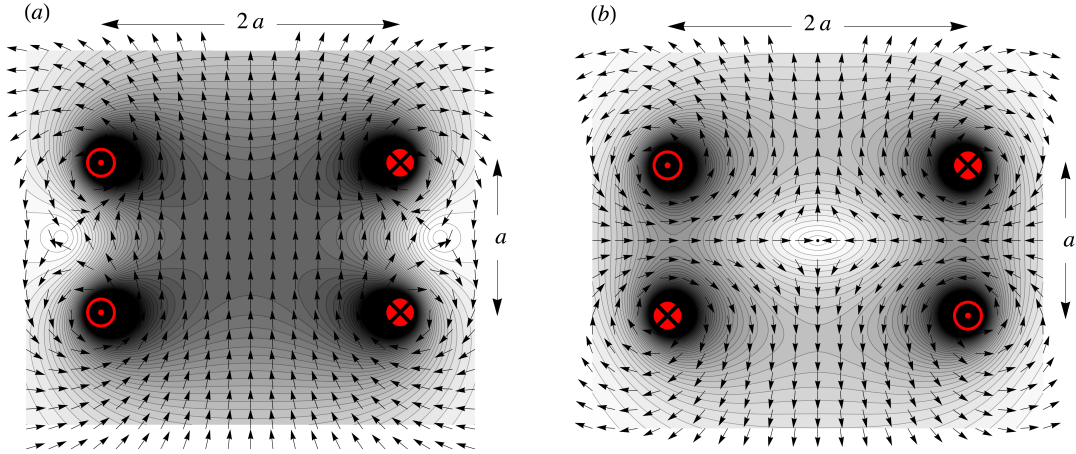


Figure 3.6: Contour field plots and vector field plots from ‘pure’ circular (a) Helmholtz and (b): anti-Helmholtz coils configurations, with separation  $a$  and diameter  $2a$ . (a): Helmholtz coils are a coaxial pair of identical circular coils spaced one radius apart with the current flowing through both coils in the same direction. (b): The same geometry as for Helmholtz coils is used but the current flows through both coils in the opposite direction.

obtained with separation of  $\sqrt{3}a$ . Experimentally different separations are often used, and our main concerns are the constant field (Helmholtz) or gradient (anti-Helmholtz). In this thesis in general we refer to ‘Helmholtz-type’ coils, where ‘Helmholtz-type’ coils will be the ones carrying current in the same sense but with separation not always one radius.

The second-order magnetic field from the Helmholtz coils, offset from the symmetry ( $z$ ) axis, results in the formula (for simplicity in Cartesian coordinates):

$$\mathbf{B}(x, y, z) = B_0(0, 0, 1) + \frac{B_2}{2} \left( -xz, -yz, z^2 - \frac{x^2 + y^2}{2} \right). \quad (3.41)$$

This equation will be used later to derive an approximation of the total field from a Ioffe-Pritchard magnetic trap (see Sec. 3.4). To first order the anti-Helmholtz coil pairs generate a field which is known as a quadrupole field.

### 3.3.4 Quadrupole trap

Many types of magnetic field were studied in the pursuit of creating an inhomogenous field with a local extremum in the magnetic field magnitude. The magnetic coil configurations with a central minimum in  $|\mathbf{B}|$  enable attraction and accumulation of the

low field seeking atoms that tend toward minima in magnetic field magnitude.

The quadrupole field was of great interest to researchers who were searching for magnetostatic trapping fields for neutral atoms [82]. The 3D quadrupole field can be written in the form ( $B_x = B_y = B_q$ ):

$$\mathbf{B}_{\text{quad}}(x, y, z) = \{B_x x, B_y y, -(B_x + B_y)z\} = B_q \{x, y, -2z\}, \quad (3.42)$$

which results in magnetic field magnitude:  $|\mathbf{B}| = B_q \sqrt{x^2 + y^2 + 4z^2}$ . From an atom's potential energy in a magnetic field  $U(\mathbf{r}) = -\boldsymbol{\mu} \cdot \mathbf{B}(\mathbf{r})$  one can write the potential energy of a ground state atom in a quadrupole magnetic field:

$$U(r(x, y, z)) = \mu_B g_F m_F B_{\text{quad}}(r(x, y, z)) = \mu_B g_F m_F B_q \sqrt{x^2 + y^2 + 4z^2}. \quad (3.43)$$

The trapping potential rises linearly from the geometrical origin at  $\{0, 0, 0\}$ . There is a quadrupole zero-field point at the centre. This point is a hyperfine level crossing region, where the hyperfine degeneracy is present. When the acting atomic force,  $\boldsymbol{\mu} \nabla |\mathbf{B}|$ , suddenly changes direction there the atoms that pass near that point will experience a change in the orientation of the atomic moment which will be no longer aligned with the local field direction. This results in non-adiabatic spin-flip transitions also called Majorana spin-flip transitions [83][84]. Trapped atoms are confined only in certain Zeeman levels that correspond to specific alignments of an atomic spin, hence spin-flip transitions may cause them to be lost from a trap.

This drawback of the quadrupole field can be tailored by removing the point of hyperfine degeneracy from the bottom of the trap. In order to avoid this lossy mechanism that drives the non-adiabatic transitions an additional uniform field may be implemented. If the direction of this field depends on time, that makes the minimum position dependent on time as well. Based on that fact studies of a new kind of magnetic trap, the time-averaged orbiting potential (TOP) magnetic traps, were carried out [83, 85, 86] (see also Appendix B).

In the Strathclyde experiment we do not use the TOP trap, although we would like to mention that a ring trap equivalent exists [49]. A stable trapping potential is formed about an electrically isolated, conducting loop in an ac magnetic field by time averaging the superposition of the external and induced magnetic fields. This setup eliminates Majorana spin-flip losses and creates a stable trapping geometry.

An alternative solution of removing the zero field from a magnetic trap was implemented during the realisation of Bose-Einstein condensation of sodium atoms. This

technique used an optical plug, a blue detuned laser beam which repels atoms from reaching the leaky region at the origin of the trap where the field is zero [87]. This successful technique when an optically plugged quadrupole trap was used is also reported in Ref. [88]. The repelling character of the laser beam will be considered in Sec. 3.6.

The next magnetic trap design we consider, known as the Ioffe-Prichard trap [89], relies on a non-zero bias offset field at the trap minimum and it will be discussed in the next section.

### 3.4 Ioffe-Prichard trap

In Sec. 3.3.1 and 3.3.2 we discussed in detail the magnetic fields from rectangular and circular coils. Having a mathematical tool in hand we can model specific coil configurations that can be treated as an assembly of individual components. That opens the possibility of theoretical studies of more complex magnetic systems.

Let us consider the example where the single components create a three dimensional magnetic trap for atoms. For this purpose we can make use of a two dimensional quadrupole field. The two dimensional quadrupole trap can be obtained by four straight bars (red) carrying current, as shown in Fig. 3.7.

Although the radial confinement is large, the field is invariant along the direction parallel to the current bars. There is a need to add another magnetic field that will provide the axial confinement. This supplementary field to the 2D linear quadrupole field can be achieved with the Helmholtz-type coils (blue), added around the four current bars (Fig. 3.7). These coils are also called pinch coils. Such a trap, consisting of two coaxial coils with the same sense current rotation and four long current bars contributing two dimensional quadrupole field has been proposed in Ref. [89] for trapping and cooling of neutral atoms, but originally was used for plasma confinement as reported in Ref. [90].

So called Ioffe-Prichard traps have played a major role and have been used extensively for Bose-Einstein condensate realisation in alkali gases. They provided wall-free confinement for particles and are well suited for atom trapping. The combined field contributions from (1) two pinch coils providing a harmonic local minimum with axial field curvature  $B_2$  and (2) quadrupole field with gradient  $B_1$  in the perpendicular plane to the axial direction results in a trap that has a large axial bias field  $B_p$  which can be compensated by applying a nulling bias field in the opposite direction  $B_n$ . The mag-

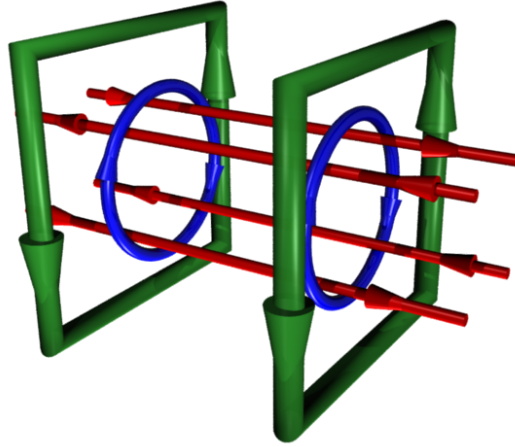


Figure 3.7: Geometry of the IP-type magnetic field coils. The two dimensional quadrupole trap is obtained by four straight bars (red) carrying current. Helmholtz-type coils (blue) with separation greater than the radius, to provide a magnetic field curvature for weak-field seeking atoms. The nulling magnetic field is generated by Helmholtz-type square (green) coils configuration. The current directions are designated by the arrows.

netic field  $B_n$  is usually generated by Helmholtz-type coils configuration [91], called nulling or compensation coils. Then the effective total bias field at the centre of the trap obeys the relation:

$$\mathbf{B}_0 = \mathbf{B}_p - \mathbf{B}_n . \quad (3.44)$$

The finite bias offset field at the trap minimum avoids Majorana transitions which is certainly an advantage when using the Ioffe-Pritchard trap configurations. However, when the magnetic field generated by the compensation coils overcomes the bias field from the pinch coils, making  $B_0 < 0$ , a double well potential is formed at the centre of the trap, with barrier height determined by the magnitude of  $B_0$  (see Fig. 3.8). The common IP trap comprises the pinch coils field of form given in equation 3.41, and a two dimensional quadrupole magnetic field that to a good approximation can be written as  $\mathbf{B}(x, y, z) = B_1(-x, y, 0)$ . The magnitude of the field from the standard IP configuration (not including the compensation/nulling coils) combines two individual contribution from pinch coils and four current bars and appears as:

$$B_{\text{IP}} = \sqrt{\left(B_0 + \frac{B_2}{2} \left(z^2 - \frac{x^2 + y^2}{2}\right)\right)^2 + B_1^2 (x^2 + y^2)} , \quad (3.45)$$

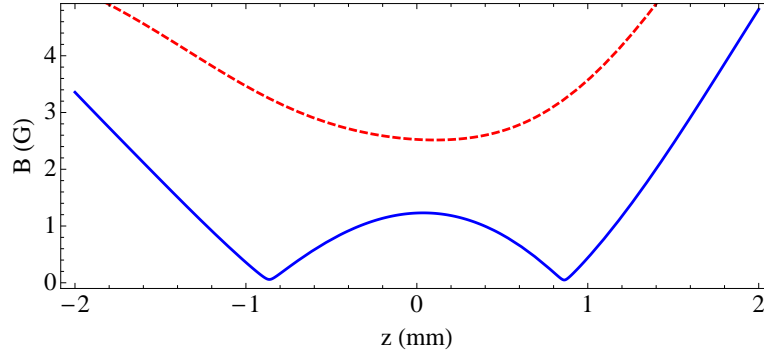


Figure 3.8: Double well potential as a result of overcoming the pinch bias field  $\mathbf{B}_p$  by the  $\mathbf{B}_n$  field. The zero-field points are at  $z_0 = \pm\sqrt{\frac{2|B_0|}{B_2}}$ , where the lossy Majorana spin-flip transitions occur. The trapping potential is in the form of two wells. The dashed line show the IP trap potential when  $B_0 > 0$ . The small asymmetry comes from the Strathclyde IP-like setup.

and its convenient form in second order Taylor expansion [56]:

$$B_{\text{IP}} = B_0 + \frac{1}{2} \left( \frac{B_1^2}{B_0} - \frac{B_2}{2} \right) r^2 + \frac{B_2}{2} z^2, \quad (3.46)$$

that make evident a harmonic, and cylindrically symmetric character of the trap (at least to second order), where  $r = \sqrt{x^2 + y^2}$ .

### 3.4.1 IP adiabatic compression

There are certain parameters, e.g. elastic collisions, phase space density that have to reach a critical level before the final stage of cooling by evaporation. In this section we mention the preparation stage prior to runaway evaporation cooling.

In order to increase the elastic collision rate and phase space density in the magnetic trap, which is needed for runaway evaporation (see Sec. 3.5), another step preceding evaporation cooling has to be performed. This can be done by altering the parameters of the trap such that trapped atoms experience compression from the magnetic trap. By changing the magnitude of the current flow through the IP and compensation coils it is possible to proportionally change the potential energy of the magnetic trap, and hence reshape of the trap. During compression atoms are being squeezed between the walls of the magnetic trap effectively increasing collisions and the density of the atomic sample at the expense of heating.

During the compression the magnetic trap frequencies change radically creating a

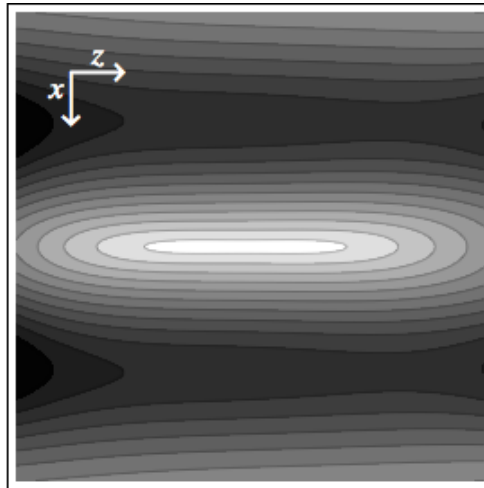


Figure 3.9: The magnetic field contours of the model IP trap in the compressed configuration. The effective potential is only parabolic, in the radial direction of the IP trap, for small distances from the origin, and becomes linear at large distances.

high confinement in the radial direction. The cylindrically symmetric nature of the compressed trap results in an elongated cigar shape trap. Fig. 3.9 shows the magnetic field contours of a model of IP trap in the compressed configuration.

Adiabatic compression of the magnetic trap is a powerful tool for increasing the density and temperature of the trapped gas and therefore the ratio of elastic to inelastic collision,  $\varphi$  (Sec. 3.5). The interplay between elastic (‘good’) and inelastic (‘bad’) collisions is critically important in the next step of cooling, namely evaporation cooling. The ratio of elastic to inelastic collisions determines the efficiency of this process. After the preparation of atoms in the magnetic field with sufficient density and therefore interatomic collisions, the final step towards Bose-Einstein condensation can be implemented. Until this stage we always tried to accumulate as many atoms as possible, but now we rely on a mechanism that necessarily results in losing atoms. Although this may seem to be unreasonable we will explain in the next section an effective method of cooling an atomic sample by removing most of the atoms from it.

### 3.5 Evaporation

Using a power law in relation to the trapping potential we can characterise the relation between the volume  $V$  of a trapped sample of atoms and its temperature  $T$ , by  $V \propto$

$T^\delta$  [7]. The parameter  $\delta$  takes certain values for different trapping potentials i.e.  $\delta = 0$  for a 3D box with infinitely high walls,  $\delta = 3/2$  for a 3D harmonic potential and  $\delta = 3$  for a 3D linear potential.

### 3.5.1 Evaporative cooling

Reaching lower temperatures requires an additional mechanism that is not based on spontaneous emission and can get rid of unwanted energy from the system. Along with the wall-free confinement proposal by Hess in 1986 [92] the idea of selective removal of the atoms from magnetic trap was introduced. This technique, in analogy with day-to-day experience, was called evaporative cooling. The main goal of evaporative cooling was to bridge the phase-space density gap between the magnetic trapping stage to BEC transition and achieve temperatures never seen before in the laboratories.

The general idea behind the evaporation cooling technique is to remove the hottest atoms from the cooled atomic sample and allow the ensemble to rethermalise to a lower temperature through collisions. This can be done by slowly reducing the ‘height’ of the magnetic trap potential and as the evaporation process continues, a decrease in temperature is observed [92].

The utility of evaporative cooling was displayed when this technique paved the way to the first creation of the BEC phenomena. Cooling by evaporation enabled scientists to reach ultra-low temperature and at the same time relatively high density atomic samples ( $> 10^{12} \text{ cm}^{-3}$ ). The only concern is due to the lifetime of the evaporated sample. Technically the lifetime is determined by inelastic collisions or any form of heating or loss from the trap. As the atomic rethermalisation process during the evaporation is based on elastic collisions the ratio between inelastic collisions to elastic collisions sets the efficiency of evaporative cooling. The drawback of evaporative cooling is definitely its lossy character. In the Strathclyde BEC experiment we start with  $\approx 10^8$  atoms in the magnetic trap and after the evaporation we end up with  $\approx 10^5$  atoms below the transition temperature  $T_c$ . Effectively after evaporation cooling we only have 0.1% of the original sample left. Gaining low temperature and high final densities requires a high initial number of atoms at the beginning of evaporation.

For evaporative cooling one needs to consider several parameters such as density, number of atoms, temperature, collisional properties, thermalisation process, phase space density. In the next section we briefly describe the relationship between these quantities and their role in the evaporation process.

If we consider the atoms in an external potential during the evaporation cooling process the key control parameter is the potential depth

$$\varepsilon_{\text{depth}} = \eta k_{\text{B}} T , \quad (3.47)$$

where  $\eta$  is the truncation parameter. For small values of  $\eta$  the evaporation occurs fast as the threshold of the trapping potential is low compared to the energy of the atoms. However fast evaporation doesn't mean efficient evaporation. The truncation parameter has to be related to the dynamics of the evaporation process and hence be time dependent to achieve the most efficient evaporation with a significant temperature drop per escaping atom. In our description we will combine evaporation models proposed by Davis *et al.* [93] and the Amsterdam group [94] [95].

The evaporation cooling model can be considered as a process of many finite steps. For each discrete step the change in truncation parameter is followed by thermalisation of the atoms left in the trap; the temperature is reduced from  $T$  to  $T_{\eta}$  and number of atoms decreases from  $N$  to  $N_{\eta}$ . To measure the decrease in temperature due to loss of the atoms from the trap one can introduce a quantitative measure:

$$\alpha \equiv \ln(T/T_{\eta}) / \ln(N/N_{\eta}). \quad (3.48)$$

That implies a power law dependence for  $\alpha = \text{const}$  during the evaporation process for the decrease of the temperature  $T_{\eta} = T(N/N_{\eta})^{\alpha}$ . For a continuous process Eq. 3.48 may be written in form of logarithmic derivatives:  $\alpha \equiv d(\ln T) / d(\ln N)$ .

For a large truncation parameter the derivation of the average energy of an escaping atom is found in Ref. [7] and [93]. For the purpose of this thesis we only present the final equation

$$\alpha = \frac{\eta}{(\delta + 3/2)} - 1 , \quad (3.49)$$

where the denominator expresses the average energy of the atoms in the 3D potential  $((\delta + 3/2)k_{\text{B}}T)$ . There is in principle no upper limit for the dimensionless quantity  $\alpha$ . For very large  $\eta$  the evaporation of a single atom from the trap would result in a prominent decrease in temperature. However this ideal situation does not apply to real life experiments as it needs an almost infinite time interval. Effective evaporation is an interplay between parameters that play different roles in the process.

### 3.5.2 Runaway evaporation

The first experiments on evaporative cooling were done using hydrogen [92]. The hydrogen model was substituted with alkali atoms where a big advantage is their elastic

cross section being approximately three orders of magnitude larger than for hydrogen. The relation between the elastic cross section, evaporative loss and inelastic collisions give a simple description of the evaporating process.

The thermalisation process depends mostly on the ratio of elastic collisions to inelastic collisions. To meet the criteria for runaway evaporation the elastic collision rate

$$n \sigma_{\text{el}} v_{\text{el}} \implies \begin{cases} n & \text{density distribution} \\ \sigma_{\text{el}} & \text{elastic collision cross - section} \\ v_{\text{el}} & \text{relative velocity between atoms} \end{cases} \quad (3.50)$$

has to be maintained or increased during the process. The magnetic trap compression (Sec. 3.4.1) helps to increase the elastic collision rate as well as the density. The regime of runaway evaporation can be expressed as

$$\wp \equiv \tau_{\text{loss}}/\tau_{\text{el}} \geq \wp_{\text{min}} = \frac{A}{\alpha(\delta - 1/2) - 1}, \quad (3.51)$$

where  $\wp = \tau_{\text{evap}}/\tau_{\text{el}}$  is the ratio of the time constant for evaporation to the elastic collision time. The relation between the ratio of elastic to inelastic collisions and truncation parameter is presented in Fig. 3.10. From the plot the minimum ratio needed for runaway evaporation can be determined<sup>1</sup>. The calculations were done using  $A$  and  $\alpha$  from the Amsterdam model [94] [95] that are valid for all range of the truncation parameter  $\eta$ :

$$\begin{aligned} \alpha &= \frac{\eta + (1 - X_{\text{ev}}/V_{\text{ev}}) - (3/2 + \gamma)}{(C/Nk) + (1 - X_{\text{ev}}/V_{\text{ev}})\xi} \\ &= \frac{\eta + \left(1 - \frac{\Gamma_{\text{inc}}(7/2+\delta, \eta)}{\Gamma_{\text{inc}}(3/2+\delta, \eta)} [\eta - (5/2 + \delta) R(3/2 + \delta, \eta)]^{-1}\right) - (3/2 + \delta) R(3/2 + \delta, \eta)}{(3/2 + \delta) \left( R(3/2 + \delta, \eta) + \left( \frac{\Gamma_{\text{inc}}(7/2+\delta, \eta)}{\Gamma_{\text{inc}}(3/2+\delta, \eta)} [\eta - (5/2 + \delta) R(3/2 + \delta, \eta)]^{-1} \right) [1 - R(3/2 + \delta, \eta)] \right)}, \end{aligned} \quad (3.52)$$

$$A = \sqrt{2}(1 - \xi\alpha)e^\eta(V_e/V_{\text{ev}}) = \sqrt{2}(1 - \xi\alpha)e^\eta(\eta - (5/2 + \delta) R(3/2 + \delta, \eta)). \quad (3.53)$$

were the following substitutions were done:

$$\frac{X_{\text{ev}}}{V_{\text{ev}}} = \frac{\Gamma_{\text{inc}}(7/2 + \delta, \eta)}{\Gamma_{\text{inc}}(7/2 + \delta, \eta)} \frac{V_e}{V_{\text{ev}}}, \quad (3.54)$$

$$\frac{V_e}{V_{\text{ev}}} = \eta - (5/2 + \delta)R(3/2 + \delta, \eta). \quad (3.55)$$

---

<sup>1</sup>Note that the collision rate is calculated for  $n_0$  whereas the cloud-averaged collision rate is smaller by a factor  $2\sqrt{2}$  and 8 in a parabolic and linear trap respectively [96].

$$\xi = (3/2 + \delta)[1 - R(3/2 + \delta, \eta)] , \quad (3.56)$$

The notation uses the incomplete gamma function  $\Gamma_{\text{inc}}$ , with definition:

$$\Gamma_{\text{inc}}(m, \eta) \equiv \frac{\int_0^\eta t^{m-1} e^{-t} dt}{E(m)} \quad \text{and} \quad R(m, \eta) \equiv \frac{\Gamma_{\text{inc}}(m+1, \eta)}{\Gamma_{\text{inc}}(m, \eta)} , \quad (3.57)$$

where  $E(m) = \int_0^\infty t^{m-1} e^{-t} dt$  is the Euler gamma function. The components of Eq. 3.52 and Eq. 3.53 and their description can be found in Ref [95].

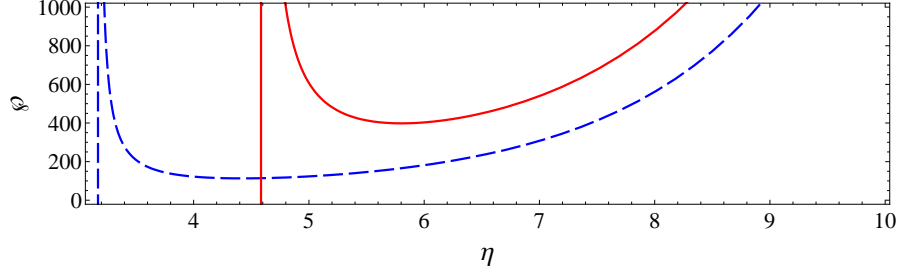


Figure 3.10: The  $\varphi \equiv \tau_{\text{loss}}/\tau_{\text{el}}$  parameter as a function of truncation parameter  $\eta$ . The minimum runaway regime plotted using Eq. 3.51 with  $A$  and  $\alpha$  parameters obtained from the Amsterdam model. The figure presents the ratio  $\varphi$  for the 3D parabolic potential (solid red line) that corresponds to the Strathclyde experimental regime and 3D linear potential (dashed blue line)

### PSD parameter

From the last section we introduced the parameter  $\alpha$  that describes the temperature change due to loss of the atoms from the trap. It is important to see not only the relation between atom loss and temperature but also phase-space density. Achieving high phase-space density is the crucial aspect on the path to BEC. The change in PSD with atom number in the trap can be expressed as [96]:

$$\gamma = -d(\ln \text{PSD})/d(\ln N) = \alpha(\delta + 3/2)/(1 + A/\varphi) - 1 , \quad (3.58)$$

where  $\gamma$  is the efficiency parameter of evaporative cooling. High  $\gamma$  in the system opens the way to achieve high phase-space densities. As  $\gamma(\varphi)$  depends on the ratio of good to bad collisions, for small  $\varphi$  beyond the runaway regime,  $\gamma$  indicates that the PSD cannot be increased. With an increase of  $\varphi$  above the  $\varphi_{\text{min}}$  the increase in  $\gamma$  can be seen and hence the PSD increase can be sustained. Figure 3.11 shows the efficiency parameter  $\gamma$  as a function of truncation parameter  $\eta$ . In the runaway regime ( $\varphi \gtrsim 400$ ) it is possible

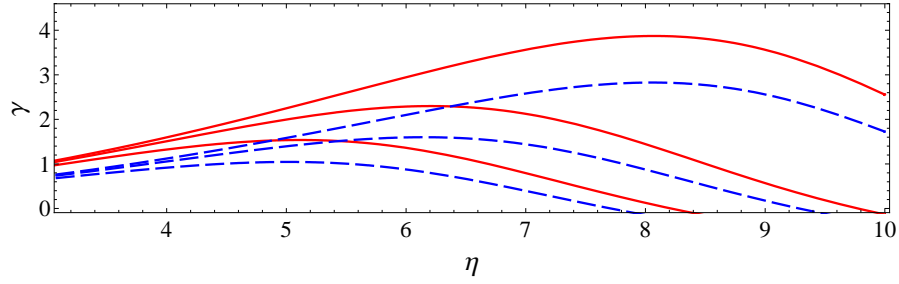


Figure 3.11: The graphical presentation of the evaporative cooling efficiency parameter  $\gamma$  as a function of truncation parameter  $\eta$ . Plots were obtained using Eq. 3.58, where  $\alpha$  and  $A$  were based on the Amsterdam model. Three different solid red lines represent a 3D parabolic potential (a good approximation of the IP-like trap, away from the linear regime) with  $\delta = 3/2$  for different values of  $\varphi$ . Upper line, middle line and lower line correspond to the ratio of good to bad collisions  $\varphi = 4000, 600, 200$  respectively. As a comparison a 3D linear potential with  $\delta = 3$  is shown as a set of three dashed blue lines for the same  $\varphi$  values in the same order.

to obtain both efficient and fast cooling along with sustainable enhancement of the density or phase space density.

From the introduction of this thesis we know that the PSD is proportional to  $n$  and  $T^{-3/2}$  (Eq. 1.2). In the beginning of this section we related the volume of a trapped sample of atoms to the temperature as  $V \propto T^{3/2}$  in a 3D harmonic potential. Hence, when substituting  $V$  to the spatial density we obtained a scaling relation for the PSD with respect to the number of atoms and temperature, in the 3D harmonic potential:

$$\text{PSD} \propto N/T^3 . \quad (3.59)$$

If the density and the average velocity of atoms in the trap vary as  $n \propto NT^{-3/2}$  and  $\langle v \rangle \propto T^{1/2}$ , then the elastic collision rate takes the form  $n\sigma_{\text{el}}v_{\text{el}} \propto N/T$ . An efficient evaporative cooling requires a constant or increasing elastic collision rate with a decreasing atom number (runaway evaporation). Therefore, we clearly see from the scaling relations that under this condition, the PSD is increased, which leads to the BEC transition.

In the next section we describe a useful tool for evaporation of atoms from the trap called an ‘RF knife’ that is a good way to experimentally achieve an energy truncating behaviour like in Eq. 3.47.

### 3.5.3 RF tool

As explained in Sec. 3.2 the hyperfine states of trapped atoms when in the presence of magnetic field are no longer degenerate. For low magnetic field the change in energy is linear and can be approximated by 0.7 MHz/Gauss between adjacent magnetic substates (for trapping state  $|F = 2, m_F = 2\rangle$  the energy shift is 1.4 MHz/Gauss) for the Rb ground state. As the magnetic fields from the magnetic trap (typically a few Gauss) determine the splitting of the magnetic sublevels the transitions between the adjacent state are the radio frequency range. At the Strathclyde BEC experiment the inhomogeneous magnetic field is provided by an IP-like trap (Sec.3.4) with the trapped atoms forming a cigar-shaped trapped cloud. The most energetic atoms are on the outside of the cigar-shaped cloud and hence they experience higher magnetic field, which results in a larger Zeeman splitting. The radio-frequency radiation can be used to change the magnetic hyperfine state of trapped atoms. An AC magnetic field applied perpendicular to  $\mathbf{B}$  is capable of driving  $|F, m_F\rangle \rightarrow |F, m_F \pm 1\rangle$  ground state transitions. Using the dependence of trapping and anti-trapping atomic states atoms can be expelled from the trapping potential by changing the atomic state. During the evaporation process the radio frequency is continuously ramped down to meet the resonance transition condition for the atoms at the outer surface of the cloud with higher than average energy. This effectively results in a shrinking 3D ellipsoidal surface.

## 3.6 Light potential

Along with the radiation-pressure and magnetic traps for neutral atoms (see Sec. 3.1.3 and 3.2) one can create another type of trap where a different trapping mechanism is utilised. Traps that rely on the electric dipole interaction with far-detuned light are known as *optical dipole* traps [97]. Using this idea we apply a repulsive potential for atoms where light induced mechanisms present in radiation-pressure traps are minimised. The generated potential depends strongly on the detuning, hence it is possible to create repulsive or attractive forces with the light. In this section we focus on the potential created by light that is far-detuned to the blue with respect to an atomic transition. Far-blue-detuned light repels atoms from the brightest parts of the laser beam .

The interest in interaction between optical dipole forces and atoms began in the early 1960's when the first suggestions of confining atoms by light were reported. In

1968 Letokhov proposed that atoms might be confined by an optical standing wave [98]. In a 2D geometry, depending on the detuning, atoms can be localised in nodes or anti-nodes of the standing wave for far-red detuned and far-blue detuned light respectively.

### 3.6.1 Two quantities - Interaction Potential and Scattering Rate

Monochromatic laser light represented by an electric field vector

$$\mathbf{E}(\mathbf{r}, t) = \hat{\mathbf{e}} \tilde{E}(\mathbf{r}) \exp[-i\omega t] + \hat{\mathbf{e}} \tilde{E}^*(\mathbf{r}) \exp[i\omega t], \quad (3.60)$$

induces a dipole moment

$$\mathbf{p}(\mathbf{r}, t) = \hat{\mathbf{e}} \tilde{p}(\mathbf{r}) \exp[-i\omega t] + \hat{\mathbf{e}} \tilde{p}^*(\mathbf{r}) \exp[i\omega t] \quad (3.61)$$

in an atom which is present within the driving field, where  $\hat{\mathbf{e}}$  is the unit polarisation vector,  $\tilde{E}(\mathbf{r})$  and  $\tilde{p}(\mathbf{r})$  are the amplitudes of the electric field and dipole moment respectively and  $\omega$  is the dipole moment driving angular frequency. We assume that the size of the atom is much smaller than the optical wavelength. The amplitude of the dipole moment and field amplitude are related by  $\tilde{p} = \alpha(\omega)\tilde{E}$ , where  $\alpha(\omega)$  is a quantity depending on the driving frequency called the complex polarisability. This quantity describes how easily the field induces the dipole moment.

When following Ref. [97] we find that the classical polarisability can be expressed as

$$\alpha = 6\pi\epsilon_0 c^3 \frac{\Gamma/\omega_0^2}{\omega_0^2 - \omega^2 - i(\omega^3/\omega_0^2)\Gamma}. \quad (3.62)$$

This equation is valid when there is no effect of saturation of the excited states. In the case when far-detuned light (i.e.  $|\Delta| \gg \Gamma$ , where  $\Delta = \omega - \omega_0$ ) is applied the excited states of atoms are not strongly populated and hence the effect of saturation is very low and thus yields very low scattering rates.

Having in hand a ready expression for polarisability we can give a formula for two main quantities when considering dipole potentials. The interaction potential of the induced dipole moment takes the form

$$U_{\text{dip}} = -\frac{\Re(\alpha)}{2\epsilon_0 c} I. \quad (3.63)$$

The potential energy is proportional to the field intensity  $I$ ,  $I = 2\epsilon_0 c |\tilde{E}|^2$ , and to the real part ( $\Re$ ) of the polarisability which represents in-phase components of the dipole

oscillation. From the potential we can straightforwardly express the dipole force that results from the gradient of energy

$$F_{\text{dip}}(\mathbf{r}) = -\nabla U_{\text{dip}}(\mathbf{r}) = \frac{\Re(\alpha)}{2\epsilon_0 c} \nabla I(\mathbf{r}). \quad (3.64)$$

Similarly we can write the absorption and reemission process in the form of scattering rate as

$$\Gamma_{\text{sc}}(\mathbf{r}) = \frac{\Im(\alpha)}{\hbar 2\epsilon_0 c} I(\mathbf{r}), \quad (3.65)$$

where the imaginary part ( $\Im$ ) of the polarisability describes the out-of-phase component of the dipole oscillation. The final expressions are [97]:

$$U_{\text{dip}}(\mathbf{r}) = -\frac{3\pi c^2}{2\omega_0^3} \left( \frac{\Gamma}{\omega_0 - \omega} + \frac{\Gamma}{\omega_0 + \omega} \right) I(\mathbf{r}), \quad (3.66)$$

$$\Gamma_{\text{sc}}(\mathbf{r}) = \frac{3\pi c^2}{2\hbar\omega_0^3} \left( \frac{\omega}{\omega_0} \right)^3 \left( \frac{\Gamma}{\omega_0 - \omega} + \frac{\Gamma}{\omega_0 + \omega} \right)^2 I(\mathbf{r}) \quad (3.67)$$

for the dipole potential and the scattering rate respectively. These equations are valid for large detunings and absence of the saturation effect. When the detuning fulfils the condition  $|\Delta| \ll \omega_0$  one can neglect the  $\frac{\Gamma}{\omega_0 + \omega}$  term by applying the rotating-wave approximation. Thus, the Eqs. 3.66 and 3.67 can be simplified to the form

$$U_{\text{dip}}(\mathbf{r}) = \frac{3\pi c^2}{2\omega_0^3} \frac{\Gamma}{\Delta} I(\mathbf{r}) \quad \text{and} \quad \Gamma_{\text{sc}}(\mathbf{r}) = \frac{3\pi c^2}{2\hbar\omega_0^3} \left( \frac{\Gamma}{\Delta} \right)^2 I(\mathbf{r}). \quad (3.68)$$

In this thesis we use the above equations (Eqs. 3.68) for all calculations considering the dipole potential. Although the equations are in compact form they show the essential physics for dipole potentials. The scaling factors are straightforward; the dipole potential scales as  $I/\Delta$  and the scattering rate scales as  $I/\Delta^2$ .

A very important sign of the detuning states the character of the light potential. The light potentials can be categorised into two types: red-detuned potentials and blue-detuned potentials. For the detuning to the red ( $\Delta < 0$ ) the dipole potential is negative and atoms are attracted to the light field. The highest light intensity gives the location of a potential minima. For the detuning to the blue ( $\Delta > 0$ ), which will be considered in this thesis, the dipole potential is positive and atoms are repelled out of the light field. In this case a point with maximum light intensity creates a potential maximum.

### 3.6.2 Dipole potential beam characteristic

From the fact that the dipole potential is a function of intensity,  $I$ , which depends on the position,  $\mathbf{r}$ , we need to consider a few beam parameters and tools for creation of

the final dipole potential.

In the Strathclyde experiment the dipole beam is generated by a 658 nm semiconductor diode that, from its manufactured nature, produces a beam with an elliptical cross section. The beam radius ( $1/e^2$ ) is a function of the axial distance  $z$  that obeys the relation:

$$w(z)_i = w(0)_i \sqrt{1 + (z/z(0)_i)^2} \quad \text{for } i = x, y, \quad (3.69)$$

$w(0)$  is the minimum value (at  $z = 0$ ) of the beam radius called the beam waist. The beam radius increases with  $z$  ( $\sqrt{2}w(0)_{x,y}$  at Rayleigh range,  $z = z(0)_{x,y}$ ).

In order to get a large enough blue-detuned dipole potential we increase the intensity by focusing the beam. At that stage we need to consider the beam waist as a function of the focal length of the focusing lens,  $f_{\text{lens}}$ , that takes form

$$w(0)_i = f_{\text{lens}} \lambda / (\pi R_i) \quad \text{for } i = x, y, \quad (3.70)$$

where  $R_i$  is radius of curvature of the wavefronts of the beam before the lens in the  $i$ -th direction.

Having the knowledge of the laser beam parameters and the lens focal length we can easily calculate the effective optical potential for the given parameters.

Another relevant approach involves the implementation of a focused light beam. Depending on the detuning the focused laser beam can act as a repeller for atoms or it can create a highly confining potential. A high intensity red detuned beam in Ref. [99] was used to create a single-well trapping potential. By using two AOM driving RF signals a single optical trap was deformed into a double-well. The effective potential results in a double well potential comprising the combination of a harmonic magnetic trap and optical dipole beam.

### 3.7 Atom interferometers

When the first Bose-Einstein condensate was created [10], it seemed to be a natural step to perform the next experiments showing the matter wave characteristics of condensates [100]. In recent years the matter-wave interference experiments have been of great interest for researchers [101, 102, 100, 103]. The potential behind the atom interferometry has been already appreciated in disciplines like precision measurement meteorology, atomic and molecular physics [104, 37].

The phase sensitivity  $\delta\Phi$  (the jitter in the relative phase between two arms of the interferometer) scales as  $\delta\Phi \propto N^{-1}$  for the condensate, where  $N$  stands for the number of bosons, whereas for cold atoms it is proportional to  $N^{-1/2}$  [105]. The condensed bosons used in precision interferometry enhance the sensitivity factor by  $N^{1/2}$  [101]. From that fact BEC interferometers are expected to be more precise than interferometers based on single atoms. Such matter-wave interference experiments are of great interest for applications in ultra-precise interferometry, and should lead to improvements in measurements of fundamental constants as well as temporal, gravitational and rotational sensing [106, 37, 104].

### 3.7.1 Atoms versus light - interferometry

Rotation sensors that rely on the Sagnac effect [107] have been developed already [108]. They are a good example to display the advantage of using atoms over photons. The superiority of making use of coherent sources of atoms rather than light can be observed when calculating the sensitivity in terms of phase change. The phase shift for an interferometer rotating at an angular velocity  $\Omega$  can be written for either photons or massive particles as follows [40]:

$$\Delta\phi = 4\pi \frac{\Omega A}{\lambda v} , \quad (3.71)$$

where  $A$  is the effective area of the interferometer and  $\Omega$  is the angular velocity of the (rotating) interferometric system. When substituting  $\lambda \rightarrow \lambda_{\text{atom}}$  from Eq. 1.3 one obtains the phase shift when matter waves are used in the interferometer

$$\Delta\phi_{\text{atom}} = 4\pi \frac{\Omega A_{\text{atom}}}{\lambda_{\text{dB}} v_{\text{atom}}} = 4\pi \Omega m A_{\text{atom}}/h \quad (3.72)$$

and in the same manner for light when  $\lambda \rightarrow \lambda_{\text{light}} = \frac{2\pi c}{\omega}$  we get the phase shift

$$\Delta\phi_{\text{light}} = 4\pi \frac{\Omega A_{\text{ph}}}{\lambda_{\text{ph}} v_{\text{ph}}} = 2\Omega \omega A_{\text{ph}}/c^2 . \quad (3.73)$$

Assuming equivalent interferometer areas ( $A_{\text{atom}} = A_{\text{ph}}$ ) the ratio of phase shifts is

$$\Phi_{\text{R}} = \frac{\Delta\phi_{\text{atom}}}{\Delta\phi_{\text{light}}} = \frac{\lambda_{\text{ph}}}{\lambda_{\text{dB}}} \frac{c}{v_{\text{atom}}} = \frac{mc^2}{\hbar\omega} . \quad (3.74)$$

This well-know ratio  $\Phi_{\text{R}}$  for 780 nm light and  $^{87}\text{Rb}$  atoms is approximately  $5 \times 10^{10}$ . It shows a great advantage of matter wave interferometers over optical interferometers in sensitivity based on Sagnac response factor [109].

A direct increase in effective area of the interferometer results in a proportional increment in the phase shift detection. Hence larger interferometers are of great interest to researchers. From Eq. 3.72 it is seen that the velocity of atoms is inversely proportional to the phase shift. As  $v_{\text{atom}} \ll c$  when considering the temporal domain slow atom interferometers result in high-sensitivity performance.

### 3.7.2 Five-step routine

In general matter wave interferometers involve several experimental stages prior to obtaining informative measurements. Depending on the type of interferometer used different techniques and methods are implemented to arrive at the same aim.

(1) *Preparation.* When one uses Bose-Einstein condensation for interferometry the first step requires access to a ready sample of BEC. The production of ultra cold atomic samples follows the standard path of reaching the BEC (for detailed description see Chapter 4). Due to the relative complexity and time needed for sub-procedures like: magneto-optical trapping, magnetic trapping and evaporative cooling required for BEC preparation this is the most time consuming stage. In analogy to optical beams the atom ‘beam’ is now ready to encounter a ‘beam splitter’, which leads to the next interferometric stage - splitting.

(2) *Splitting.* After preparation of the initial state the atoms represented by a wave function are split into two (or more) spatially separated states. Separation of these states originating from the single initial state is performed coherently. The Strathclyde splitting based on the far-off resonance dipole beams requires slow ( $\approx 200$  ms) ramping up of the potential barrier that separates two (or more) parts of the BEC.

(3) *Sensing.* Spatially separated wave packets undergo different interaction strengths with the medium they travel in due to their distinct spatial locations. During that stage the two branches of the atom ‘beam’ acquire different quantum phases. The Strathclyde experiment confines two wave packets in a two dimensional magnetic ring guide ( $\phi = 10$  cm) or a three dimensional harmonic trap with 11 Hz trap frequency along the direction of atom movement.

(4) *Redirection.* After the atomic branches reach their maximum relative spatial separation additional action has to be taken in order to recombine a two wave packets. As well as splitting the recombination should be performed without altering the coherent properties of the wave packets. Once again the relative spatial separation decreases in time and the atomic packets eventually overlap and the last stage occurs - detection.

(5) *Detection.* During overlap of the two branches of the atomic ‘beam’ the interference fringes can be observed. Measurement of the phase shift provides information about the environment.

## 3.8 Type of interferometer

Among the wide variety of interferometers we can differentiate two main groups that are classified due to the method of splitting. In this section we mention atom interferometers based on (1) momentum space splitting and (2) position space splitting.

### 3.8.1 Momentum space splitting

In this thesis we will not give detailed description of existing types of interferometers however we would like to mention that a large variety of atom interferometers have been built in the last decade (see Ref. [109]) but we only refer to some of them without going into detail.

For atom interferometers the ‘beamsplitter’ present in step (2) of the five-step path can be accomplished by different atomic tools. For example, in a Mach–Zender type of interferometer [110], step (2) is taken up by a diffraction grating. First demonstration of the three mechanical grating atom interferometer was reported by Keith *et al.* in 1991 [111]. In 1995 instead of the material gratings Rasel *et al.* [112] applied light gratings in the Kapitza–Dirac regime that showed more efficiency over their mechanical equivalent. Another method of splitting the atomic beam can be implemented using Raman transitions that coherently split the atomic wave packets into a superposition between two hyperfine states, which results in differential momentum in each interferometer arm [30]. The above examples of interferometers are only used for demonstration of atom interferometers where the splitting occurs in momentum space. Using diffraction gratings or pulses of light the momentum is transferred to the initial wave packet. The wave is split in momentum space and as a result separation in momentum space (but also in position space) take place. In the next subsection another type of interferometer will be considered where the splitting step is performed in position space. This category of atom interferometer is related to the Strathclyde interferometric setup.

### 3.8.2 Position space splitting

Magnetic waveguides and traps are commonly used for the manipulation of cold atoms or BECs. The relatively simple modelling and technical implementation of the magnetic confinements for the atoms also offers setups useful for atom interferometry. Confined BEC interferometers are characterised by a method of splitting of the wave function that in this case is based on coordinate space rather than momentum space. Among the ultra-cold atom interferometers one may find a range of confining setups, e.g. ring-shaped guide [47] as presented in Fig. 3.13 or multiple wells. Both examples are presented in this thesis (see Sec. 4.4 and Sec. 6.2.5).

### 3.8.3 Implementation of a confined BEC interferometer

In this section we focus on double well potentials for use as a confined atom interferometer, specifically we consider BEC confinement based on a three dimensional harmonic trap and an optical potential.

#### Double well potential

In Sec. 3.4 we showed how to create a double well potential with compensation coils in the IP configuration trap. However this simple procedure is not suitable when coherent splitting of the atomic wave packet is required. The zero magnetic field crossing causes incoherent spin flip transitions (see Sec. 3.3.3).

The Strathclyde double-well potential is created by using a far blue detuned beam that modifies the original harmonic potential from the magnetic trap. A single condensate was split symmetrically (along the axial direction of the IP trap) between two wells of the potential.

Condensates realised in this potential were released allowing ballistic expansion and overlap of two parts of BEC. The mean field interaction is lowered dramatically when the parts of the BEC are released from the trap. The detailed experimental procedure is present in Chapter 4.

The density distribution in each well is symmetric with respect to the centre of two potential wells  $n_{\text{left}} \approx n_{\text{right}}$ . If the part of the condensate in the left well has a phase  $\phi_{\text{left}}$  and, in a similar manner, the condensate in the right well has a phase  $\phi_{\text{right}}$ , the relative phase between the two condensates follows

$$\phi_{\text{rel}} = \phi_{\text{right}} - \phi_{\text{left}} . \quad (3.75)$$

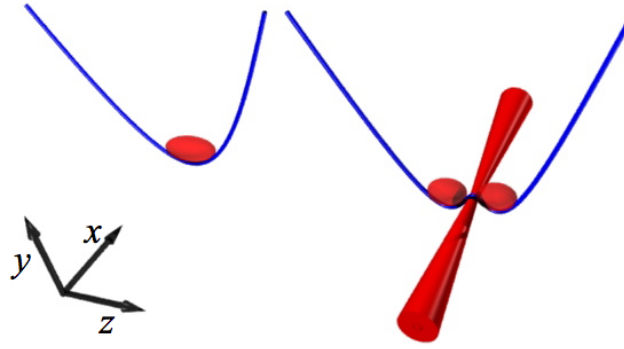


Figure 3.12: Schematic of a double well potential with a dipole beam. A trapping potential (shown in blue) is changed from a (a) single well into a (b) symmetric double well, by applying a dipole beam.

The condensates in the left and right potential wells can be described by the wave functions [99]

$$\begin{aligned}\Psi_{\text{left}}(\mathbf{r}, t) &= [n_{\text{left}}(\mathbf{r}, t)]^{\frac{1}{2}} e^{i \frac{m}{2\hbar t} |\mathbf{r} + \frac{\mathbf{d}}{2}|^2 + \phi_{\text{left}}} \\ \Psi_{\text{right}}(\mathbf{r}, t) &= [n_{\text{right}}(\mathbf{r}, t)]^{\frac{1}{2}} e^{i \frac{m}{2\hbar t} |\mathbf{r} - \frac{\mathbf{d}}{2}|^2 + \phi_{\text{right}}},\end{aligned}\quad (3.76)$$

where  $\mathbf{d}$  is the distance between the two well minima. The relative phase between two expanding BECs can be observed in the density profile of two mutually interfering condensates. For long enough experimental expansion times in the presence of gravity the integrated density profile for the interference of two wave packets results in a modulated Gaussian profile (assuming that the  $n_{\text{left}}$  and  $n_{\text{right}}$  are gaussians) that takes the form [99]:

$$n(\mathbf{r}, t) = n_{\text{left}} + n_{\text{right}} + 2[n_{\text{left}}n_{\text{right}}]^{1/2} \cos\left(\frac{md}{\hbar t} + \phi_{\text{rel}}\right), \quad (3.77)$$

where  $(\frac{md}{\hbar t})^{-1} = \lambda_{\text{spacing}}$  is the period of the resulting interference pattern. This fringe spacing  $\lambda_{\text{spacing}}$  dependence agrees well with the experimental realisation when two parts of the BEC undergo a free fall ballistic expansion. We will show in Sec. 6.3 that certain corrections to this formula have to be considered when other magnetic fields are applied during the overlap time.

### 3.8.4 Geometry suited for atom interferometry

In this section we would like to present the cold atom storage rings that are generated with magnetic fields where the (fixed) radius of the ring is determined by the radii of the ring's magnetic elements. However, to date there are number of experiments

that utilise an adjustable ring radius by applying different experimental techniques, e.g. time-orbiting ring trap (TORT) [44] or a combination of a magnetic trap for RF-dressed atoms [46].

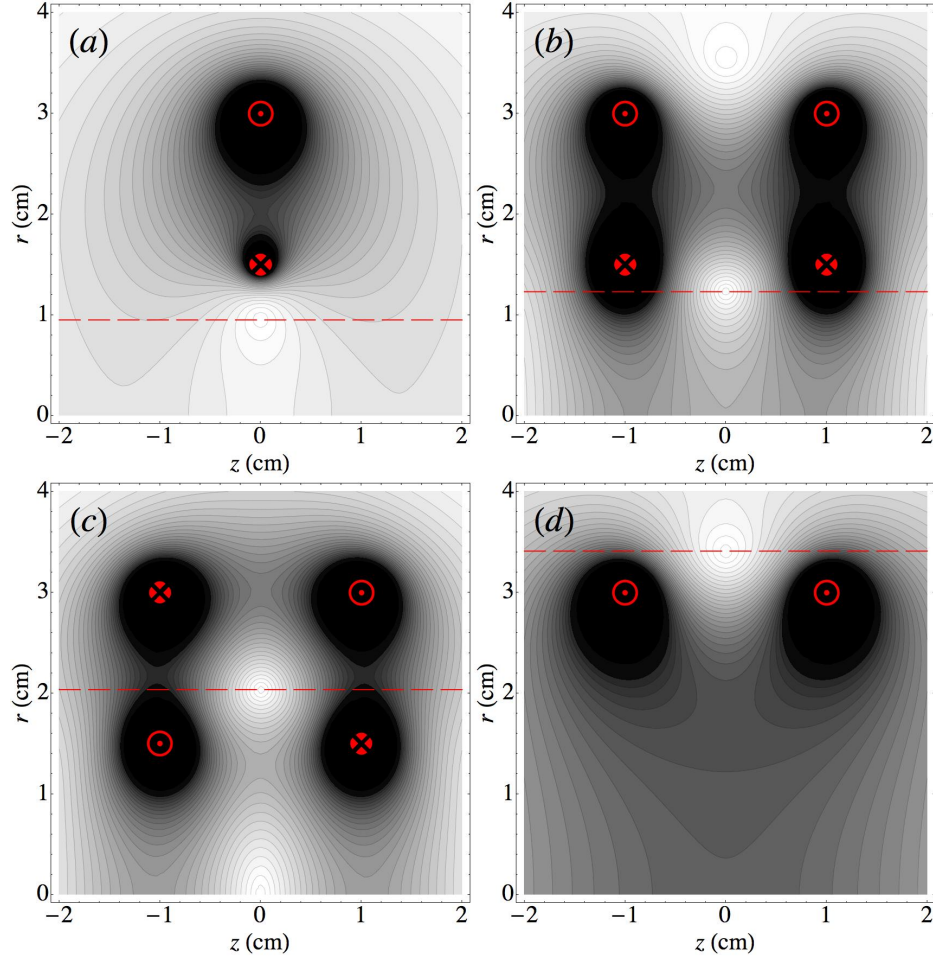


Figure 3.13: Examples of ring geometries for cold atoms or BECs. The circular coils have the radii  $r_1 = 1.5$  and  $r_2 = 3$  cm for the smaller / bigger coils respectively. The dashed line indicates a  $y$ -coordinate where the minimum field from a magnetic ring is located.

The circular magnetic guides models follow Ref. [113]. The simplest geometry for creating a ring trap is with two concentric co-planar circular coils of radius  $r_1$  and  $r_2 > r_1$ , carrying currents with magnitudes  $I_1$  and  $I_2 > I_1$  respectively, in opposite directions. This setup is shown in Fig. 3.13 (a), where the current ratio between two coils is  $\frac{I_1}{I_2} = 0.35$ . In practice such a storage ring coil configuration would require an in-vacuo coil system (due to the proximity of the trapping part to the inner ring). Alternatively, an ex-vacuo coil system can be formed by two concentric, equally spaced,

pairs of opposing Helmholtz-type coils as is shown in Fig. 3.13 (b). The current ratio between two coils, for this figure, is  $\frac{I_1}{I_2} = 1.25$ . In this setup the vacuum cell can be placed between the two co-planar coil pairs separated by  $\pm x_0$  ( $x_0 = 1$  cm). Images (c) and (d) (Fig. 3.13) depict storage rings formed of four or two circular coils. In (c) the current magnitude is the same for all coils,  $I_{1(+x_0)} = I_{1(-x_0)} = I_{2(+x_0)} = I_{2(-x_0)}$ , and orientation of the currents is different from (b) (see Fig. 3.13). In (d) two co-axial circular coils with radius  $r_2$  were separated by  $\pm x_0$ . The current was the same sense for both coils. The Strathclyde setup for a giant storage ring utilises the (c) configuration from Fig. 3.13 but with a larger radius of 5 cm (see Sec. 4.4).

## Experimental setup

This chapter will outline the experimental setup and main components which were used at Strathclyde University to create and manipulate a Bose-Einstein condensate. We will begin with a description of the laser system and its frequency stabilisation. This will be followed by a description of the Strathclyde double-MOT experimental setup and the unique hybrid trap for cold atoms and BECs, including the toroidal magnetic storage ring. A general description of the current controllers will be given. We will conclude with a section detailing the absorption imaging technique and finally the implementation of a laser beam for optical dipole splitting of the BECs.

### 4.1 The laser system

In laser cooling the atom's hyperfine structure imposes certain criteria on a source of light for cooling and trapping. A specific laser wavelength and its temporal stability are necessary ingredients for magneto-optical trapping. The number of atoms trapped in the MOT is highly dependent on laser frequency [114]. Therefore one has to pay high attention to the frequency of the laser used in laser cooling. For rubidium the D2 transition ( $\nu = 384.2$  THz) has a linewidth of  $\Gamma = 6.07$  MHz and so for the laser cooling of Rb atoms the linewidth of the laser must be stabilised to  $\sim 1$  MHz, to obtain high cooling and trapping efficiency in the MOT.

Semiconductor diode lasers play an important role in optical and atomic physics. Although these devices are compact, simple, and relatively inexpensive they have to be accompanied with other tools to provide the desired light output. As the diodes have a short semiconductor cavity they do not offer reliable frequency output and temporal

stability. Typically the large linewidth from a semiconductor diode,  $\sim 100$  MHz, comes along with poor tunability [115]. In order to narrow the laser linewidth ( $\sim 1$  MHz) and improve tunability one can provide an external, frequency-selective, optical feedback using an external-cavity diode laser (ECDL) [116]. Another method of obtaining the narrow laser linewidth (1.3 MHz), which is sufficient for laser cooling and trapping experiments, was reported in Ref. [117].

#### 4.1.1 ECDL

The main feature of the ECDL is the use of laser light from the diode fed back into the cavity by a diffraction grating mounted in the Littrow configuration [118]. Altering the angle of the grating allows the selection of the desired wavelength which is sent back into the diode along the incident beam. The ECDL used in the experiment is based on three key components; namely the **laser diode** (Sanyo DL-LS1027 with  $\sim 50$  mW at 780 nm, Sharp GH07P28F1C with  $\sim 150$  mW at 780 nm), the **diffraction grating** (gold-coated 1800 lines/mm holographic grating on a  $15 \times 15 \times 3$  mm<sup>3</sup> substrate) and the **collimating lens** (an aspheric optic with focal length of 6.2 mm). A broad region of laser frequencies is achieved by using a piezo element (PZT). Schematic diagram of laser design is presented in Fig. 4.1. The signal generator feeds a sweeping signal to the piezo which then is attached to the front plate (see Fig. 4.1). The detailed technical information and description of how to construct an extended-cavity diode laser can be found in Ref. [115].

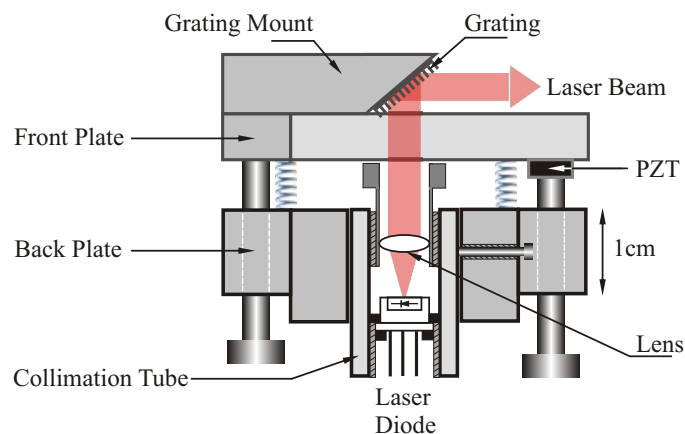


Figure 4.1: Schematic diagram of the extended-cavity laser, viewed from above.

### 4.1.2 Temperature and current control

The output frequency of the semiconductor laser is very sensitive to changes in temperature and injection current [119], as these parameters affect the laser wavelength. The stability of the laser can be improved by stabilising the temperature ( $\sim 10$  mK) and isolating the diode from surroundings by placing it in an enclosed box, which avoids any sudden change in temperature, e.g. from draughts. A laser stabilized passively in this way is then locked (actively stabilised) to the peak of a rubidium saturated absorption line (Sec. 4.1.5). The other effects, like change in air pressure and humidity, environment temperature, piezo-electric element drift and acoustic disturbance, affecting laser output frequency will not be considered in this section, however they can exist and cause unwanted noise fluctuation and must be minimised. However, these other effects happen on a long time-scale and are easy to correct for, as long as the range over which one can correct (e.g. the PZT scan range) is as wide as the range over which drifts occur.

#### Temperature controller

The temperature was controlled by a commercial device, FTP-4000 laser driver and temperature controller, connected to a Peltier thermoelectric cooler (TEC). To allow an accurate measure of the temperature of the diode one uses a thermistor ( $10$  k $\Omega$ ) that provides a feedback to the temperature controller. The controller is designed for low noise operation, hence one of the important aspects is to use a low-noise power supply.

#### Current controller

The laser diode drive current was supplied by a modified constant current controller – Thorlabs LD1255R – housed in an enclosed box. This driver enabled operating laser diodes in a constant current mode up to a maximum of 250 mA. A low current noise and low temperature drift were certainly advantageous when using this controlling device. The usual diode driving current was  $\sim 150$  mA, with the detected noise at level 74 nA.

### 4.1.3 Experimental upgrade

Up to the beginning of 2006, the Strathclyde laser system for the BEC experiment was based solely on home-built lasers. Since then we replaced two, out of three, lasers by a commercial system. A considerable amount of time was spent testing and applying the commercial laser system Toptica DL100 and the Toptica DLX. After consideration the Toptica DLX at 780 nm with 1 W of output power was implemented. Before the laser system upgrade each MOT (HP and LP) was operating using optical power from one home-built laser (60 mW off the grating output power for each MOT). Now the Toptica DLX laser system supplies trap light for both MOTs simultaneously. The extra power gained by upgrading the laser system and built-in optical fibre dock simplified alignment of the optical systems in the experiment. It also improved the quality of the beam, as it is spatially filtered when passing through the optical fibre output of the DLX. The output beam from the optical fibre has a 1:1 aspect ratio, which eliminated the need of correction of the semiconductor diode laser's natural, elliptical beam shape. Improvement of our laser system made the optical system more compact and easy to control.

Each MOT requires a repump beam. However, due to the lower power needs of the repump light, compared to the cooling light, the repump light for both MOTs was based on a single home-built laser.

We applied a similar laser setup for building the blue-detuned laser which was used for splitting BECs. The fact that this laser is so far away from the atomic resonance means we did not use an ECDL for this setup. Drifts in wavelengths were tolerable with the general experimental noise (see Sec. 3.6).

### 4.1.4 Controlling the laser

In order to *talk* to the atoms, in the magneto-optical trap, we need to first *tell* the laser at what frequency the atoms *answer*. As we deal with multilevel atoms there are many atomic transitions. A good and accurate way of recognising atomic transitions using the laser beam is to give a sample of atoms for the laser to *taste*; in the technique of absorption spectroscopy. The frequency dependent signal in the form of the photodiode current from a saturated absorption spectrum provides a frequency reference for controlling the laser.

The  $^{87}\text{Rb}$  ground states are linked to the lowest-lying excited states with the D1

and D2 line (see Fig. 2.1). For our experimental purposes we only consider the D2 line as it is used for the cooling transition. On the D2 line each ground state,  $F$ , has transitions constrained by transition rules ( $\Delta F = 0, \pm 1$ ) that results in three allowed transitions per ground state. The excited state hyperfine splittings,  $5p \ ^2P_{3/2}$ ,  $\{F' = 0 \Leftrightarrow 1, F' = 1 \Leftrightarrow 2, F' = 2 \Leftrightarrow 3\}$  in terms of frequency gap are  $\approx \{72 \text{ MHz}, 157 \text{ MHz}, 267 \text{ MHz}\}$  respectively (Fig. 2.1). To resolve these transitions from the Doppler-broadened absorption profiles ( $\approx 500 \text{ MHz}$ ) one needs to resolve the signal on the scale of the natural linewidth ( $\Gamma = 6.07 \text{ MHz}$ ).

### Absorption spectroscopy

Spectrum that resolves the hyperfine structure is a good frequency marker, which is a reliable reference for tuning and locking laser frequency [120]. However the hyperfine structure is often hidden within the dominating Doppler broadened signal. In order to extract the precise hyperfine transitions one needs to use Doppler-free spectroscopy. The setup of saturated absorption laser spectroscopy used at Strathclyde is presented in Fig. 4.2.

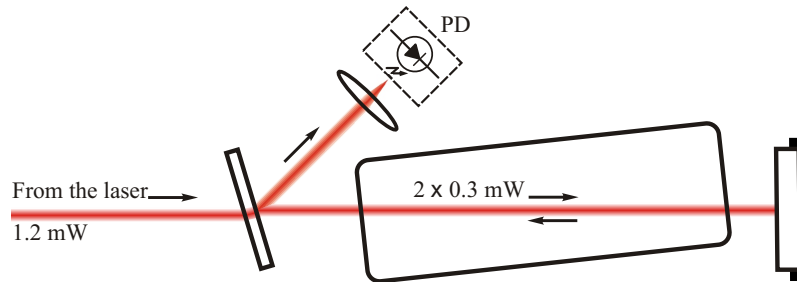


Figure 4.2: The trapping laser saturated absorption spectrometer. The single beam is provided directly from the laser pick-off with 1.2 mW power. To reduce power broadening only a fraction (1/4) of the beam intensity is used. The 75/25 beam splitter (BS) directs  $300 \mu\text{W}$  through the absorption cell. The area of the beam is  $\sim 1.2 \text{ mm}^2$ , which corresponds to  $\approx 24 \text{ mW/cm}^2$ , which satisfies the requirement of high intensity ( $I \gg I_{\text{sat}}$ ). The ingoing beam is referred to as the pump beam and the reflected beam is referred to as the probe beam.

The atoms enclosed in the glass cell displayed in Fig. 4.2 exhibit the Maxwellian

velocity distribution  $N(v)$ <sup>1</sup> centred at  $v = 0$ . When the laser beam passes through the cell the atoms absorb photons from the laser when the relative photon-atom frequency matches the atomic transition frequency. The direction of propagation of two counter-propagating beams makes them interact with atoms of different velocities. For <sup>87</sup>Rb, the D2 line has three atomic transitions for each of the ground levels (Fig. 2.1). Using saturated absorption spectroscopy we can obtain narrow absorption features on the scale of the natural linewidth, and easily resolve these transitions from their Doppler-broadened absorption profiles. For multilevel excited states there are more observable features within the Doppler absorption spectrum. Crossover peaks show up when the laser frequency matches half of the frequency interval between the excited atomic states. These crossover peaks act as particularly useful frequency markers for laser locking, as they produce large transmission dips (see Fig. 4.4). For detailed explanation of the saturated absorption mechanism see Refs. [121, 122, 123]

The photodiode signal of absorption profiles obtained from the Rb vapour cell, shown in Fig. 4.3, provides a frequency guide that can be used when locking the laser. The frequency correction applied to the laser is made by fine adjustment of the cavity length through the diffraction grating attached to the piezo-electric transducer (PZT) or by altering the laser diode current.

In the discussion of saturated absorption spectroscopy we consider two very important mechanisms that are needed to resolve the Doppler-free features. The first is known as *saturation* and the other mechanism is *hyperfine pumping* [121]. Both velocity dependent mechanisms alter the populations in the atomic states.

In a two-level atom model approximation the time averaged population limit between the ground and excited state is imposed by the saturation effect from the high intensity laser beam used for absorption spectroscopy. In the saturation regime,  $I \gg I_{\text{sat}}$  one can reach the upper limit of 50% of the population in the excited state.<sup>2</sup>

In the multi-level approach where there are multiple ground states accessible from the excited states the *hyperfine pumping* mechanism alters the absorption of saturated absorption spectroscopy. For <sup>87</sup>Rb the ground state splits into two hyperfine state (see

---

<sup>1</sup> $N(v) = \sqrt{\frac{m_{\text{Rb}}}{2\pi k_B T}} e^{-\frac{m_{\text{Rb}} v^2}{2k_B T}}$

<sup>2</sup>Stimulated emission is proportional to population in the excited state, whereas absorption is proportional to population in ground state; and 50% of the atomic population in ground and excited state is a result of stimulated emission and absorption balance (spontaneous emission is very weak in the  $I \gg I_{\text{sat}}$  limit).

Fig. 2.1). If the pump-probe system interacts with the upper ground state  $F' = 2$  but atoms decay to the lower ground state  $F = 1$  then they are no longer in the pump-probe detection system. This mechanism is referred to as ‘dark state sink’ in Ref. [121] and may contribute greatly to the reduction of the absorption.

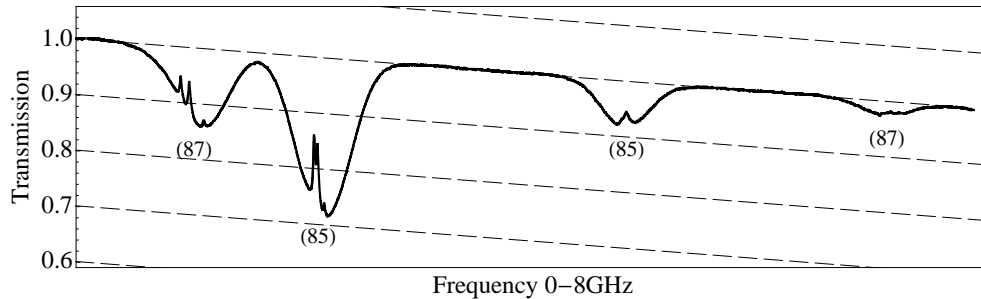


Figure 4.3: Experimental Doppler-broadened absorption spectrum of the rubidium D2 line. The  $^{85}\text{Rb}$  absorption profiles are separated by  $\approx 3.036$  GHz and the  $^{87}\text{Rb}$  isotope profiles are separated by 6.835 GHz. The total magnitude of the frequency scan was approximately 8 GHz. The above spectrum was obtained by ‘stitching together’ of different spectra with the smaller scan range.

In Fig. 4.4 it is possible to see the enhanced absorption signal at locking frequency for the repump laser. For details see Ref. [124].

#### 4.1.5 Locking

The Strathclyde laser locking setup is based on a frequency modulation technique, known as *dither locking*. The saturated absorption spectroscopy signal was converted into the derivative signal using electronics that combine the modulated photodiode signal and the modulation itself (with a variable phase shift). The obtained signal have a linear (zero-crossing) response to laser frequency near the centre of the absorption line. An integrator can therefore be used to lock the laser to a zero in the derivative signal, which means locking to the top of an absorption peak. The derivative curve acts as a good error signal in the feedback loop connected to an op-amp based integrator.<sup>3</sup>

---

<sup>3</sup>A linear signal through a zero-crossing is a good indicator if the frequency is drifting up or down, unlike a peak signal.

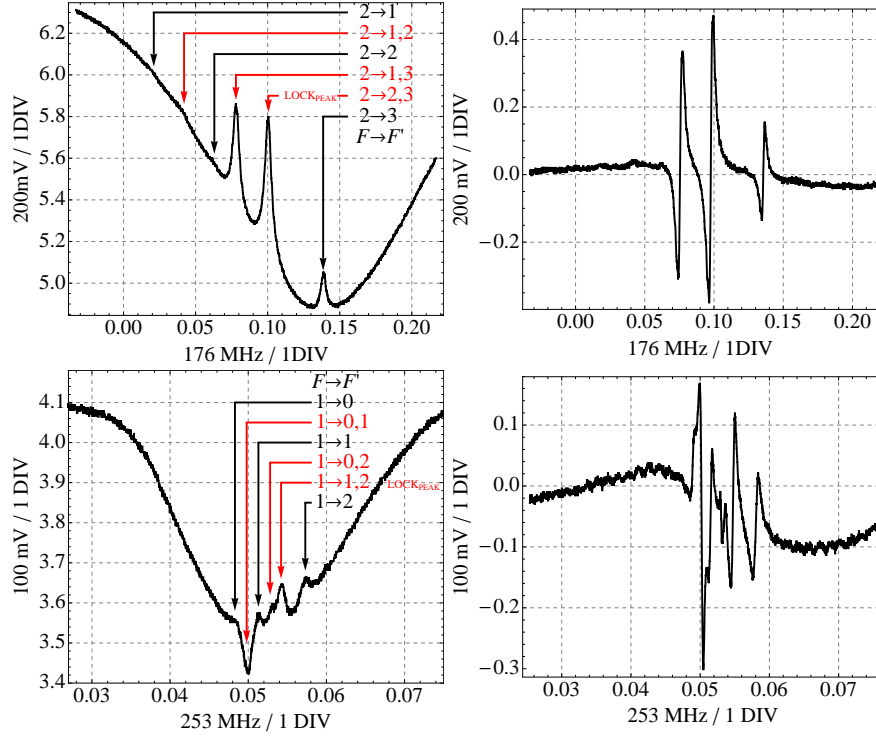


Figure 4.4: Experimental saturated absorption spectra of  $^{87}\text{Rb}$   $F = 2 \rightarrow F'$  (top) and  $F = 1 \rightarrow F'$  (bottom) transitions and their corresponding signal derivatives for the laser lock (right). Black arrows indicate  $F \rightarrow F'$  transitions with frequency  $\nu_1$ ,  $\nu_2$ ,  $\nu_3$ , whereas red arrows correspond to cross-over peaks at frequencies  $\{\frac{\nu_1+\nu_2}{2}, \frac{\nu_1+\nu_3}{2}, \frac{\nu_2+\nu_3}{2}\}$ .

#### 4.1.6 Correction to the right frequency

The trap laser was locked to the  $^{87}\text{Rb}$   $F = 2 \rightarrow F' = 2, 3$  cross-over peak. Therefore the frequency of the trap laser is 133.7 MHz detuned to the red from the main  $^{87}\text{Rb}$  cooling transition  $F = 2 \rightarrow F' = 3$ . The final frequency selection can be made by using an acousto-optical modulator (AOM). The beam passing through an AOM is up-shifted by a frequency interval equal to the frequency of the RF signal fed to the AOM. For the trap laser the AOM shifts the frequency of the beam to the blue by  $133.7 - \Delta_{\text{trap}}$  MHz, where  $\Delta_{\text{trap}}$  is the trap detuning used in magneto-optical traps. The typical HP (LP) MOT detuning is 17.8 (15.4) MHz, hence the RF frequency fed to the AOMs is 115.9 (118.3) MHz.

Similarly the repump beam, as it interacts with different atomic states, needed to be corrected in terms of frequency by a different AOM. The repump laser was locked

to  $^{87}\text{Rb}$   $F = 1 \rightarrow F' = 1, 2$  cross-over peak. The frequency interval between this cross-over peak and the adjacent resonance transitions ( $F = 1 \rightarrow F' = 1$ ,  $F = 1 \rightarrow F' = 2$ ) is equal to  $\pm 78.4$  MHz. The repump AOM shifts the lock-point frequency to the blue by 78.4 MHz, and is set for the main repumping transition ( $5s^2S_{1/2}$ )  $F = 1 \rightarrow (5p^2P_{3/2})$   $F' = 2$ .

We use six<sup>4</sup> acousto-optical modulators to control the experiment. Three are used for controlling the trapping and repumping light for the HP and LP MOT. One AOM is implemented to obtain the right frequency light for transferring the atoms from the HP to LP MOT – the ‘push’ beam (AOM: 133.7 MHz  $\rightarrow \Delta_{\text{push}} = 0$ ,  $F = 2 \rightarrow F' = 3$ ). We use light of the same frequency for imaging, therefore this AOM provides the light for both beams: pushing and imaging. In the experiment another resonant transition, optical pumping ( $\sigma_+$ ) :  $F = 2 \rightarrow F' = 2$ , is achieved with a separate AOM. The frequency shift on this AOM (133.7 MHz) is the opposite way to the pushing / imaging beam. This separate AOM provides precise control in switching of the beam. An experimental AOM setup is shown in Fig. 4.5 where one can see the separation between different orders of the beam. The first order beam corresponds to a frequency upshifted beam by the frequency directly applied to the AOM.

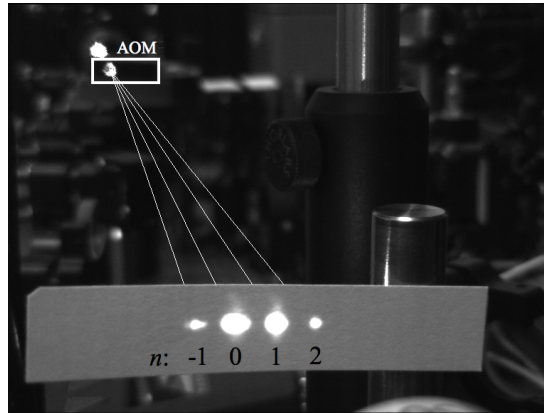


Figure 4.5: Experimental beam deflection after an acousto-optical modulator. Altering the orientation of the crystal inside the AOM allows control of the intensity for the  $n$ -th order beam, and also depends on the amplitude of the RF signal applied to the crystal.

---

<sup>4</sup>One acousto-optical modulator is used for controlling the dipole beam (see Sec. 6.2).

### 4.1.7 Dipole beam

In order to deliver a dipole beam that is far blue-detuned from the D2 lines we had to provide an additional laser source. A commercially available diode at 658 nm wavelength was a good candidate to implement into a known laser design setup. At that wavelength (compared to the atomic resonance at 780 nm) the frequency instability of the laser is not an issue, hence there was no need of locking the laser to a certain frequency. A free running laser diode mounted with a collimation lens at constant temperature and stable current was a good source for the purpose of the experiment. Typical dipole beam parameters are highlighted in Tab. 4.1.

Dipole beam parameters	$\lambda$	$w(0)_y$	$w(0)_z$	Power	$\Gamma_{sc}$	$U_{dip}$
	658 nm	13.7 $\mu\text{m}$	8.8 $\mu\text{m}$	50 mW	0.5 Hz	32.7 $\mu\text{m}$

Table 4.1: Dipole beam parameters. The calculations of the above values were done using a focal distance  $f_{\text{lens}} = 8$  cm. The trap depth ( $U_{\text{dip}}$ ) and scattering rate ( $\Gamma_{\text{sc}}$ ) were calculated using Eqs. 3.66 and 3.67.

## 4.2 Low and High Pressure MOTs

The idea behind the double MOT setup is to separate spatially two differentially pumped experimental chambers. The general lab lore says that for pressure of  $10^{-9}$  Torr we expect atoms to have a magnetic lifetime of 1 s [125]. This dependence between the pressure and the magnetic lifetime results in lifetimes of 10 s and 100 s for chamber pressures of  $10^{-10}$  and  $10^{-11}$  Torr respectively. In the Strathclyde experiment the HP chamber pressure is directly affected by the atoms from the getters (alkali metal dispensers). It results in a relatively higher chamber pressure. When the getters are not running the pressure in the HP chamber is much lower. In general we have pressures of  $\sim 10^{-9}$  and  $\sim 10^{-11}$  Torr in the HP and LP MOT chambers respectively.

The vacuum system for the MOTs (Fig. 4.6) is made of stainless steel that is very immune to magnetisation. The construction of the HP chamber allows trapping beams to penetrate the interior of the chamber through the glass viewports. The MOT viewports are anti-reflection (AR) coated for normally-incident 780 nm light. In the double MOT setup the HP MOT acts as a source of atoms and is used to multiply load [126]

the LP part of the vacuum system where the LP MOT is situated. The loading rate of the HP MOT is controlled by the current passing through SAES alkali metal dispensers [127, 128]. The two MOT chambers are connected through the 30 cm transfer tube ( $\phi = 5$  mm). Instead of a stainless steel chamber at the LP MOT end, there is a special quartz vacuum cell. The LP MOT cell is formed within a ‘square donut’ shape, where the side-length of the square chamber is  $\approx 12$  cm. The unique shape of the vacuum cell provides the geometry not only for implementing the magneto-optical trapping but also for the toroidal magnetic trap that will be described in Sec. 4.4.

In order to create the magneto-optical traps the vacuum system has to be accompanied with lasers. A large variety of optical elements is still needed to build a compact and space limited setup. High precision and carefulness were inseparable aspects for aligning and altering the existing optical setup. As was mentioned in Sec. 4.1.3 the trap laser beams for both MOTs were derived from one laser, namely a TOPTICA DLX laser (1W, 780 nm).

The trapping laser beams for the HP and LP MOTs have separate beam expanders to control beam size and collimation. The lenses used for beam expansion provides  $10\times$  ( $14\times$ ) beam size increase for the HP (LP) MOT. For maintenance and consistency in the experiment the intensity of the individual trapping beams was measured regularly using the photodiode head of a power meter. The  $1\text{ cm}^2$  square detector was irradiated by each beam and the maximum power was recorded. For the HP trapping beams this yielded:  $I_x \approx 8.0\text{ mW/cm}^2$ ,  $I_y \approx 7.9\text{ mW/cm}^2$ ,  $I_z \approx 7.8\text{ mW/cm}^2$ . Similarly for the LP MOT the intensities of the beams were measured:  $I_{\pm x} \approx 6.3\text{ mW/cm}^2$ ,  $I_{\pm y} \approx 6.8\text{ mW/cm}^2$ ,  $I_{\pm z} \approx 6.4\text{ mW/cm}^2$ . For the HP MOT three retroreflecting mirrors were used, hence the total intensity provided for the HP (LP) MOT was  $I_{\text{HP(LP)}}(tot) = 2(I_x + I_y + I_z)$ . The number of atoms in the MOTs is quite sensitive to the alignment of the lasers, but the intensity imbalance between the trapping beams is relatively forgiving and even with a  $\sim 20\%$  difference in beam intensity it is still possible to create a stable MOT with large atom number.

Each incoming HP trapping beam is retroreflected after it passes the HP chamber. The retroreflecting mirrors used in the MOT may introduce an unwanted optical feedback to the diode laser. To avoid light conflicts between the diode laser and a reflected beam the  $-40\text{ dB}$ , LINOS FI-780-5 SV-BB, optical isolator (OI) is implemented for the repump laser and a  $-60\text{ dB}$  OI for the trapping beam.

The top view of the Strathclyde double MOT setup is present in Fig.4.6. For

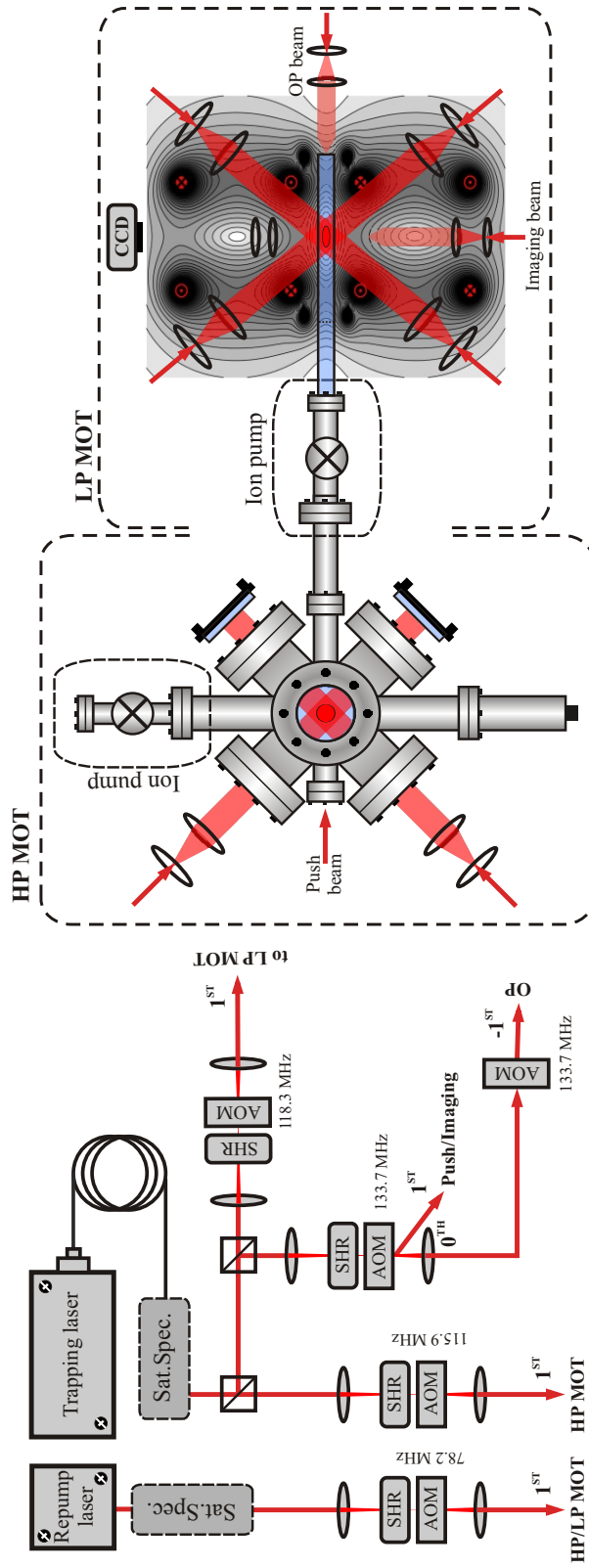


Figure 4.6: The double MOT optical setup. The trap / repump laser provide the trapping / repumping light for both MOTs (HP and LP). Also, laser beams for pushing the atoms, as well as optical pumping (OP) and probing are derived from the trap laser. The contours visible at the LP end of the figure represent the magnetic field in the MOT configuration from the Strathclyde hybrid trap (see Sec. 4.3). The centres of the two MOTs are separated approximately by 50 cm. The focusing lenses (  $f = 250$  mm) before and after each acousto-optical modulator (AOM) and shutter (SHR) were used for the laser beams used for trapping. The photograph of the actual setup is shown in Fig. 4.7.

clarity not all the elements are shown, e.g. OI's, periscopes – raising the height of the horizontal laser beams, anamorphic prism pairs – expanding a laser's beam profile from elliptic to circular, (non)polarising beam splitters – splitting laser light into two beams with (different) the same intensities, waveplates setting the polarisations of the beam.

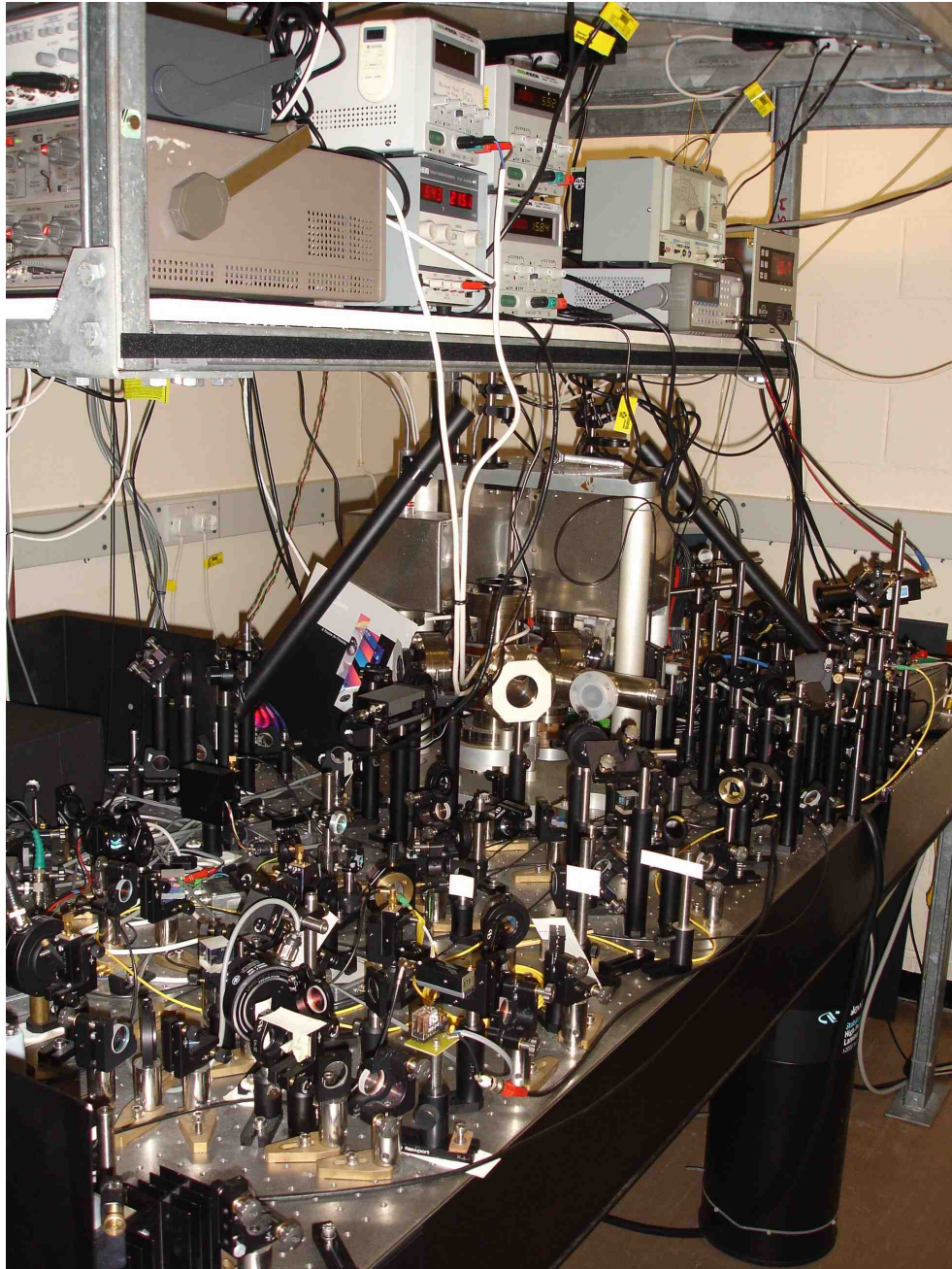


Figure 4.7: Optical table setup at Strathclyde University (2009).

Shutters are important elements of the BEC experimental setup. They eliminate light leakage into the regions where it could cause unwanted effects on atoms (when left

open this can drastically decrease the magnetic trap lifetime). In the Strathclyde experiment we used commercially available shutters (LS6T2 Uniblitz). Four shutters were implemented for: the trapping laser after the fibre, LP MOT, pushing / imaging / pumping and the repump beam (all shutters were also connected to the door lock security system). Several tests were done with a home-built shutter (based on PCB Power Relay - G2R-2 5DC) that can also be implemented with the experiment. These shutters are the optional and cheaper version for the experiment. Additionally AOMs are used as very fast optical shutters.

Six acousto-optic modulators are currently employed in the BEC experiment: three were used for frequency-shifting the three laser beams used for trapping, two were used for frequency-shifting the push/pump/probe laser beams, and one to control the dipole beam.

### 4.3 Hybrid trap

Controlled motion of neutral atoms using magnetic wave guides has appealed to the imagination of researchers from the field of modern atomic physics. Rapid development of magnetic structures made from current carrying wires has been seen over the past few years [129, 130, 131, 43]. These setups gave a promising perspective for wide use of magnetic guides not only for cold atoms but also for BECs.

In the previous section the experimental setup of a double MOT involves the generation of two independent quadrupole fields for the purpose of magneto-optical trapping. The magnetic field for the HP MOT is generated from the standard anti-Helmholtz type circular coil configuration, whereas the LP MOT magnetic field comes from the hybrid coil configuration. The Strathclyde magnetic coil design at the LP end (see Fig. 4.8) allows the realisation of different magnetic geometries. Firstly: to generate a 3D MOT quadrupole magnetic field needed in the first stage towards reaching BEC – i.e. a MOT, secondly: to generate a Ioffe-Prichard like magnetic trap, thirdly: to generate a pure toroidal magnetic storage ring, fourthly: to choose the split ratio of the condensate when inside the storage ring.

By using the hybrid trap we can avoid a lossy process of transferring atoms from the magneto-optical trap to a separate magnetic trap. The unique setup also enables us to create cold atomic samples and even BECs already within a section of the ring, at the same time getting rid of the need for a transfer between the magnetic trap and the

ring. Another advantage, when employing the hybrid trap, is that we can operate the trap using the same power supplies. These aspects are certainly of practical advantage when using the hybrid trap.

The Strathclyde hybrid trap combines the following current carrying components:

- four two-turn circular coils,  $\phi = 2 \times 12.5$  cm and  $2 \times 7.5$  cm
- four three-turn square coils, with a side  $a = 7.5$  cm
- a single straight wire

The schematic of the hybrid trap is presented in Fig. 4.8, where different colours were used to distinguish different parts of the coils setup.

The four two-turn red circular coils generate a 2D toroidal magnetic quadrupole field. They provide ring confinement for the atoms.

The four three-turn blue rectangular coils (also called ‘pinch’ coils due to their atom localisation character) are used interchangeably for Ioffe-Prichard trapping of the atoms and for operating the MOT. When the direction of the current is in the same sense for all four rectangular coils the hybrid trap operates in the IP mode, and when the direction of the current in one of the pinch coils pairs is reversed the trap operates in the MOT configuration. A different ratio between the currents in the square coils (when all operated with the same current sense) can provide a magnetic field gradient, which then can be applied for magnetic field gradient splitting of a cloud of atoms inside the ring.

The green straight wire, in Fig. 4.9, generates a bias field at the centre of the toroidal quadrupole field from the blue circular coils. The additional azimuthal magnetic field removes an unwanted zero field line from the purely toroidal quadrupole field and hence prevents the atoms from lossy transitions, like Majorana spin flips [132]. The resulting effect of adding the azimuthal magnetic field to the toroidal quadrupole field is presented in Fig. 4.11(b).

### 4.3.1 Hybrid trap – MOT / IP and ring

The four (two-turn) circular coils under maximum current operation carry a current of two-turn $\times$ 500 A. The four (three-turn) rectangular coils can generate magnetic fields using: 3-turn $\times$ 500 A. When using relatively high currents in the system the elimination of heating had to be considered. In our experiment the passive elements of the magnetic

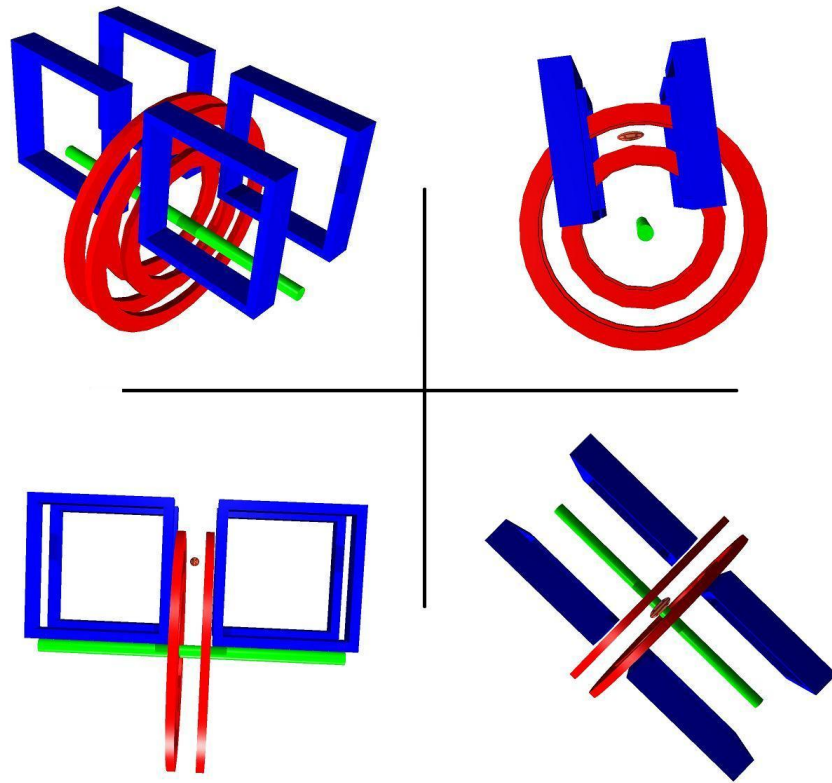


Figure 4.8: Different views of the magnetic coil system of the Strathclyde magnetic storage ring. Four circular coils (red) with average radius of 5 cm generate the storage ring magnetic field minimum. The square coils (blue), with side lengths of 7.5 cm, localise atoms in the magneto-optical trap or magnetic trap depending on their current direction. Additionally, the axial straight wire (green) adds an extra azimuthal magnetic field to the system, and therefore it removes the zero field from the toroidal quadrupole field generated by the red coils.

trap (rectangular coils, circular coils) utilised copper rectangular cross section pipes. This allows internal water cooling during coils operation.

The typical parameters of the hybrid trap are: MOT with maximum field gradients of  $(210, -140, -70)$  G/cm in the  $(x, y, z)$  directions respectively, IP-like magnetic trap with bias field  $B_0 \approx 1$  G (the compensation of the bias field is done by additional rectangular pair of coils),  $B_1 = 230$  G/cm,  $B_2 = 60$  G/cm<sup>2</sup>. The straight wire adds 0 – 10 G (0 – 250 A) at the centre of the quadrupole toroidal magnetic field from the circular coils.

## MOT

The hybrid trap in the MOT operation settings utilises a magnetic field from the ring and square coils. The combination of these coils can be supplemented by a three-dimensional spatially constant offset field (bias field), effectively changing the position of the field minimum, and hence the position of the MOT. The theoretical model (obtained from the Biot-Savart law) of MOT magnetic field contours is shown in Fig. 4.9. The larger gradient of magnetic field seen in the radial direction (Fig. 4.9) when the

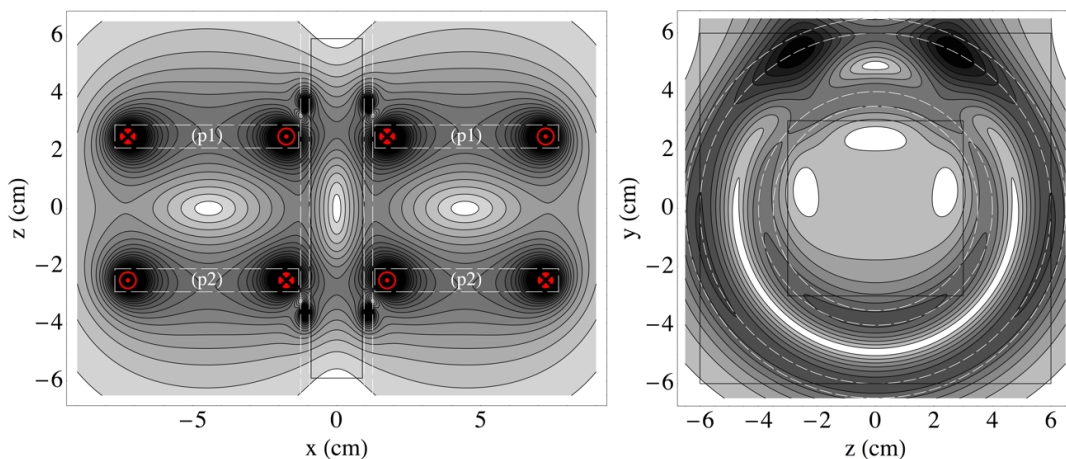


Figure 4.9: (LHS) The top view of the theoretical magnetic field contour plot for the magnetic coils system working in the MOT configuration (magnetic field slice at  $z = 4.8$  cm). A pair of square coils ( $p1$ ) conduct the current in the reverse direction relative to the other pair of coils ( $p2$ ), which results in the generation of a 3D quadrupole field. (RHS) The side view of the magnetic field contour plot in the MOT configuration (magnetic field slice at  $x = 0$  cm). The scales in the images are in centimetres. Dashed lines estimate the positions of the magnetic coils and the solid lines mark the outside edges of the vacuum glass cell.

coils are in the MOT configuration results in a slightly elongated magnetic field shape. The atoms in the MOT have a shape that is more like a 3D ellipsoid. The centre of the MOT magnetic field matches the position of the cigar-shaped Ioffe-Pritchard magnetic trap, which is presented in the next section.

### Magnetic trap

Reversing the current direction in one pair of the square coils and adding an extra field from compensation coils results in the transformation of the MOT magnetic field to an IP magnetic trap field in the hybrid trap. The potential minimum from both traps must be in the same place to prevent sloshing, and the ‘shape’ (curvature) of the potential must be the same (mode-matched) to prevent breathing. The theoretical representation of the hybrid trap working under the IP configuration, without a magnetic field from the compensation coils, is shown in Fig. 4.10.

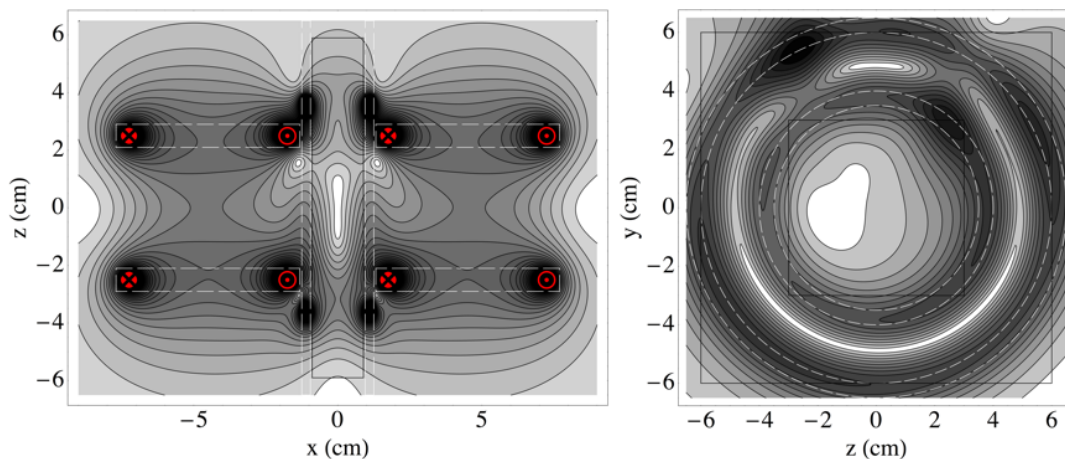


Figure 4.10: (LHS) The top view of the theoretical magnetic field contour plot for the magnetic coil system working in the IP configuration (magnetic field slice at  $z = 4.8$  cm). All square coils conduct the current in the same direction, which results in the generation of an IP field. (RHS) The side view of the magnetic field contour plot in the non-compressed IP like configuration (magnetic field slice at  $x = 0$  cm). The scales in the images are in centimetres. Dashed lines estimate the position of the magnetic coils and the solid lines mark the edges of the vacuum glass cell.

The transition between the two distinct field geometries is performed experimentally after the further cooling in optical molasses. The IP magnetic trap is turned on and then compressed over  $\approx 400$  ms, which results in an increase of the density and temperature of the atoms. The creation of the compressed magnetic trap enables further cooling by applying evaporative techniques to the atoms. Having an atomic sample prepared (cold atoms or BEC) they can be launched into the magnetic guide provided by the magnetic field from the circular coils. In the next section we describe

in detail the Strathclyde storage ring.

## 4.4 The toroidal magnetic storage ring

A useful extension of the magnetic guidance of neutral atoms was in the form of the closed loop guide. In 2001 the first demonstration of an electrostatic ring for molecules was reported [41] when a group in Netherlands used a dipole ring to trap neutral deuterated ammonia molecules and then a few months later the first atomic storage ring for neutral atoms was realised [42] by a group in the USA using neutral  $^{87}\text{Rb}$  atoms. The storage ring for neutral atoms demonstrated in Ref. [42] consisted of a simple two-wire magnetic guiding structure. The first magnetic storage ring [42] had a diameter of 2 cm with a less than 1 s lifetime for trapped atoms. The loading process was relatively inefficient, only about 15 % of the MOT atoms were transferred into the guide. In our work we show that the way to avoid such a lossy loading process is to use a hybrid trap (Sec. 4.3). All the details and advantages of the Strathclyde storage ring will be described in the next section.

### 4.4.1 Giant storage ring

The Strathclyde storage ring utilises a quadrupole magnetic field from a four-loop geometry. In the theoretical section (see Sec. 3.3.2) we showed how to obtain the magnetic field from a single current carrying coil in terms of elliptic integrals. A toroidal quadrupole magnetic field generated by the four concentric circular coils can be represented as:

$$\begin{aligned} \mathbf{B}_{\text{ring}}(q, z) &= \sum_{i=1}^2 \mathbf{b}_{R+(-1)^{i+1}\delta_R} \left( q, z + [(-1)^{i+1} \delta_z] \right) - \sum_{i=1}^2 \mathbf{b}_{R+(-1)^i\delta_R} \left( q, z + [(-1)^{i+1} \delta_z] \right) \\ &= \mathbf{b}_{R+\delta_R}(q, z + \delta_z) + \mathbf{b}_{R-\delta_R}(q, z - \delta_z) - \mathbf{b}_{R+\delta_R}(q, z - \delta_z) - \mathbf{b}_{R-\delta_R}(q, z + \delta_z) \end{aligned} \quad (4.1)$$

It generates a more symmetric version of the magnetic field than a setup composed of only two concentric current carrying loops (Fig. 3.13).

The magnetic ring-shaped guides are especially useful for performing ultra-sensitive atom interferometry. The fact that the effective enclosed area of the ring is proportional to the potential sensitivity encouraged us to increase the size of the storage ring. In our experiment (Eq. (4.1))  $R \approx 5.0$  cm and the radial  $\delta_R$  and axial displacement  $\delta_z$

are equal to 1.25 cm and 1.35 cm respectively. This geometry places a zero magnetic field at a slightly smaller distance than  $R$ . This effect is shown in Fig. 4.11 where the magnetic field magnitude is plotted along the vertical axis.

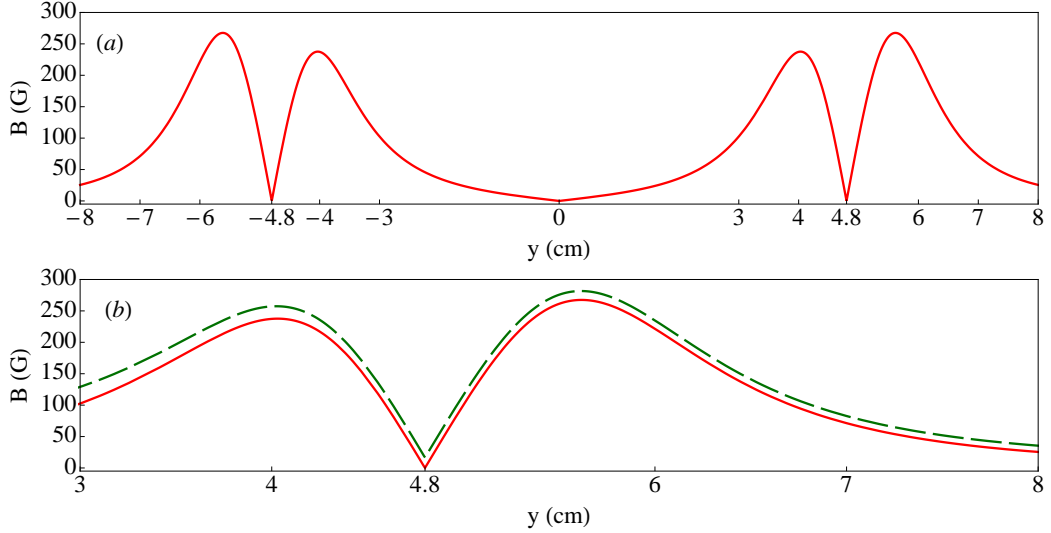


Figure 4.11: (a) The magnetic field magnitude (along  $y$  axis) from the giant storage ring (the red solid line). The maximum field magnitude at 500 A sent through the coils is 267 G at  $y = 5.6$  cm. The ring configuration coils place the minimum magnetic field at  $y = 4.8$  cm. That results in a ring magnetic guide with the diameter of 9.6 cm. (b) The green dashed line represents the magnetic field from four circular coils and the axial straight wire, which adds an extra azimuthal magnetic field.

The ‘BEC-friendly’ storage ring has additional advantages. Our storage ring may accommodate  $\approx 5 \times 10^8$  atoms. The magnetic trap lifetime is about 40 times longer compared to the first storage ring [42] and is equal to 40 s. Our cold atom magnetic storage ring is the biggest in the world with  $72 \text{ cm}^2$  of an effective enclosed area. The shape of the ring also provides high optical access for easy imaging.

## 4.5 Current control

The controllable current flow through the coils is of great importance when dealing with atoms in the magnetic field. Depending on the magnitude of the current that is being sent through the MOSFETs, which are used for controlling the current flow, their specification have to be chosen carefully taking into account the maximum power a MOSFET can dissipate. To generate the three different magnetic field configurations

(magneto-optical trap, Ioffe-Pritchard magnetic trap and storage ring) a system of five water-cooled MOSFET banks was used. Each of the MOSFET banks contained 20 single BUK555 MOSFETs. The sources (drains) of the MOSFETs were attached onto two parallel copper bars with a cross section of  $20 \times 10 \text{ mm}^2$ . The MOSFETs were bolted down and additionally thermal paste was used for better conductivity. The copper bar was connected to the water cooling system that helped to dissipate the power off the MOSFETs.

Sometimes the experiment experienced a problem from a faulty MOSFET that blew up shorting the circuit and letting most of the current go through it without any control. Eventually all older model MOSFETs BUK555-60H 60 V, 41 A, 125 W (now obsolete) were replaced by PHP125O6T 55 V, 75 A, 187 W MOSFETs which have a higher rating. In addition to the PHP125NO6T MOSFETs a set of IRFP2907 75 V, 209 A, 470 W MOSFETs was tested. For testing purposes a single bank of MOSFETs was built. The IRFP2907 MOSFET's specification (max 209 A / 10 V at continuous drain current) enabled us to build a more compact bank since only ten of them were needed on one MOSFET bank. This improvement can be applied in the future to gain more space on an already busy optical table.

During the experiment MOSFETs have to deal with relatively high powers. Each MOSFETs bank has to be able to cope with a power dissipation of  $5 \text{ V} \times 500 \text{ A} \Rightarrow 2.5 \text{ kW}$ . That power is split equally on the individual MOSFETs in parallel, hence using 20(10) MOSFETs on one bank we must ensure power dissipation of at least 125 W (250 W) on a single MOSFET. The on-state resistance of a BUK555-60H / PHP125NO6T / IRFP2907 MOSFET is  $38 \text{ m}\Omega / 8 \text{ m}\Omega / 4.5 \text{ m}\Omega$  yielding a total MOSFET bank on-state resistance of  $1.9 \text{ m}\Omega / 0.4 \text{ m}\Omega / 0.45 \text{ m}\Omega$ .

The circuit used to control the MOSFET banks which regulate the currents in the coils will be described in Sec. 4.5.1. The currents in the magnetic coils originate from the same 5 V, 500 A power supply and as shown in Fig. 4.12 the coils are connected in series configuration, which ensures high stability and optimal magnetic field noise cancellation, as reported in Ref. [133].

#### 4.5.1 Driving circuit

The design of the coil driver is based on an integrator, which enables or limits the flow of current through the coils. The input voltage was provided by a separate analogue signal from the computer. Digital-to-analog converter (DAC) voltage output from the

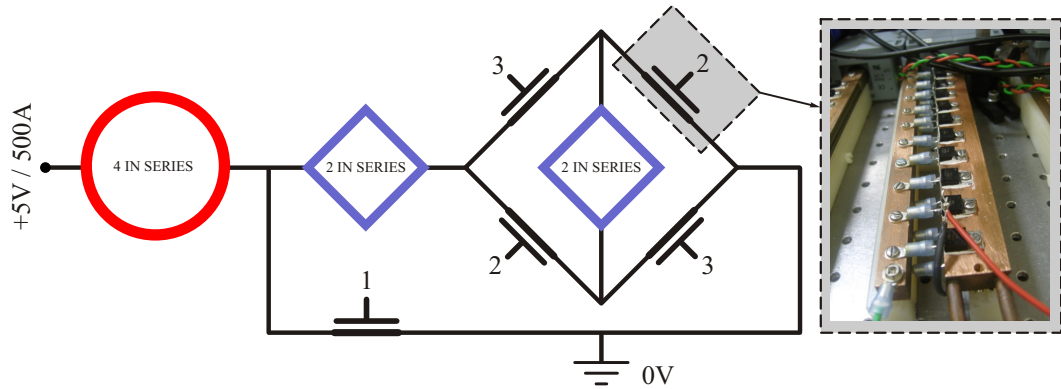


Figure 4.12: MOSFET bank system.

computer when fed straight to the current stabilisation mechanism introduced AC noise to the electronic system (more than  $200 \mu\text{V}$ ). The problem was solved by first sending the DAC voltage through a differential amplifier. In our instance we set the gain on the amplifier to 1 and take a difference between the shell (zero) and core (signal) of the BNC connector from the DAC. An adjustable gain resistor on the integrator was set in such a way that the RC constant allowed fast (less than 1ms) magnetic field switching but also preventing unwanted oscillation.

The fast feedback to the current stabilisation mechanism (a differential amplifier prior to an integrator) was provided by a high frequency response (150 kHz) current sensor. The current sensing was done using a non-invasive closed loop Hall effect sensor (CSNR-161). Thermal insensitivity and accurate measurements made the sensor model ideal. The normal rms AC current noise (reading at sense resistor  $0.150 \mu\text{V}$ ) to DC current (reading at sense resistor 8 V) ratio was approximately  $2 \times 10^{-5}$ . With a  $\pm 16 \text{ V}$  low-noise floating power supply and  $33 \Omega$  sense resistor the sensor could measure currents up to 500 A.

The circuit used to control the MOSFET banks which regulate currents in the MOT and IP coils is shown in Appendix E. The design is slightly modified for the coil-driver used for controlling the torus, bias, molasses coils and azimuthal wire (see Appendix E).

#### 4.5.2 DAC specification

The resolution of the voltage applied to the controlling circuit depends on the hardware used in the experiment. The Strathclyde BEC experiment is equipped with a 12-bit DAC card (National Instruments PCI-6713). A 12-bit DAC card means that there are

$2^{12}$  steps over the control voltage sent to the current drivers, i.e. the output voltage of the DAC can be adjusted between  $\pm 10$  V and 12-bit resolution corresponds to step intervals of  $\approx 5$  mV ( $4.88 \times 10^{-3}$  V). For future improvement 12-bit DAC card can be replaced with a 16-bit DAC card which is now available commercially.

## 4.6 Dipole beam setup

The Strathclyde laser beam for optical dipole splitting is generated by 150 mW of light from a free-running 658 nm diode laser, far to the blue of the Rb D2 resonance at 780 nm. In order to create a high intensity dipole beam we used an 80 mm focal length achromat lens. The elliptical diode laser beam shape was focused to beam waists of  $8.8 \mu\text{m}$  and  $13.7 \mu\text{m}$  in the axial and radial direction, respectively. The alignment of the dipole potential was facilitated by combining the 658 nm beam with a ‘tracer’ 780 nm repump ( $F = 1 \rightarrow F' = 2$ ) beam on a beam splitter to create a co-propagating beam with a much higher scattering rate and optical potential [134].

Experimental positioning of the dipole beam required accuracy and care as there was a limited space to accommodate an additional beam. The dipole beam was implemented at a slight angle with respect to the glass cell ( $yz$ -plane) to prevent the focusing lens for the dipole beam from disturbing the imaging beam path. To achieve a slight tilt on the focusing lens we design a mount (Fig. 4.14) that enabled adjustable tilt of the focusing lens. A schematic of the dipole beam experimental setup is presented in Fig. 4.13, where it is shown that the optical dipole laser beam propagates perpendicular to the BEC’s longitudinal axis.

## 4.7 Cameras

The CCD cameras are indispensable elements in the BEC lab. The main purpose of the cameras is to record information regarding what happens in the experiment. In the Strathclyde BEC experiment we use three separate CCD cameras for general control and optimisation and one camera for temperature measurement of the cold atoms and BEC.

The first camera displays the relative position and size of the cloud of atoms that is present in the HP MOT. This camera points at the HP MOT through the polarising beam splitter which is also used for directing the pushing beam responsible for transfer between the MOTs. This setup enables us to make accurate in situ alignment of the

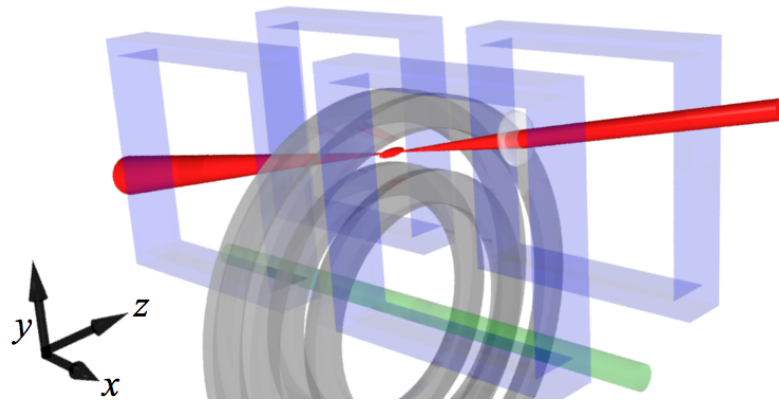


Figure 4.13: Experimental setup of the dipole beam. The ellipticity of the dipole beam is not shown in this model, however in the experiment the elliptical diode laser beam shape was focused to beam waists of  $8.8 \mu\text{m}$  and  $13.7 \mu\text{m}$  in the axial and radial direction, respectively. A photograph of the actual setup is shown in Fig. 4.14

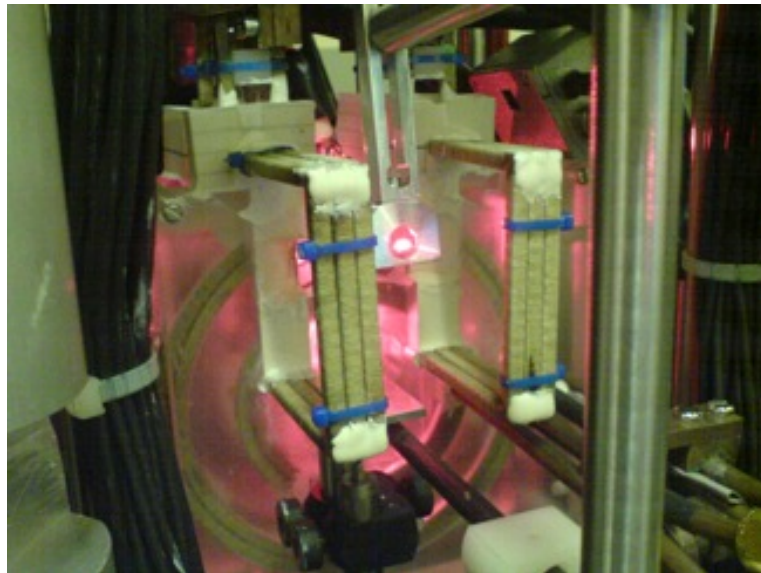


Figure 4.14: Experimental setup of the dipole beam – a photograph of the actual setup. The dipole beam in operation – lens reflection and scattered light from the glass cell are visible.

push beam in the HP MOT. The use of this camera is especially helpful when observing the creation of the HP atomic cloud after locking the lasers. It confirms straight away that the lasers are properly locked to the chosen transitions.

Another two cameras (which are also set in continuous display mode) point at the LP MOT cell. The LP MOT is more demanding on the laser beam alignment than

the HP MOT. The arrangement of the cameras enables us to observe the LP MOT atoms in two perpendicular planes. The size, position and amount of compression of the MOT atomic cloud is clearly displayed in  $xy$  and  $yz$  planes. These two cameras are also helpful when performing the final alignment of the optical molasses. For relatively long molasses expansion times ( $\approx 1$  s) very sensitive CCD cameras show any unwanted drift movement of the atomic cloud. During the long molasses expansion the cameras enable us to see large deviations in beams intensities or the imbalance of magnetic fields when cooling in optical molasses.

For the experimental determination of the density and temperature of atomic clouds the fourth camera is implemented. The working principle and software implementation will be described in the next section.

### 4.7.1 Absorption imaging

In this section we will cover methods used to obtain information about the total concentration as well as the spatial distribution of atomic clouds. By exploiting the absorption properties of the atoms we are able to gain quantitative information about the atomic sample.

Let us consider a near-resonant laser beam (probe) with an intensity in the regime  $I < I_{\text{sat}}$  shining through a cloud of atoms. The initial laser light intensity is attenuated before it reaches the detector due to partial absorption of the light by atoms. The atoms are detected by imaging the shadow of the atomic sample through a lens system onto a CCD camera. This technique is a destructive imaging process since the atomic sample is being heated by photon scattering when the picture is taken. The relative amount of light absorbed by atoms along a particular, single ray through the atomic cloud gives the column optical density. The observable optical depth (OD) as a function of the cross section for light absorption  $\sigma_0$  and density of the atomic cloud  $n(\mathbf{r})$  at a given point in space  $\mathbf{r}$  can be expressed with the incident light intensity  $I_{\text{in}}$  by the Beer's law relation:

$$I_{\text{out}} = I_{\text{in}} e^{-\text{OD}(\mathbf{r})} = I_{\text{in}} e^{-\sigma_0 \int n(\mathbf{r}) dx} , \quad (4.2)$$

Experimentally the OD for an atomic sample is obtained by recording three CCD images – one of probe light with the atoms (shadow frame,  $I_{\text{atoms}}$ ), one of probe light without the atoms (normalisation frame,  $I_{\text{probe}}$ ) and one without the probe light and without the atoms. The third frame (background frame,  $I_{\text{background}}$ ) gives a correction for the background noise. The experimental sequence of three images is shown in

Fig. 4.15. In order to obtain quantitative information about the atomic cloud one must take three images from which the relative absorption signal can then be interpreted. To get a quantitative absorption image we calculate the OD of each pixel, which is given by

$$\text{OD} = \ln \left( \frac{I_{\text{probe}} - I_{\text{background}}}{I_{\text{atoms}} - I_{\text{background}}} \right). \quad (4.3)$$

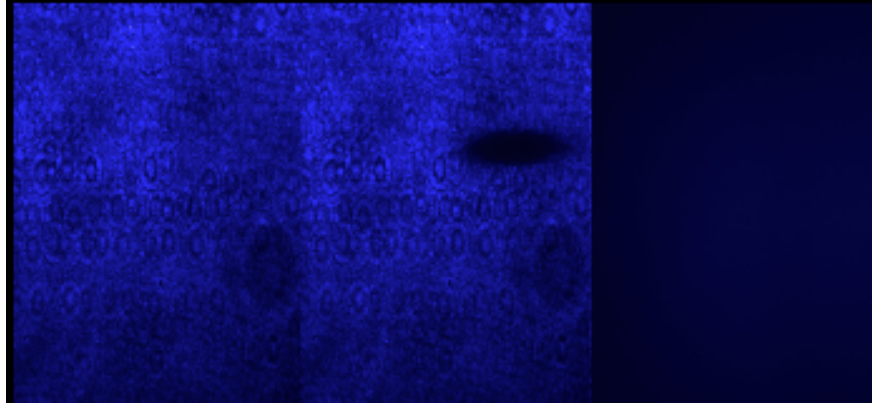


Figure 4.15: Experimental sequence of absorption imaging. From left: probe beam without atoms, probe beam with atoms, background image (no laser light). Distortions of the probe beam are due to the poor quality of the glass LP MOT cell.

The time interval between the images was set to be 40 ms, to match the frequency of the lights in the experimental room. The multiple of 50 Hz provides the same background condition for three images.

The Strathclyde experimental setup uses a set of lenses after the laser light passes through the atoms to focus the image onto a CCD camera. The laser beam, prior to probing the atomic sample is spatially filtered, by sending it through an optical fibre. A  $\lambda/4$  waveplate is placed in the optical path of the imaging beam, after the fibre, to set the circular polarisation. A circularly polarised, collimated  $350 \mu\text{W}/\text{cm}^2$  probe laser beam (derived from the resonant push beam) is sent through the atomic cloud. A schematic of the Strathclyde absorption imaging set-up is presented in Fig. 4.16.

The resolution of the imaging system must be sufficient to detect a small object like the BEC cloud. A pixel size of  $10 \mu\text{m}^2$  with optical magnification of  $\sim 2$  provided high resolution of the experimental images. Experimental data from the ballistic expansion of small clouds was used to calibrate the magnification of the imaging camera. Comparison of the parabolic atomic centre-of-mass motion with the expected  $y = -gt^2/2$  led to the magnification factor  $M = (1.94 \pm 0.07)$  (see Fig. 4.17).

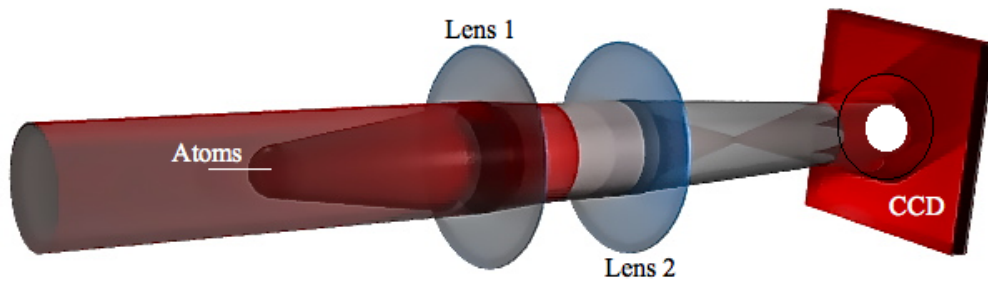


Figure 4.16: Optical system for absorption imaging. After the light passes through the cloud, the image is focused onto a CCD camera by two lenses.

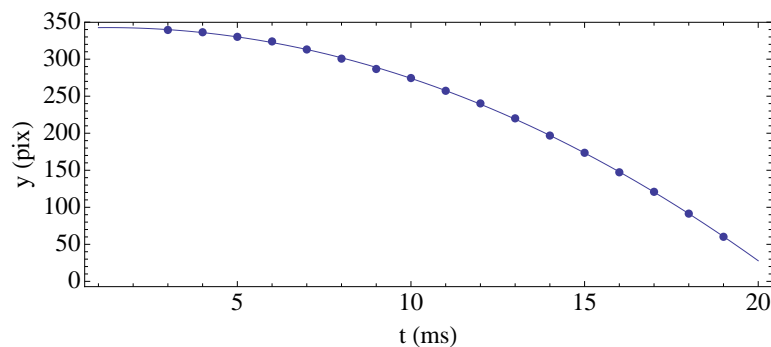


Figure 4.17: Ballistic expansion data for calibration of the magnification parameter.

#### 4.7.2 Camera software development

In the Strathclyde experiment we used a commercially available CCD camera, namely the Andor luca<sup>EM</sup> DL658M. Our CCD camera is a back-illuminated CCD array composed with  $658 \times 496$  pixels with individual pixel size of  $10 \times 10 \mu\text{m}^2$ . The maximum pixel readout rate is 12 MHz and the maximum frame rate is about 30 Hz, which is a sufficient number for recording three images in a imaging sequence. The readout noise is advertised to be  $<1e$  per pixel with the Electron Multiplication function turned on and 25 electrons per pixel (rms) in the fastest readout mode. The quantum efficiency at 780 nm is around 25 %.

Considerable time was spent developing camera software, testing and optimising the performance. The camera software driver was generated in LabVIEW code to match the existing software for controlling the BEC experiment. Here we present the final

schematic of the main routine implemented for the camera (see Fig. 4.18).

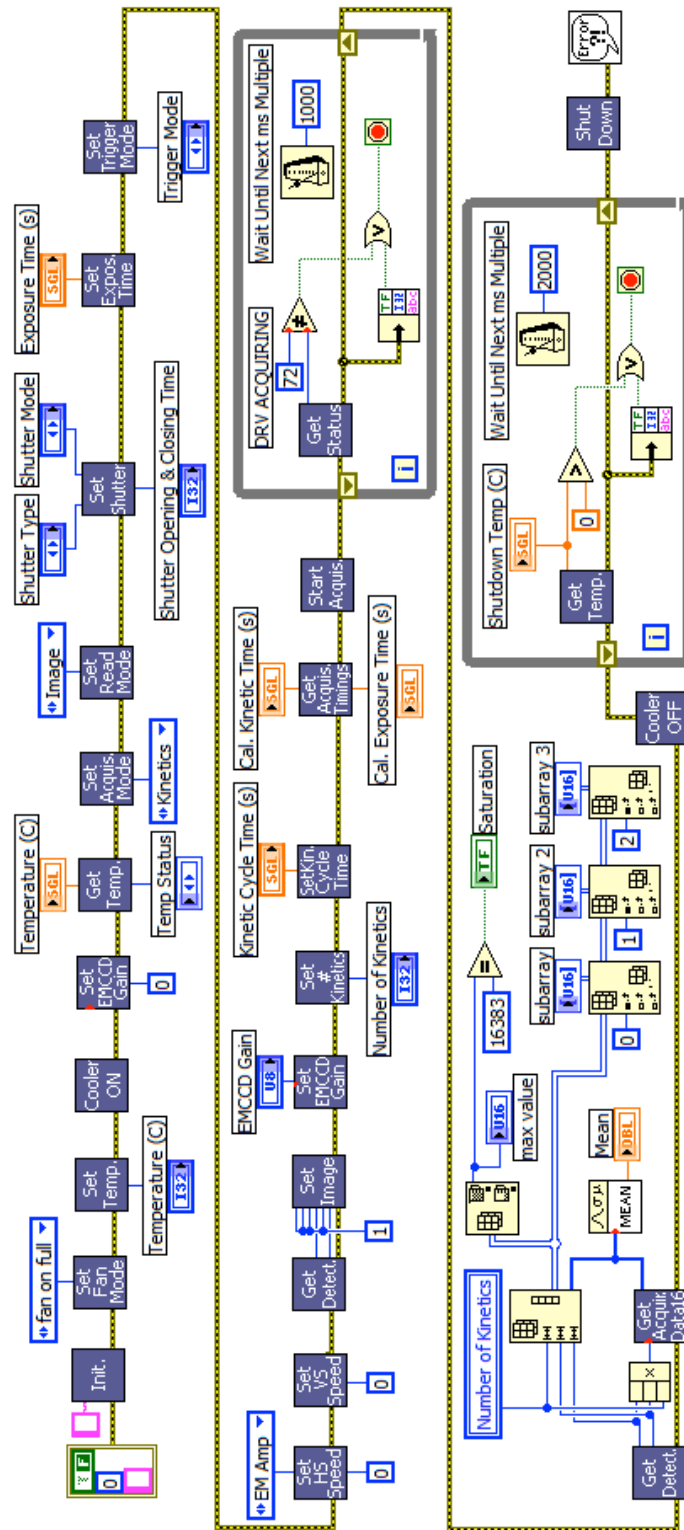


Figure 4.18: Andor luca<sup>EM</sup> DL658M CCD camera operating scheme. Internal structure imported from the LabVIEW interface.

## BEC – selected methods

In this chapter we describe a few experimental aspects that were checked, tested and optimised in order to make the procedure of reaching BEC even more efficient and reliable. We include the outline of the magneto-optical trap loading, application of the optical pumping beam and related magnetic fields, magnetic trap compression and its characteristics, and ultimately the evaporative cooling dynamics to the final result – BEC. We also mention a few aspects that improve on the existing BEC experiment, highlighting simplifications which can be made to the system.

### 5.1 Magneto-optical trap – loading sequence

As described in Sec. 4.2 in the Strathclyde experiment we use a double magneto-optical trap setup connected by a transfer tube. After the atoms are trapped in the HP MOT they are transferred to the LP MOT using a resonant laser pulses. The LP MOT collects a large number of atoms ( $\approx 10^9$ ) when a continuous sequence of  $n$  pulses is applied (see Fig. 5.1).

In our vacuum system the HP MOT and LP MOT are separated horizontally and light pressure can be used to quickly accelerate the atoms to  $\approx 25$  m/s.

#### 5.1.1 Push beam

The push beam responsible for transferring atoms from the HP MOT into the LP MOT provides a kinetic energy kick to the atoms. It pushes atoms out of the HP MOT as it matches the resonant transition of the trapped atoms. The HP MOT light is off when the push beam is pushing atoms out of the HP MOT region. The direction of

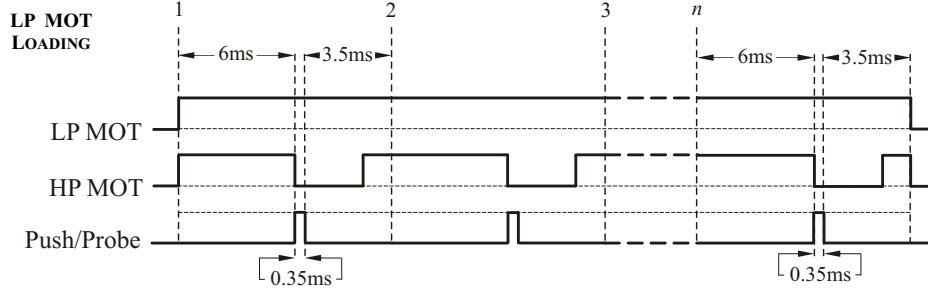


Figure 5.1: The MOT loading sequence in representation of line triggers. The push beam with time interval of 0.35 ms is related to the brown ‘(e)’ curve, later on in this section, in Fig. 5.2.

the push beam has to be chosen carefully as the atoms have to be collected at the LP MOT end, hence no influence of the resonant beam can be present at the LP MOT. By misaligning the beam from the LP MOT centre by a small angle, it can still overlap with the HP MOT centre. The intensity of the push beam is  $\approx 1.5 \text{ mW/cm}^2$ .

Depending on the time interval of the pulses used in the loading sequence (Fig. 5.1) we observe different transfer efficiency in the LP MOT loading. Fig. 5.2 shows the push beam time duration dependence on the signal recorded on a photo detector (PD) detecting the fluorescence signal 10 cm away from the LP MOT cloud, which is a good predictor of number of atoms in the MOT.

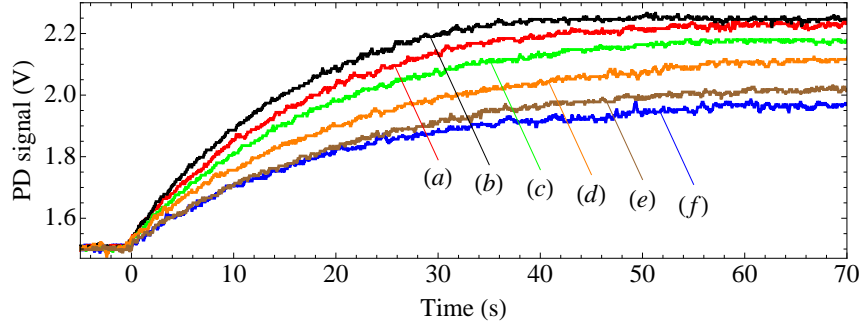


Figure 5.2: The MOT loading for different timing of the push beam. The photodetector signal was recorded for: (a) 0.15 ms, (b) 0.2 ms, (c) 0.25 ms, (d) 0.30 ms, (e) 0.35 ms, (f) 0.4 ms push beam pulses.

If the number of atoms is  $N_{\text{HP}}$ ,  $N_{\text{LP}}$  in the HP and LP MOT with lifetimes  $\tau_{\text{HP}}$  and  $\tau_{\text{LP}}$  respectively then the efficiency of loading the atoms in the LP MOT can be represented as

$$\mathcal{N}_{\text{eff}} = \frac{N_{\text{LP}}/\tau_{\text{LP}}}{N_{\text{HP}}/\tau_{\text{HP}}} \rightarrow N_{\text{LP}} = (\mathcal{N}_{\text{eff}} R) \tau_{\text{LP}}, \quad (5.1)$$

where  $R$  is the HP MOT loading rate. The estimated value for transfer efficiency between our two MOT chambers is about 20% which is still sufficiently high for good LP MOT initial conditions for BEC.

## 5.2 Optical pumping and magnetic trap

The trapping state  $|F = 2, m_F = 2\rangle$  is the quantum state where the Strathclyde condensation occurs. In order to have as many ‘good’ elastic collisions as possible between atoms a high number of atoms in the magnetic trap has to be provided, as it gives a better chance to reach the BEC transition through evaporation cooling.

After further cooling in red detuned optical molasses ( $\Delta_m \approx -50$  MHz, 25 ms) we apply a technique known as optical pumping (OP), prior to placing the atoms in the magnetic trap. Before optical pumping atoms are distributed relatively evenly between the magnetic sublevels of the ground state ( $F = 2$ ). Optical pumping is a process whereby one increases the population of atoms in a particular quantum state. For magnetic trapping the main advantage of the optical pumping is to enhance the population of weak field seeking states (see Sec. 3.2.1).

The beauty of optical pumping on the  $(\sigma_+) F = 2 \rightarrow F' = 2$  is that when the atom reaches the  $|2, 2\rangle$  ground state further  $\sigma_+$  light absorption is forbidden and this state effectively is a ‘dark’ state. It is in principle possible to drive the optical pumping transition on the  $(\sigma_+) F = 2 \rightarrow F' = 3$  and then avoid the need to use a repump beam as the decay  $F' = 3 \rightarrow F = 1$  is forbidden by the selection rules, however this introduces a high level of heating, as photon absorption continues even after an atom is pumped into the final state  $|2, 2\rangle$ .

### 5.2.1 Field synchronisation

As the optical transition must have a clearly specified polarisation, namely  $\sigma_+$ , there is a need to apply a magnetic field. It is enough to use a 1 G magnetic field during optical pumping. The synchronisation of the magnetic field with the laser beam is a very important aspect. The field is switched on during the application of the OP beam, which has a typical time duration of 2 ms.

It is also important, after atoms are placed in the weak field seeking state, to turn the magnetic trap on to catch the atoms. Through monitoring the Hall-effect sensor signal we could observe the timing of the magnetic trap switching. The main

improvement to the optical pumping consisted of synchronising the optical pumping with magnetic trapping fields. Fig. 5.3 shows old - inefficient timing of the IP trap (a) and the accurately synchronised IP trap switching with the OP (b). The difference

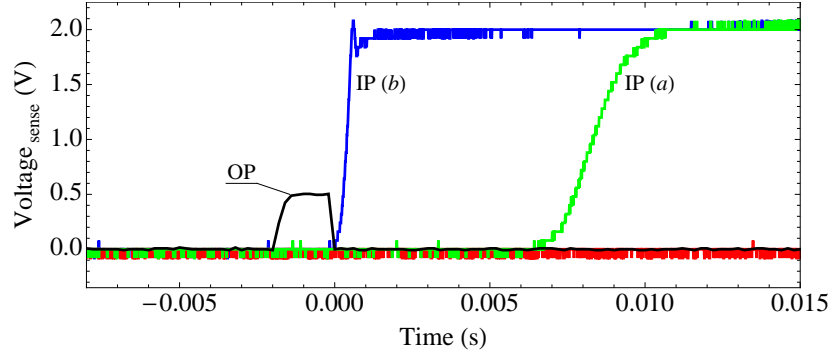


Figure 5.3: Current monitor during magnetic trap turn on. The OP curve represents the magnetic field generated along the OP beam. The IP(a) trace shows non-synchronised magnetic trap field, whereas IP(b) represents the new magnetic trap turn on.

between the IP(a) and IP(b) trace from Fig. 5.3 makes it look as if the time constant of the driving circuit was altered, however this was achieved in another way. The DAC voltage controlling the IP(b) current was initialised 5 ms earlier (to compensate for the delay) compared to IP(a) and was set to 10 V for 1ms and then it was reduced to its normal value of 2 V.

The synchronisation of IP trap switching with the OP resulted in an increase in the number of atoms in the magnetic trap. For the IP(a) case the number of atoms in the magnetic trap was  $\approx 4.4 \times 10^7$  for only 10s of MOT loading. Fig. 5.4 shows the density comparison after the switching was altered (to IP(b)) and the optical pumping beam was on or off. The transfer efficiency into the ground state  $|2, 2\rangle$  was improved, IP(a)  $\rightarrow$  IP(b), by about 30%, which is a significant number when reaching the BEC transition.

To see more clearly the effect of optical pumping on the sample of atoms the cloud profiles from Fig. 5.4 were analysed. They are shown in Fig. 5.5. Experimentally, the atoms are optically pumped for 0.5 ms as longer pumping times yield noticeable atomic heating with no improvement in transfer efficiency. The intensity of the OP beam was set to  $0.35 \text{ mW/cm}^2$ . For large atomic clouds that are too optically thick to (resonant) OP light the detuning and timing of the beam were adjusted to get the highest transfer efficiency with optical pumping.

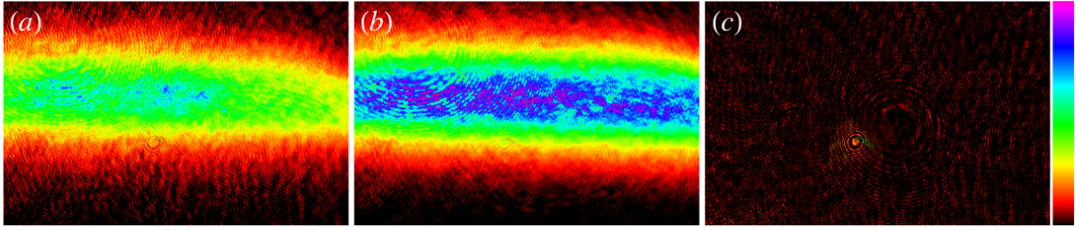


Figure 5.4: Density plots ( $651 \times 421$ ) pix showing the cold atoms in the magnetic trap after magnetic compression. The efficiency improved by synchronising the OP magnetic field for circular  $\sigma_+$  polarisation with the IP magnetic trap. When the OP was off the number of atoms was  $2.0 \times 10^7$  – (a), whereas with OP on we get  $5.8 \times 10^7$  – (b). A background picture (c) was taken as well.

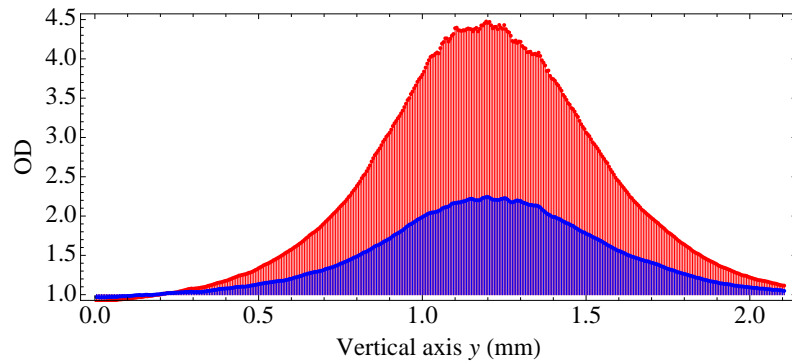


Figure 5.5: Clouds profiles (along the vertical axis from Fig. 5.4 (a) and (b)) and their optical depths (OD). When the OP was off the number of atoms was  $2.0 \times 10^7$ , whereas with OP on we get  $5.8 \times 10^7$ .

### 5.3 Magnetic trap

In Sec. 3.4 we provided an explanation of how we can create the magnetic trap using the IP coil configuration and additional compensation coils. The behaviour of the magnetic field from IP and compensation coils directly determine creation of the BEC. The magnetic field parameters are crucial during the achievement of the BEC. In this section we discuss a few aspects of the magnetic trap operation. We begin with adiabatic compression of the magnetic trap.

#### 5.3.1 Magnetic trap compression

During the magnetic trap compression stage the IP current controller was primed at 10 V in order to induce a rapid turn-on of the IP FET banks, and then set to drive

the current from 125  $\mapsto$  450 A (DAC voltage: 2 V  $\mapsto$  7.2 V) over 400 ms. The change in IP magnetic field was accompanied with the change in magnetic field from the compensation coils generating the bias field. During the the magnetic trap compression we monitored the Hall-effect sensor signals (see Fig. 5.6). During the compression the

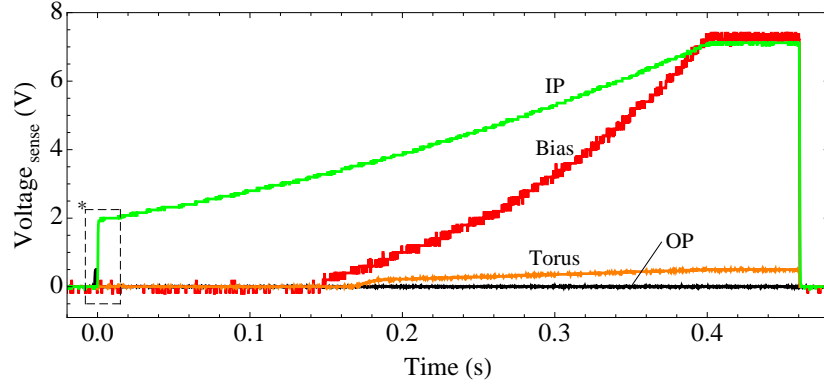


Figure 5.6: The compression of the magnetic trap – current monitor. The torus coils were set to be slightly on in order to be ready for launching atoms within the storage ring (see Fig. 6.32). The dashed box with the ‘\*’ is related to Fig. 5.3.

depth of the trap is high enough to prevent the atoms from being lost from the trap.

Adiabatic compression of the trap at Strathclyde is the final step prior to runaway evaporation. By compressing the trap we ‘adiabatically’ increase the density and temperature of the atomic sample and hence the ratio of good to bad collisions. At the end of the compression stage the conditions are satisfied for application of efficient evaporation cooling.

In the fully compressed magnetic trap the characteristic parameters, namely trap frequencies, take new values as the shape of the trap is altered. Measuring trap frequencies will be described in the next section as these are important parameters, e.g. for calculating the temperature of the atoms released from the trap.

### 5.3.2 Measuring trap frequencies

The harmonic character of the IP magnetic trap is directly related to the behaviour of the trapped atoms. This characteristic of the trap can be seen when the atoms are trapped or released from the trap. Atoms present in the harmonic magnetic trap experience a potential

$$U(\mathbf{r}, t) = \frac{1}{2} \sum_{i=x,y,z} m\omega_i^2(t) r_i^2, \quad (5.2)$$

where the important quantities  $\omega_i$  represent the (time-dependent) angular frequencies in the  $i$  direction within the trap.

The Strathclyde Ioffe-Prichard magnetic trap is (approximately) cylindrically symmetrical about the axial direction, which implies symmetry in two frequencies,  $\omega_x = \omega_y$ . The axial frequency  $\omega_z$  is an order of magnitude lower, which corresponds to weaker trapping confinement. The different trapping frequencies are reflected in the ballistic expansion of the atoms released from the trap. The anisotropic ballistic expansion of the cloud will be described in Sec. 5.5.1.

For measuring the trap frequencies we use a simple method using an external perturbation. Let us consider atoms sitting in the harmonic trap in equilibrium. If the external perturbation affects the atoms they are no longer in equilibrium in the harmonic trap. After the system has been perturbed we observe the spatial oscillations of the atomic cloud within the magnetic trap. By recording the final position of the atomic cloud, after a variable trap holding time, we can calculate the trapping frequencies.

Before taking measurements, using the imaging system, atoms were prepared in the magnetic trap. The atoms were adiabatically compressed and then cooled to the BEC transition with temperatures of  $\approx 40$  nK and  $\approx 60$  nK in the radial and axial directions respectively. The final position of the cloud was measured to be the peak of a two dimensional gaussian fit to the atomic cloud image. In order to get more accurate measurements we used 10 ms drop times to accentuate the harmonic motion.

The external perturbation was in the form of a magnetic field perturbation to provide a small motion to the atoms sitting within the harmonic trap. To create the perturbation in the radial direction we had a few options. One could (1) drop or raise the IP total magnetic field, (2) change the magnetic field from the compensation coils or (3) apply the azimuthal field from the straight wire. Basically any magnetic field that changes the equilibrium gravitational sag would work. However using the compensation coils or IP coils there was a chance of making a spin flip transition with a zero field crossing. For Majorana spin-flip-free perturbation we decreased the bias field from compensation coils. We applied a ‘square pulse’ in time to create the perturbation. The time interval of the applied pulse was 5 ms, which corresponded to a half of the estimated oscillation period in the magnetic trap. One concern was that the atoms could experience too much kick and that would cause them to reach anharmonic parts of the trap.

To get the atoms moving axially a field gradient in the axial direction had to be

applied. The MOT coils are perfectly suited to generate this perturbation. The applied pulse needed to be longer,  $\approx 50$  ms, to match the longer axial trap frequency. To make a gradient field we kept the IP field constant and the MOT field was pulsed. The Strathclyde hybrid IP-MOT configuration uses the same coils for both traps, that means the total current in the two pinch coils is the same, but the difference current changes. Again, the magnitude of the perturbation field was chosen carefully to avoid spin-flip transitions.

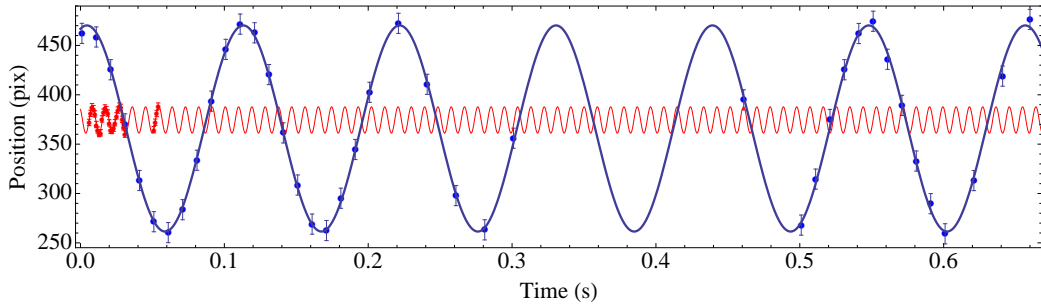


Figure 5.7: The magnetic trap frequencies measurement. The sine wave with the larger amplitude and lower period corresponds to the axial direction of the trap, with trapping frequency of  $(10 \pm 1)$  Hz, whereas the other sine wave (smaller amplitude, higher period) shows the radial oscillations, with trapping frequency of  $(108 \pm 1)$  Hz.

The radial trap frequency was measured to be  $(108 \pm 1)$  Hz, whereas the axial trap frequency exhibited weaker confinement and hence the measured period of oscillations was  $(10 \pm 1)$  Hz. The results of these measurement are shown in Fig. 5.7.

### 5.3.3 Current noise in the magnetic trap

Low current noise and low current drift are essential in the generation of reproducible samples of BEC. In this section we present the results of how steady the current controllers are, by monitoring the current flow using the same setting for each experimental run. The Hall effect sensors were used to monitor the current in the coils and they provided a feedback signal to the controlling driver (see Sec. 4.5.1). We monitored the voltage across the sense resistor of the bias and IP coils driver.

The drift and random oscillation which was sensed on the coils can affect the BEC generation significantly, depending on their amplitude, e.g. the full bias coil DC voltage ( $\approx 7$ ) corresponds to 30 G change in the magnetic field magnitude. Hence 2.5 mV (2.5 mV of scatter shown in Fig. 5.8) voltage amplitude corresponds to 10.7 mG change

in magnetic field magnitude ( $2.5 \text{ mV} / 7 \text{ V} \times 30 \text{ G} = 10.7 \text{ mG}$ ). For state  $|2, 2\rangle$  when the field amplitude alters by  $10.7 \text{ mG}$  atoms experience  $15.0 \text{ kHz}$  frequency shift (as  $1 \text{ G} \mapsto 1.4 \text{ MHz}$ ).

Three separate sets of measurement were taken for the bias coils as well as the IP coils. The first few runs of the experiment act like a warm-up sequence before the reading of the sense resistor voltage provides more consistent results. To see this effect clearly the experiment had to be run from its ‘cold’ stage; usually after an hour break when the power supplies were turned off. Warm up can be observed especially for the bias coils in Fig. 5.8. The time range for the warmup stage takes about a few

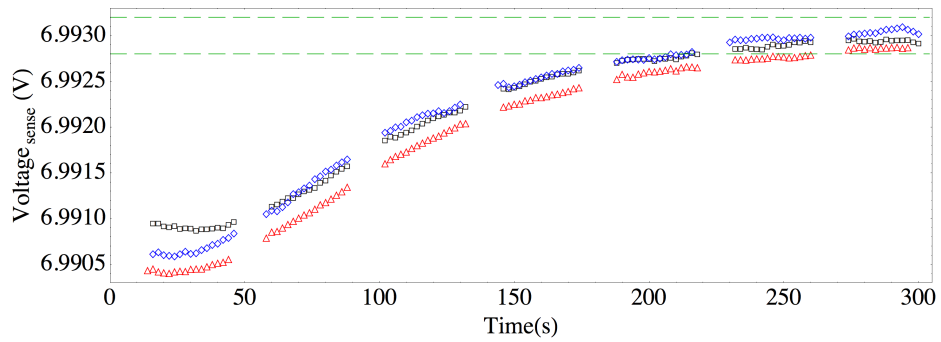


Figure 5.8: The magnetic field monitored using sense resistor in the driving circuit for the bias compensation coils from the ‘cold stage’. In the plot,  $1 \text{ mV}$  change on the scale corresponds to  $6 \text{ kHz}$  frequency shift for the  $|2, 2\rangle$  quantum state. Each bunch of points represents one experimental BEC sequence. The length of one BEC run was approximately  $42 \text{ s}$ . One can observe the first runs of the experiment from being ‘cold’ to a more stable usable stage. The dashed horizontal lines indicate the range of voltages we zoom in of later times in Fig. 5.9.

experimental BEC sequence runs (time). Accurate measurements were taken using an Agilent 34411A Digital Multimeter. For remote control of the digital multimeter a LabView code was composed. The adjustable setting enabled us to take measurements of the sense resistor voltage every  $2 \text{ s}$ . For this measurement the main BEC LabView program was run in continuous mode with  $10 \text{ s}$  of LP MOT loading and  $31.25 \text{ s}$  of evaporation. The loading stage did not use the IP magnetic configuration hence in Fig. 5.8, 5.9 we observe  $10 \text{ s}$  gaps between experimentally bunched data points. The bias coils were used when the MOT loading stage is on but only a small current is allowed to run through the coils  $\approx 0.05 \text{ A}$ , which is not shown in Fig. 5.8 and Fig. 5.9.

We only focus on the part that has the most importance on BEC creation – its final stage, during the evaporative cooling.

After a ‘warm-up’ stage we can observe a ‘settle down’ stage where the current is stabilised at a more constant level. A few sets of data points for the bias coils were recorded and presented in Fig. 5.9. The drift and random oscillation which was sensed

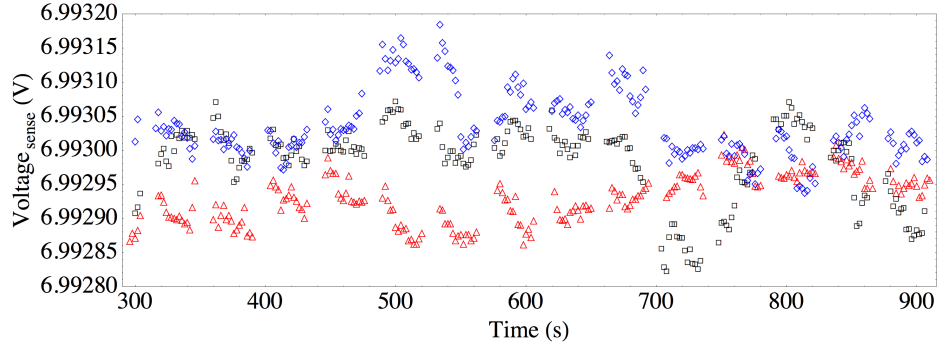


Figure 5.9: The magnetic field monitored using the sense resistor in the Hall effect sensor for the bias compensation coils after the ‘warm-up’ stage. The voltage amplitude of 0.4 mV corresponds to 2.4 mG frequency change (for state  $|2, 2\rangle$ ). Each bunch of points represents one experimental BEC sequence. The length of one BEC run was approximately 42 s.

on the bias coils affect the BEC generation insignificantly. Similarly as for the bias coils the warm-up stage was observed for the IP coils. The effect is presented in Fig. 5.10, where again three time-spaced experiments were performed and data was recorded. Interestingly one can observe 2.0 mV of drift on the sense resistor in the Hall effect sensor in the opposite direction to the Fig. 5.8.

### 5.3.4 Spin flips

A high accuracy in controlling the magnetic field is needed when exciting oscillations in the magnetic field. In this section we show what can happen when two magnetic fields are not synchronised and one switches faster than the other, creating a zero in the magnetic field experienced by the atoms. As an example we use the IP setup from the Strathclyde experiment where the two main contributions to the axial magnetic field come from the IP and compensation coils. Switching off the IP coils faster than the bias coils leads to a zero-field crossing at the centre of the magnetic trap. As we explained earlier (Sec. B.1) if this happens faster than the Larmor frequency atoms are

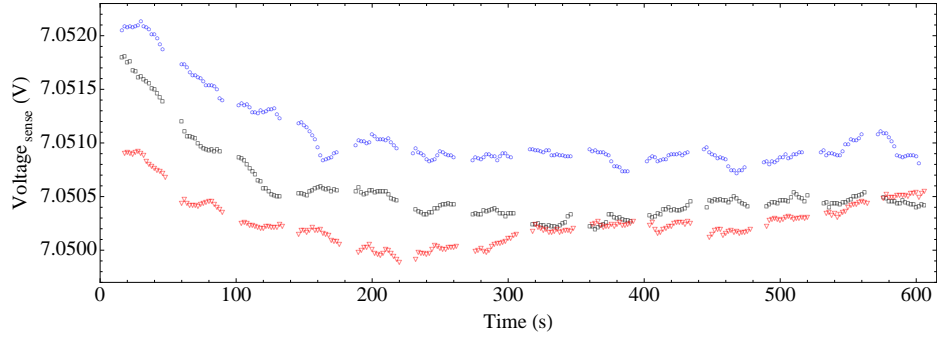


Figure 5.10: The magnetic field monitored using the sense resistor in the Hall effect sensor for the IP configuration coils. In the plot, 2 mV change on the scale corresponds to 12 kHz frequency shift for the  $|2, 2\rangle$  quantum state. Each bunch of points represents one experimental BEC sequence. The length of one BEC run was approximately 42 s.

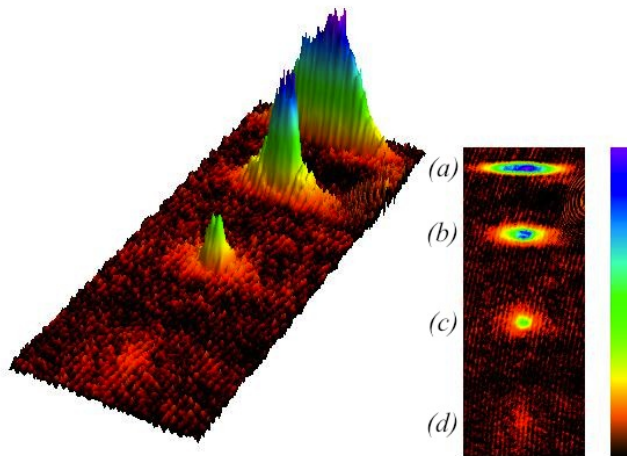


Figure 5.11: Absorption images of atomic clouds after 5 ms free expansion. Four distinct different spin components are observed corresponding to  $^{87}\text{Rb}$  states  $|F = 2, m_F = (a) 2, (b) 1, (c) 0, (d) - 1\rangle$ .

spin-flipped to different spin states [83][84], which results in the redistribution of the atoms throughout the different magnetic states. This effect is shown in Fig. 5.11 where several magnetic states, namely  $|F, m_F\rangle = |2, 2\rangle, |2, 1\rangle, |2, 0\rangle, |2, -1\rangle$ , exhibit different magnetic trapping properties.

## 5.4 Experimental evaporative cooling

After the compression of the magnetic trap filled with atoms, radio frequency evaporative cooling was applied to achieve higher values of phase space density leading to macroscopic quantum degeneracy. The typical time needed to satisfy continual run-away parameters for radio-frequency based evaporation in our magnetic trap is of order 20 – 30 s. This is the most time-consuming step in the condensate production. The typical evaporation used in the Strathclyde experiment consists of a one-step, continuous evaporation between  $\sim 30 \mapsto 5$  MHz. The evaporation process is controlled by an external frequency generator (Agilent 33250A, 80MHz Frequency Generator) controlled by computer through a GPIB card.

The choice of strategy for the evaporation cooling also depends strongly on the starting conditions of the cloud. For example Ref. [135] uses a linear frequency ramp, whereas for the Strathclyde setup an exponential evaporation ramp works well. The time-dependent RF frequency followed the form

$$\nu_{\text{RF}}(t) = (\nu_{\text{start}} - \nu_{\text{stop}}) \exp^{-t/\tau_{\text{RF}}} + \nu_{\text{base}} \quad \text{for } t \geq 0. \quad (5.3)$$

Parameters from Eq. 5.3 enables modelling the evaporation ramp in order to get the

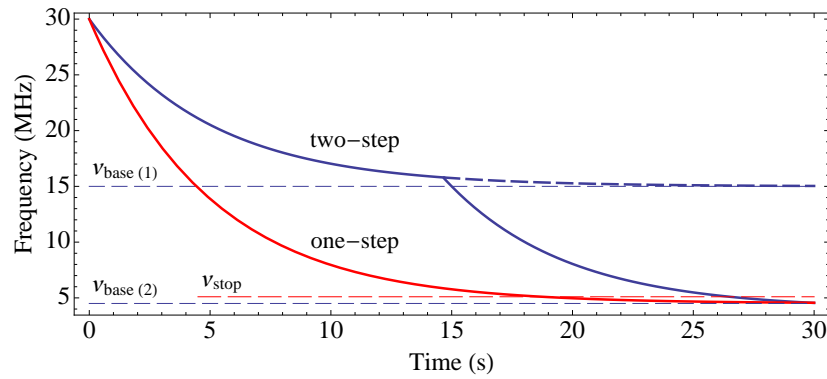


Figure 5.12: Experimental frequency ramp for evaporative cooling in the Strathclyde experiment. One-step solid line represents the experimental ramp when the measurements for Fig. 5.13 were taken. Two-step frequency ramp as a suggestion for further experiments may enable better control of the thermalisation process. The red dashed line shows an example of  $\nu_{\text{stop}}$  that corresponds to the stop frequency of the evaporation. For clarity the  $\nu_{\text{stop}}$  was chosen for  $\approx 19$  s for one-step evaporation.

most efficient process. Altering the time constant,  $\tau_{\text{RF}}$ , along with a negative frequency,  $\nu_{\text{base}}$ , even linear evaporation ramps can be obtained. The Strathclyde experimental frequency ramp is shown in Fig. 5.12. We also included an optional two-stage evaporation what may be used in the future for the optimum trajectory of the evaporation process.

Having set the evaporation trajectory we can record the number of atoms and their temperature, and see if they exhibit the runaway evaporation characteristic. The reduction in atom number as well as the temperature drop during the evaporation sequence is shown in Fig. 5.13, where we can see the evidence of the runaway evaporation on a logarithmic scale. The examples of atomic cloud density and size during

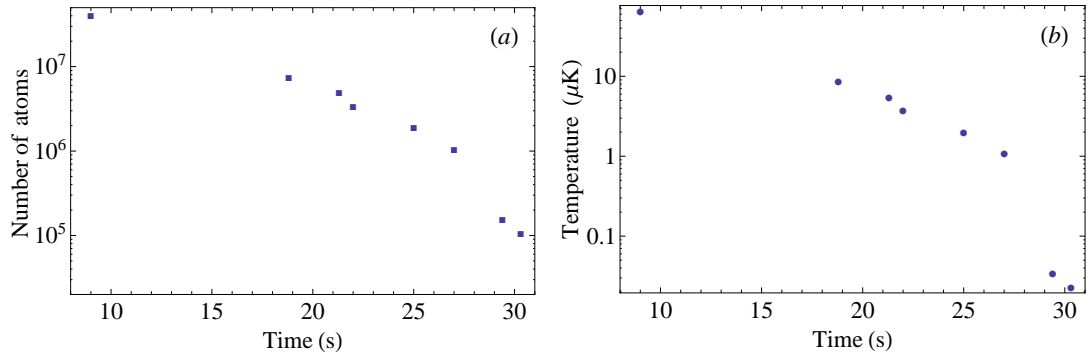


Figure 5.13: Dynamics of (a) the number of atoms and (b) the temperature during the evaporation ramp. The highest [lowest] data point corresponds to (a)  $(4.1 \pm 0.2) \times 10^7$  [ $(1.1 \pm 0.2) \times 10^5$ ] atoms, (b)  $(65 \pm 5)$  [ $(0.023 \pm 0.005)$ ]  $\mu\text{K}$ .

the evaporation process is shown in Fig. 5.14. The pictures were taken after 1 ms drop time after the magnetic trap was turned off. When reaching the BEC transition not only the optical density of the atomic cloud pictures was taken into account, but we also monitored the changes in the atomic cloud's collision rate and phase-space density as the evaporation parameters were varied.

### Evaporation and timing jitter

The communication process between the computer, namely the BEC LabView sequence program and the frequency generator possesses a variable time delay. This time delay is random and happens twice during the experimental sequence. The first time is when the computer signal is sent to the frequency generator and the second time is when

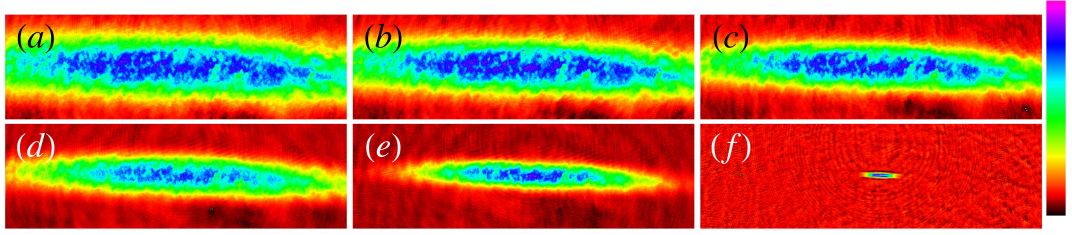


Figure 5.14: Atomic cloud density plots during the evaporation process. The time of evaporation and final frequency changes for every image ( $200 \times 650$  pix); (a) 8.77 s/9.5 MHz, (b) 10.00 s/9 MHz, (c) 11.49 s/8 MHz, (d) 13.70 s/7 MHz, (e) 17.24 s/6 MHz, (f) 31.25 s/5 MHz,

the evaporation is finished and the computer has to start data acquisition. A simple illustration of this sequence is shown below:

Magnetic compression  $\rightarrow \ominus \rightarrow$  **Evaporation**  $\rightarrow \ominus \rightarrow$  Data acquisition

The communication time fluctuation is of order 10 ms ( $\pm 5$  ms) before the start of evaporation and the same fluctuation when the evaporation (10 s evaporation) is finished. That gives 20 ms jitter out of 10 s evaporation time. When relating this value to the atoms sitting in the dark in the magnetic time these time fluctuations are acceptable and they do not affect the final result.

#### 5.4.1 Magnetic noise and evaporation

The importance of magnetic noise on the evaporation can be considered in the same terms as the magnetic field to frequency dependence, well known from the Zeeman effect. Magnetically trapped atoms are in the  $|F, m_F\rangle = |2, 2\rangle$  quantum ground state. A magnetic field with magnitude of 1 G shifts the magnetic sublevel  $m_F = 2$  by 1.4 MHz. That would cause a radical change in evaporation dynamics, hence any noise must be removed when generating a reliable BEC. The comparison of magnetic field magnitudes and corresponding frequency shifts are displayed in Tab. 5.1.

In our consideration the magnetic sublevel  $m_F = 1$  is treated as the anti-trapping state in the experiment, hence when measuring magnetic field noise we use numbers for magnetic sublevel  $m_F = 2$ .

A sensitive Hall probe (MAG-03MC Three Axis Magnetic field sensor) was placed as close as possible to the place where the BEC is created. The observed noise spectrum

State	$ 2, 2\rangle$			$ 2, 1\rangle$		
Magnetic field amplitude	1 G	10 mG	2.5 mG	1 G	10 mG	2.5 mG
Corresponding frequency	1.4 MHz	14 kHz	3.5 kHz	0.7 MHz	7 kHz	1.75 kHz

Table 5.1: State dependent magnetic field noise amplitude and related frequency shift of the atomic state.

is presented in Fig. 5.15, The measurements done with a sensitive Hall probe showed

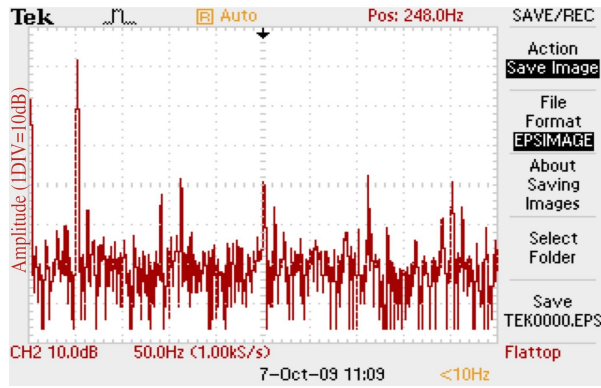


Figure 5.15: The Fourier spectrum of noise obtained when the Hall probe was measuring the magnetic noise level along the  $y$  axis. One division corresponds to 50 Hz, hence the most distinguished 50 Hz noise (mains) contribution in the Fourier spectra is present one division from the left.

that the magnetic noise is insignificant and does not affect the evaporation dynamics. The detailed measurements of the BEC position relative to a 50 Hz noise from the mains, which show no correlation to the BEC dynamics will be provided in Sec. D.1.2.

## 5.5 BEC

One might say that the evaporation cooling stage is the most exciting stage during the BEC generation. Eventually, after many hours of preparation, optimisation and getting acquainted with the experiment the final fruits of your work are at hand. The sudden increase in the density of the cloud and appearance of a bimodal cloud proclaims the formation of a Bose-Einstein condensate. Additionally, the anisotropic velocity distribution of the condensate and the agreement with the predicted transitions

temperatures ensure that the BEC has been created. The observation of this ‘magic’ transition fully pays off the work put into the preparation stages. Typical values of the atomic parameters obtained at the BEC transition are shown in Tab. 5.2.

Atomic parameter	$N_0$	$\langle n \rangle$ ( $\text{cm}^{-3}$ )	$T_{\text{radial}}$ (K)	$T_{\text{radial}}$ (K)	PSD
Value at BEC transition	$4.5 \times 10^5$	$7.7 \times 10^{12}$	$60 \times 10^{-9}$	$20 \times 10^{-9}$	48

Table 5.2: Typical atomic parameters during the production of the Strathclyde BEC, obtained from a single run of the experiment. The parameter  $N_0$  gives the number of atoms of a pure condensate.

The Strathclyde experimental data during the final stage of evaporation cooling is shown in Fig. 5.16. The pictures were obtained through absorption imaging (see Sec. 4.7.1). The absorption images were taken 25 ms after the atoms were released from the trap and show the formation process of the condensate. When the final frequency of the RF signal is ramped down to 4.580 MHz, the atoms are still a thermal cloud. When the final,  $\nu_{\text{stop}}$ , frequency decreases, to 4.555 MHz, the density of the atomic cloud at the centre increases suddenly. It shows that macroscopic condensation have begun. A further decrement of the final frequency, to 4.540 MHz, leads to an almost pure condensate with  $4.5 \times 10^5$  atoms. The usual optical depth of the BEC from the images presented in this thesis was  $\sim 4$ .

A source of much information on the Bose condensed gases comes from the images of the atomic cloud expansion. The dynamics of the expansion are a significant aspect in determining the properties of the coherent matter wave, such as velocity distribution and aspect ratio of the cloud. In the next section we will examine the last element, namely the aspect ratio dynamics of a BEC cloud.

### 5.5.1 Ballistic expansion dynamics

Atoms in the form of a pure condensate are in the same quantum state and they exhibit this quantum character during their ballistic expansion in contrast to the ballistic expansion of the thermal atoms. As the evolution of the condensate size during free fall is anisotropic, we can introduce and distinguish the scaling parameters for each  $i$ -th direction. During the ballistic expansions the radius  $R_i(t)$  of the Bose-Einstein condensate evolve as:

$$R_i(t) = \ell_i(t) R_i(0), \quad (5.4)$$

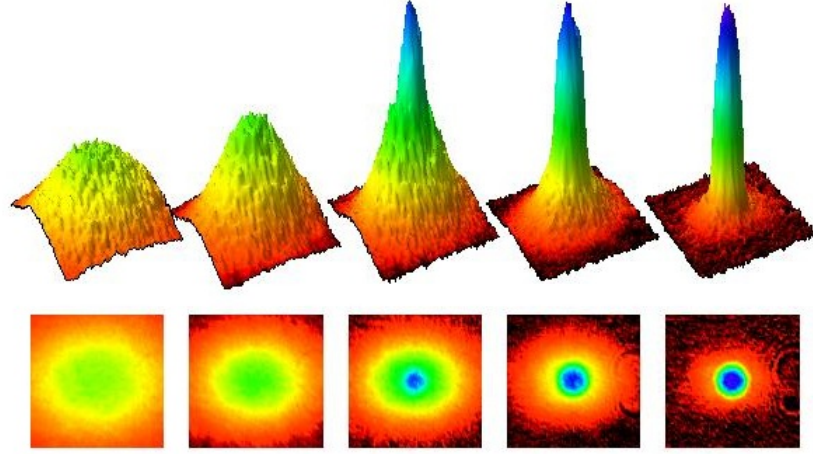


Figure 5.16: The formation of the Strathclyde Bose-Einstein condensate as the final RF frequency is lowered during evaporative cooling. Final RF frequencies are (left to right) 4.580 MHz, 4.560 MHz, 4.555 MHz, 4.550 MHz, 4.540 MHz. Top row contains a three-dimensional pictures of the formation of the BEC (absorption versus two spatial dimensions). The height of the peak is the optical density of the atom cloud. Each picture is an average of three experimental sets, where the size of each individual picture is  $0.4 \text{ mm}^2$ .

where  $\ell_i$  is the scaled size of the condensate expanding freely, after time  $t$ , in the  $i$ -th direction. For the axially symmetric cigar shaped trap (e.g our IP trap):  $\ell_1 = \ell_2 = \ell_\perp$  and  $\ell_3 = \ell_\parallel$ . The dynamics of the macroscopic wave function is contained in the evolution of the scaling parameters  $\ell_i$ , ( $i = 1, 2, 3$ ). The condensate density can be written in the form of a time-dependent inverted paraboloid [136]:

$$n(\mathbf{r}, t) = N |\psi(\mathbf{r}, t)|_{TF}^2 = \frac{\mu - \sum_{i=1}^3 \frac{1}{2} m \omega_i^2(0) r_i^2 \ell_i^2(t)}{g \prod_{i=1}^3 \ell_i(t)} = \Xi \longrightarrow \begin{cases} \text{true} & \forall \Xi > 0 \\ |\psi|_{TF}^2 = 0 & \text{otherwise} \end{cases} . \quad (5.5)$$

The Strathclyde experimental IP magnetic trap is in a cigar-shaped form. The four square coils from the hybrid design (Sec. 4.3) provide the axial curvature for the trap, which results in an effective potential experienced by atoms in anisotropic form as shown in Eq. 5.2. From Eq. 5.5 we can see that the ballistic expansion dynamics depends strongly on the trapping frequencies. The axial and radial magnetic trapping frequencies are 10 Hz ( $\omega_\parallel$ ) and 108 Hz ( $\omega_\perp$ ) respectively ( $\omega_1 = \omega_2 \equiv \omega_\perp \gg \omega_\parallel$ ). When

the Thomas-Fermi [4] regime applies, the ballistic expansion obeys [136, 137]:

$$\frac{\ell_{\perp}(t)}{\ell_{\parallel}(t)} = \frac{(\omega_{\parallel}/\omega_{\perp})\sqrt{1 + \omega_{\perp}^2 t^2}}{1 + (\omega_{\parallel}/\omega_{\perp})^2[\omega_{\perp} t \arctan(\omega_{\perp} t) - \ln \sqrt{1 + \omega_{\perp}^2 t^2}]}, \quad (5.6)$$

for the weakly interacting Bose-Einstein condensate. The experimental results of the expansion dynamics are presented in Fig. 5.17, where they are in agreement with the theoretical result (Eq. 5.6). It was readily observable that the expansions along the axial and radial directions are not isotropic. The Bose-Einstein condensate was falling and freely expanding only in the presence of gravity.

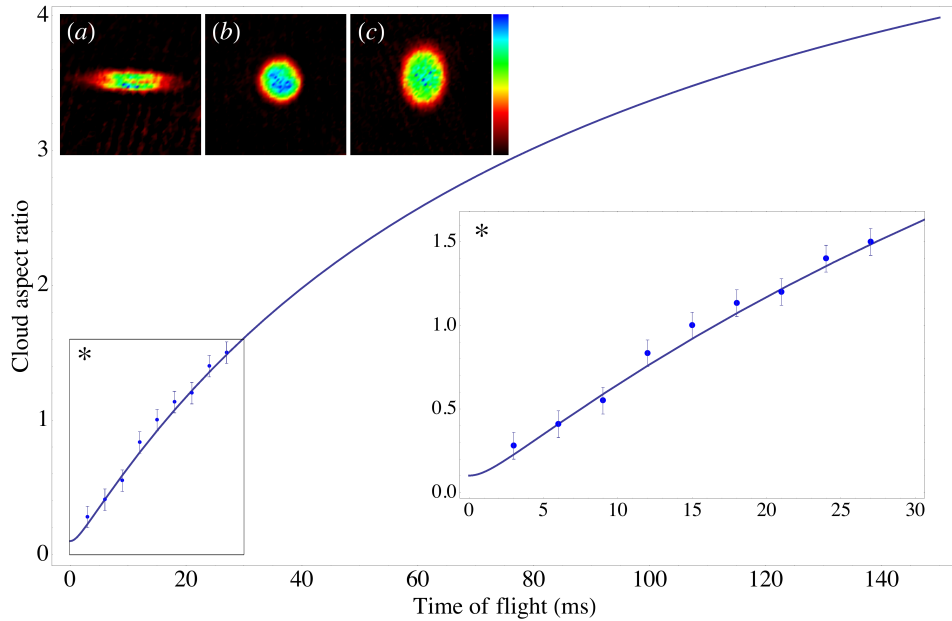


Figure 5.17: The ballistic expansion of BEC in free fall. The aspect ratio  $\ell_{\perp}(t)/\ell_{\parallel}(t)$  (radial to axial) was recorded after atoms were released from the magnetic trap. The theoretical solid line (Eq. 5.6) is plotted along with the experimental results. The experimental magnetic trap frequencies were  $\omega_{\perp} = 2\pi \times 108\text{Hz}$  and  $\omega_{\parallel} = 2\pi \times 10\text{Hz}$ . The experimental pictures ( $0.5\text{mm}^2$ ) are presented in the top-left corner – (a) 3 ms, (b) 18 ms and (c) 27 ms.

In this chapter we covered a few experimental aspects that were adjusted or modified in order to be able to obtain a reliable matter wave source. In the next chapter we will focus on advanced implementation and manipulation of the Bose-Einstein condensates. We will present a progress report on the Strathclyde atom interferometry experiment using matter waves. The outline of new techniques implemented for BEC

manipulation and experimental results analysis will also be described, including: the optical dipole sidebands BEC splitting, development of the anti-gravitational system for BEC and Fourier processing for analysing and correcting the experimental data.

## BEC – manipulation

### 6.1 Optical dipole potential

The dipole potentials realised with far-detuned light are particularly appealing due to very small perturbations from photon scattering, e.g. when using far enough detuned light heating from spontaneous emission is negligible. This feature of light interaction with atoms was appreciated in many experiments [100, 138, 139, 140, 141]. The optical dipole potential, widely used in the field of atom optics, e.g. in so called tweezing [140, 141], in its simplest form consists of a single, focused Gaussian laser beam. The Strathclyde experimental setup utilises the optical dipole force for splitting BECs. Using blue detuned laser light that is far away from  $^{87}\text{Rb}$  resonant atomic transitions we are able to generate dipole potentials that create a potential barrier at the centre of the place where the BEC is generated. That makes it possible to split the BEC into two parts when only a single beam is applied.

#### 6.1.1 Dipole beam position

The technical side of alignment requires a high performance accuracy. After aligning the dipole beam we could see its first effects on BECs. As the BEC, and the dipole beam, are both very small objects the dipole beam was applied first of all to cold atomic clouds, which had a temperature ( $\sim 900$  nK) slightly higher than the BEC transition temperature. This atomic cloud provided more atoms (a bigger target for alignment) and the final position of the dipole beam could be set with a high precision. The temperature and number of atoms in the atomic cloud was adjusted through the final frequency of the evaporative cooling. The dipole beam was turned on before the evap-

oration and the dipole potential was present through the whole process of evaporation. When the final evaporation frequency was set at 5.050 MHz, there were a sufficient number of atoms to surround the dipole potential and hence to point to its exact location. The hole in the atomic cloud shown in Fig. 6.1 (b) indicates the position of the dipole beam. For lower final evaporation frequencies we approach the stage when a single dipole beam splits the atomic cloud into two parts. This effect is presented in Fig. 6.1 (a). By changing the intensity of the dipole beam we could alter the splitting between the two cloud parts. In a later section (Sec. 6.4.1) we will consider this aspect in more detail.

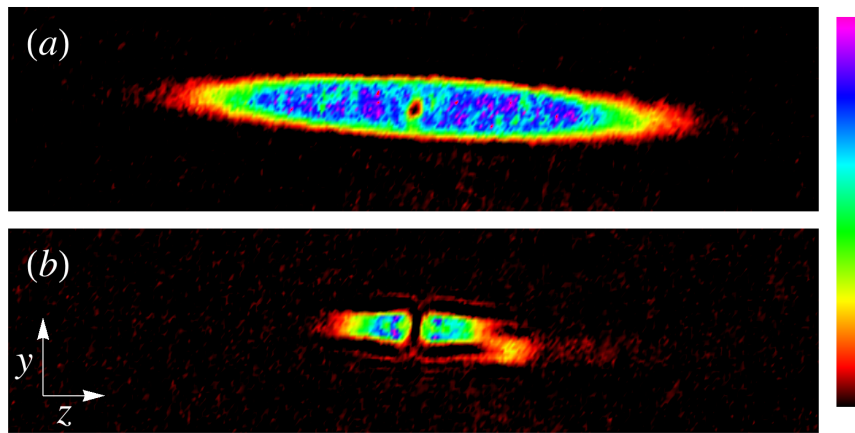


Figure 6.1: Absorption images of the applied optical dipole beam potential on the atoms in the magnetic trap. Two different final evaporation frequencies (a) 5.050 MHz, (b) 4.950 MHz were applied to clarify where the centre of the dipole beam is. The size of each image is  $1.5 \text{ mm} \times 0.3 \text{ mm}$ .

### 6.1.2 Optical dipole force

A precise understanding of the splitting dynamics is important, as it is not only of fundamental, but also of technological interest. For example splitting and merging processes are rudimentary operations in atom interferometers, where the BEC provides an excellent tool to study this issue experimentally [111, 109]. There are also other interesting features generated implying different splitting dynamics. As reported in Ref. [142], it is possible, under certain conditions, to create oscillating vortex/rings and solitons, which are performed by density engineering using a blue detuned laser beam.

In this thesis we will not focus on the shock waves or solitons formation and their behaviour. Rather than taking this as the aim of our experimental pursuit we treat these features as obstacles on the way to obtain the interference fringes between two parts of the condensate. However we mention that these features exist under certain conditions. The observation of these previously unseen (at Strathclyde) experimental features taught us how to overcome such effects. After discovering them in our setup we had to adjust the dipole beam operation. In the following set of experiments we look at the dynamics of splitting a BEC with a repulsive barrier that is suddenly turned on at the centre of the BEC. We present the experimental results of the effects of short light pulses on the BEC in the harmonic trap.

### 6.1.3 Impact

We first create BECs with  $4.3 \times 10^5$  atoms in the magnetic trap without the presence of the dipole barrier. The atoms were magnetically confined by an elongated trap with a roughly 10 (axial/radial) cloud size ratio. After we cooled the sample to about 200 nK using forced radio-frequency evaporation the cloud is left in the trap to rethermalise over a time of 85 ms. Then the 658 nm, 50 mW dipole beam was shone at the BEC for 5 ms,<sup>1</sup> rapidly pulsing on the repulsive barrier. The optical dipole laser beam propagated perpendicular to the BEC's longitudinal axis, as shown previously in Fig. 4.13.

The experimental images of dipole beam impact on the BEC sample are shown in Fig. 6.2. Different time intervals between the rapid switching off of the dipole beam are shown and an absorption image was taken for each time interval, when the atoms were released from the magnetic trap. The properties of the dipole beam exerts significant influence on the condensate. Image (a) shows a clean separation between two horizontal parts of the BEC. Directly after turning the dipole barrier off, the two parts of the condensates start to expand toward each other. When atoms are stroked with the dipole beam they are still in the magnetic trap. The higher trapping frequency in the radial direction provides much stronger confinement in that direction. The optical dipole beam is aligned perpendicular to the axial direction, which means that is parallel to the radial axis, and hence the main effect of application of the high intensity dipole beam is seen in the axial directions. The effect displayed in the set of images occurs due to repulsion from the blue detuned light. Atoms get pushed by the light and pass

---

<sup>1</sup>An acousto-optical modulator enabled the accurate control over the timing of the dipole beam. The other technique using an AOM will be outlined in Sec. 6.2.

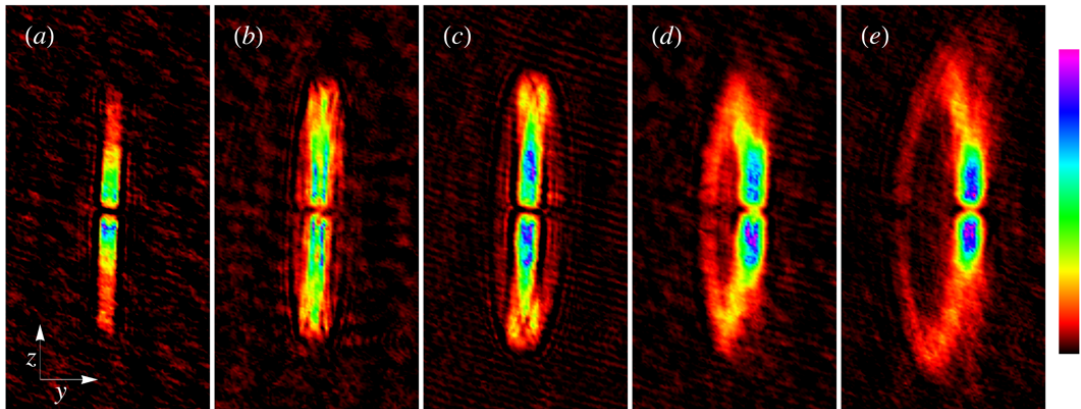


Figure 6.2: Rapid injection of the dipole beam. The size of individual images is  $0.475 \text{ mm} \times 1.025 \text{ mm}$  in the  $y$  and  $z$  directions respectively. The  $y$  axis is aligned with gravity. The time intervals are (a)  $50 \mu\text{s}$ , (b)  $500 \mu\text{s}$ , (c)  $1 \text{ ms}$ , (d)  $2 \text{ ms}$ , (e)  $3 \text{ ms}$  after the beam is rapidly turned off and the atoms are released from the magnetic trap.

the momentum to their neighbours and so on via atomic interaction, which eventually is seen as an echo at the edges of the condensate. The different drop times enable us to see the effect more clearly.

Splitting a BEC with a repulsive potential barrier from an optical dipole beam can lead to shock waves as reported in Ref. [143]. Therefore, it is important to learn what should be avoided when trying to achieve adiabatic splitting of the BEC.

#### 6.1.4 Splitting in an adiabatic manner

In our experiment splitting of the condensate was done in two ways. One was to create BECs in the magnetic trap in the presence of the dipole beam, which resulted in the generation of two independent BECs. However, for practical interferometric applications a single condensate must be split smoothly into two condensates with a fixed relative phase [144, 145] to prevent phase jitter in the interference fringes. In the Strathclyde experiment the dipole beam was ramped up after the evaporation cooling. The smooth (linear ramp) turning on of the dipole beam was done over 200 ms. The effect of splitting the BEC using this method is shown in Fig. 6.3. The dipole beam was switched off at the same time as the atoms were released from the magnetic trap.

Similar results of spatial splitting the BEC can be obtained by switching the dipole beam before the evaporation. The main difference is that two condensates do not have

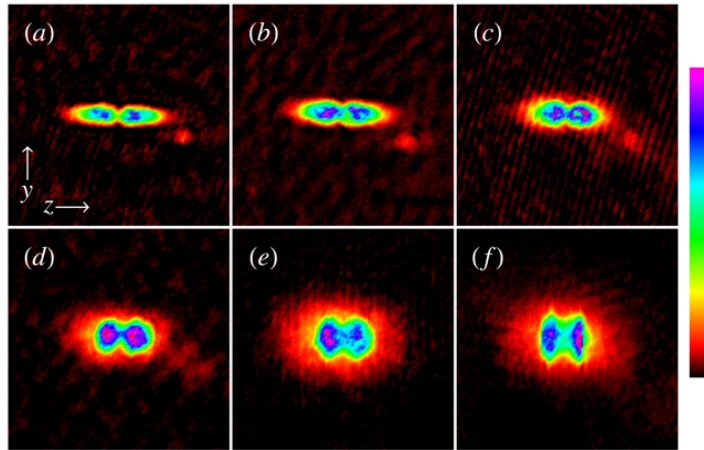


Figure 6.3: Adiabatic splitting of the BEC. The images were taken after variable time intervals after the BECs were released from the magnetic trap. The ballistic expansions are (a) 3 ms, (b) 5 ms, (c) 8 ms, (d) 15 ms, (e) 20 ms, (f) 25 ms.

a fixed relative phase between each other, and the phase is random from shot to shot.

We also carried on a few experiments where the dipole beam was turned on before the evaporation, but its intensity was sufficiently low that the atoms in the resulting double well potential had a common phase-lock between two parts of the condensate. This is an optional way of creating two parts of condensates, which have a fixed relative phase between each other.

## 6.2 Controlling the dipole beam

As acousto-optical modulators (AOMs) can vary the deflection angle and beam intensity of a dipole beam via the applied RF frequency and power, respectively, they are a useful tool for creating arbitrary patterns in BEC experiments through the time-averaged optical dipole potential [146, 147, 148]. However, their use with BECs has largely been through red-detuned light, although blue-detuned potentials [138] offer substantially lower decoherence rates.

### 6.2.1 AOM drive

We split our blue-detuned dipole laser beam into two beams, with variable separation, via an 80 MHz AOM. As the first order beam from an AOM is deflected proportional to the RF drive frequency, if we use an RF spectrum consisting of multiple spectral

components we can form multiple simultaneous beams [144]. Our adiabatic splitting is induced by dipole beam sidebands driven by amplitude modulation of the RF carrier frequency fed to the AOM. The amplitude modulation is obtained by mixing two frequencies, a stable carrier frequency  $\nu_0 = 80$  MHz and a variable frequency modulation signal  $0 < \nu_{\text{mod}} < 20$  MHz, yielding two tunable sidebands at  $\nu = \nu_0 \pm \nu_{\text{mod}}$  (see Fig. 6.4). The RF modulation frequency came from a computer-controlled synthesised

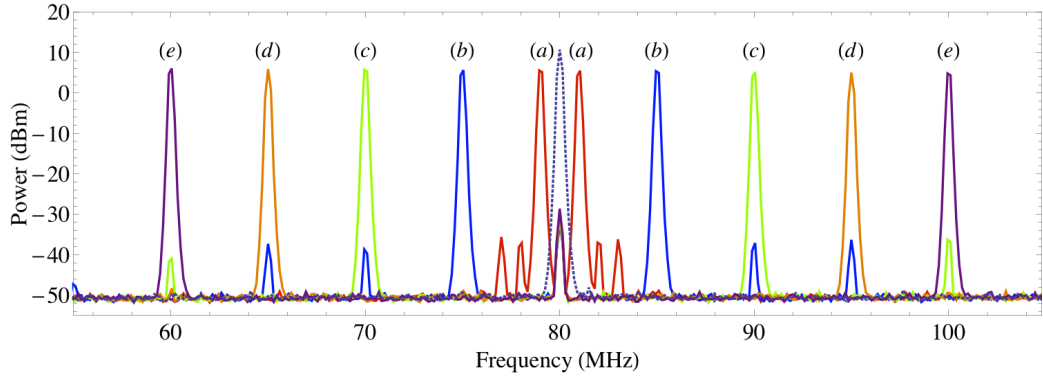


Figure 6.4: RF spectrum sidebands. Experimental sidebands spectrum, with the suppression of the carrier frequency signal, recorded on the RF spectrum analyser. The sideband traces correspond to different frequency modulation signals ( $\nu_{\text{mod}}$ ): (a) 1 MHz, (b) 5 MHz, (c) 10 MHz, (d) 15 MHz, (e) 20 MHz. For monitoring purposes a  $\sim 20$  dB signal attenuator was used, hence the smaller amplitude of the spectrum peaks shown.

signal generator (Agilent is a 33220A, 20 MHz). A standard double balanced mixer (Minicircuits ZLW-1) is used to mix the signal and carrier RF signals. The scheme of the driving setup is present in Fig. 6.5. The decrease in amplitude of the carrier frequency from the sidebands is of order 40 dB, and the carrier frequency dipole beam has a negligible effect on the atoms. The linear response of RF drive frequency to beam deflection results in two beams at relative deflection angles  $\delta\theta = \pm 2.5$  mrad for 20 MHz modulation frequency.

The 5 mA rated DAC voltage was converted to a 25 mA signal that controls the RF switch connected to the AOM. We build an additional circuit that enabled fine tuning of the signal directed to the switch. The circuit was based on a differential amplifier with extra adjustable offset. The details of this circuit can be found in Appendix E.

The position of the AOM (see Fig. 6.6) was offset by a distance  $d_1 = 10$  cm from the

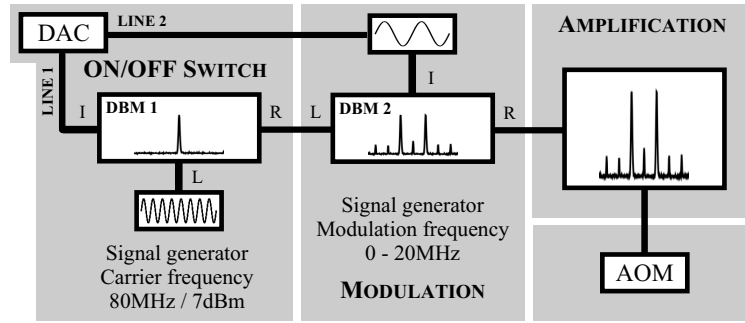


Figure 6.5: The schematic diagram of the RF signal processing. Digital signals from the computer were converted into analog lines using a digital-analog converter (DAC) card. One analog line fed the double-balanced mixer (DBM1) that acted as a switch for carrier frequency to be sent to DBM2. At DBM2 the sidebands were added by mixing the carrier signal with RF sine wave modulation frequency, which was controlled through the second analog line. The final amplification of the mixed signals was achieved using a standard 30 dBm RF amplifier.

focal point of a  $1\times$  beam expander comprised of two  $f_1 = 25$  cm focal length plano-convex lenses. After a (non-critical) propagation distance  $d_2$  the beams are focused by an achromat lens with focal length  $f_2 = 8$  cm. Although the RF power in the sidebands is constant a small drop in the optical power of the beams is observable at large displacements due to reduced AOM diffraction efficiency.

### 6.2.2 Dipole beam displacement

The ray transfer matrix technique is well known for ray tracing [149]. Ray transfer matrix analysis is a useful technique in designing optical systems where each optical element and the paths between the elements are represented by  $2 \times 2$  matrices. A final product matrix with elements  $ABCD$  is formed by multiplying the appropriate element matrices in sequence from start point to end point. In  $ABCD$  matrix analysis the element's effect is described by a  $2 \times 2$  matrix, which can be represented as (valid for small  $\delta\theta$ ):

$$\begin{pmatrix} \delta z' \\ \delta\theta' \end{pmatrix} = \begin{pmatrix} A_{oc} & B_{oc} \\ C_{oc} & D_{oc} \end{pmatrix} \begin{pmatrix} \delta z \\ \delta\theta \end{pmatrix}, \quad (6.1)$$

optical  
component

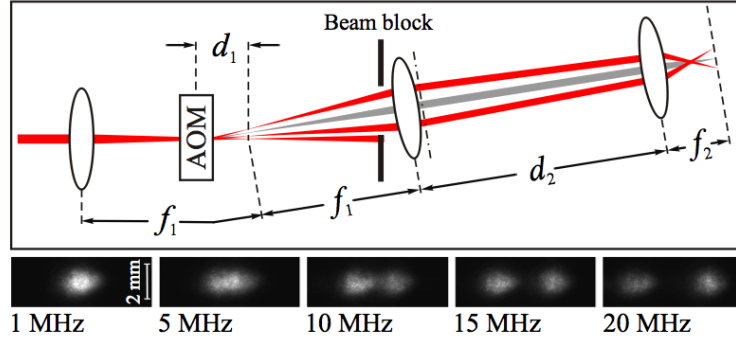


Figure 6.6: The 658 nm dipole beam optical path for splitting the BEC. The acousto-optic modulator (AOM) was offset a distance  $d_1$  from the focal point of the  $1\times$  beam expander to enable output beam deflection at the beam waist after the final lens. The modulated RF carrier frequency results in two RF sidebands and suppressed carrier resulting in two optical beams with spatial separation determined by the RF modulation frequency as seen in the experimental beam image series. The bottom pictures were taken at the position of the beam block.

where  $\begin{pmatrix} \delta z \\ \delta \theta \end{pmatrix}$  is the input beam described by a vector with transverse offset  $\delta z$  and offset angle  $\delta \theta$  from a reference axis and  $\begin{pmatrix} \delta z' \\ \delta \theta' \end{pmatrix}$  is the output beam represented as the product of a transfer matrix and the input beam. The primed quantities refer to the beam after passing through the optical system. Following the diagram, from Fig. 6.6, we obtain the  $ABCD$  matrix which characterises the entire system in the form:

$$M_{\text{sys}} = \begin{pmatrix} 1 & d_1 + f_1 \\ 0 & 1 \end{pmatrix}_{\text{AOM} \rightarrow \text{lens}_1} \begin{pmatrix} 1 & 0 \\ -1/f_1 & 1 \end{pmatrix}_{\text{lens}_1} \begin{pmatrix} 1 & d_2 \\ 0 & 1 \end{pmatrix}_{\text{lens}_1 \rightarrow \text{lens}_2} \begin{pmatrix} 1 & 0 \\ -1/f_2 & 1 \end{pmatrix}_{\text{lens}_2} \begin{pmatrix} 1 & f_2 \\ 0 & 1 \end{pmatrix}_{\text{lens}_2 \rightarrow \text{BEC}}, \quad (6.2)$$

where one can distinguish several steps corresponding to different transfer matrices. We start from the place where the beams are deflected by the AOM and finish at the place where the BEC is created. Multiplying the matrices from individual components we get a  $2 \times 2$  matrix for the entire system. For simplifying the matrix the following substitutions are used:  $v = 1 - \frac{d_1 + f_1}{f_1}$ ,  $\vartheta = \frac{d_1 + f_1 + d_2 v}{f_2}$ ,  $\varphi = \frac{1}{f_1} + \frac{1 - d_2/d_1}{f_2}$ , which results in the final product:

$$M_{\text{sys}} \begin{pmatrix} \delta z \\ \delta \theta \end{pmatrix} = \begin{pmatrix} \delta z (v - \vartheta) + \delta \theta [d_1 + f_1 + d_2 v + (v - \vartheta) f_2] \\ -\delta z \varphi + \delta \theta \left(1 - \frac{d_2}{f_1} - \varphi f_2\right) \end{pmatrix}. \quad (6.3)$$

From the matrix representation we can clearly distinguish the formulae for final beam angle and offset from a reference axis. After numerical simplification one can show that the final  $\delta\theta$ -dependent deflection distance  $\delta z'$  depends only on:  $d_1$ ,  $f_1$ ,  $f_2$ ,  $\delta\theta$  and takes the form  $\delta z' = d_1 f_2 \delta\theta / f_1$ , which results in a final beam displacement of  $\pm 80 \mu\text{m}$  for a modulation frequency of 20 MHz (Fig. 6.6). Fig. 6.7 displays  $\delta z'$  for three different lenses ( $f_2$ ), when  $\delta\theta = 5 \times 10^{-3}$  rad, and  $\delta z'(\delta\theta)$  dependence, when  $d_1 = 10$  cm.

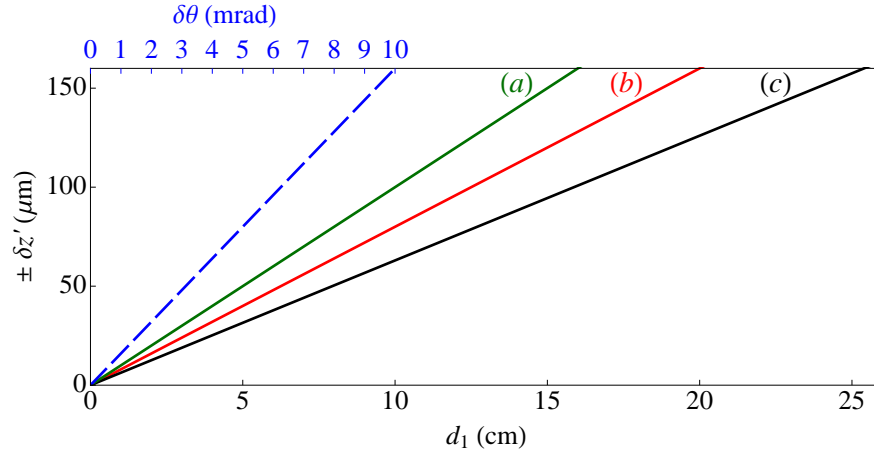


Figure 6.7: The output beam offset as a function of final lens focal distance for three chosen lenses: (a)  $f_2 = 100$  mm, (b)  $f_2 = 80$  mm, (c)  $f_2 = 63$  mm (for  $\delta\theta = 5$  mrad). The dashed line represents the effect on the output offset beam when the input deflection angle is altered; the distance  $d_1$  was set at 10 cm, which corresponds to  $\delta z' = \pm 80 \mu\text{m}$  in magnitude at  $\delta\theta = 5$  mrad.

### 6.2.3 Single beam deflection

After the theoretical prediction of the final displacement of the beam experimental steps were taken to prove the correctness of the theory and to make the final calibration. In this section we apply a technique described in Sec. 6.2.1, when an AOM is driven by different carrier frequencies, which results in altering the deflection angle.

In our first experiment we offset the AOM by  $d = 5.5$  cm and implemented a lens with the focal length of  $f_2 = 80$  mm. We used acousto-optical modulator with centre frequency at 80 MHz and bandwidth of 25 MHz. We applied the drive RF frequency to the AOM within the range 60 – 100 MHz. Such a wide frequency amplitude change resulted in the slight decrease in diffraction efficiency on AOM when the frequency

was out of the bandwidth range. Although a drop in efficiency occurred it was still possible to obtain a high intensity optical dipole beam. The intensity at the extreme diffraction angles was approximately half of the intensity of the beam at 80 MHz carrier frequency, hence the important factor was to supply enough intensity in order to be able to manipulate the BECs.

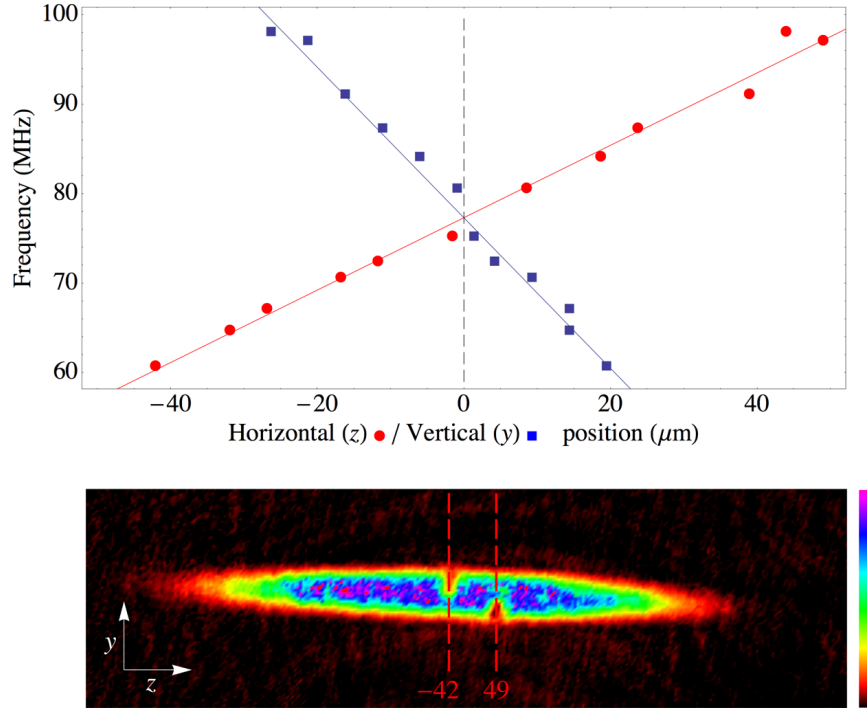


Figure 6.8: (top) Final position of the dipole beam dependence on the AOM driving frequency. The resultant horizontal extremes of the dipole beam position are at:  $-42 \mu\text{m}$  for 60.70 MHz and  $49 \mu\text{m}$  for 95.10 MHz which corresponds to  $= 91 \mu\text{m}$  separation. The dashed line represents the ideal calibrated setting where the vertical movement of the dipole beam is removed. (bottom) Absorption image ( $1.4 \text{ mm} \times 0.4 \text{ mm}$ ) of two sidebands imprinting their potential on a cold atomic cloud at  $\nu_{\text{mod}} = 20 \text{ MHz}$ .

Fig. 6.8 shows in detail the single beam position dependence on the frequency applied to the AOM. The change in AOM driving frequency ( $\pm 20 \text{ MHz}$ ) corresponds to different deflection angles ( $\pm 2.5 \text{ mrad}$ ), which results in spatial variation of the of the output dipole beam. The unwanted vertical shift was compensated by setting additional translation stage under the AOM allowing final alignment of the dipole beam. The maximum horizontal deflection achieved with first order deflection optical

dipole beam was experimentally measured to be  $\pm \sim 9$  pixels, which corresponded to  $\pm \sim 45\mu\text{m}$ , which is in good agreement with the theoretical calculation ( $\pm 44\mu\text{m}$ ; see Sec. 6.2.2). The absorption image shown in Fig. 6.8 was taken, in the presence of two sidebands during the evaporative cooling. In order to see a clear location of the sidebands, atoms were partially evaporated from the magnetic trap.

### 6.2.4 Sideband BEC splitting

A considerable amount of time was spent adjusting and removing the unwanted vertical splitting asymmetry the double optical plug. By adjusting two mirrors we could correct a horizontal and vertical path of the beam. Eventually there was a constant vertical height for the dipole beam for the full range of AOM frequencies.

When the evaporative cooling is performed until the BEC transition is obtained, the adjustable sidebands are used for splitting the condensate. Changing different parameters like the offset distance  $d_1$ , the focal length of the final dipole lens  $f_2$ , we could set much larger separation distances when applying the sidebands technique. An example of large separation of two BEC clouds by  $250\mu\text{m}$  (center-of-mass (COM) distance) with a double optical plug is shown in Fig. 6.9. In a later section we will show that it

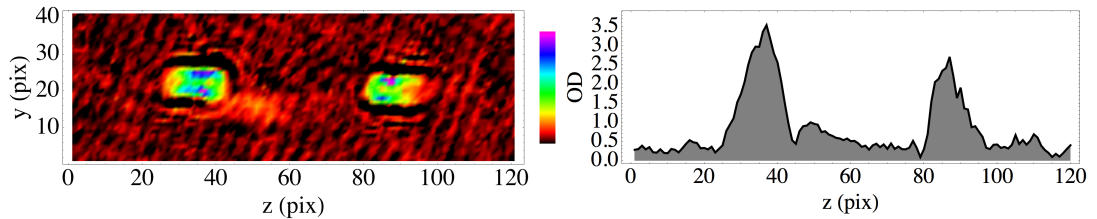


Figure 6.9: Macroscopic splitting of BEC with a double optical plug. (left) Absorption image, ( $0.6\text{ mm}\times 0.2$ ) mm, showing large separation between two BEC clouds. (right) Density profile after integrating absorption image from the left. The COM separation is  $\sim 250\mu\text{m}$ .

is possible to obtain interference fringes from this setting, when two BEC clouds are separated by  $1/4$  of a millimetre.

### 6.2.5 Optical fork

When the plug's drive RF spectrum is altered in order to split the BEC into multiple wells – an ‘optical fork’ for BEC can be created. By attenuating the carrier signal and applying large modulation ( $> 10\text{ MHz}$ ) we can create three BECs. An example of

BECs in a triple-well potential is shown in Fig. 6.10 (top). However, leaving the carrier signal unsuppressed the optical plug results in three distinguishable beams where the power is equally distributed between them. Three beams combined with a magnetic trap potential enable four-well confinement for BECs (See Fig. 6.10 (bottom)).

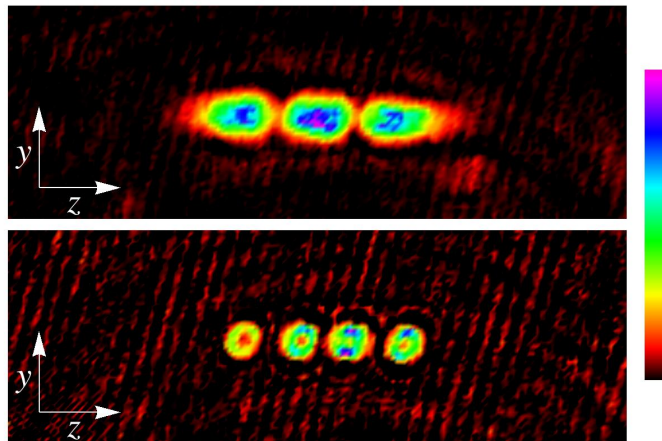


Figure 6.10: The BEC arrays in the ‘optical fork’ potential. Absorption images,  $800\ \mu\text{m} \times 275\ \mu\text{m}$ , present the application of a multiple dipole beam.

Depending on the magnitude of the RF modulation frequency and suppression of the higher order sidebands the prong distance of the ‘optical fork’ may be altered and the technique can be extended to 2,4,6... etc., with the carrier signal unsuppressed, or 3,5,7... etc., with the carrier signal suppressed.

## 6.3 Levitation

The phenomenon of levitation has always been attractive. In contrast to magicians who developed and perfected a variety of tricks to display ‘free flotation’ of objects, or even human bodies, in the air without any visible physical means, physicists have investigated a few effects that make true levitation possible with clear justification.

### 6.3.1 Magnetic levitation

Magnetic levitation is a result of a quantum effect that involves the same forces of nature as in the Stern-Gerlach experiment [74]. Cold neutral atoms, which possess magnetic moments oriented parallel to a static magnetic field  $\mathbf{B}$  may be suspended against gravity in a minimum of the combined gravitational and magnetic field. In this thesis

we demonstrate the application of a magnetic levitation field to support the atoms against gravity.

Every BEC experiment is equipped with a variety of magnetic fields. Field gradients and constant fields are abundantly distributed around the vacuum cell where the BEC is created. A precise control over timing and field magnitude has to be assured in order to meet the high requirements for very sensitive and demanding Bose-Einstein matter wave. Certainly, having fully controllable and reliable fields is a must when the other sets of experiments are performed using a BEC.

### 6.3.2 Application of the anti-gravity system

One example of the experiments employing BEC manipulation is an interference pattern generated from two overlapping BECs. In this experiment the fringe spacing  $\lambda$  arises from the de Broglie waves of two condensates and takes the known form (Sec. 3.8.3):

$$\lambda = \frac{ht}{md} \quad (6.4)$$

where  $h$  is Planck's constant,  $m$  is the atomic mass and  $d/t = v$  is the relative speed between two point-like condensates as a function of their center-of-mass separation  $d$  and expansion time  $t$ .<sup>2</sup> The duration of ballistic expansion in freefall,  $t$ , is usually limited by the size of the imaging area and the dimensions of the BEC vacuum cell – times around 100 ms lead to long drops of 49 mm. To eliminate the inconvenience of gravity a levitation field can be used [16] whereby a magnetic field gradient counteracts the gravitational acceleration. The levitation field keeps the atoms in the region of interest for time intervals ( $t > 80$  ms) which are long enough to make our interference pattern optically resolvable.

### 6.3.3 Levitation field origin

When one wants to employ the levitation field it is possible to choose between available gradient fields from the existing experimental coil configuration. Let us consider two possible scenarios of making the anti-gravity gradient field where only one will be followed experimentally. In Fig. 6.11 we show the example of two independent quadrupole fields schemes that can be used to generate the magnetic field for levitation using the existing Strathclyde magnetic coils setup.

---

<sup>2</sup>e.g for 100 ms ballistic expansion the fringe spacing from two overlapping condensates separated originally by 0.25 mm is of order  $1.8 \mu\text{m}$ , which is below the single pixel resolution ( $5 \mu\text{m}^2$ ).

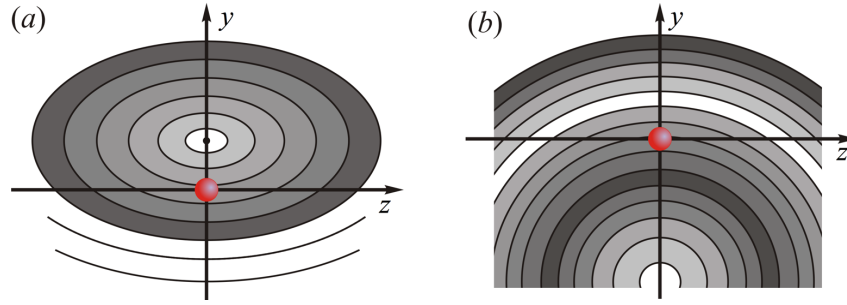


Figure 6.11: Illustration of the anti-gravity (levitation) field. The levitation field generated by different coils configurations: (a) the  $B_{\text{MOT}} + B_{\uparrow}$ , where  $B_{\uparrow}$  is the constant field in  $y$ -direction, (b) the toroidal quadrupole field from four circular coils with an additional vertical constant field,  $B_{4 \text{ coils}}^{\text{quad}} + B_{\uparrow}$ , in order to create the magnetic field minimum above the place where the atoms are. The effective force from the magnetic field gradient counteracts the gravitational force.

The experimental trials showed that good levitation conditions are readily obtained using configuration (b) from Fig. 6.11. Our experimental levitation field is provided by the existing four circular coils [47], which form the toroidal quadrupole field. The levitation mechanism uses the weak-field-seeking  $|2, 2\rangle$  atoms of the BEC which are attracted to the local field minimum. After creation of a BEC in the magnetic trap by a 30 s evaporative cooling cycle, anti-gravity conditions are obtained with a vertical magnetic field gradient. If the gravitational force has to be compensated with the force from a magnetic gradient we can write

$$F_B = F_g \implies \mu_B B = mg \implies B = \frac{mg}{\mu_B}, \quad (6.5)$$

and therefore the vertical gradient for levitation is of order 15 G/cm. An additional vertical constant magnetic field  $B_{\uparrow}$  is added to the quadrupole magnetic field to reduce lensing [150] in the vertical and imaging directions. The  $B_{\uparrow}$  offset field is generated by a pair of rectangular coils that at a different stage of the experiment are used for optical molasses. The direction of the offset field is parallel to gravity but with the opposite sign. The effect of adding the upward constant magnetic field to the field from four circular coils is showed, in the model contour field, in Fig. 6.12. We note that the magnetic field focusing occurs in the radial plane, whereas the axial dimension exhibits a defocusing magnetic field effect.

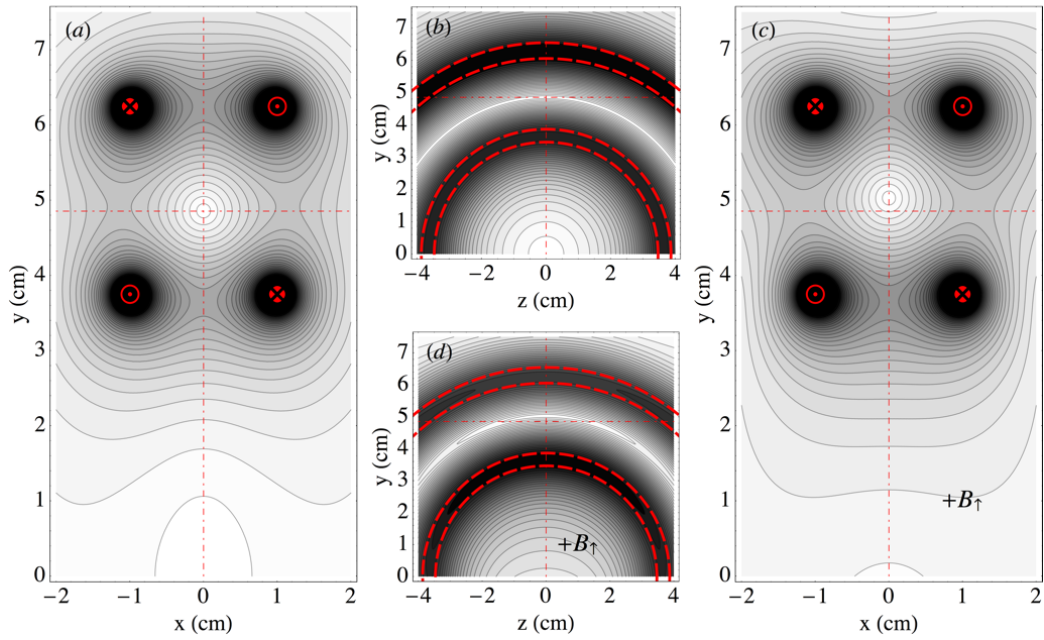


Figure 6.12: Contour field plots from four circular coils. Model fields in (a) and (b) (magnetic field slice at  $z = 0$  and  $x = 0$  respectively) show a pure field from two pairs of the circular coils which form the toroidal quadrupole field in experimental  $xy$  and  $zy$  axes respectively. Model fields in (c) and (d) (magnetic field slice at  $z = 0$  and  $x = 0$  respectively) present contours of the magnetic field when the extra offset field ( $B_{\uparrow}$ ) was added. The crossing of dashed-dot lines mark the original position of the magnetic field minimum from four circular coils.

### 6.3.4 Triggering levitation

The levitation field requires an accurate time setting during the experiment. The application of the levitation field can not be too early nor too late, as it would cause decoherence in BEC or even atom loss. The magnetic field for levitation is applied after the magnetic trap compression, evaporation cooling and final rethermalisation of the atomic sample in the magnetic trap. The time line when the levitation is applied is shown in Fig. 6.13.

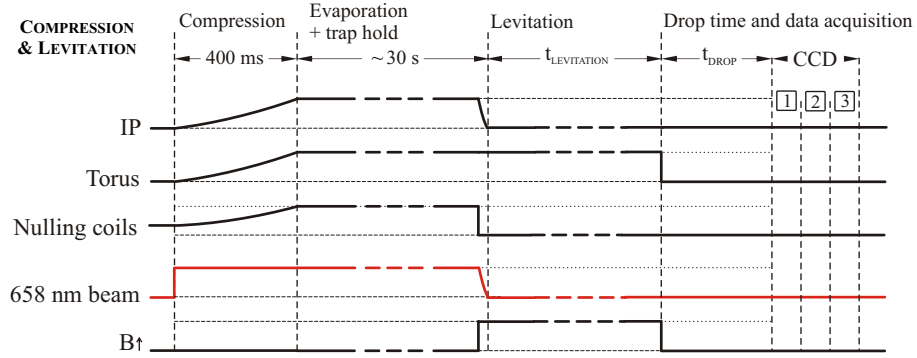


Figure 6.13: Time line of levitation. For the experiments when the cigar-shaped BEC was split by the light potential the blue-detuned beam (658 nm) was on already during the evaporation.

### 6.3.5 Parameters of the levitation field

The combined fields from both coils  $B_{4 \text{ coils}}^{\text{quad}} + B_{\uparrow}$  allows complete cancellation of the vertical forces. The approximately linear field gradient (see Fig. 6.14) experienced by atoms effectively holds them at a certain position. By calibrating the magnetic fields we could optimise and reach anti-gravity conditions.

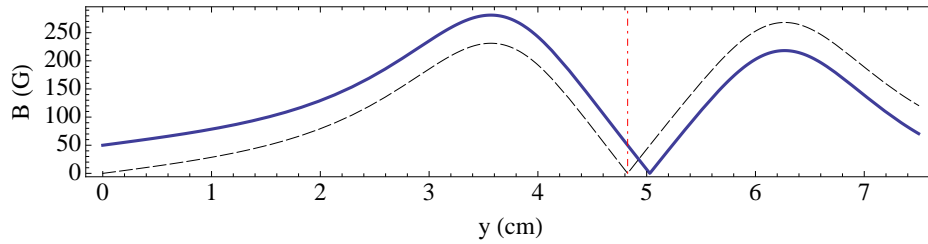


Figure 6.14: Magnetic field levitation vertical ( $y$ ) magnitude. When extra offset field  $B_{\uparrow} = 50 \text{ G}$  is added and  $B_{4 \text{ coils}}^{\text{quad}}$  carry current of 500 A atoms experience gradient of  $\approx 250 \text{ G/cm}$ , that is much more than is needed to create the anti-gravity conditions ( $15 \text{ G/cm}$ ). Dashed line represents magnetic field with no addition of the extra offset field  $B_{\uparrow}$ .

During the levitation the aspect ratio of the BEC cloud changes in time differently from when atoms undergo a free expansion. An example of atoms in the levitation field is show in Fig. 6.15 From the potential used for the levitation field (Fig. 6.12) the atoms exhibit a weak outward directed force in the horizontal direction. Our BEC is levitated in an axial ( $z$ ) potential which is approximately an inverted parabola,  $U_z = -m\omega^2 z^2/2$ , due to the circular nature of our toroidal quadrupole field. The

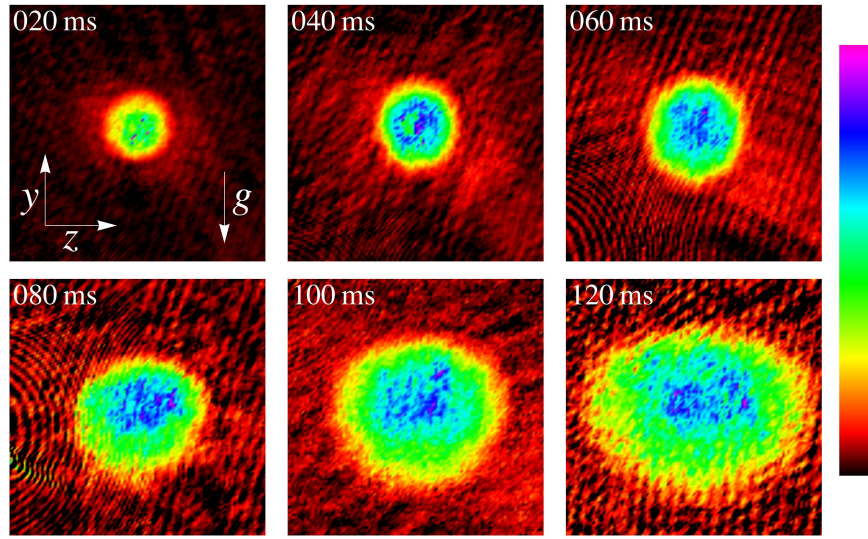


Figure 6.15: Density plots of the BECs in the levitation field. The dimensions of each image are  $(0.5 \text{ mm} \times 0.5 \text{ mm})$ . Levitation times are given in the top-left corners of each picture. In this particular case the levitation field was in the form:  $B = 15 \text{ G/cm} - \epsilon_B$ , where  $\epsilon_B$  is a small magnetic field value; hence the atoms exhibit a small momentum aligned with gravity.

magnitude of  $\omega$  corresponds to that of a rigid pendulum, i.e.  $\omega = \sqrt{g/r} = 14 \text{ rad/s}$ , where  $g$  is the acceleration due to gravity and  $r = 5 \text{ cm}$  is the radius of our ring. With an initial horizontal position  $z_0$  the horizontal classical motion for a particle with initial velocity  $v_0$  is as follows:

$$z(t) = z_0 \cosh(\omega t) + v_0 \sinh(\omega t)/\omega, \quad (6.6)$$

$$z'(t) = z_0 \omega \sinh(\omega t) + v_0 \cosh(\omega t). \quad (6.7)$$

For a levitation field of  $15 \text{ G/cm}$  the vertical motion is not affected. The anti-trapping potential that affects the horizontal motion can be characterised by finding  $\omega$  from Eq. 6.6.

### 6.3.6 Finding omega

The angular frequency of the anti-trapping potential can be found by analysing the expanding atomic cloud in the levitation field. After the BEC was created different durations of levitation field were applied and at each time a picture of the expanding BEC in the levitation field was taken. To observe the profile of the BEC we integrated

the picture matrix along the vertical axis  $y$ . This revealed the  $z$  cross section of the atomic cloud. Optical depth (OD) is displayed on one axis and position ( $z$ ) on the other. For each set of data we fit 1D gaussians and the standard deviation is extracted,  $\sigma$ . The values of  $\sigma$  were plotted versus time. Additionally the examples of 1D gaussian fits to the experimental data are included and are shown in Fig. 6.16.

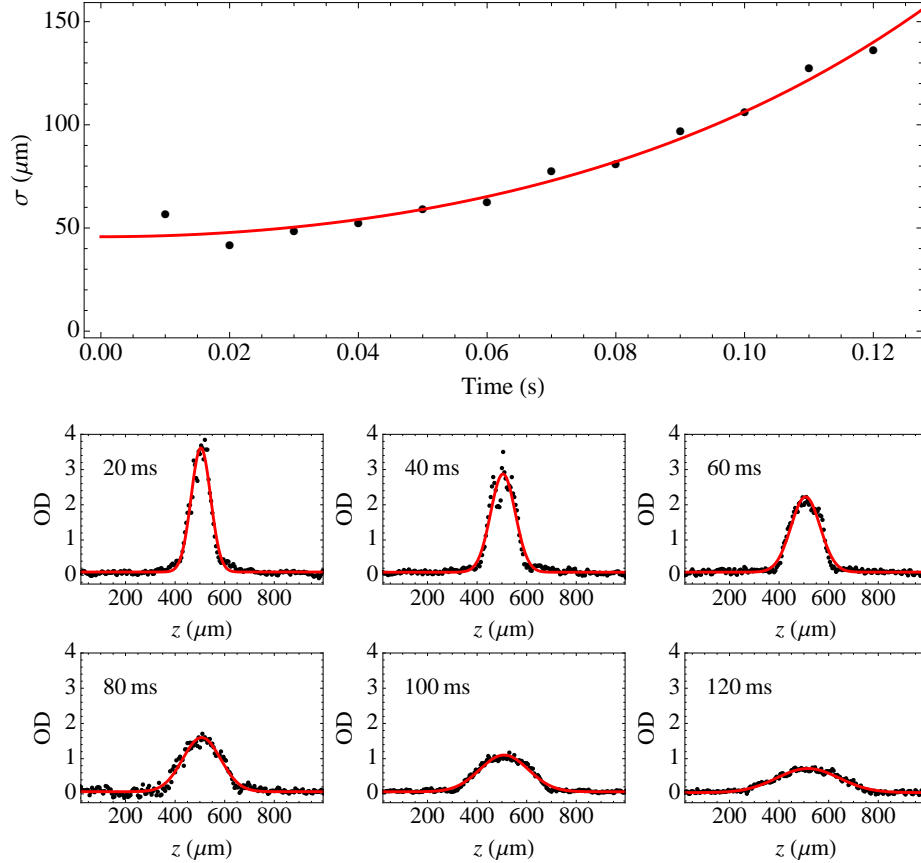


Figure 6.16: Temporal atom distribution in the levitation field. The top image presents the width ( $\sigma$ ) of the atomic clouds versus time of levitation. The fit function is in the form  $\langle z(t) \rangle = (\langle z_0^2 \rangle \cosh^2(\omega t) + \frac{1}{\omega^2} \langle v_0^2 \rangle \sinh^2(\omega t))^{1/2}$ . The examples of the fitted 1D gaussians for different levitation times are shown in the bottom half.

The magnitude of  $\omega = (14.8 \pm 0.6)$  rad/s, found from the data in Fig. 6.16, shows good agreement with theoretical prediction from the geometric potential. This value of  $\omega$ , which characterises the anti-trapping potential in the levitation field, has significant influence on the experiment where the interference fringes of two parts of condensate are performed in the levitation field. This will be discussed in Sec. 6.4.2.

## 6.4 Interference

In the previous sections (Sec. 6.1 and 6.3) we described the tools and methods used in the BEC manipulation. In this section we present results when applying the optical plug and levitation field experimentally for obtaining interference patterns with atoms.

The combination of optical plug and magnetic trap resulted in the creation of a double well potential. In the Strathclyde experiment two parts of a BEC (or two independent BECs) occupied two sites of the double-well potential. The recombination of the two sites in the levitation field resulted in an interference pattern, after  $\approx 100$  ms. In our initial experiments we obtained a wave interference pattern with two independent BECs, as the optical plug was present through the evaporative cooling.

### 6.4.1 Fringe spacing as a function of separation

The computer controlled Digital to Analog Converter (DAC) voltage was used to set the power of the dipole beam. When the threshold power, necessary to drive the AOM (DAC voltage  $\approx 0.6$  V) was satisfied, the first order deflection beam was directed on the focusing lens and its power could be directly measured before the lens. The effective power of the 658 nm beam varied from 0 to  $\sim 60$  mW just before the focusing lens. The DAC voltage dependence of the power transmitted through an 658 nm AOM is presented in Fig. 6.17.

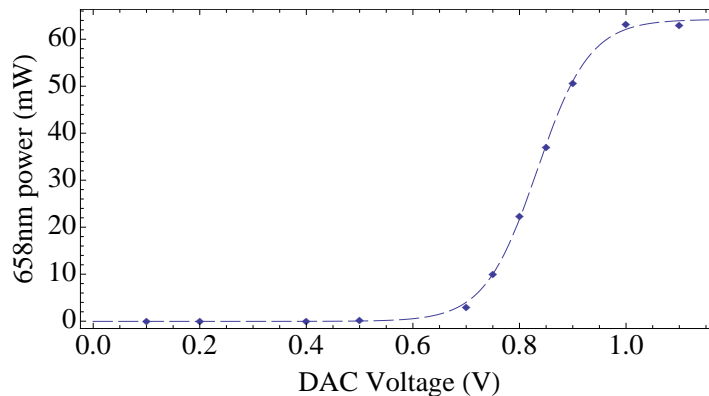


Figure 6.17: Dipole beam optical power dependence on the computer controlled voltage. A DAC voltage enabled a smooth control over the optical plug.

In the Strathclyde experiment when the intensity of the 658 nm beam was increased and the interference period was measured, we observed a decrease in the fringe period

(see Fig. 6.18). That observation (see Sec. 6.4.2), in general, agrees with the fringe period formula,  $\lambda = \frac{ht}{md}$ , as the lower intensity of the beam means an effectively thinner optical potential between the two parts of the BEC, and hence a smaller separation between them. Very similar results were reported with sodium atoms, where an argon ion laser was used for a blue detuned far off resonant laser [100] for splitting the condensate.

Fig. 6.19 presents density plots of the fringe patterns for different amounts of power in the optical dipole beam. The first two images (1-2) exhibit curved interference fringes. The effect of straight fringes is observable in images, from 3<sup>rd</sup> to 21<sup>st</sup>, in Fig. 6.19. We note that similar interference patterns were observed in Ref. [100]. The fringe period for each image was obtained by Fourier analysis that will be described in a later section (see Sec. 6.5). The pictures of the interference pattern were taken after 130 ms of levitation in the magnetic field. The 658 nm beam was left turned on during the evaporation and switched off at the same time as the magnetic trap used for evaporation. The range of the interference spacing for these conditions embraces periods from  $\approx 14.3 \mu\text{m}$  to  $\approx 28.6 \mu\text{m}$ . Detailed fringe period ( $\lambda$ ) dependence on the OD power is shown in Fig. 6.18.

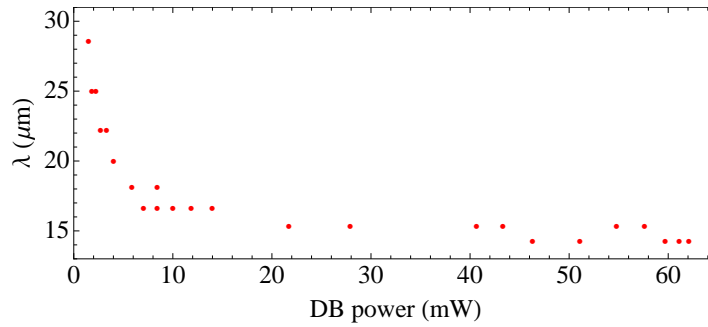


Figure 6.18: Fringe period versus power of the 658 nm dipole beam (DB).

When observing interference patterns we also consider the visibility of the fringes. The fringe visibility can be written as:

$$\text{Visibility} = \frac{S_{\max} - S_{\min}}{S_{\max} + S_{\min}} \quad (6.8)$$

where  $S_{\max}$  is the maximum signal of the oscillations and  $S_{\min}$  the minimum signal of the oscillations. The average fringe visibility in Fig. 6.19 was 30 %, however visibility at the level of 60 % was also possible. The example of 60 % fringe visibility is shown in Fig. 6.20. The picture was taken after a 135 ms of magnetic levitation. The method

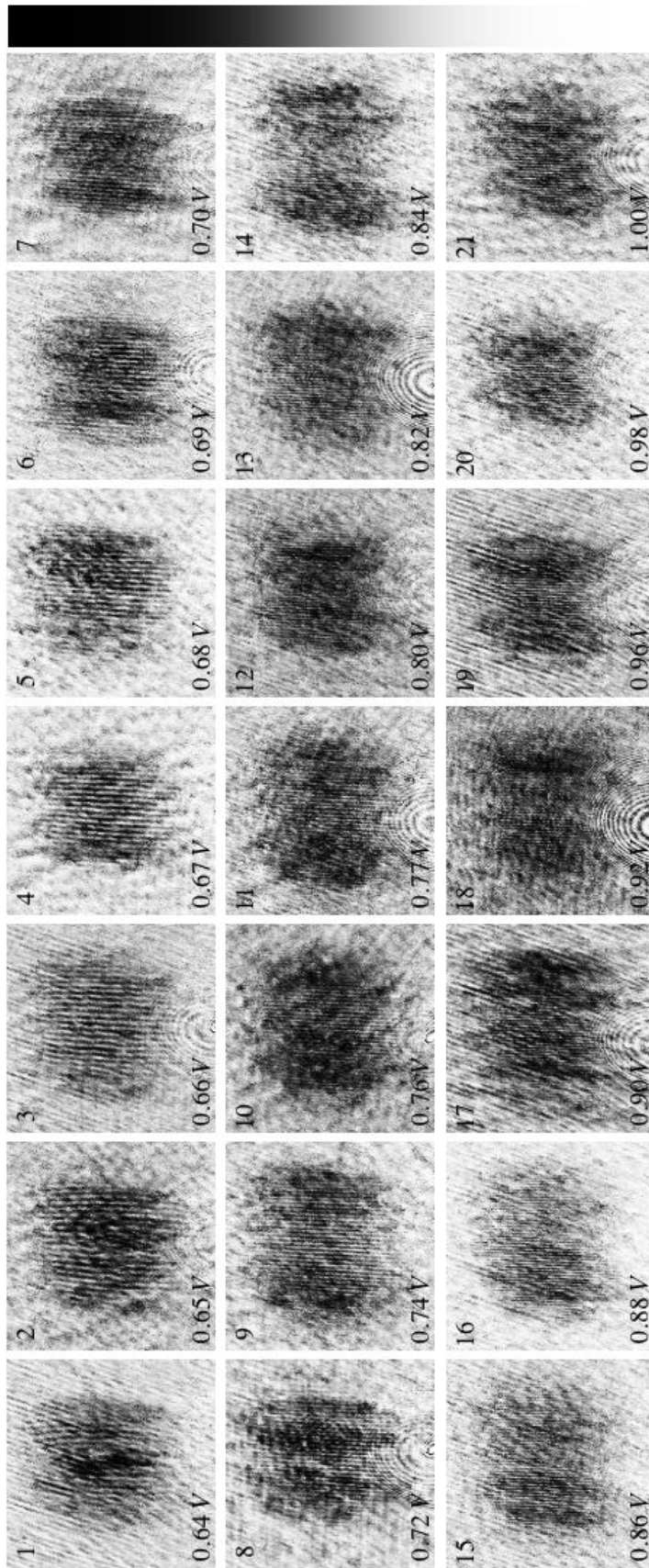


Figure 6.19: Absorption images of the fringe patterns for varied intensity of the dipole beam, taken after 130 ms of levitation. The dark central fringe visible in image 1 was excluded from determination of the fringe spacing. The corresponding DAC voltages are indicated in the bottom-left corner of each image, hence the corresponding power of the dipole beam can be read from Fig. 6.17 and a related visibility of the interference fringes are depicted in Tab. 6.1.

of how the fringe visibility was calculated will be discussed in more detail in Sec. 6.5. Here we only present the absorption images and their density profile in the integrated part of the image.

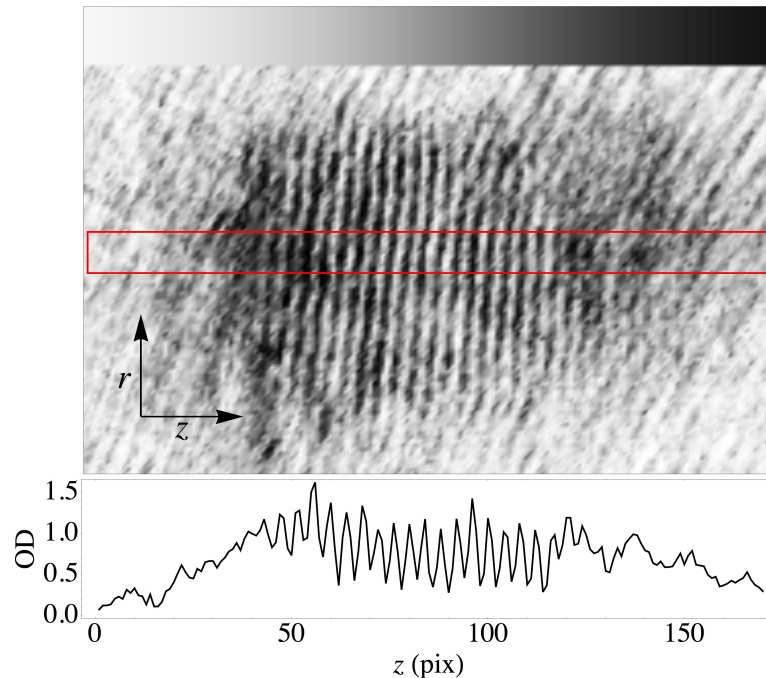


Figure 6.20: Interference patterns ( $850 \times 500 \mu\text{m}^2$ ) for  $60 \mu\text{m}$  separated BECs. The bottom image present integrated average density profile of region of interest (ROI:  $848 \times 50 \mu\text{m}^2$ ), that is marked by the red solid frame in the top image.

Fig. 6.20 represents an example of the high contrast interference pattern when two BEC clouds were originally separated by  $60 \mu\text{m}$  (COM distance) with a single optical plug then recombined using the levitation magnetic field. The interference pattern when the BEC is split from a COM separation of  $60 \mu\text{m}$  to  $250 \mu\text{m}$  over 80 ms, returned to  $60 \mu\text{m}$  separation over 80 ms and then levitated for 150 ms has clear continuous spatial fringes with 30% contrast. The details can be found in Appendix C.

#### 6.4.2 Levitation field correction

The fringe separation can be altered not only by changing the splitting potential width. According to Eq. 6.4, the ballistic expansion of the two parts of the condensate create a fringe spacing that linearly increases with time. With a fixed separation between the condensates,  $d$ , the fringe spacing is directly proportional to the time when the ballistic

DAC (V)	0.64	0.65	0.66	0.67	0.68	0.69	0.70	0.72	0.74	0.76
Visibility %	22	25	39	43	28	26	27	42	25	28
	0.80	0.82	0.84	0.86	0.88	0.90	0.92	0.96	0.98	1.00
	23	28	29	27	38	30	22	36	33	36

Table 6.1: Computer controlled DAC voltage and corresponding visibility of the interference pattern – data was taken from Fig.6.19.

expansion occurs. Hence, when measuring the fringe separation resulting from two ballistically expanding BEC for different expansion times the fringe separation should follow the solid straight line from Fig. 6.21. However, the results deviate significantly from the theoretical prediction. This fact can be reasoned when taking into account the levitation field applied during ballistic expansion of BECs.

As mentioned in Sec. 6.3.5 atoms are levitated in an axial potential,  $U_z$ , which is approximately an inverted parabola, due to the circular nature of our quadrupole field. The characteristic magnitude of  $\omega$ , measured in Sec. 6.3.6, corresponded to the theoretical value imposed by the experimental setup  $\omega = \sqrt{g/r}$  (rad/s), where  $g$  is the acceleration due to gravity and  $r = 5$  cm is the radius of our ring.

Fringe spacing in the potential  $U_z$  is modified from Eq. 6.4 to  $\lambda' = \lambda \sinh(\omega t)/\omega$ . This interference fringe spacing dependence on the levitation potential is clearly observable in Fig. 6.21.

## 6.5 Fringe pattern – Fourier processing

In this section we will show how to reveal periodicity as well as the relative strength of a periodic component in the experimental data. For recognition of a periodic component we use a very useful analysing tool, namely Discrete Fourier Transform (DFT).

The continuous Fourier transform is defined as

$$\mathcal{F}[f(t)](\nu) = \int_{-\infty}^{+\infty} f(t) e^{-2\pi i \nu t} dt . \quad (6.9)$$

We can generalise it to the case when the function is no longer continuous but takes form of discrete values,  $f(t) \rightarrow f(t_k)$ , with  $t_k = k\Delta$  for  $k = 0, 1, \dots, N - 1$ , where  $\Delta$  is

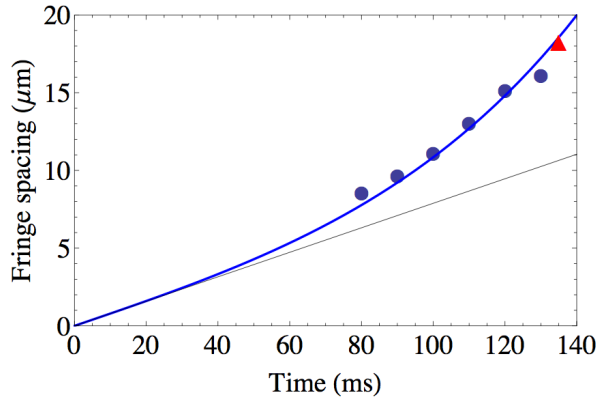


Figure 6.21: Fringe spacing as a function of levitation time. Ballistic expansion theory for  $d = 60 \mu\text{m}$  separated BECs (straight line) and experimental data (points) are shown as well as a blue  $\sinh(\omega t)/\omega$  curve using  $\omega = 14 \text{ rad/s}$  (a geometrical ring property), which has a  $d = 60 \mu\text{m}$  fit. The model aptly represents the fringe spacing in an inverted parabolic potential. The data point represented by the triangle is derived from the image in Fig. 6.20.

the step size. This results in the discrete Fourier transform

$$F_n = \mathcal{F}_k [f(t_k)]_{k=0}^{N-1} (n) \longrightarrow \sum_{k=0}^{N-1} f(t_k) e^{-2\pi i k n / N}, \quad (6.10)$$

and its inverse transform, extracting the original discrete function:

$$f(t_k) = \mathcal{F}_n^{-1} [F_n]_{n=0}^{N-1} (k) \longrightarrow \frac{1}{N} \sum_{n=0}^{N-1} F_n e^{2\pi i k n / N}. \quad (6.11)$$

Interpreting the DFT involves dealing with complex numbers. The discrete Fourier transform of a real sequence of numbers is a sequence of complex numbers of the same length. As the DFT is a complex function hence we can write the components as:

$$F_n = |F_n| e^{i\phi(n)}. \quad (6.12)$$

The amplitude spectrum can be obtained by calculating modulus of the Fourier transform complex function  $|F_n|$ . The squared modulus of a Fourier complex function is a real function describing spectral power density, it means the ratio of how different spectral elements contribute to the total power. If  $f(t_k)$  is real, the DFT obeys the symmetry  $F_{N-n} = F_n^*$  for  $n = 1, 2, \dots, N-1$ . This relation leads to the symmetric amplitude's spectrum plot. The Fourier spectrum  $F_n$  for  $n = 0, 1, 2, \dots, N-1$  of the real discrete values  $f_n$  has an axis of symmetry at  $N/2$  ( $\Re(F_n) = \Re(F_{N-n})$ ).

### 6.5.1 Fourier transformation and fringe spacing

As the interference pattern is in form of a periodic function, it is a quite straight forward mechanism when detecting periodicity using Fourier tool. The interference pattern is readily detected, analysed and finally presented in the form of frequency spectrum. In this section we will briefly explain how to obtain the frequency spectrum and calculate the fringe spacing.

From the original picture when the interference pattern was recorded only a part, region of interest (ROI), was selected for further processing. Fourier spectra was obtained by extracting all rows from ROI  $\mapsto \{R_1, R_2, R_3, \dots, R_n\}$ , then the Fourier spectra  $\mathcal{F}_i(R_i)$  was calculated for each individual row and finally the average spectra  $|\mathcal{F}_i(R_i)|/n$  was generated. Fig. 6.22 presents the Fourier spectra for six experimental fringe patterns. Each picture represents Fourier transformation of the fringe pattern,

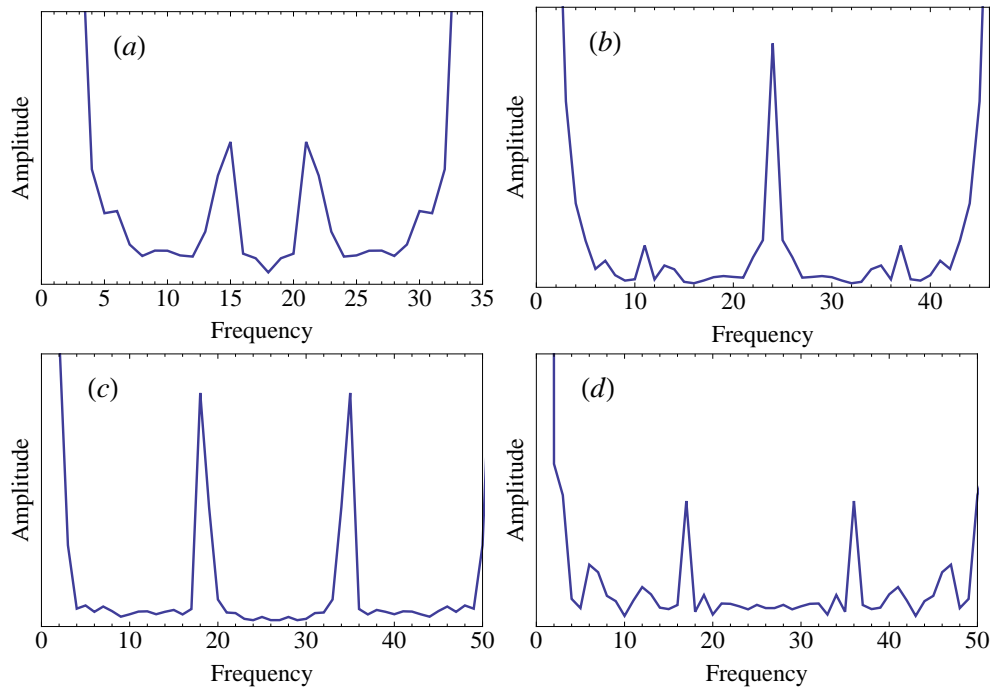


Figure 6.22: Fourier spectra of the experimental interference patterns recorded after (a) 80 ms, (b) 95 ms, (c) 120 ms, (d) 130 ms. The corresponding fringe separation was found to be: (a)  $\sim 8 \mu\text{m}$ , (b)  $\sim 10 \mu\text{m}$ , (c)  $\sim 15 \mu\text{m}$ , (d)  $\sim 16 \mu\text{m}$ .

obtained using different levitation times. The original pictures were taken with dimensions  $160 \times 160$  pixels. From that image the ROI was selected. Selecting the submatrix allowed us to see the interference periodicity more perceptibly. For the image marked

by (a), (b) in Fig. 6.22 the dimension of the ROI are  $35 \times 20$  pixels,  $45 \times 20$  pixels respectively (columns $\times$ rows). The images (c), (d) are extracted from  $50 \times 20$  ROIs. The amplitude of the Fourier spikes corresponds to contrast of the fringe pattern. When the periodicity of the fringes is not correlated with the pixel array we see decrease in amplitude of the Fourier spikes (Fig. 6.22 (a) and (d)).

The Fourier spike positions can be converted into fringe spacing using:

$$\lambda = \frac{N_{\text{tot}}}{N_{\text{peak}} - 1} P_{\text{size}} , \quad (6.13)$$

where the  $N_{\text{peak}}$  is the fringe occurrence frequency within the ROI with total width of  $N_{\text{tot}}$ , and  $P_{\text{size}}$  is the pixel size. This formula was used for calculation the fringe separation versus time in Sec. 6.4.2, in Fig. 6.21.

### 6.5.2 Fringe tilt correction - methods

For an ‘ideal’ interference pattern the interference fringes are aligned with the CCD sensor columns. This simplifies the measurement of the interference fringe contrast from the recorded image. However fringe pattern might occur tilted with respect to the pixel array. In this section we describe how to apply two different techniques for straightening the interference fringe pattern, which helps to obtain a clear signal for calculation the visibility (contrast) of the fringes.

#### Fourier tool

As the interference fringes possess the phase information, one might take the advantage of applying the phase related correction for straightening the fringe pattern. In this section we present step-by-step method of how to apply phase correction to the experimental data. We will start off with a raw image displaying the interference pattern from two independent matter wave samples. The relatively big phase shift in the interference pattern will undergo mathematical transformations and the appropriate method explanation will be given. Eventually we will show the final graphical effect of the original raw picture after applying the phase correction.

A single raw image from the experiment takes form of a  $658 \times 496$  elements matrix. That corresponds to the size and number of pixels in the CCD sensor. From that matrix only a part, where the atoms were, was extracted. For our purpose which is to see the interference pattern from two BECs was enough to take a  $150 \times 100$  pix submatrix. The density plot of this region is shown in Fig. 6.23.

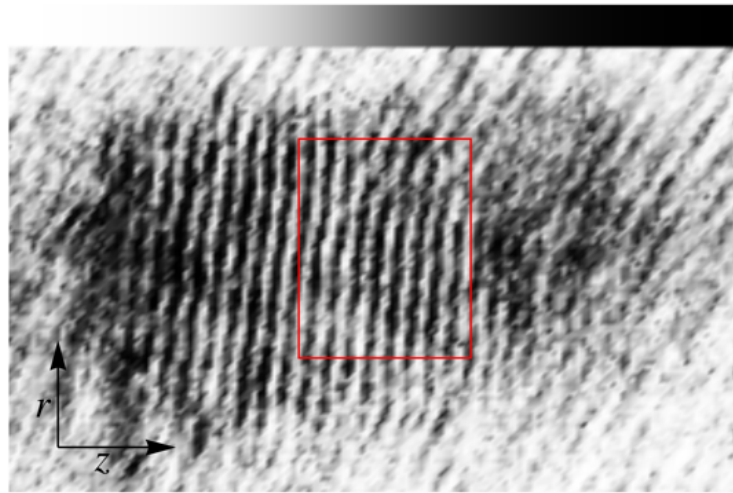


Figure 6.23: Interference pattern obtained by overlapping two BECs in the magnetic levitation field. The image size is  $150 \times 100$  pixels, where 1 pixel corresponds to  $5 \mu\text{m}$ . The red solid frame in the picture embraces the  $35 \times 50$  pix ROI that will be used for later calculation.

In order to analyse the fringes we can go even further and cut the region of interest to smaller area where the fringe pattern is the most distinguishable. The solid box in Fig. 6.23 gives a final ROI that will be used for our later analysis. The size of the frame is 35 pix horizontally and 50 pix vertically. The extracted frame is presented in Fig. 6.24 (left). The right hand side picture in Fig. 6.24 shows the average spectra

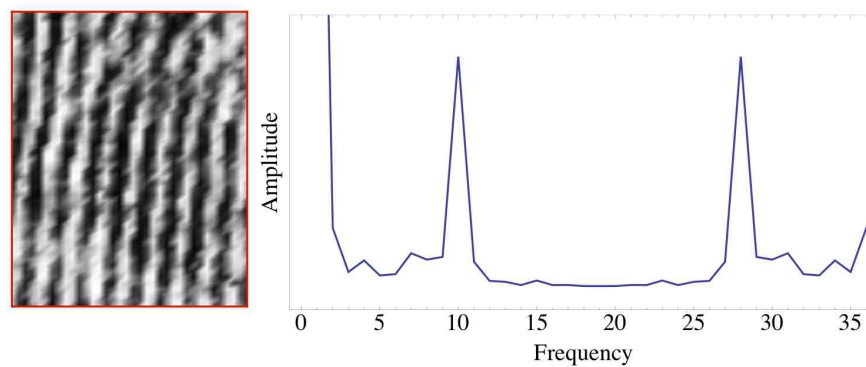


Figure 6.24: The selected ROI ( $35 \times 50$  pix) from Fig. 6.23 with the high contrast interference fringes and its Fourier representation.

$\sum_i^n \mathcal{F}_i(R_i) / n$  of ROI (left), as discussed in Sec. 6.5.1. From the spectra we can calculate fringe period between density maxima. Fourier spectra in frequency domain results in two frequency components with an opposite relative phase. First peak occurs at 10 and

the second at 28. These points carry the information and are most sensitive to phase correction when straightening the fringe pattern.

The fringe tilt directly corresponds to the phase change along the fringes. It is clearly visible in Fig. 6.24 (left) that the phase shift is significant. Before we apply a phase correction factor we need to find the phase changes in the ROI, by scanning individual rows. The phase argument,  $\phi_i$ , is extracted from the Fourier transform of each row  $\mathcal{F}_i(R_i)$ . Starting from row  $R_1$  (bottom) and finishing at row  $R_{50}$  (top) we record the argument and plot it in Fig. 6.25 to see how the phase changes as we go along the ROI.

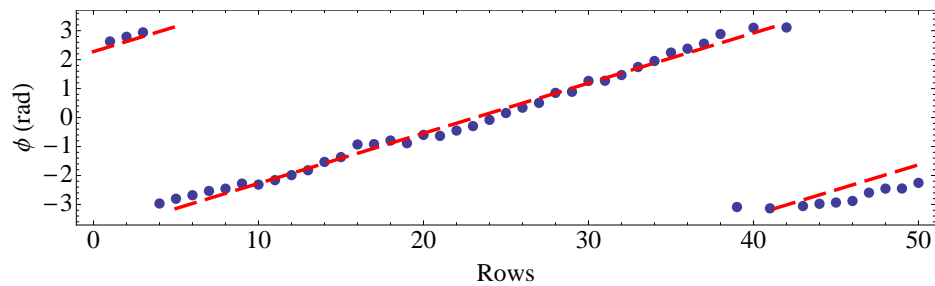


Figure 6.25: The phases of the Fourier components of the fringes for the red selected areas in Fig. 6.23. A dashed red line represents a linear phase shift fit to the phases of the Fourier components. It was a good approximation to a sawtooth linear phase shift over a whole range of rows. The slope determination factor was found to be 0.17 rad/row.

The monotonically increasing function,  $\phi_{\text{corr}} = \mathcal{G}R + \phi_0$ , was fitted to the phase change with respect to the rows. The gradient,  $\mathcal{G}$ , was found to be 0.17 rad/row and  $\phi_0$  was found to be  $-5.9$  rad. Phase correction factor was applied to the 10<sup>th</sup> and 28<sup>th</sup> element from each row  $R_i$  but with the opposite phase,  $e^{-i\phi_{\text{corr}}}$  and  $e^{i\phi_{\text{corr}}}$  respectively. That results in the phase correction shift, and hence the fringe pattern straightening. To see the graphical effect one need to take the absolute value of the inverse Fourier transform of the phase corrected data (Eq. 6.11). The application of the formula is displayed in Fig. 6.26 together with the uncorrected raw experimental data.

Fig. 6.26 (b) provides a Fourier processed matrix from which one can obtain a new density profile of the interference fringes. This corrected image can then be averaged over the image rows to obtain the data points in Fig. 6.27. The density profile showing the visibility of the fringe pattern, with their sinusoidal fit (green curve), is shown in Fig. 6.27. When calculating the fringe visibility the background level was measured

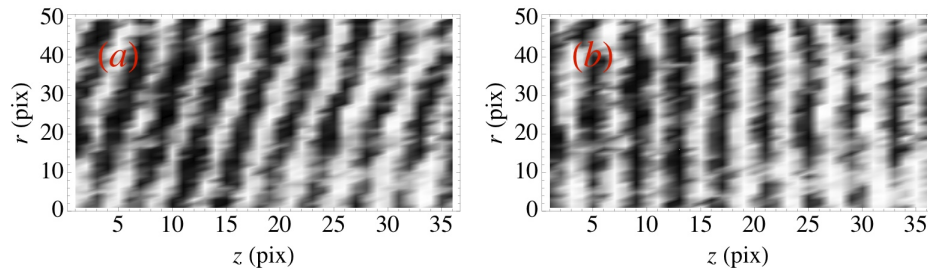


Figure 6.26: Interference pattern (a) before the phase correction (b) after the phase correction. The images aspect ratio changed to 1/2 to see more clearly the effect of straightening the fringe tilt. .

and subtracted from the data.

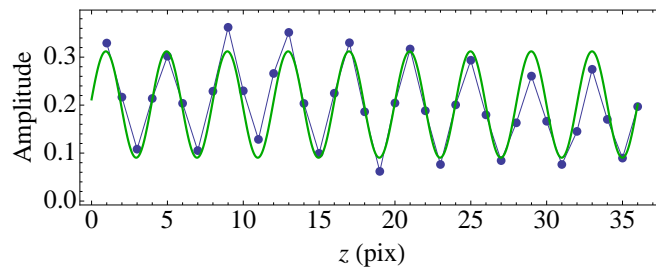


Figure 6.27: Density profile of the fringe pattern from the Fourier corrected image. Each data point in the plot corresponds to the pixel averaged over the image rows. The sinusoidal fit demonstrate the high contrast (60%) interference pattern. The auxiliary thin blue lines (straight lines between the data points) act as a reference for the sine wave.

### Subpixels arrays

Similar result to the straightening the interference fringe pattern using Fourier transformation we obtain using the subpixel method. In this simple way of straightening the fringe pattern we create the additional copies of columns for more precise control in a column shift.

Let the number of columns be, in the original ROI,  $n_o$ . In this setting the smallest row shift, with respect to the other row of ROI, is a one original column. If each column will have its own adjacent copy and the aspect ratio of the ROI will be kept the same, as originally, the smallest row shift will be no longer limited by one original column, but a half of the original column. The new ROI has  $n_o + n_o \times N$ , where  $N$  in this example

is equal 1 as only one copy of each column was created. Creating the additional copy of the columns and keeping the ROI aspect ratio constant is the same process as we divide one column into two identical parts. Instead of generating only a one copy of the column the routine can be performed creating  $N > 1$  copies of the each column, making even more accurate method of straightening the fringes.

We only introduce the additional subcolumns as the fringe pattern is going to straighten to the vertical axis. However the same subpixeling can be done for rows as well, but for our purpose we will only introduce horizontal subpixels. Having the additional horizontal subpixels to play with we follow the procedure of finding the phase change the same way as in Sec. 6.5.2. The most important part using that method is to convert an obtained phase shift into a subpixel shift.

In order to do so we can use the Eq. 6.13 and relate it to the phase shift including the additional subcolumns in the ROI. After introducing the additional columns the new fringe spacing is  $\lambda_N = \frac{N_{\text{tot}}}{N_{\text{peak}} - 1} \times N$ . Therefore, the phase correlation with the new pixel shift  $\Delta x_N$  can be expressed as:

$$\Delta x_N = \frac{\phi}{2\pi} \times \lambda_N = \frac{\phi}{2\pi} \frac{N_{\text{tot}}}{N_{\text{peak}} - 1} \times N, \quad (6.14)$$

where  $\Delta x_N$  was rounded off to the nearest integer. The processed experimental data with the interference pattern is present in Fig. 6.28 where the additional columns were introduced. We first add extra two copies to each column – (a), then five copies – (b) and finally ten extra column copies – (c). The fewer extra columns we add the more grainy the interference pattern is obtained, as we expect.

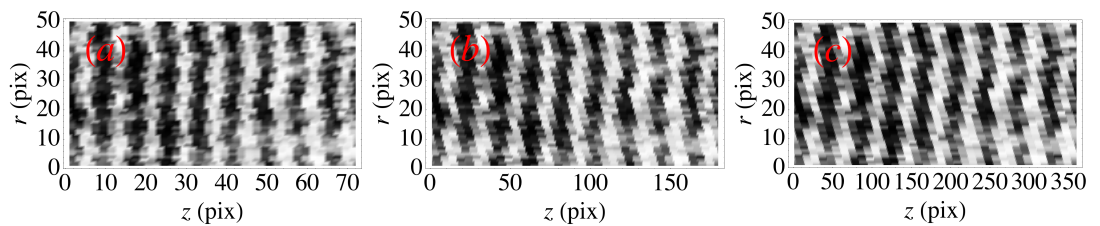


Figure 6.28: Straightening interference pattern using the subpixels method. Three processed images with additional number of copies of the columns  $N$ : (a) 2 (b) 5, (c) 10. The images aspect ratio changed to 1/2 to see more clearly the subpixel effect on straightening the fringe tilt.

Similarly as for Fourier method the corrected image can then be averaged over the image rows to obtain the blue dots in Fig. 6.29. The density profile showing the visibility

of the fringe pattern, with their sinusoidal fit (red curve), is shown in Fig. 6.29. When calculating the fringe visibility the background level was measured and subtracted from the data.

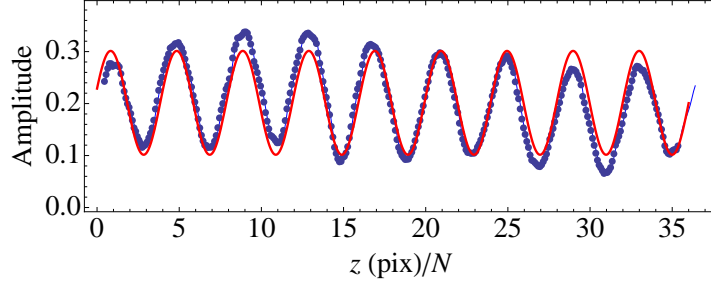


Figure 6.29: Density profile of the fringe pattern from the subpixels processed image. The sinusoidal fit demonstrate the high contrast (53%) interference pattern ( $N = 10$ ).

## 6.6 Coherent properties of the BEC

The matter wave interference experiment provides an undisputed proof of the coherence properties of a single Bose-Einstein condensate when interfering with the second one. In this section we approach a theoretical interference using a coherence of two condensates. We present a theoretical condensates dynamics in terms of time dependent Schrödinger equation (TDSE) and by adding the interatomic interactions we solve a Gross-Pitajevski (GP) equation.

### 6.6.1 Quantum interference

The solution to Schrödinger equation provides a neat theoretical demonstration of the interference between two condensates. First of all, one has to choose an appropriate, time and position dependent, wave function that describes two condensates. In our calculation the condensates at time  $t = 0$  will be represented by two Gaussian wave packets with the width  $\sigma_g$ . The wave function for two initially separated wavepackets ( $2z_0$ ) before the ballistic expansion (for  $t = 0$ ) can be written in form

$$\Psi(0, z) = \mathcal{N}(c_1\psi_1(0, -z_0) + c_2\psi_2(0, +z_0)) = \mathcal{N}\frac{1}{\sqrt{2}}\sum_{i=1}^2 e^{-\frac{[z+(-1)^i z_0]^2}{2\sigma_g^2}}, \quad (6.15)$$

where  $\mathcal{N} = \frac{1}{\pi^{1/4}\sqrt{\sigma_g}}$  is the normalisation factor. For simplicity we choose factors  $c_1 = c_2 = 1/\sqrt{2}$ , that implies an equal atomic distribution between two parts of the

coherently split BEC. The dynamics of the wave function from Eq. 6.15 is determined by a numerical calculation of the time dependent Schrödinger equation.

Our numerical calculations were done using *Mathematica* software.<sup>3</sup> A typical set of parameters used in our experiment involved: initial separation of two wave-packets:  $2z_0 = 50 \mu\text{m}$ , mass of  $^{87}\text{Rb}$ :  $m = 87 \times 1.66 \times 10^{-27} \text{ kg}$ , inverted harmonic levitation potential frequency:  $\omega = \text{gravity}/r_{\text{ring}} = 14 \text{ rad/s}$ , where  $r_{\text{ring}}$  is the radius of the ring, the Planck constant  $\hbar = 1.05 \times 10^{-34} \text{ J s}$ , and the boundary conditions set at:  $\pm 500 \mu\text{m}$ . The interatomic interaction (repulsion) was chosen after we scaled the time dependent Schrödinger equation and only a qualitative change of the interaction parameter,  $g$ , was made from 0 to 10.

In our first calculation we neglect the interatomic interactions and use a time dependent Schrödinger equation of the form

$$-\frac{\hbar^2}{2m} \frac{\partial^2 \Psi}{\partial z^2} + U_z(z) \Psi = i\hbar \frac{\partial \Psi}{\partial t}. \quad (6.16)$$

First of all let consider an interference effect without any external potential ( $U_z(z) \rightarrow 0$ ). The absence of confining potential for atoms results in a free-fall ballistic expansion of two BECs. The solution of Eq. 6.16 leads to the time dependent dynamics presented in Fig. 6.30.

As we described in Sec. 6.3, the experimental limitation require implementation of the additional fields that make the interference pattern detectable. Depending on the potential introduced by external field the dynamics of two overlapping BECs changes, and hence the fringe spacing (Sec. 6.4.2). The experimental procedure at Strathclyde implies an external potential used for magnetic field levitation. The potential is generated by the toroidal coils but only a part of the potential is seen by atoms and it can be approximated by an inverted harmonic potential  $-m\omega^2 z^2/2$ . When the Schrödinger equation is enriched with this potential from the levitation field it takes the following form

$$-\frac{\hbar^2}{2m} \frac{\partial^2 \Psi}{\partial z^2} - (m\omega^2 z^2/2) \Psi = i\hbar \frac{\partial \Psi}{\partial t}. \quad (6.17)$$

The dynamics of two clouds in the levitation field can again be calculated numerically using above equation (Eq. 6.17). The result is presented in Fig. 6.31 (red). When adding the interatomic interactions,  $g|\Psi|^2$ , to the Eq. 6.17 we obtain the GP equation in the

---

<sup>3</sup>Solving the time dependent Schrödinger equation we used ‘NDSolve’ package from *Mathematica* software.

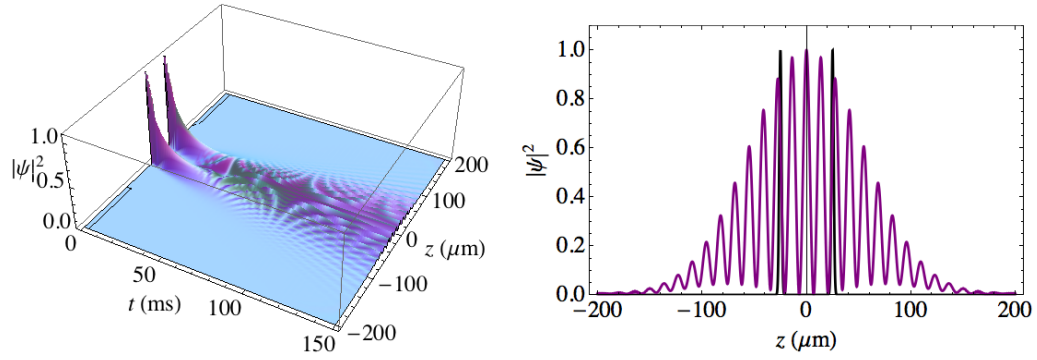


Figure 6.30: The theoretical spatio-temporal dynamics of two BECs in a free fall ballistic expansion. Left: The dynamics of two BECs separated by distance  $2z_0 = 50 \mu\text{m}$  over time of  $0 - 150$  ms. Right: Two single narrow gaussian peaks (black) represent two BECs at initial time  $t = 0$ . The normalised interference pattern displayed as a product of two overlapping wave functions at time 150 ms.

form:

$$-\frac{\hbar^2}{2m} \frac{\partial^2 \Psi}{\partial z^2} - (m\omega^2 z^2/2) \Psi + g |\Psi|^2 = i\hbar \frac{\partial \Psi}{\partial t} . \quad (6.18)$$

When solving this equation with the interatomic repulsion term included it can be seen from Fig. 6.31 that the nonlinear term in the Schrödinger equation only affects the width of the final distribution, but not the fringe period. Theory clearly indicates that the fringe spacing is not altered by interatomic repulsion. Interestingly the fringe separation has a similar dependence to that attributed to interatomic repulsion in interferometry experiments on a chip, albeit at higher atomic density [151].

## 6.7 Magnetic ring experiments

In this section we will present the last results when using the Strathclyde storage ring. A few possible scenarios with an experimental data presented will be outlined, including: transferring atoms into the magnetic field ring minimum, launching atoms within the ring, observing atoms after one or two revolutions and finally splitting atoms at the top of the ring and recombining them after one revolution.

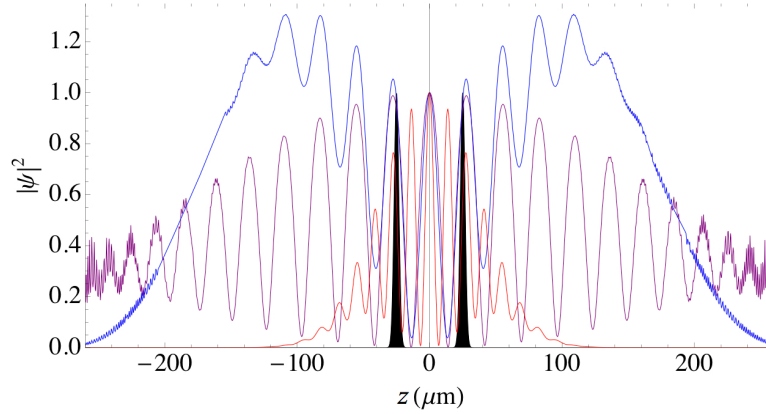


Figure 6.31: Relative theoretical probability distributions (fringes, with even symmetry about  $z = 0$ ) obtained when two Gaussian initial wavepackets (black) are released for 150 ms in a potential:  $U_z = 0$  (red),  $U_z = -m\omega^2 z^2/2$  (blue/purple curves). The interatomic repulsion parameter,  $g$ , is either zero (blue curve) or 10 (purple curve). Increasing the nonlinear term in the Schrödinger equation only affects the width of the final distribution, but not the fringe period.

### 6.7.1 Ring transfer

After accumulating atoms or BEC in the magnetic trap they can be launched into the magnetic ring. In this section we present the method how to transfer a BEC into the ring as due to imperfect manufacturing the magnetic waveguide and trap are slightly offset with respect to each other.

The trap was designed in a way to overlap the field minima of the MOT, the magnetic trap and the storage ring. We are able to create a BEC inside the ring, however due to imperfections of the setup, the BEC is generated approximately  $94 \text{ pix} \approx 470 \text{ } \mu\text{m}$  away from the ring minimum magnetic guide. The careful transfer of the atoms into the ring minimum has to be applied. The transfer must be performed adiabatically to prevent a coherence loss of the condensate or avoid exciting the breathing modes or sloshing. The adiabatic transfer into the ring depends mainly on two aspects: (1) time - over which the transfer is done, and (2) the way how the magnetic fields are implemented. The typical time allowing for adiabatic transfer was checked experimentally to be from 50 to 80 ms. This time corresponds to creating net velocity of the atoms 9.4 mm/s to 5.9 mm/s respectively by changing the gradient of the magnetic field during the transfer. These velocities are true for a linear change in the magnetic field as

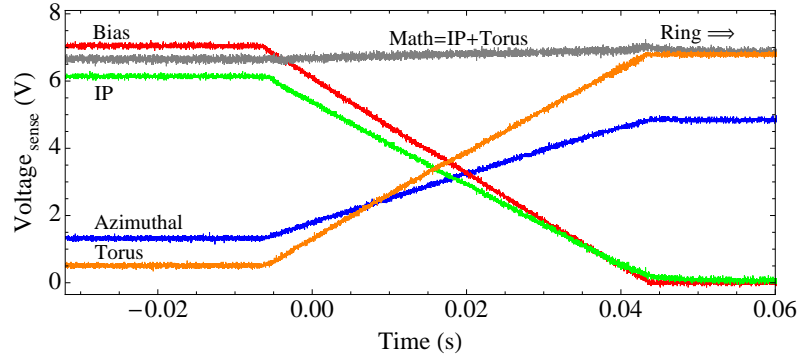


Figure 6.32: The linear magnetic field dependance during the ring transfer. The signals represent the Hall-effect sensor outputs for different magnetic coils (going from the left top: Bias, Math, IP, Azimuthal and Torus). The far right side shows the region when the ring waveguide is in full operation. The azimuthal field is responsible for removing the zero magnetic field from the centre of the magnetic ring guide.

presented in Fig. 6.32. The experimental trials were done also using an exponential switching, however the linear ramp provided the best control over the cancellation between IP and torus coils. The Hall-effect current sensors were monitored during the transfer. This provided a direct measurement of how the magnetic fields alter when transferring the atoms. The *Math* function shown in Fig. 6.32 adds together the current sensed on the IP trap and torus waveguide. Approximately flat output on the Math channel provides a disturbance-less transfer. The slopes presented in Fig. 6.32 were optimised by observing the temperature of the transferred atoms. The density plots of the 50 ms transfer into the magnetic ring minimum are presented in Fig. 6.33 (a) and (b). After the atoms were transferred into the ring minimum one could make further stages of experiment using the giant toroidal magnetic waveguide. The example of the atoms being launched into the magnetic ring, shown in Fig. 6.33 (c) – (e), demonstrates the instance when the whole cloud of atoms is directed in the  $-z$  direction. This scenario corresponds to the atoms being released from a place, which is slightly offset from the top of the ring. After optimisation of the transfer technique we could move forward and observe the first effects of launching atoms within the ring. What was considered first consisted of observing atoms after a single rotation in the giant ring.

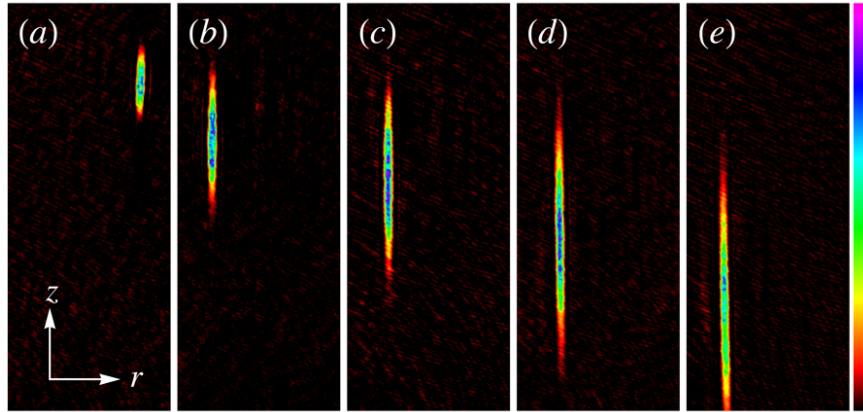


Figure 6.33: The transfer of the BEC from the IP magnetic trap into the ring minimum. The absorption images (a) and (b) correspond to the BEC in the magnetic trap and ring respectively. The transfer was done over 50 ms. The absorption images (c), (d) and (e) show beginning stage of the atoms being launched within the ring for different time intervals; 10 ms, 20 ms and 30 ms respectively.

## 6.7.2 Comet

### 1 revolution

The atoms traveling around the ring had to overcome the ring circumference path with length of  $\sim 30$  cm. It was necessary to wait a sufficient amount of time to see the atoms reappearing on the other side of the ring. As the atoms traveled vertically they had to climb the potential when approaching the top of the ring from the other side. We used a magnetic field gradient in the final stage of the one revolution trajectory to see the atoms in the CCD camera viewing region. The one-revolution atomic cloud, when it arrived at the top, looked like a comet where the dense core of the atomic sample was followed by its tail. The example of the experimental data after one revolution in the magnetic storage ring is shown in Fig. 6.34.

The absorption image (Fig. 6.34) was taken after 740 ms of propagation of the atomic sample inside the ring and 5 ms drop time. The radial temperature of the cloud was estimated to be 15 nK. The wiggly tail of the comet after one revolution might originate from the magnetic perturbation as a result of applying the magnetic field gradient to the atoms. The magnetic field gradient was applied only at the end (last 200 ms of the propagation within the ring) of the experiment. Similar BECs dynamics, when a wiggly atomic tail was seen, was reported in Ref. [152]. According to Ott *et*

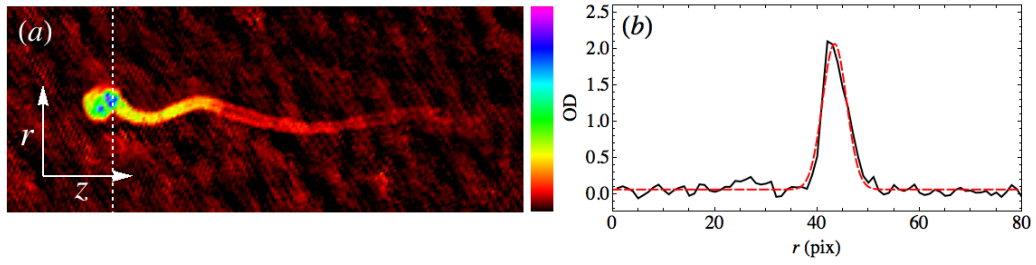


Figure 6.34: The comet-like cloud after one revolution (+5 ms drop time) in the giant storage ring. Dimensions of the density plot (a) are  $200 \times 80 \text{ pix}^2$  ( $1.0 \times 0.4 \text{ mm}^2$ ). The dashed line indicates the slice of the image, which is presented in the optical density plot (b).

*al.* [152] these characteristic oscillations were due to the anharmonicity of the magnetic waveguide. On the other hand, we can also suspect that the wiggly tail can be an evidence of nonlinearity caused by creation of vortices in the condensate, which travels within the circular path (one revolution in the ring). In order to dispel doubts related to this problem one could shift the position of the imaging camera and observe the BEC after one revolution without an additional magnetic field gradient, which might cause the magnetic field irregularities.

## 2 revolutions

The ‘top of the hill’ in the magnetic ring can be treated as a relative place. When applying the magnetic field gradient atoms can be directed in both directions depending on the magnetic field gradient sign. This offset magnetic field gradient is the combination of the IP, MOT and azimuthal coil, which can control the launching direction of the BEC. However in the two-revolution experiment we did not use this method for launching the atoms into the ring. We used initial position, which was already offset from the top of the ring and atoms experienced acceleration (due to gravity) to one side of the ring only.

Similarly to one-revolution experiment, when waiting for long enough time ( $\sim 1 \text{ s}$ ) we could see the atomic cloud appearing again at the ‘top’ of the ring after two, almost full, revolutions in the magnetic ring. This time atoms did not have enough kinetic energy to climb to the top of the potential from the ring. However they could return and come back to the place where they started. No additional magnetic field gradient was applied. The absorption image is presented in Fig. 6.35 (a).

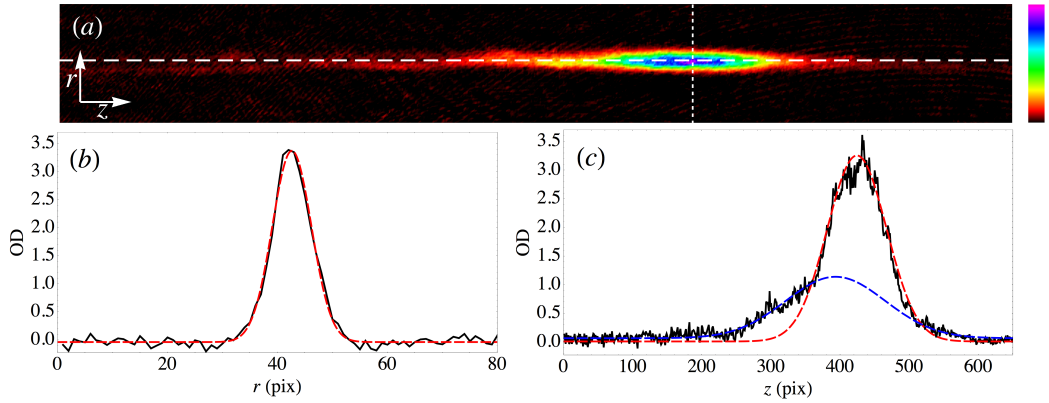


Figure 6.35: The comet like cloud after two revolutions in the giant storage ring. Dimensions of the density plot (a) are  $650 \times 80 \text{ pix}^2$  ( $3.25 \times 0.40 \text{ mm}^2$ ). The dashed lines indicate the slices of the image, which are presented in the optical density plot: (b) for  $r$  axis and (c) for  $z$  axis.

It is difficult to give an accurate number for the temperature in the axial direction as we can observe the focusing from the atom climbing the top of the ring. The misleading temperature would be obtained if the cloud would be still compacting, giving a deliberately low temperature during the free fall measurement. Hence, one can only consider a rough estimate what the actual temperature is in the  $z$  direction. The radial temperature could be measured with better accuracy if the multiple drop times pictures were taken.

### Towards the giant interferometer

As the condensates are formed inside and at the top of our vertically-orientated storage ring we can split BEC into two counter-rotating parts under gravity (or by applying a magnetic field gradient). After a single revolution two parts might overlap at the top of the ring exhibiting the interference fringes. The giant magnetic storage ring capable of generating interferometric fringes with BECs would be a world-leading precision atom interferometer. The example of returning two atomic packets after a single revolution inside the ring is shown in Fig. 6.36. The density plot (a) with an average integrated density projection (b).

When the condensate is split it into two parts, then one can affect how much the two halves overlap at the top of the ring by weakening or strengthening the trap while they rotate around the ring. If they come back to a lower height than they were at,

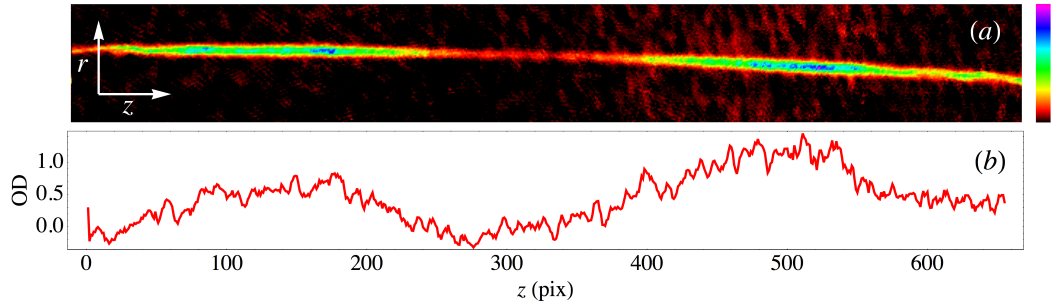


Figure 6.36: The recombination of two counter-rotating parts of the atomic cloud inside the giant storage ring. They recombine here after one revolution. Dimensions of the image are  $654 \times 80 \text{ pix}^2$  ( $3.27 \times 0.40 \text{ mm}^2$ ). We can control the split ratio as well as the overlap.

they will collide fast, if they come back to a higher height than they were before they will not reach the top again, from conservation of energy. Experimentally, it can be done applying the azimuthal field – it can be ramped slowly up during rotation to see atoms collide harder.

The absorption image (Fig. 6.36) was taken after 990 ms of propagation of the atomic sample inside the ring. The relatively long time compared to a single revolution is due to a beginning stage, when atoms are set at the top of the ring and it takes a while for them to go in the opposite directions under only gravity. When we split the BEC evenly, it has a slow launch velocity and takes longer ( $\sim 1 \text{ s}$ ) for a revolution than if we launch from the side ( $\sim 700 \text{ ms/revolution}$ ). An option would be to use Bragg scattering [153, 154] to coherently launch two pulses of condensate in different directions around the ring.

In this section we have described the achieved experiments with a storage ring for cold  $^{87}\text{Rb}$  atomic clouds and BECs with an area of  $7200 \text{ mm}^2$ . Our goal is a highly sensitive Sagnac atom interferometer, in which we are aided by our ring area. Rotation sensitivity for a single revolution of  $\delta\Phi = \hbar/(8m\pi r_{\text{ring}}\sqrt{N}) = 3 \times 10^{-11} \text{ rad/s}$  is feasible.

To date we have unfortunately not seen interference fringes between two clouds after one revolution. We have not had enough accurate (limited by the experimental hardware) control over the velocities of the two counter-propagating parts of the BEC, needed in order to optically resolve the interference pattern. However we implemented successfully an optional method of making the interference fringes optically resolvable using levitation field (see Secs. 6.3 and 6.4). The same mechanism can be implemented

for two parts of BEC after one revolution in the ring. Two atomic clouds can be stopped next to each other after one revolution (e.g. using dipole beam or light sheet) and then the levitation field can be applied.

When achieving interference patterns with BECs in the levitation field with a conjunction of the dual-frequency optical dipole beam we understood better the experimental conditions and gained valuable practice. We also discovered a magnetic field related problems and we found solution how these obstacles can be eliminated (see Sec. 7.2 and Appendix D). After making suggested (see Sec. 7.2 and Appendix D) experimental improvements we are hopeful that we will be able to achieve fringes in the near future.

# Conclusions

## 7.1 Summary

In this thesis we began with an introduction to the concept of Bose-Einstein condensation (BEC) and the mechanisms used to obtain it. Also, in Chapter 1 we considered the application of the BEC in atom interferometry.

Chapter 2 provided a fundamental theory of the macroscopic occupation of the atomic ground state. We gave a description of the quantum structure of Rubidium atoms also showing its graphical representation. The mechanism of repumping atoms from the ground state and optical pumping process, for changing the population of atoms in particular quantum states, were introduced. The theoretical basis for the Bose-Einstein statistics were followed by a quantum mechanical description, including a nonlinear Schrödinger equation, which was used later on in this thesis (Sec. 6.6) for analysing the atomic interference phenomena.

The theory behind the methods used to reach BEC was the topic of Chapter 3. We provided a brief outline of laser cooling, from laser-atom interaction to magneto-optical traps. In this chapter we have also described general properties of the atoms in the magnetic field, finally giving useful theoretical models for building practical magnetic fields for atom trapping. As an example the magnetic trapping of atoms in a Ioffe-Pritchard trap was considered. This was followed by a section which gave the idea behind the evaporation cooling technique when going towards the BEC transition. Knowing the path to reaching macroscopic quantum condensation we introduced theoretically an additional tool for manipulation of the BEC, namely a light potential. Chapter 3 was ended with a general description of atom interferometers, including a

five-step routine characterising the working principle of an atom interferometer.

Chapter 4 described the experimental setup for BEC at Strathclyde, including the description of the laser system, double MOT optical bench setup, hybrid trap and its relation to the giant toroidal storage ring, and imaging system.

Selected methods for optimising the creation of BEC were detailed in Chapter 5. We focused on several aspects of BEC realisation, including optimisation of the magneto-optical traps and optical pumping, characterisation of the magnetic trap and analysis of the experimental evaporation cooling technique, ending with the generation of a BEC sample.

The experimental manipulation of the BEC was reported in Chapter 6, where we included description of applying optical dipole potentials for splitting BECs. In this chapter we described a scheme for producing two individual Bose condensates using a dual frequency AOM scheme for an optical plug in conjunction with magnetic levitation. By imposing side bands on the AOM RF drive a (spatial) multicomponent plug can be formed and by varying the frequency of the side bands the separation of condensates can be adjusted. Compensating the vertical acceleration due to gravity by applying a bias magnetic field and gradient we were able to perform the first atom interferometry experiments at Strathclyde. The interference pattern was analysed using Fourier processing, where two methods of straightening the fringes were detailed. We also provided a theoretical analysis of the effect of the magnetic fields on the fringe spacing with and without atomic interactions. We touched on a few aspects of the giant storage ring for cold atoms and BECs. Additionally, we have begun investigate the experimental noise in the Strathclyde experimental BEC setup.

Finally in this chapter possible improvements of the existing Strathclyde BEC apparatus are reviewed, and possible directions for future prospects are discussed.

## 7.2 Improvements and future prospects

The existing problem with spatial fluctuations of the BEC opens possibilities of improving the experimental setup. As the experiment experienced an evidence of the current coils cross-talk we analysed the existing setup and in this section we give a possible solution, which removes the current cross-talk between the coils. In Sec. 4.5 we presented the existing schematic of the coil configuration and current controllers. Here, in Fig. 7.1 we present the improved version of this schematic.

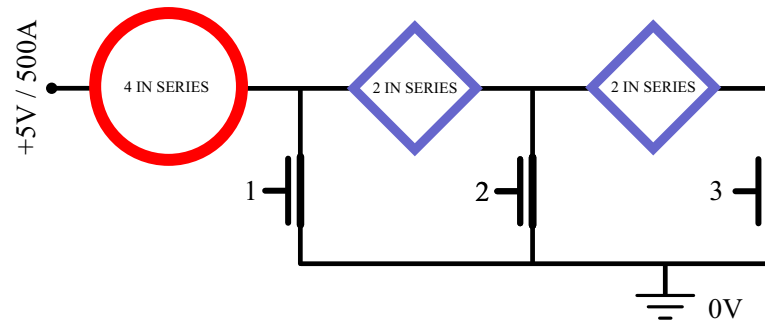


Figure 7.1: A prospective option for simplifying the coils setup. Three MOSFET banks instead of the existing five would clarify the setup and possibly get rid of the current cross-talks between the coils.

The simplification of the existing coil setup consists of separation of the current controller (set of MOSFETs) for the individual coils. The existing setup does not provide enough control over the magnetic field from the hybrid trap operating in the IP/MOT configuration. The relative current in the variable orientation current coils is not a value that we can rely on. In the prospective setup one can drive the hybrid trap in the IP mode using the existing coil setup, however for the MOT mode we can add an additional field that generates an uniform field altering the magnetic field from IP to MOT-mode. This field can be obtained using the existing compensation coils from the IP configuration or extra coils that can be implemented to the experiment.

A tested new MOSFET bank could be utilised in all current controllers. The IRFP2907 MOSFET's specification (max 209 A / 10 V at continuous drain current) enables us to build a more compact bank since there is a need of using only ten of them (instead of 20) on one controlling bank. This improvement can be applied in the future to gain more space on an already busy optical table.

MOSFETs are the semiconductor devices, which have threshold voltage for turning them on – typically  $\sim 3.2$  V between the gate and source. The integrator in the feedback loop in our existing current driver circuit has to integrate the signal until it reaches the threshold voltage for turning the MOSFETs on. In appendix E we present the optional current driver with adjustable voltage offset, which removes the need of using an integrator in the circuit. This coil-driver might increase the speed with which the coils can be switched on. This solution can be of further consideration when making improvements to the existing experimental setup.

The creation of spatial interference between split BECs with macroscopic separation offers a promising outlook for future atom interferometry based measurements, e.g. our degenerate gas experiments in macroscopic ring geometries [49, 47]. We have in mind a prospective performance of the atom interferometry with controlled phase by forming condensates with a weak link (due to lower dipole beam power) and raising the barrier between condensates immediately before interferometric experiments. We will also carry out experiments with the plug's RF spectrum altered to create BECs in multiple wells – an ‘optical fork’ for BECs, toward the limit of a 1D optical lattice with dynamic spacing. A weak carrier and small separation between dipole beams will also allow the formation of a three-well BEC, ideal for ‘STIRAP’ experiments [155] transferring a BEC from the left quantum well (say) to the right quantum well, effectively bypassing the second quantum well.

## Appendix – Magnetic fields

### A.1 Magnetic field from square coils

Let define a segment of wire along the  $x$  axis with length  $2x_0 = 2a$  (having ends at the positions  $(\pm x_0, 0, 0)$ ) by

$$\mathbf{l} = \{x_0, 0, 0\} \longrightarrow d\mathbf{l} = \{dx_0, 0, 0\},$$

$$\mathbf{r} = \{x - x_0, y, z\} \longrightarrow |\mathbf{r}| = \sqrt{(x - x_0)^2 + y^2 + z^2},$$

to obtain the magnetic field in the form:

$$\mathbf{B} = \frac{\mu_0 I}{4\pi} \int_{x_0=-a}^{x_0=a} \frac{d\mathbf{l} \times \mathbf{r}}{|\mathbf{r}|^3} = \frac{\mu_0 I}{4\pi} \int_{x_0=-a}^{x_0=a} \frac{\{0, -z dx_0, y dx_0\}}{\left((x - x_0)^2 + y^2 + z^2\right)^{3/2}} \quad (\text{A.1})$$

$$= \frac{\mu_0 I}{4\pi} \{0, -z, y\} \int_{x_0=-a}^{x_0=a} \frac{dx_0}{\left((x - x_0)^2 + y^2 + z^2\right)^{3/2}}. \quad (\text{A.2})$$

Making a substitution

$$(x - x_0) = \sqrt{y^2 + z^2} \tan \theta \longrightarrow -dx_0 = \sqrt{y^2 + z^2} (d \tan \theta),$$

where  $d \tan \theta = \sec^2 \theta d\theta$ , the magnetic field is represented as:

$$\mathbf{B} = \frac{\mu_0 I}{4\pi} \{0, -z, y\} \int_{\theta_{-a}}^{\theta_a} \frac{-\sec^2 \theta d\theta}{\left((y^2 + z^2) (1 + \tan^2 \theta)\right)^{3/2}} \quad (\text{A.3})$$

$$= \frac{\mu_0 I}{4\pi} \{0, -z, y\} \frac{1}{y^2 + z^2} \int_{\theta_{-a}}^{\theta_a} (-\cos \theta d\theta) \quad (\text{A.4})$$

$$= \frac{\mu_0 I}{4\pi} \{0, -z, y\} \frac{1}{y^2 + z^2} (-\sin \theta_a + \sin \theta_{-a}) \quad (\text{A.5})$$

We can rearrange the above equation using  $\sin \theta = \frac{x-x_0}{\sqrt{((x-x_0)^2+y^2+z^2)}}$ , and hence the magnetic field from a finite segment of the wire placed along the  $x$  axis takes the form:

$$\mathbf{B} = \mathbf{B}_{\text{Seg}[x]} = \frac{\mu_0 I}{4\pi} \{0, -z, y\} \frac{1}{y^2 + z^2} \left[ -\frac{x-a}{\sqrt{(x-x_0)^2 + y^2 + z^2}} + \frac{x+a}{\sqrt{(x-x_0)^2 + y^2 + z^2}} \right]. \quad (\text{A.6})$$

We can write similarly to Eq. A.6 another possible position of the single finite wire

$$\mathbf{B}_{\text{Seg}[y]} = \frac{\mu_0 I}{4\pi} \{z, 0, -x\} \frac{1}{x^2 + z^2} \left[ -\frac{y-a}{\sqrt{x^2 + (y+a)^2 + z^2}} + \frac{y+a}{\sqrt{x^2 + (y+a)^2 + z^2}} \right], \quad (\text{A.7})$$

for a segment of wire along the  $y$  axis with length  $2a$ , and

$$\mathbf{B}_{\text{Seg}[z]} = \frac{\mu_0 I}{4\pi} \{-x, y, 0\} \frac{1}{x^2 + y^2} \left[ -\frac{z-a}{\sqrt{x^2 + y^2 + (z+a)^2}} + \frac{z+a}{\sqrt{x^2 + y^2 + (z+a)^2}} \right], \quad (\text{A.8})$$

for a segment of wire along the  $z$  axis with length  $2a$ . The magnetic field for a square single coil can be composed using four contributions from straight finite wires. For four wire segments with length  $2a$  each in the  $xy$  plane in cartesian coordinates there are four contributions:

$$\begin{aligned} S_i &: (x+a, 0, 0)_{\text{Seg}[y]} & S_{ii} &: (0, y+a, 0)_{\text{Seg}[x]} \\ S_{iii} &: (x-a, 0, 0)_{\text{Seg}[y]} & S_{iv} &: (0, y-a, 0)_{\text{Seg}[x]} \end{aligned} \quad (\text{A.9})$$

Using the above coordinates and Eqs. A.6-A.8 the resulting magnetic field from the square coil takes the form:

$$\begin{aligned} B_x = \frac{\mu_0 I z}{4\pi} & \left[ (z^2 + (x+a)^2)^{-1} \left( -\frac{y+a}{\sqrt{(x+a)^2 + (y+a) + z^2}} - \frac{y-a}{\sqrt{(x+a)^2 + (y-a) + z^2}} \right) + \right. \\ & \left. (z^2 + (x-a)^2)^{-1} \left( \frac{y+a}{\sqrt{(x-a)^2 + (y+a) + z^2}} - \frac{y-a}{\sqrt{(x-a)^2 + (y-a) + z^2}} \right) \right], \end{aligned} \quad (\text{A.10})$$

$$\begin{aligned} B_y = \frac{\mu_0 I z}{4\pi} & \left[ (z^2 + (y-a)^2)^{-1} \left( \frac{x+a}{\sqrt{(x+a)^2 + (y-a) + z^2}} - \frac{x-a}{\sqrt{(x-a)^2 + (y-a) + z^2}} \right) - \right. \\ & \left. (z^2 + (y+a)^2)^{-1} \left( \frac{x+a}{\sqrt{(x+a)^2 + (y+a) + z^2}} - \frac{x-a}{\sqrt{(x-a)^2 + (y+a) + z^2}} \right) \right], \end{aligned} \quad (\text{A.11})$$

$$\begin{aligned}
B_z = & \frac{\mu_0 I}{4\pi} [(y+a)(z^2+(y+a)^2)^{-1} \left( \frac{x+a}{\sqrt{(x+a)^2+(y+a)+z^2}} - \frac{x-a}{\sqrt{(x-a)^2+(y+a)+z^2}} \right) + \\
& (x+a)(z^2+(x+a)^2)^{-1} \left( \frac{y+a}{\sqrt{(x+a)^2+(y+a)+z^2}} - \frac{y-a}{\sqrt{(x+a)^2+(y-a)+z^2}} \right) - \\
& (y-a)(z^2+(y-a)^2)^{-1} \left( \frac{x+a}{\sqrt{(x+a)^2+(y-a)+z^2}} - \frac{x-a}{\sqrt{(x-a)^2+(y-a)+z^2}} \right) - \\
& (x-a)(z^2+(x-a)^2)^{-1} \left( \frac{y+a}{\sqrt{(x-a)^2+(y+a)+z^2}} - \frac{y-a}{\sqrt{(x-a)^2+(y-a)+z^2}} \right)].
\end{aligned} \tag{A.12}$$

## A.2 Magnetic field equations - current loops

In Cartesian coordinates the magnetic field from a single current loop (radius  $a$ ) can be represented as:

$$B_x = \frac{\mu_0 I x z}{2\pi\alpha^2\beta\rho^2} [(a^2+r^2)E(m) - \alpha^2 K(m)] , \tag{A.13}$$

$$B_y = \frac{\mu_0 I y z}{2\pi\alpha^2\beta\rho^2} [(a^2+r^2)E(m) - \alpha^2 K(m)] = \frac{y}{x} B_x , \tag{A.14}$$

$$B_z = \frac{\mu_0 I x z}{2\pi\alpha^2\beta} [(a^2-r^2)E(m) + \alpha^2 K(m)] , \tag{A.15}$$

where  $K(m)$  and  $E(m)$  are complete elliptic integrals of the first and second kind respectively.

$$K(m) = \int_0^{\frac{\pi}{2}} \frac{d\theta}{\sqrt{1-m\sin^2\theta}} , \tag{A.16}$$

$$E(m) = \int_0^{\frac{\pi}{2}} d\theta \sqrt{1-m\sin^2\theta} . \tag{A.17}$$

The elliptic integral argument  $m$  is in the form:

$$m = \frac{4ar \sin \theta}{a^2 + r^2 + 2ar \sin \theta} . \tag{A.18}$$

The spatial derivatives of the magnetic field components are as following: (for simplifying the relations the following substitutions are used:  $r^2 \equiv x^2 + y^2 + z^2$ ,  $\rho^2 \equiv x^2 + y^2$ ,  $\alpha^2 \equiv a^2 + \rho^2 + z^2 - 2a\rho$ ,  $\beta^2 \equiv a^2 + \rho^2 + z^2 + 2a\rho$ ,  $m = 1 - \alpha^2/\beta^2$ ,  $\zeta = x^2 - y^2$ ).

$$\frac{\partial B_x}{\partial x} = \frac{\mu_0 I z}{2\pi\alpha^4\beta^3\rho^4} \{ [a^4(-\zeta(3z^2+a^2) + \rho^2(8x^2-y^2)) -$$

$$\begin{aligned}
& a^2(\rho^4(5x^2 + y^2) - 2\rho^2 z^2(2x^2 + y^2) + 3z^4\zeta) - \\
& r^4(2x^4 + \zeta(y^2 + z^2))]E(m) + \\
& [a^2(\zeta(a^2 + 2z^2) - \rho^2(3x^2 - 2y^2)) + r^2(2x^4 + \zeta(y^2 + z^2))] \alpha^2 K(m) \} \text{A.19}
\end{aligned}$$

$$\begin{aligned}
\frac{\partial B_x}{\partial y} &= \frac{\mu_0 I x y z}{2\pi \alpha^4 \beta^3 \rho^4} \{ [3a^4(3\rho^2 - 2z^2) - r^4(2r^2 + \rho^2) - \\
& 2a^6 - 2a^2(2\rho^4 - \rho^2 z^2 + 3z^4)] E(m) + \\
& (r^2(2r^2 + \rho^2) - a^2(5\rho^2 - 4z^2) + 2a^4) \alpha^2 K(m) \} \quad \text{(A.20)}
\end{aligned}$$

$$\begin{aligned}
\frac{\partial B_x}{\partial z} &= \frac{\mu_0 I x}{2\pi \alpha^4 \beta^3 \rho^2} \{ [(\rho^2 - a^2)^2(\rho^2 + a^2) + \\
& 2z^2(a^4 - 6a^2\rho^2 + \rho^4) + z^4(a^2 + \rho^2)] E(m) - \\
& ((\rho^2 - a^2)^2 + z^2(\rho^2 + a^2)) \alpha^2 K(m) \} \quad \text{(A.21)}
\end{aligned}$$

$$\begin{aligned}
\frac{\partial B_y}{\partial x} &= \frac{\mu_0 I x y z}{2\pi \alpha^4 \beta^3 \rho^4} \{ [3a^4(3\rho^2 - 2z^2) - r^4(2r^2 + \rho^2) - \\
& 2a^6 - 2a^2(2\rho^4 - \rho^2 z^2 + 3z^4)] E(m) + \\
& (r^2(2r^2 + \rho^2) - a^2(5\rho^2 - 4z^2) + 2a^4) \alpha^2 K(m) \} = \frac{\partial B_x}{\partial y} \quad \text{(A.22)}
\end{aligned}$$

$$\begin{aligned}
\frac{\partial B_y}{\partial y} &= \frac{\mu_0 I z}{2\pi \alpha^4 \beta^3 \rho^4} \{ [a^4(\zeta(3z^2 + a^2) + \rho^2(8y^2 - x^2)) - \\
& a^2(\rho^4(5y^2 + x^2) - 2\rho^2 z^2(2y^2 + x^2) - 3z^4\zeta) - \\
& r^4(2y^4 - \zeta(x^2 + z^2))] E(m) + \\
& [a^2(-\zeta(a^2 + 2z^2) - \rho^2(3y^2 - 2x^2)) + r^2(2y^4 - \zeta(x^2 + z^2))] \alpha^2 K(m) \} \quad \text{(A.23)}
\end{aligned}$$

$$\begin{aligned}
\frac{\partial B_y}{\partial z} &= \frac{\mu_0 I x}{2\pi \alpha^4 \beta^3 \rho^2} \{ [(\rho^2 - a^2)^2(\rho^2 + a^2) + \\
& 2z^2(a^4 - 6a^2\rho^2 + \rho^4) + z^4(a^2 + \rho^2)] E(m) - \\
& ((\rho^2 - a^2)^2 + z^2(\rho^2 + a^2)) \alpha^2 K(m) \} = \frac{y}{x} \frac{\partial B_x}{\partial z} \quad \text{(A.24)}
\end{aligned}$$

$$\begin{aligned}
\frac{\partial B_z}{\partial x} &= \frac{\mu_0 I x}{2\pi \alpha^4 \beta^3 \rho^2} \{ [(\rho^2 - a^2)^2(\rho^2 + a^2) + \\
& 2z^2(a^4 - 6a^2\rho^2 + \rho^4) + z^4(a^2 + \rho^2)] E(m) - \\
& ((\rho^2 - a^2)^2 + z^2(\rho^2 + a^2)) \alpha^2 K(m) \} = \frac{\partial B_x}{\partial z} \quad \text{(A.25)}
\end{aligned}$$

$$\begin{aligned} \frac{\partial B_z}{\partial y} = & \frac{\mu_0 I x}{2\pi\alpha^4\beta^3\rho^2} \{ [(\rho^2 - a^2)^2(\rho^2 + a^2) + \\ & 2z^2(a^4 - 6a^2\rho^2 + \rho^4) + z^4(a^2 + \rho^2)] E(m) - \\ & ((\rho^2 - a^2)^2 + z^2(\rho^2 + a^2))\alpha^2 K(m) \} = \frac{\partial B_y}{\partial z} \end{aligned} \quad (\text{A.26})$$

$$\frac{\partial B_z}{\partial z} = \frac{\mu_0 I z}{2\pi\alpha^4\beta^3} \{ [6a^2(\rho^2 - z^2) - 7a^4 + r^4] + a^2(a^2 - r^2)K(m) \}$$

# Appendix – Time-averaged orbiting potential

## B.1 Time-averaged orbiting potential magnetic traps

As explained in Sec. 3.2.1 the weak field seeking atoms are attracted to the local field minimum  $B_{\min}$ . Consider a field minimum moving with a speed matching the speed of the atomic particles. Fast enough to be never caught by atoms and at the same time slow enough to tempt atoms to move towards it. A similar mechanism is used in greyhound racing. The racing dogs are ‘chasing’ a fake rabbit without any chance of catching it. One can make the same thing happen at a smaller scale, when instead of dogs we use atoms and instead of a fake decoy we use a magnetic field minimum. By choosing the right speed of the local field minimum the atoms are not allowed to reach it preventing the lossy Majorana spin-flip process at the minimum. The path of the magnetic field minimum can be strictly specified. First of all consider a movement of the local field minimum in 2D (plane  $xy$ ). In the time-averaged orbiting potential (TOP) quadrupole magnetic trap, the magnetic field consists of two parts. The standard TOP trap combines (1) a spherical quadrupole field with (2) a time dependent bias field,  $B_{\text{bias}(t)}$ , rotating in the horizontal plane (here the  $xy$  plane). The inhomogeneous magnetic field generated by quadrupole trap configuration (see Fig. 3.6(b) for anti-Helmholtz coils configuration) near the origin of the trap can be represented in the form [156]:

$$\mathbf{B}_{\text{quad}} = B_q(x, y, -2z) \tag{B.1}$$

where  $B_q$  is the field gradient. The time dependent bias field is a second contribution to the total magnetic field  $\mathbf{B}_{\text{TOP}}$ . It takes the form of a homogenous field that rotates with angular frequency  $\omega_{\text{rot}}$  around the  $z$  axis and in the  $xy$  plane:

$$\mathbf{B}_{\text{bias}(t)} = B_0(\cos \omega_{\text{rot}}t, \sin \omega_{\text{rot}}t, 0) \quad (\text{B.2})$$

The equations B.1 and B.2 result in the total magnetic field  $\mathbf{B}_{\text{TOP}} = \mathbf{B}_{\text{quad}} + \mathbf{B}_{\text{bias}(t)}$  which has a magnitude which can be represented as:

$$\begin{aligned} B_{\text{TOP}} &= \sqrt{B_q^2 \left( x + \frac{B_0 \cos \omega t}{B_q} \right)^2 + B_q^2 \left( y + \frac{B_0 \sin \omega t}{B_q} \right)^2 + 4B_q^2 z^2}, \\ &= B_0 \underbrace{\sqrt{1 + \frac{2B_q}{B_0} (x \cos \omega t + y \sin \omega t) + \frac{B_q^2}{B_0^2} (x^2 + y^2 + 4z^2)}}_{\sqrt{1+\epsilon}}. \end{aligned} \quad (\text{B.3})$$

The time averaged potential is obtained by taking the Taylor expansion of  $B_{\text{TOP}} = B_0\sqrt{1+\epsilon}$  to second order and omitting spatial terms which time-average to zero ( $\cos(\omega t) \rightarrow 0, \sin(\omega t) \rightarrow 0$ )

$$\begin{aligned} B_{\text{TOP}} &\approx B_0 \left( 1 + \frac{\epsilon}{2} - \frac{\epsilon^2}{8} \right) \\ &= B_0 \left[ 1 + \frac{1}{2} \left( \frac{B_q^2 (x^2 + y^2 + 4z^2)}{B_0^2} \right) - \frac{1}{8} \left( \left( \frac{2B_q (x/\sqrt{2})}{B_0} \right)^2 + \left( \frac{2B_q (y/\sqrt{2})}{B_0} \right)^2 \right) \right] \\ &= B_0 + \frac{B_q^2}{4B_0} (x^2 + y^2 + 8z^2) , \end{aligned} \quad (\text{B.4})$$

making use of the relations:  $\cos^2(\omega t) = \frac{1}{2} + \frac{1}{2} \cos(2\omega t)$ ,  $\sin^2(\omega t) = \frac{1}{2} - \frac{1}{2} \cos(2\omega t)$ ,  $\cos(\omega t) \sin(\omega t) = \frac{1}{2} \sin(2\omega t)$ . When  $B_0 \neq 0$  the trap minimum is changed to  $B_0$  at the origin. That offset makes it impossible for atoms to be lost from the trap by reaching field minimum. The effective potential for the TOP trap takes form:

$$U(x, y, z) = \mu_B g_F m_F \left[ B_0 + \frac{B_q^2}{4B_0} (x^2 + y^2 + 8z^2) \right] , \quad (\text{B.5})$$

and its graphical representation for an atom like  $^{87}\text{Rb}$  is considered, which is trapped in a state with: Fig. B.1(a) the total angular momentum quantum number  $F = 1$  and the corresponding magnetic quantum number  $m_F = -1$ , Fig. B.1(b) the total angular momentum quantum number  $F = 2$  and the corresponding magnetic quantum number  $m_F = 2$ .

The TOP trap has found application in many experiments. Hence the study of modified TOP trap caught researchers interest. The bias field from TOP trap was

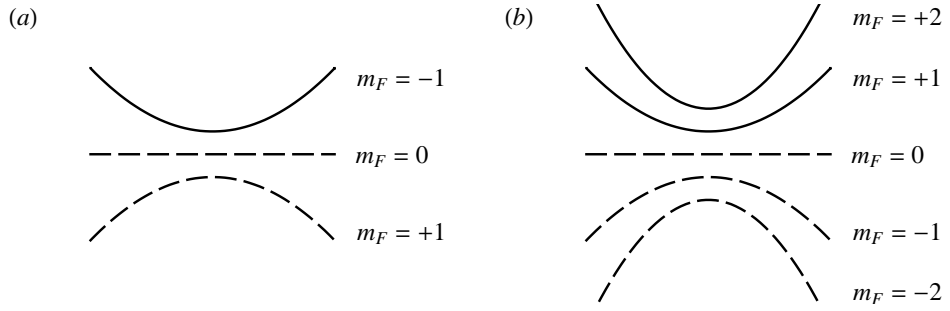


Figure B.1: The effective time-averaged orbiting potential. (a) The trapping state for the total angular momentum quantum number  $F = 1 \mapsto |1, -1\rangle$ , (b) The trapping states for the total angular momentum quantum number  $F = 2 \mapsto \{|2, 2\rangle, |2, 1\rangle\}$ . The effective potential is only parabolic for small distances from the origin, and becomes linear at large distances.

enriched by motion in the third dimension. In the literature it can be found under the name  $z$ TOP trap [86]. Adding a time dependent term to the third dimension results in a bias field oscillation in 3D space. The theoretical approach to the  $z$ TOP trap where the bias field changes in time creating a saddle shaped magnetic potential can be written in the form:

$$\mathbf{B}_{z\text{TOP}} = B_q (x\hat{\mathbf{x}} + y\hat{\mathbf{y}} - 2z\hat{\mathbf{z}}) + B_{bias(t)} (\cos(\omega_t t)\hat{\mathbf{x}} + \sin(\omega_t t)\hat{\mathbf{y}}) + B_z \cos(\omega_\tau t)\hat{\mathbf{z}}. \quad (\text{B.6})$$

The experimental application needs to ensure adiabatic motion of atoms within the trap. Hence the frequencies of the time dependent bias field have to be accurately chosen. One must move slower than the Larmor frequency, and also must be greater than the trap frequencies to prevent atoms from escaping from the trap by reaching the zero field minimum.

## Appendix – Article

This Appendix contains our journal article entitled “Spatial interference from well-separated split condensates” – published in Physical Review A.

PHYSICAL REVIEW A **81**, 043608 (2010)**Spatial interference from well-separated split condensates**

M. E. Zawadzki, P. F. Griffin, E. Riis, and A. S. Arnold\*

SUPA, Department of Physics, University of Strathclyde, Glasgow G4 0NG, United Kingdom†

(Received 10 November 2009; published 13 April 2010)

We use magnetic levitation and a variable-separation dual optical plug to obtain clear spatial interference between two condensates axially separated by up to 0.25 mm—the largest separation observed with this kind of interferometer. Clear planar fringes are observed using standard (i.e., nontomographic) resonant absorption imaging. The effect of a weak inverted parabola potential on fringe separation is observed and agrees well with theory.

DOI: 10.1103/PhysRevA.81.043608

PACS number(s): 03.75.Dg

**I. INTRODUCTION**

It has been more than a decade since Andrews and co-workers' [1] impressive demonstration of the wavelike nature of coherent matter via the spatial interference of  $^{23}\text{Na}$  Bose-Einstein condensates (BECs). Such matter-wave interference experiments are of great interest for applications in ultraprecise interferometry [2] and should lead to drastic improvements in measurements of fundamental constants as well as temporal, gravitational, and rotational sensing. Here we obtain spatial BEC interference that promises significant potential for improved measurements. We use a magnetic levitation field [3] to spatially interfere two atomic clouds with relatively large spatial separations of 0.25 mm. Moreover, we use an atomic species,  $^{87}\text{Rb}$ , with four times the mass used in Ref. [1] and, hence, a four times smaller de Broglie wavelength for the same atomic velocities. We find tomographic imaging [1] is not required, and standard absorption imaging suffices for good-contrast 60% (30%) interference at separations of  $60\ \mu\text{m}$  ( $250\ \mu\text{m}$ ). We also identify a clear relationship between the interference fringe period and the magnetic levitation time in an inverted parabola trap potential.

Experiments on atomic interference have developed rapidly in the last decade and it is now possible to interfere single particles in quantum walks using the relative population of atoms in a particular state [4]. A Ramsey-type BEC interferometer using Bragg scattering has also obtained the largest time-integrated separation in condensate interference experiments [5]. Similar advances have so far been unobtainable with “Young-type” spatial interference patterns, in which the de Broglie waves of two expanding wave packets, initially spatially separate, give rise to the interference. Condensate wave function irregularities and vortices are observable only with such spatial interferometers. Recently radial splitting of condensates [6] using rf dressed potentials [7] has become popular [Fig. 1(a)], as high-contrast spatial interference fringes can be obtained due to the “point source”-like properties of the condensates when viewed along the BEC axis. Note, however, that in the radial splitting geometry, typical chip BECs can only yield interference patterns for split distances up to  $26\ \mu\text{m}$  [8] or times of about 400 ms (for  $9\text{-}\mu\text{m}$  separation) [9]. Here we split our cigar-shaped BEC with a far-detuned optical dipole laser beam that propagates perpendicular to the BEC's

longitudinal axis [Fig. 1(b)], a geometry similar to that in Ref. [1], where interference from  $40\text{-}\mu\text{m}$  BEC separation was obtained. We use a dual optical plug [Fig. 1(c)] to extend our condensate separation from  $60$  to  $250\ \mu\text{m}$  and back, observing a visibility of 30% after an experimental time of 300 ms.

It should be stressed that if two independent condensates are formed (as in this experiment), or the splitting period is too long relative to the difference in chemical potentials of the two condensates, then the interference pattern has a random phase [1,8]. For practical interferometric applications a single condensate must be smoothly split into two condensates with a fixed relative phase [6,9,16]. In future we intend to extend our proof-of-principle interferometry into the phase-coherent regime.

**II. EXPERIMENT**

The BEC was created in the experimental setup described in detail in Ref. [10]. Our Ioffe-Pritchard magnetic trap has frequencies of 10 and 108 Hz in the axial and radial direction, respectively. Atoms are trapped in the  $|F=2, m_F=2\rangle$  trapping state, with a 40-s magnetic trap lifetime and  $5 \times 10^5$  atoms in a pure BEC. The condensate creation and manipulation were observed by standard absorption imaging. The imaging beam propagated perpendicular to the BEC axis and a  $2\times$  beam expander was used for imaging onto an Andor Luca CCD camera. The size of individual pixels is  $10\ \mu\text{m}$ , corresponding to  $5\ \mu\text{m}$  at the BEC's location.

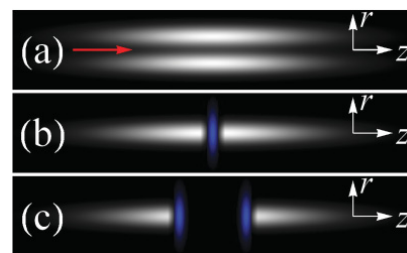


FIG. 1. (Color online) Schematic illustrating different BEC splitting geometries: (a) radial splitting using, e.g., rf dressed potentials [(red) arrow at left indicates imaging direction for fringe observation]; (b) axial splitting using a blue-detuned dipole beam; (c) the variable-separation axial splitting using dual dipole beams reported on in this paper.

\*a.arnold@phys.strath.ac.uk

†URL: www.photonics.phys.strath.ac.uk/AtomOptics/

ZAWADZKI, GRIFFIN, RIIS, AND ARNOLD

PHYSICAL REVIEW A **81**, 043608 (2010)

Our dipole beam is generated by 50 mW of light from a free-running 658-nm diode laser, far to the blue of the Rb  $D_2$  resonance at 780 nm. To create a high-intensity dipole beam we used an 80-mm-focal-length achromat lens. The elliptical diode laser beam shape was focused to beam waists of 8.8 and 13.7  $\mu\text{m}$  in the axial and radial direction, respectively. This yields a maximum potential of 30  $\mu\text{K}$  that completely isolates split condensates from each other, and tunneling effects can be neglected. The dipole beam allows fully coherent and adiabatic splitting of the BEC, with an estimated condensate photon scattering rate of 1 MHz per atom. The alignment of the dipole potential was facilitated by combining the 658-nm beam with a “tracer” 780-nm repump ( $F = 1 \rightarrow F' = 2$ ) beam [11] on a beam splitter to create a copropagating beam with a much higher scattering rate and optical potential. For all experiments in this paper the dipole beam was on throughout evaporative cooling to BECs—resulting in the creation of two independent samples of coherent matter with a random relative phase.

As acousto-optical modulators (AOMs) can vary the deflection angle and beam intensity of a dipole beam via the applied rf and power, respectively, they are a useful tool for creating arbitrary patterns in BEC experiments through the time-averaged optical dipole potential [12–14]. However, their use with BECs has largely been through red-detuned light, although blue-detuned potentials [15] offer substantially lower decoherence rates.

### III. DUAL OPTICAL PLUG

We split our blue-detuned dipole laser beam into two beams, with variable separation, via an 80-MHz AOM. As the first-order beam from an AOM is deflected proportionally to the rf drive frequency, if we use an rf spectrum consisting of multiple spectral components we can form multiple simultaneous beams [16]. Our adiabatic splitting is induced by dipole beam sidebands driven by amplitude modulation of the rf carrier frequency fed to the AOM. The amplitude modulation is obtained by mixing two frequencies, a stable carrier frequency  $\nu_0 = 80$  MHz and a variable frequency modulation signal  $0 < \nu_{\text{mod}} < 20$  MHz, yielding two tunable sidebands at  $\nu = \nu_0 \pm \nu_{\text{mod}}$ . The rf modulation frequency comes from a computer-controlled synthesized signal generator. A standard double-balanced mixer is used to mix the signal and carrier rf signals. The decrease in amplitude of the carrier frequency from the sidebands is of order 40 dB, and the carrier frequency dipole beam has a negligible effect on the atoms. The linear response of the rf drive frequency to beam deflection results in two beams at relative deflection angles  $\delta\theta = \pm 2.5$  mrad for a 20-MHz modulation frequency.

For low modulation frequencies, the two dipole beams have a good spatial overlap, effectively resulting in a single beam with a beat phenomenon at the modulation frequency; that is, the beam intensity varies in brightness sinusoidally in time with period  $T = 1/(2\nu_{\text{mod}})$ . To highlight the low heating rate of blue detuned light, we used this beating to perform an experiment similar to that in Ref. [13]: we studied heating as a function of intensity modulation frequency of the dipole beam during evaporation to a BEC. Heating was observed as the fraction of the BEC lost after rf evaporation in a double-well potential composed of the magnetic trap with a

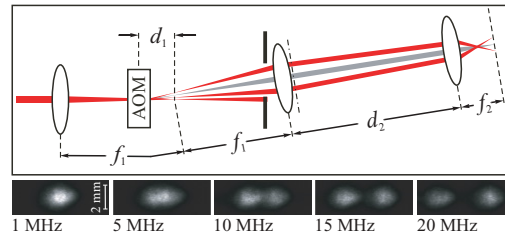


FIG. 2. (Color online) The 658-nm dipole beam path for splitting the BEC. The acousto-optical modulator (AOM) was offset by a distance  $d_1$  from the focal point of the  $1\times$  beam expander to enable output beam deflection at the beam waist after the final lens. The modulated rf carrier frequency results in two rf sidebands and a suppressed carrier, resulting in two optical beams with spatial separation determined by the rf modulation frequency as shown in the experimental beam image series.

dipole beam that had a sinusoidally modulated intensity. The main result was that no heating was observed for modulation rates greater than 1 kHz, a limit significantly lower than the 30–40 kHz in Ref. [13]. In principle the trap might be adiabatically deformable at modulation frequencies less than 1 kHz, however, because of atomic motion in the harmonic magnetic trap, care would then need to be taken that the trap modulation does not interfere with evaporation.

The position of our AOM (Fig. 2) was offset by a distance  $d_1 = 10$  cm from the focal point of a  $1\times$  beam expander comprised of two planoconvex lenses with  $f_1 = 25$  cm focal length. After a (noncritical) propagation distance  $d_2$  the beams are focused by an achromat lens with focal length  $f_2 = 8$  cm. Using standard paraxial  $ABCD$  matrices one can show that the waist after the  $f_2$  lens yields beam displacements  $\delta z = d_1 f_2 \delta\theta / f_1 = \pm 80$   $\mu\text{m}$  for a modulation frequency of 20 MHz (Fig. 2). Although the rf power in the sidebands is constant, a small drop in the optical power of the beams is observable at large displacements due to reduced AOM diffraction efficiency. The largest achievable center-of-mass (c.m.) separation of two BECs by the repulsive potential of the dipole beams was 250  $\mu\text{m}$ , with spatial interference between separated condensates still clearly observable. We believe this is the largest splitting observed in a “Young-type” spatial BEC interferometer.

### IV. FRINGES

The anisotropic character of a cigar-shaped Ioffe-Pritchard trap leads to two different expansion velocities, as the mean-field forces from a repulsive BEC are proportional to the condensate’s density gradient; hence the expansion velocity is much greater in the radial direction than the axial direction. Moreover, using a dipole beam to create a macroscopic axial separation of our matter waves, we need a concomitantly longer expansion time for BEC recombination and interference than is required for radially split BECs [6].

The fringe spacing  $\lambda$  arises from the de Broglie waves of two condensates and takes the familiar form:

$$\lambda = h/(mv), \quad (1)$$

SPATIAL INTERFERENCE FROM WELL-SEPARATED ...

PHYSICAL REVIEW A **81**, 043608 (2010)

where  $h$  is Planck's constant,  $m$  is the atomic mass, and  $v = d/t$  is the relative speed between two pointlike condensates as a function of their c.m. separation  $d$  and expansion time  $t$ . The duration of ballistic expansion in free fall is usually limited by the size of the imaging area and the dimensions of the BEC vacuum cell: times of about 100 ms lead to long drops of 49 mm, and the corresponding condensate speed of 1 m/s leads to blurred images. To eliminate the inconvenience of gravity, a "levitation" field can be used [3] whereby a magnetic field gradient counteracts the gravitational acceleration. The levitation field keeps the atoms in the region of interest for time intervals ( $t > 80$  ms) that are long enough to make our interference pattern optically resolvable.

Our levitation field is provided by the existing four circular coils that form the toroidal quadrupole field [10] of our ring Ioffe-Pritchard trap. The levitation mechanism uses the weak-field-seeking  $|2, 2\rangle$  atoms of the BEC, which are attracted to the local field minimum. After creation of a BEC in the magnetic trap by a 25-s evaporative cooling cycle, "antigravity" conditions are obtained with a vertical gradient of 15 G/cm. An additional vertical constant field is added to the quadrupole magnetic field to reduce lensing [17] in the vertical and imaging directions.

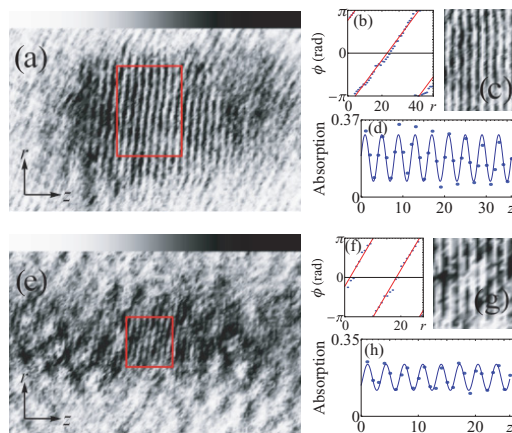


FIG. 3. (Color online) Interference patterns ( $0.8 \times 0.5 \text{ mm}^2$ ) for (a)  $60\text{-}\mu\text{m}$ -separated BECs and (e) BECs split  $60\text{-}\mu\text{m}$ – $250\text{-}\mu\text{m}$ – $60\text{-}\mu\text{m}$  over a 160-ms period. In both cases the pictures were taken after a further 135 ms of magnetic levitation, which, for (a), corresponds to the triangle in Fig. 4. The phases of the Fourier components of the fringes for the selected areas in the (red) boxes in (a) and (e) can be obtained [(blue) points in (b) and (f)] and fit with a sawtooth linear phase shift [(red) curves in (b) and (f)]. These sawtooth phase corrections can then be applied to the Fourier transform, before performing the inverse transform shown in (c) and (g). These corrected images can then be averaged over the image rows to obtain the (blue) circles in (d) and (h), with their sinusoidal fits [(blue) curves]. Absorption is measured using the natural logarithm. Each row or column (i.e., pixel) corresponds to  $5 \times 5 \mu\text{m}^2$ . The fringe period in (e) is shorter than in (a), as the condensates have a residual counterpropagating velocity after the  $250\text{-}\mu\text{m} \rightarrow 60\text{-}\mu\text{m}$  separation phase.

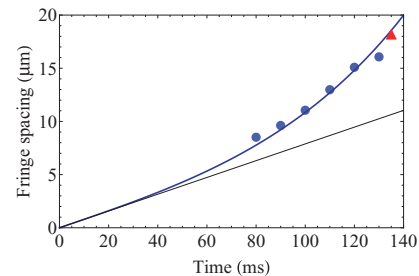


FIG. 4. (Color online) Fringe spacing as a function of levitation time. Ballistic expansion theory for  $d = 60\text{-}\mu\text{m}$ -separated BECs [diagonal (black) line] and experimental data (circles) are shown, as well as a [thick (blue)]  $\sinh(\omega t)/\omega$  curve using  $\omega = 14 \text{ rad/s}$  (a geometrical ring property), which has a  $d = 60\text{-}\mu\text{m}$  fit. The model aptly represents the fringe spacing in an inverted parabolic potential. The triangle was derived from the image Fig. 3(a).

Figure 3(a) represents an example of the high-contrast (60%) interference pattern when two BEC clouds were originally separated by  $60\text{-}\mu\text{m}$  (c.m. distance) with a single optical plug, then recombined using the levitation magnetic field. Standard (i.e., nontomographic [1]) absorption imaging is used. The interference pattern when the BEC is split from a c.m. separation of  $60\text{-}\mu\text{m}$  to one of  $250\text{-}\mu\text{m}$  over 80 ms, returned to  $60\text{-}\mu\text{m}$  separation over 80 ms, and then levitated for 150 ms has clear continuous spatial fringes with 30% contrast [Fig. 3(e)]. To straighten our experimental fringes we first obtain, for each image row, the phase of the Fourier component associated with the fringes [Figs. 3(b) and 3(f)]. We then apply a linear phase fit across all rows of the Fourier transform, before inverse Fourier transforming to obtain the images shown in Figs. 3(c) and 3(g). By averaging these corrected images over all rows, removing the background, and fitting sine curves to the experimental data, we obtain the fringes and their contrast [Figs. 3(d) and 3(h)].

Our BEC is levitated in an axial potential that is approximately an inverted parabola,  $U_z = -m\omega^2 z^2/2$ , due to

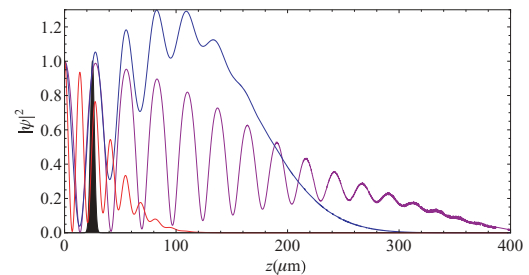


FIG. 5. (Color online) Relative theoretical probability distributions (fringes; with even symmetry about  $z = 0$ ) obtained when two Gaussian initial wave packets (black) are released for 150 ms in a potential:  $U_z = 0$  (red) and  $U_z = -m\omega^2 z^2/2$  (blue and purple curves). Interatomic repulsion is either absent (red and blue curves) or present (purple curve). Increasing the nonlinear term in the Schrödinger equation affects the width of the final distribution but not the fringe period.

ZAWADZKI, GRIFFIN, RIIS, AND ARNOLD

PHYSICAL REVIEW A **81**, 043608 (2010)

the circular nature of our toroidal quadrupole field. The magnitude of  $\omega$  corresponds to that of a rigid pendulum, that is,  $\omega = g/r = 14$  rad/s, where  $g$  is the acceleration due to gravity and  $r = 5$  cm is the radius of our ring. By solving the one-dimensional, time-dependent, Schrödinger equation (with and without a nonlinear interatomic repulsion), one can show that the fringe spacing in the potential  $U_z$  is modified from Eq. (1) to  $\lambda' = \lambda \sinh(\omega t)/\omega$ . This interference fringe spacing dependence on the levitation potential is clearly observable in the experimental fringe periodicity (Fig. 4). Theory also clearly shows that the fringe spacing is not altered by interatomic repulsion (Fig. 5). Interestingly the fringe separation has a similar dependence to that attributed to interatomic repulsion in interferometry experiments on a chip, albeit at a higher atomic density [6].

### V. CONCLUSIONS

The creation of spatial interference between split BECs with macroscopic separation offers a promising outlook for future

atom interferometry-based measurements, for example, our degenerate gas experiments in macroscopic ring geometries [10]. We intend to extend our proof-of-principle experiments and perform interferometry with a controlled phase by forming condensates with a weak link (due to a lower dipole beam power) and raising the barrier between condensates immediately before interferometric experiments. We will also carry out experiments with the plug's rf spectrum altered to create BECs in multiple wells—an “optical fork” for BECs, toward the limit of a one-dimensional optical lattice with dynamic spacing. A weak carrier and small separation between dipole beams will also allow the formation of a three-well BEC, ideal for STIRAP experiments [18] transferring a BEC from the left quantum well (say) to the right quantum well, effectively bypassing the second quantum well.

This experiment was supported by the UK EPSRC and SUPA. P.F.G. received support from the RSE/Scottish Government Marie Curie Personal Research fellowship program.

- 
- [1] M. R. Andrews, C. G. Townsend, H.-J. Miesner, D. S. Durfee, D. M. Kurn, and W. Ketterle, *Science* **275**, 637 (1997).
- [2] T. L. Gustavson, P. Bouyer, and M. A. Kasevich, *Phys. Rev. Lett.* **78**, 2046 (1997); S. Gupta, K. Dieckmann, Z. Hadzibabic, and D. E. Pritchard, *ibid.* **89**, 140401 (2002); Y.-J. Wang, D. Z. Anderson, V. M. Bright, E. A. Cornell, Q. Diot, T. Kishimoto, M. Prentiss, R. A. Saravanan, S. R. Segal, and S. Wu, *ibid.* **94**, 090405 (2005).
- [3] M. H. Anderson, J. R. Ensher, M. R. Matthews, C. E. Wieman, and E. A. Cornell, *Science* **269**, 198 (1995); D. J. Han, M. T. DePue, and D. S. Weiss, *Phys. Rev. A* **63**, 023405 (2001); T. Weber, J. Herbig, M. Mark, H.-C. Nägerl, and R. Grimm, *Science* **299**, 232 (2003).
- [4] H. Schmitz, R. Matjeschk, Ch. Schneider, J. Glueckert, M. Enderlein, T. Huber, and T. Schaetz, *Phys. Rev. Lett.* **103**, 090504 (2009); M. Karski, L. Förster, J.-Min. Choi, A. Steffen, W. Alt, D. Meschede, and A. Widera, *Science* **325**, 174 (2009).
- [5] O. Garcia, B. Deissler, K. J. Hughes, J. M. Reeves, and C. A. Sackett, *Phys. Rev. A* **74**, 031601(R) (2006); J. H. T. Burke, B. Deissler, K. J. Hughes, and C. A. Sackett, *ibid.* **78**, 023619 (2008).
- [6] T. Schumm, S. Hofferberth, L. M. Andersson, S. Wildermuth, S. Groth, I. Bar-Joseph, J. Schmiedmayer, and P. Krüger, *Nature Phys.* **1**, 57 (2005).
- [7] O. Zobay and B. M. Garraway, *Phys. Rev. Lett.* **86**, 1195 (2001); Y. Colombe, E. Knyazchyan, O. Morizot, B. Mercier, V. Lorent, and H. Perrin, *Europhys. Lett.* **67**, 593 (2004).
- [8] Y. Shin, C. Sanner, G.-B. Jo, T. A. Pasquini, M. Saba, W. Ketterle, D. E. Pritchard, M. Vengalattore, and M. Prentiss, *Phys. Rev. A* **72**, 021604(R) (2005).
- [9] G.-B. Jo, Y. Shin, S. Will, T. A. Pasquini, M. Saba, W. Ketterle, D. E. Pritchard, M. Vengalattore, and M. Prentiss, *Phys. Rev. Lett.* **98**, 030407 (2007).
- [10] A. S. Arnold, C. S. Garvie, and E. Riis, *Phys. Rev. A* **73**, 041606(R) (2006); P. F. Griffin, E. Riis, and A. S. Arnold, *ibid.* **77**, 051402(R) (2008).
- [11] K. M. O'Hara, S. R. Granade, M. E. Gehm, T. A. Savard, S. Bali, C. Freed, and J. E. Thomas, *Phys. Rev. Lett.* **82**, 4204 (1999).
- [12] R. Onofrio, D. S. Durfee, C. Raman, M. Köhl, C. E. Kuklewicz, and W. Ketterle, *Phys. Rev. Lett.* **84**, 810 (2000).
- [13] S. K. Schnelle, E. D. van Ooijen, M. J. Davis, N. R. Heckenberg, and H. Rubinsztein-Dunlop, *Opt. Express* **16**, 1405 (2008).
- [14] K. Henderson, C. Ryu, C. MacCormick, and M. G. Boshier, *New J. Phys.* **11**, 043030 (2009).
- [15] N. Houston, E. Riis, and A. S. Arnold, *J. Phys. B* **41**, 211001 (2008).
- [16] Y. Shin, M. Saba, T. A. Pasquini, W. Ketterle, D. E. Pritchard, and A. E. Leanhardt, *Phys. Rev. Lett.* **92**, 050405 (2004).
- [17] I. Bloch, M. Köhl, M. Greiner, T. W. Hänsch, and T. Esslinger, *Phys. Rev. Lett.* **87**, 030401 (2001); A. S. Arnold, C. MacCormick, and M. G. Boshier, *Phys. Rev. A* **65**, 031601(R) (2002); *J. Phys. B* **37**, 485 (2004); M. Köhl, Th. Busch, K. Mølmer, T. W. Hänsch, and T. Esslinger, *Phys. Rev. A* **72**, 063618 (2005).
- [18] M. Rab, J. H. Cole, N. G. Parker, A. D. Greentree, L. C. L. Hollenberg, and A. M. Martin, *Phys. Rev. A* **77**, 061602(R) (2008).

## Appendix – System noise

### D.1 Hot on the trail of the BEC fluctuation

In any kind of sensor it is crucial to obtain a consistent measurement. Atom interferometry as a mean of measuring tool requires a reliable performance of the wave interference pattern. Unfortunately the spatial fluctuation of the Strathclyde small interferometer prevents observation of reproducible ‘shots’ of the interference experiment. A major disruption is caused by an irreproducible turn-off of the relatively high current magnetic trap.

#### D.1.1 Spatial fluctuation

The problem we face now is a spatial fluctuation of the BEC location. When using relatively long times (for BECs) of order 100 ms the spatial fluctuation are significant when compared to the size of the BEC. The turn-off of the magnetic trap initiates ballistic expansion or magnetic levitation, hence the effect of the spatial fluctuation is seen from the moment when the atoms are released from the trap and it also gets larger with time. The vertical and horizontal final BEC locations, for several experimental runs, are shown in Fig. D.1.

The data points were taken in the pure levitation field for different levitation times 20 – 130 ms. To estimate the position of the BEC two 1D gaussians were fitted in the horizontal and vertical direction to the atomic cloud. The peak value of each gaussian was taken as the position of the centre of the atomic cloud.

To narrow down the reason of a BEC spatial fluctuation a few tests were carried on. When the spatial fluctuation gets larger with time that may suggest fluctuation of the initial conditions. The spatial fluctuation of the BEC position was narrowed down to

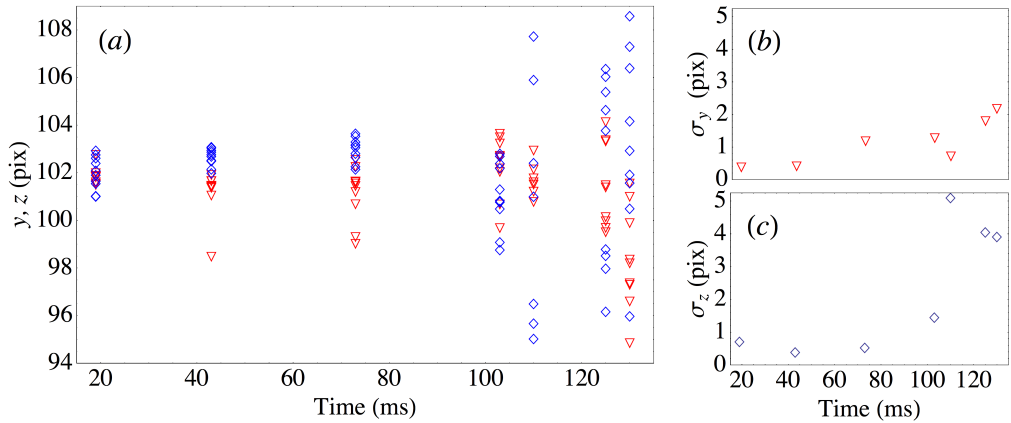


Figure D.1: The vertical fluctuation of the final position of the BEC cloud in the levitation field. The standard deviations for the data from (a) are shown in the (b) and (c) image, for vertical and horizontal data respectively.

two possibilities: (1) a current noise, (2) a magnetic gradient irregularity that changes the position of the potential that results in a velocity change and hence in a different spatial position. In the next sections we investigate these possible contributions to the spatial BEC noise.

### D.1.2 System Noise

As the atoms are ultra-sensitive to change in the electro-magnetic fields it was obligatory to check the external noise that could affect the behaviour (spatial position) of the trapped atoms. Every BEC lab utilises different power supplies that can be potentially treated as a AC current noise source. An uncontrollable time dependent oscillation field, which occurs within range of the trapped atoms might cause problems. The 50 Hz noise usually generated by the mains power supply at 230 V is sent to the different devices used in the lab and hence spreads readily in the laboratory.

#### Phase of the 50 Hz noise

In our search for the cause of the spatial fluctuations we investigated a dependence between the phase of the 50 Hz noise and the final BEC position. At the same time as recording the relative phase of the 50 Hz noise, using a trigger point from the experimental sequence (see Fig. D.2), we recorded the final position of the BEC. The trigger point ( $t = 0$ ) set always the same time interval relative to when the BEC was imaged.

The relations for horizontal and vertical displacements on the phase of the 50 Hz noise are shown, using polar plots, in Fig. D.3.

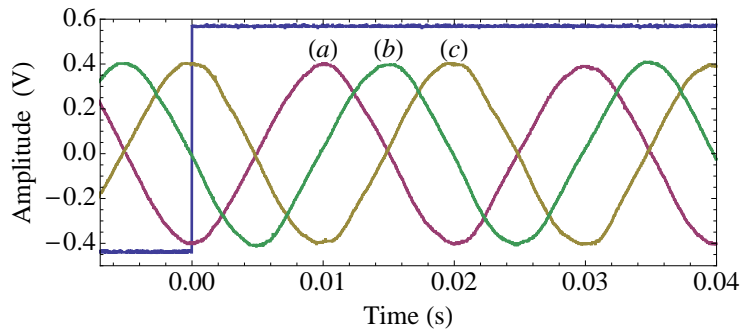


Figure D.2: The 50 Hz current noise as a reference signal for the spatial fluctuation correlation. The step function represents a trigger line that sets a reference for the phase of the 50 Hz sine signal. Each wave was recorded for a different experimental run. These are only representations of the existing phase shift, out of the 100 experimental records. For clarity three waves were chosen with different phase shift: (a)  $\phi = 0$  – no phase shift, (b)  $\phi \approx \pi/4$ , (c)  $\phi \approx \pi$ .

In order to see spatial fluctuation of the BEC (more clearly) it was dropped for 28 ms. The position of the BEC was calculated by finding the 1D gaussian fit to the axial and radial coordinates. The peak of the gaussian was chosen to be the centre of the cloud. Polar plots (see Fig. D.3) reveal that there is no correlation between the phase of the 50 Hz noise and the BEC position.

### D.1.3 Current irregularity

After finding that there is no correlation between the 50 Hz noise and spatial fluctuation, the problem seemed to be originating from the magnetic field irregularity and the magnetic field turn off was examined.

One unwanted effect was discovered when monitoring the current on the sense resistors connected with the Hall effect sensors. The hybrid configuration of the magnetic trap allowed random surges of the current from one coil to the other during the turn off. Especially this effect was seen on the torus coils as they are permanently placed in the current flow loop (see Fig. 4.12). An example of this effect is shown in Fig. D.4.

The blue trace was recorded when the toroidal coils were run by themselves, whereas the red trace, with the current injection feature during the current switch off, corre-

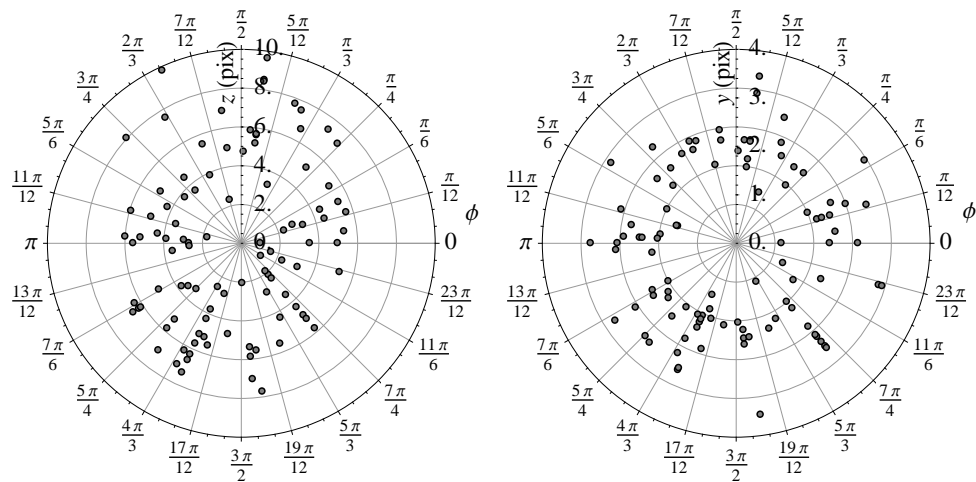


Figure D.3: Polar plot representation of the 50 Hz noise phase shift dependence on BEC final position. The position of the BEC is given in a relative pixels.

sponding to the configuration of IP and torus operating together. The typical values used for levitation experiments were  $\approx 0.55$  V that corresponds to  $\approx 35$  A current in the coils. The smooth switch on and off is very important as any magnetic field perturbation may affect the BEC itself and also its position after the ballistic expansion.

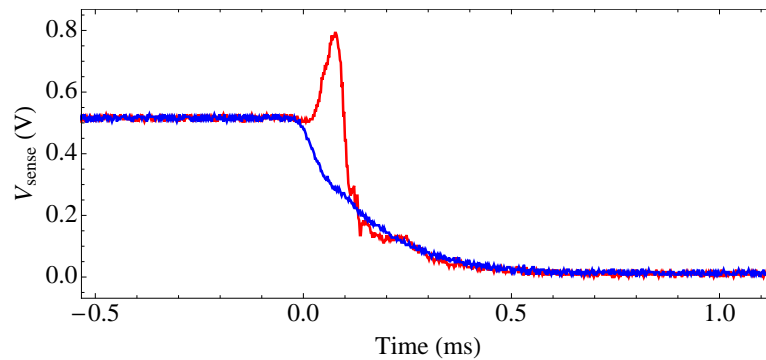


Figure D.4: Current surge visible when monitoring the current flow on the sense resistor from the Hall effect probe. The blue trace presents the current flow when only toroidal coils are in operation and when they are switched off at time 0. The red trace was recorded when the IP coils were in operation together with the toroidal coils. The ‘talk’ between the coils is seen in the shape of the peak that corresponds to the additional current surge.

The surge of current was removed by altering the time constant of the torus driving circuit and also by changing the parameters responsible for turn off ramp from the DAC. However it showed that the cross-talk between the coils might be a serious problem for our future atom interferometry measurements.

To date we have no experimental solution ready, however we know how to fix the existing problem. We would like to mention that there is a way of rearranging the coils setup and the current driver, in a way that enhances experimental control. However it requires more time and hence we only limit ourselves to the discussion and description of the possible prospect setup. In Sec. 7 we included the schematic of how the setup can be altered avoiding any current cross-talks between the coils. The details of the experimental circuit setup can be found in Appendix E.

## Appendix – Electronic circuits

### E.1 RF switch controlling circuit

The dipole beam control was based on the digital signal from the computer, which was converted into an analog line using a digital-analog converter. The analog line fed to the double-balanced mixer that acted as a switch for the carrier frequency.

Typical current requirement of the RF switch is of order  $\sim 25$  mA. The 5 mA DAC voltage was converted to a 25 mA signal that controls the RF switch connected to the AOM. We built a circuit that enabled a fine tuning of the signal directed to the switch. The circuit was based on a differential amplifier with an adjustable offset, as shown in Fig. E.1.

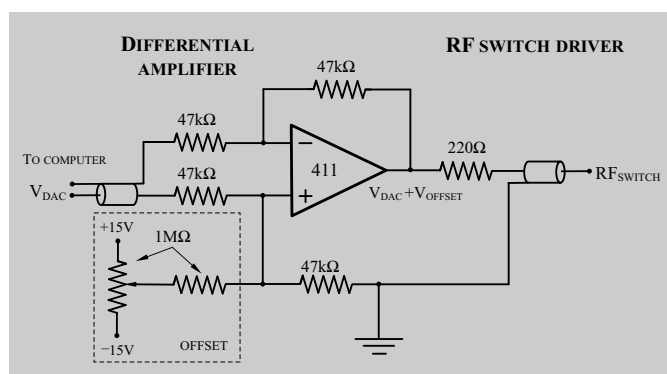


Figure E.1: The circuit diagram for the dipole beam RF switch controlling signal. 411=LF 411 Low Offset, Low Drift JFET Input Operational Amplifier (typical output source current 25 mA at 25°C). The 5 mA DAC voltage was converted to a 25 mA signal that controls the RF switch connected to the AOM. The offset voltage was used for fine tuning of the AOM controller.

## E.2 Proposed MOSFET bank driver

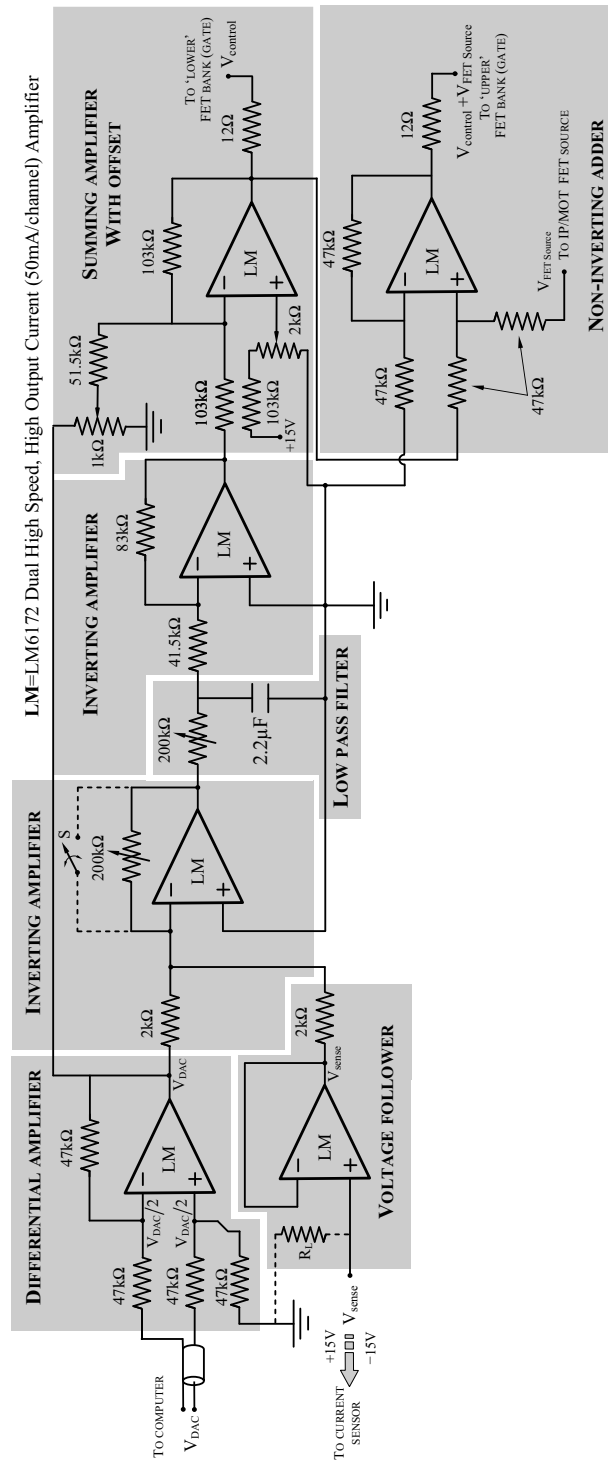
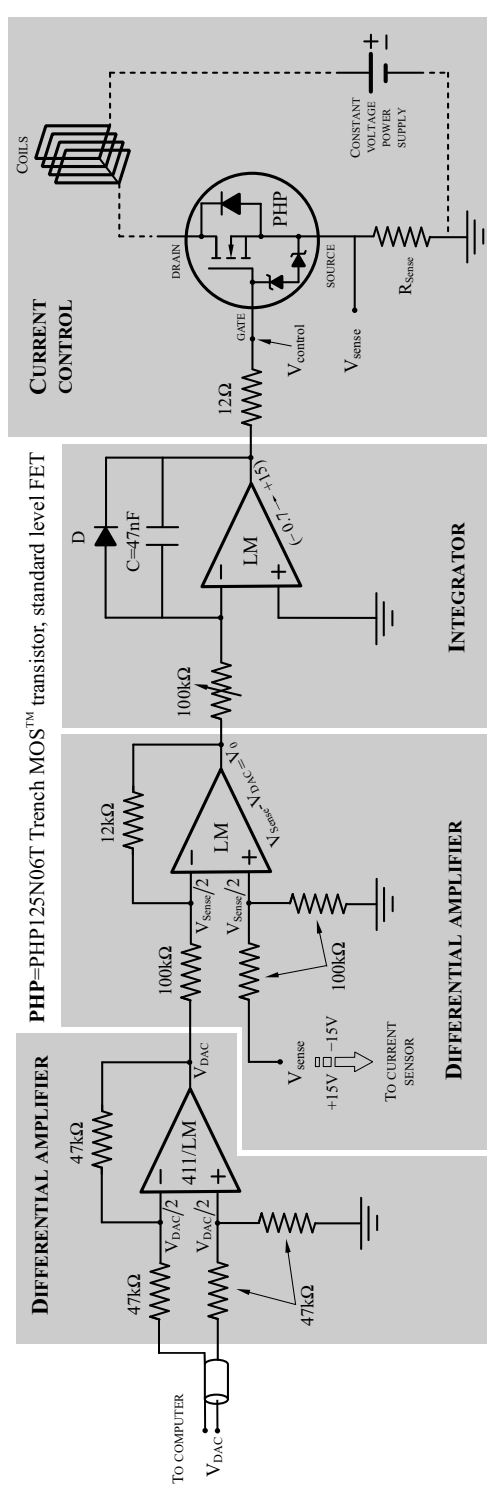


Figure E.2: The proposed coil-driver circuit diagram

The feed forward loop provides the offset to the  $V_{control}$ , that increases the speed with which the coils can be switched on. The optional switch ( $S$ ) can be used to set the gain to minimum and hence simplify the adjustments to the circuit. The optional load resistor  $R_L$  can be added to avoid instability due to strong feedback when driving high capacity load.



### E.4 The coil-driver electronic circuit



**411**=LF411CN Single Op-amp    **D**=1N 4002 Silicon Diode (100V, 1A)    **LM**=LM6172 Dual High Speed, High Output Current (50mA/channel) Amplifier

The circuit controls the bias compensation coils from the IP coils. Similar circuits are used for the three coil-drivers for the bias coils. The filtering capacitors (100 nF and 22 nF) were placed in parallel across the  $\pm 15$  V, 200 mA supply to decrease noise. The silicon diode was used to prevent the control voltage becoming more than 0.7 V negative. Two PHP125N06T MOSFETs were placed in parallel to make more efficient power dissipation and provide reliable current switching. In order to obtain efficient dissipation of energy generated by the sense resistor and MOSFETs the circuit was built on a heatsink. For maximum heat transfer a heat sink compound was applied between the resistor base (MOSFET base) and heat sink chassis mounting surface.

Figure E.4: The coil-driver electronic circuit diagram.

# Bibliography

- [1] *Bose-Einstein Condensation*, A. Griffin, D. W. Snoke, and S. Stringari, eds., (Cambridge Uni. Press, Cambridge, 1996).
- [2] S. Bose, *Z. Phys.* **26**, 178 (1924).
- [3] A. Einstein, *Sitz. Preuss. Akad. Wiss* p. 261 (1924).
- [4] F. Dalfovo, S. Giorgini, and L. P. Pitaevskii, “Theory of Bose-Einstein condensation in trapped gasses,” *Rev. Mod. Phys.* **71**, 463 (1999).
- [5] *Bose-Einstein Condensation in Dilute Gases*, C. J. Pethick and H. Smith, eds., (Cambridge Uni. Press, Cambridge, 2002).
- [6] V. Bagnato, D. E. Pritchard, and D. Kleppner, “Bose-Einstein condensation in an external potential,” *Phys. Rev. A* **35**, 4354 (1987).
- [7] *Laser Cooling and Trapping*, H. J. Metcalf and P. van der Straten, eds., (Springer-Verlag, New York, 1999).
- [8] *Statistical Thermodynamics*, E. Schrödinger, ed., (Cambridge Uni. Press, Cambridge, 1952).
- [9] G. Taubes, “Hot on the trail of a cold mystery,” *Science* **265**, 184 (1994).
- [10] M. H. Anderson, J. R. Ensher, M. R. Matthews, C. E. Wieman, and E. A. Cornell, “Observation of Bose-Einstein condensation in a dilute atomic vapor,” *Science* **269**, 198 (1995).

- [11] K. B. Davis, M.-O. Mewes, M. R. Andrews, N. J. van Druten, D. S. Durfee, D. M. Kurn, and W. Ketterle, “Bose-Einstein condensation in a gas of sodium atoms,” *Phys. Rev. Lett.* **75**, 3969 (1995).
- [12] C. C. Bradley, C. A. Sackett, and R. G. Hulet, “Bose-Einstein Condensation of Lithium: Observation of Limited Condensate Number,” *Phys. Rev. Lett.* **78**, 985 (1997).
- [13] S. Cornish, N. Claussen, J. Roberts, E. Cornell, and C. Wieman, “Stable  $^{85}\text{Rb}$  Bose-Einstein Condensates with Widely Tunable Interactions,” *Phys. Rev. Lett.* **85**, 1795 (2000).
- [14] G. Modugno, G. Ferrari, G. Roati, R. J. Brecha, A. Simoni, and M. Inguscio, “Bose-Einstein Condensation of Potassium Atoms by Sympathetic Cooling,” *Science* **294**, 1320 (2001).
- [15] G. Roati, M. Zaccanti, C. D’Errico, J. Catani, M. Modugno, A. Simoni, M. Inguscio, and G. Modugno, “ $^{39}\text{K}$  Bose-Einstein condensate with tunable interactions,” *Phys. Rev. Lett.* **99**, 010403 (2007).
- [16] T. Weber, J. Herbig, M. Mark, H.-C. Nägerl, and R. Grimm, “Bose-Einstein condensation of cesium,” *Science* **299**, 232 (2003).
- [17] D. G. Fried, T. C. Killian, L. Willmann, D. Landhuis, S. C. Moss, D. Kleppner, and T. J. Greytak, “Bose-Einstein condensation of atomic hydrogen,” *Phys. Rev. Lett.* **81**, 3811 (1998).
- [18] A. Robert, O. Sirjean, A. Browaeys, J. Poupard, S. Nowak, D. Boiron, and C. W. A. Aspect, “Bose-Einstein condensation of potassium atoms by sympathetic cooling,” *Science* **292**, 461 (2001).
- [19] A. Griesmaier, J. Werner, S. Hensler, J. Stuhler, and T. Pfau, “Bose-Einstein condensation of chromium,” *Phys. Rev. Lett.* **94**, 160401 (2005).
- [20] S. Kraft, F. Vogt, O. Appel, F. Riehle, and U. Sterr, “Condensation of alkaline earth atoms:  $^{40}\text{Ca}$ ,” *Phys. Rev. Lett.* **103**, 130401 (2009).
- [21] S. Stellmer, M. K. Tey, B. Huang, R. Grimm, and F. Schreck, “Bose-Einstein condensation of strontium,” *Phys. Rev. Lett.* **103**, 200401 (2009).

- [22] Y. Takasu, K. Maki, K. Komori, T. Takano, M. K. K. Honda, T. Yabuzaki, and Y. Takahashi, “Spin-singlet Bose-Einstein condensation of two-electron atoms,” *Phys. Rev. Lett.* **91**, 040404 (2003).
- [23] T. Fukuhara, Y. Takasu, S. Sugawa, and Y. Takahashi, “Quantum degenerate Fermi gases of ytterbium atoms,” *J. of Low Temp. Phys.* **148**, 441 (2007).
- [24] T. W. Hänsch and A. L. Schawlow, “Cooling of gases by laser radiation,” *Opt. Commun.* **13**, 68 (1975).
- [25] D. Wineland and H. Dehmelt, “Principles of the stored ion calorimeter,” *J. Appl. Phys.* **46**, 919 (1975).
- [26] S. Chu, L. Hollberg, J. E. Bjorkholm, A. Cable, and A. Ashkin, “Three-dimensional viscous confinement and cooling of atoms by resonance radiation pressure,” *Phys. Rev. Lett.* **55**, 48 (1985).
- [27] E. L. Raab, M. Prentiss, A. Cable, S. Chu, and D. E. Pritchard, “Trapping of neutral sodium atoms with radiation pressure,” *Phys. Rev. Lett.* **59**, 2631 (1987).
- [28] D. E. Pritchard, “Cooling neutral atoms in a magnetic trap for precision spectroscopy,” *Phys. Rev. Lett.* **51**, 1336 (1983).
- [29] F. Riehle, T. Kisters, A. Witte, J. Helmcke, and C. J. Bordé, “Optical Ramsey spectroscopy in a rotating frame: Sagnac effect in a matter-wave interferometer,” *Phys. Rev. Lett.* **67**, 177 (1991).
- [30] M. Kasevich and S. Chu, “Atomic interferometry using stimulated Raman transitions,” *Phys. Rev. Lett.* **67**, 181 (1991).
- [31] D. W. Keith, C. R. Ekstrom, Q. A. Turchette, and D. E. Pritchard, “An interferometer for atoms,” *Phys. Rev. Lett.* **66**, 2693 (1991).
- [32] O. Carnal and J. Mlynek, “Young’s double-slit experiment with atoms: A simple atom interferometer,” *Phys. Rev. Lett.* **66**, 2689 (1991).
- [33] A. Peters, K. Y. Chung, B. Young, J. Hensley, and S. Chu, “Precision atom interferometry,” *Philos. Trans. R. Soc. London, Ser. A* **355**, 2223 (1997).
- [34] B. P. Anderson and M. A. Kasevich, “Macroscopic quantum interference from atomic tunnel arrays,” *Science* **282**, 1686 (1998).

- [35] A. Lenef, T. D. Hammond, E. T. Smith, M. S. Chapman, R. A. Rubenstein, and D. E. Pritchard, “Rotation sensing with an atom interferometer,” *Phys. Rev. Lett.* **78**, 760 (1997).
- [36] T. L. Gustavson, P. Bouyer, and M. A. Kasevich, “Precision rotation measurements with an atom interferometer gyroscope,” *Phys. Rev. Lett.* **78**, 2046 (1997).
- [37] S. Gupta, K. Dieckmann, Z. Hadzibabic, and D. E. Pritchard, “Contrast interferometry using Bose-Einstein condensates to measure  $h/m$  and  $\alpha$ ,” *Phys. Rev. Lett.* **89**, 140401 (2002).
- [38] M. S. Chapman, T. D. Hammond, A. Lenef, J. Schmiedmayer, R. A. Rubenstein, E. T. Smith, and D. E. Pritchard, “Photon scattering from atoms in an atom interferometer: coherence lost and regained,” *Phys. Rev. Lett.* **75**, 3783 (1995).
- [39] C. Ekstrom, J. Schmiedmayer, M. S. Chapman, T. D. Hammond, and D. E. Pritchard, “Measurement of the electric polarizability of sodium with an atom interferometer,” *Phys. Rev. A* **51**, 3883 (1995).
- [40] *Atom Interferometry*, P. R. Bergman, ed., (Academic Press, New York, 1997).
- [41] F. M. H. Crompvoets, H. L. Bethlem, R. T. Jongma, and G. Meijer, “A prototype storage ring for neutral molecules,” *Nature* **411**, 174 (2001).
- [42] J. A. Sauer, M. D. Barrett, and M. S. Chapman, “Storage ring for neutral atoms,” *Phys. Rev. Lett.* **87**, 270401 (2001).
- [43] S. Wu, W. Rooijakkers, P. Striehl, and M. Prentiss, “Bidirectional propagation of cold atoms in a “stadium”-shaped magnetic guide,” *Phys. Rev. A* **70**, 013409 (2004).
- [44] S. Gupta, K. W. Murch, K. L. Moore, T. P. Purdy, and D. M. Stamper-Kurn, “Bose-Einstein condensation in a circular waveguide,” *Phys. Rev. Lett.* **95**, 143201 (2005).
- [45] M. B. Crookston, P. M. Baker, and M. P. Robinson, “A microchip ring trap for cold atoms,” *J. Phys. B* **38**, 3289 (2005).
- [46] O. Morizot, Y. Colombe, V. Lorent, H. Perrin, and B. M. Garraway, “Ring trap for ultracold atoms,” *Phys. Rev. A* **74**, 023617 (2006).

- [47] A. S. Arnold, C. S. Garvie, and E. Riis, “Large magnetic storage ring for Bose-Einstein condensates,” *Phys. Rev. A* **73**, 041606(R) (2006).
- [48] W. H. Heathcote, E. Nugent, B. T. Sheard, and C. J. Foot, “A ring trap for ultracold atoms in an RF-dressed state,” *New J. Phys* **10**, 043012 (2008).
- [49] P. Griffin, E. Riis, and A. Arnold, “A smooth inductively coupled ring trap for atoms,” *Phys. Rev. A* **77**, 051402(R) (2008).
- [50] A. A. Radzigand and B. M. Smirnov, *Reference Data on Atoms, Molecules, and Ions* (Springer-Verlag, Berlin, 1985).
- [51] H. N. Russell and F. A. Saunders, “New regularities in the spectra of the alkaline earths,” *Astrophysical Journal* **61**, 38 (1925).
- [52] D. A. Steck, “Rubidium 87 D line data,” available online at <http://steck.us/alkalidata> **61**, revision 2.0.1, 2 May (2008).
- [53] M. R. Matthews, D. S. Hall, D. S. Jin, J. R. Ensher, C. E. Wieman, E. A. Cornell, F. Dalfovo, C. Minniti, and S. Stringari, “Dynamical response of a Bose-Einstein condensate to a discontinuous change in internal state,” *Phys. Rev. Lett.* **81**, 243 (1998).
- [54] V. Boyer, B. Desruelle, P. Bouyer, C. Westbrook, and A. Aspect, “Electromagnet for Bose-Einstein condensation,” *Annales de Physique* **23**, 197 (1998).
- [55] Y. Torii, Y. Suzuki, M. Kozuma, and T. Kuga, “Realization of Bose-Einstein condensation in a rubidium vapor using a simple double magneto-optical trap,” <http://phys3.c.u-tokyo.ac.jp/torii/bec/proceeding.html> .
- [56] A. S. Arnold, “Preparation and manipulation of an  $^{87}\text{Rb}$  Bose-Einstein condensate,” PhD thesis, University of Sussex (1999).
- [57] N. Bogoliubov, *J. Phys. (Moscow)* **11**, 23 (1947).
- [58] H. M. J. M. Boesten, C. C. Tsai, J. R. Gardner, D. J. Heinzen, and B. J. Verhaar, “Observation of a shape resonance in the collision of two cold  $^{87}\text{Rb}$  atoms,” *Phys. Rev. A* **55**, 636 (1997).
- [59] G. Baym and C. J. Pethick, “Ground state properties of magnetically trapped Bose-condensed rubidium gas,” *Phys. Rev. Lett.* **76**, 6 (1996).

- [60] E. F. Nichols and G. F. Hull, "A preliminary communication on the pressure of heat and light radiation," *Phys. Rev. (Series I)* **13**, 307 (1901).
- [61] R. Frisch, *Z. Phys.* **86**, 42 (1933).
- [62] D. Wineland and W. Itano, *Bull. Am. Phys. Soc.* **20**, 639 (1975).
- [63] W. D. Phillips and H. Metcalf, "Laser deceleration of an atomic beam," *Phys. Rev. Lett.* **48**, 596 (1982).
- [64] S. Chu, L. Hollberg, J. E. Bjorkholm, A. Cable, and A. Ashkin, "Three-dimensional viscous confinement and cooling of atoms by resonance radiation pressure," *Phys. Rev. Lett.* **55**, 48 (1985).
- [65] P. D. Lett, W. D. Phillips, S. L. Rolston, C. E. Tanner, R. N. Watts, and C. I. Westbrook, "Optical molasses," *J. Opt. Soc. Am. B* **6**, 2084 (1989).
- [66] A. Ashkin, "Acceleration and trapping of particles by radiation pressure," *Phys. Rev. Lett.* **24**, 156 (1970).
- [67] A. Ashkin, "Atomic-beam deflection by resonance-radiation pressure," *Phys. Rev. Lett.* **25**, 1321 (1970).
- [68] *Fundamentals of Statistical and Thermal Physics*, F. Reif, ed., (McGraw-Hill, New York, 1965), p. 574.
- [69] C. S. Adams and E. Riis, "Laser cooling and trapping of neutral atoms," *Prog. Quant. Electron* **21**, 1 (1997).
- [70] P. D. Lett, R. N. Watts, C. I. Westbrook, W. D. Phillips, P. L. Gould, and H. J. Metcalf, "Observation of atoms laser cooled below the Doppler limit," *Phys. Rev. Lett.* **61**, 169 (1988).
- [71] J. Dalibard and C. Cohen-Tannoudji, "Laser cooling below the Doppler limit by polarization gradients: simple theoretical models," *J. Opt. Soc. Am. B* **6**, 2023 (1989).
- [72] P. J. Ungar, D. S. Weiss, E. Riis, and S. Chu, "Optical molasses and multilevel atoms: theory," *J. Opt. Soc. Am. B* **6**, 2058 (1989).
- [73] S. A. Hopkins and A. V. Durrant, "Parameters for polarisation gradients in three-dimensional electromagnetic standing waves," *Phys. Rev. A* **56**, 4012 (1997).

- [74] O. Stern and W. Gerlach, *Z. Phys.* **8**, 110 (1921).
- [75] P. J. Mohr, B. N. Taylor, and D. B. Newell, “The 2006 CODATA recommended values of the fundamental physical constants, Web Version 5.1,” available at <http://physics.nist.gov/constants> (National Institute of Standards and Technology, Gaithersburg, MD 20899, 31 December 2007) .
- [76] E. Arimondo, M. Inguscio, and P. Violino, “Experimental determinations of the hyperfine structure in the alkali atoms,” *Rev. Mod. Phys.* **49**, 31 (1977).
- [77] M. Misakian, “Equations for the magnetic field produced by one or more rectangular loops of wire in the same plane,” *J. Res. Natl. Inst. Stand. Technol.* **105**, 557 (2000).
- [78] R. H. Good, “Elliptic integrals, the forgotten functions,” *Eur. J. Phys.* **22**, 119 (2001).
- [79] *Handbook of Mathematical Functions*, M. Abramowitz and I. A. Stegun, eds., (Reprinted from 1964 National Bureau of Standards, US Department of Commerce, New York: Dover, 1972).
- [80] J. Simpson, J. Lane, C. Immer, and R. Youngquist, “Simple analytic expressions for the magnetic field of a circular current loop,” from: <http://ntrs.nasa.gov/archive> .
- [81] E. Raab, M. Prentiss, A. Cable, S. Chu, and D. Pritchard, “Trapping of neutral sodium atoms with radiation pressure,” *Phys. Rev. Lett.* **59**, 2631 (1987).
- [82] T. Bergeman, G. Erez, and H. J. Metcalf, “Magnetostatic trapping fields for neutral atoms,” *Phys. Rev. A* **35**, 1535 (1987).
- [83] W. Petrich, M. H. Anderson, J. R. Ensher, and E. A. Cornell, “Stable, tightly confining magnetic trap for evaporative cooling of neutral atoms,” *Phys. Rev. Lett.* **74**, 3352 (1995).
- [84] D. M. Brink and C. V. Sukumar, “Majorana spin-flip transitions in a magnetic trap,” *Phys. Rev. A* **74**, 035401 (2006).
- [85] V. G. Minogin, J. A. Richmond, and G. I. Opat, “Time-orbiting-potential quadrupole magnetic trap for cold atoms,” *Phys. Rev. A* **58**, 3138 (1998).

- [86] E. Hodby, G. Hechenblaikner, O. M. Maragò, J. Arlt, S. Hopkins, and C. J. Foot, “Bose-Einstein condensation in a stiff TOP trap with adjustable geometry,” *J. Phys. B* **33**, 4087 (2000).
- [87] K. B. Davis, M.-O. Mewes, M. R. Andrews, N. J. van Druten, D. S. Durfee, D. M. Kurn, and W. Ketterle, “Bose-Einstein condensation in a gas of sodium atoms,” *Phys. Rev. Lett.* **75**, 3969 (1995).
- [88] D. S. Naik and C. Raman, “Optically plugged quadrupole trap for Bose-Einstein condensates,” *Phys. Rev. A* **71**, 033617 (2005).
- [89] D. E. Pritchard, “Cooling neutral atoms in a magnetic trap for precision spectroscopy,” *Phys. Rev. Lett.* **51**, 1336 (1983).
- [90] Y. V. Gott, M. S. Ioffe, and V. G. Telkovskii, *Nuclear Fusion, 1962 Suppl., Pt. 3* (International Atomic Energy Agency, Vienna, 1962), p. 1045.
- [91] N. R. Thomas, C. J. Foot, and A. C. Wilson, “Double-well magnetic trap for Bose-Einstein condensates,” *Phys. Rev. A* **65**, 063406 (2002).
- [92] H. Hess, “Evaporative cooling of magnetically trapped and compressed spin-polarized hydrogen,” *Phys. Rev. Lett.* **34**, 3476 (1986).
- [93] K. B. Davis, M.-O. Mewes, and W. Ketterle, “An analytical model for evaporative cooling of atoms,” *Appl. Phys. B* **60**, 155 (1995).
- [94] O. J. Luiten, M. W. Reynolds, and J. T. M. Walraven, “Kinetic theory of the evaporative cooling of a trapped gas,” *Phys. Rev. A* **53**, 381 (1996).
- [95] J. T. M. Walraven, “Quantum dynamics of simple systems,” *Proceedings of the Forty Forth Scottish Universities Summer School in Physics* 44 (1994).
- [96] W. Ketterle and N. J. Druten, “Evaporative cooling of trapped atoms,” *Adv. Atom. Mol. Opt. Phys.* **37** (1996).
- [97] R. Grimm, M. Weidemüller, and Y. B. Ovchinnikov, “Optical dipole traps for neutral atoms,” *Adv. At. Mol. Opt. Phys.* **42**, 95 (2000).
- [98] V. S. Letokhov, *JETP Lett.* **7**, 272 (1968).

- [99] Y. Shin, M. Saba, T. A. Pasquini, W. Ketterle, D. E. Pritchard, and A. E. Leanhardt, “Atom interferometry with Bose-Einstein condensates in a double-well potential,” *Phys. Rev. Lett.* **92**, 050405 (2004).
- [100] M.-R. Andrews, C. G. Townsend, H.-J. Miesner, D. S. Durfee, D. M. Kurn, and W. Ketterle, “Observation of interference between two Bose condensates,” *Science* **275**, 637 (1997).
- [101] M. A. Kasevich, “Coherence with atoms,” *Science* **298**, 1363 (2002).
- [102] U. V. Poulsen and K. Molmer, “Quantum beam splitter for atoms,” *Phys. Rev. A* **65**, 033613 (2002).
- [103] Y. Shin, C. Sanner, G.-B. Jo, T. A. Pasquini, M. Saba, W. Ketterle, and D. E. Pritchard, “Interference of Bose-Einstein condensates split with an atom chip,” *Phys. Rev. A* **72**, 021604(R) (2005).
- [104] Y. J. Wang, D. Z. Anderson, V. M. Bright, E. A. Cornell, Q. Diot, T. Kishimoto, M. Prentiss, R. A. Saravanan, S. R. Segal, and S. Wu, “Atom Michelson interferometer on a chip using a Bose-Einstein condensate,” *Phys. Rev. Lett.* **94**, 090405 (2005).
- [105] J. M. Jacobson, G. Björk, , and Y. Yamamoto, “Quantum limit for the atom-light interferometer,” *Appl. Phys. B* **60**, 187 (1995).
- [106] T. L. Gustavson, P. Bouyer, and M. A. Kasevich, “Precision rotation measurements with an atom interferometer gyroscope,” *Phys. Rev. Lett.* **78**, 2046 (1997).
- [107] G. Sagnac, “L’*é*ther lumineux démontré par l’effet du vent relatif d’*é*ther dans un interféromètre en rotation uniforme,” *Comptes Rendus* **157**, 708 (1913).
- [108] A. Lenef, T. D. Hammond, E. T. Smith, M. S. Chapman, R. A. Rubenstein, and D. E. Pritchard, “Rotation sensing with an atom Interferometer,” *Phys. Rev. Lett.* **78**, 760 (1997).
- [109] A. D. Cronin, J. Schmiedmayer, and D. E. Pritchard, “Atom Interferometers,” *Rev. Mod. Phys.* **81**, 1051 (2008).
- [110] L. Zehnder, *Z. Instrumentenkunde* **11**, 275 (1891).

- [111] D. Keith, C. R. Ekstrom, Q. A. Turhette, and D. Pritchard, “An interferometer for atoms,” *Phys. Rev. Lett.* **66**, 2693 (1991).
- [112] E. M. Rasel, M. K. Oberthaler, H. Batelaan, J. Schmiedmayer, and A. Zeilinger, “Atom wave interferometry with diffraction gratings of light,” *Phys. Rev. Lett.* **75**, 2633 (1995).
- [113] A. Arnold, “Adaptable-radius, time-orbiting magnetic ring trap for Bose-Einstein condensates,” *J. Phys. B* **37**, 29 (2004).
- [114] K. Lindquist, M. Stephens, and C. Wieman, “Experimental and theoretical study of the vapor-cell Zeeman optical trap,” *Phys. Rev. A* **46**, 4082 (1992).
- [115] A. S. Arnold, J. S. Wilson, and M. G. Boshier, “A simple extended-cavity diode laser,” *Rev. Sci. Instrum.* **69**, 3 (1998).
- [116] C. E. Wieman and L. Hollberg, “Using diode lasers for atomic physics,” *Rev. Sci. Instrum.* **62**, 1 (1991).
- [117] P. D. McDowall and M. F. Andersen, “Acousto-optic modulator based frequency stabilized diode laser system for atom trapping,” *Rev. Scient. Instrum.* **80**, 053101 (2009).
- [118] R. Wyatt and W. J. Devlin, “10 kHz linewidth 1.5  $\mu\text{m}$  InGaAsP external cavity laser with 55 nm tuning range,” *Electron Lett.* **19**, 110 (1983).
- [119] *Semiconductor Physics and Devices*, D. A. Neamen, ed., (3rd edition, McGraw-Hill, New York, 2003).
- [120] W. Demtroder, *Laser Spectroscopy* (Springer, Berlin, 1998).
- [121] D. A. Smith and I. G. Hughes, “The role of hyperfine pumping in multilevel systems exhibiting saturated absorption,” *Am. J. Phys.* **72**, 5 (2004).
- [122] M. E. Zawadzki, “Something ‘cool’ – the journey to Bose - Einstein Condensation,” MPhil Thesis, University of Strathclyde (2007).
- [123] Ph 77 Advanced Physics Laboratory – Atomic and Optical Physics, “Saturated absorption spectroscopy”, available at <http://www.its.caltech.edu> .

- [124] C. P. Pearman, C. S. Adams, S. G. Cox, P. F. Griffin, D. A. Smith, and I. G. Hughes, "Polarization spectroscopy of a closed atomic transition: applications to laser frequency locking," *J. Phys. B* **35**, 5141 (2002).
- [125] K. J. Weatherill, J. D. Pritchard, P. F. Griffin, U. Dammalapati, C. S. Adams, and E. Riis, "A versatile and reliably reusable ultrahigh vacuum viewport," *Rev. Sci. Instrum.* **80**, 026105 (2009).
- [126] K. Gibble, S. Chang, and R. Legere, "Direct observation of *s*-wave atomic collisions," *Phys. Rev. Lett* **75**, 2666 (1995).
- [127] C. Wieman, G. Flowers, and S. Gilbert, "Inexpensive laser cooling and trapping experiment for undergraduate laboratories," *Am. J. Phys.* **63**, 317 (1995).
- [128] U. D. Rapol, A. Wasan, and V. Natarajan, "Loading of a Rb magneto-optic trap from a getter source," *Phys. Rev. A* **64**, 023402 (2001).
- [129] J. Denschlag, D. Cassetari, and J. Schmiedmayer, "Guiding neutral atoms with a wire," *Phys. Rev. Lett.* **82**, 2014 (1999).
- [130] D. Müller, D. Z. Anderson, R. J. Grow, P. D. Schwindt, and E. A. Cornell, "Guiding neutral atoms around curves with lithographically patterned current-carrying wires," *Phys. Rev. Lett.* **83**, 5194 (1999).
- [131] N. H. Dekker, C. S. Lee, V. Lorent, J. H. Thywissen, S. P. Smith, M. Drndic, R. M. Westervelt, and M. Prentiss, "Guiding neutral atoms on a chip," *Phys. Rev. Lett.* **84**, 1124 (2000).
- [132] D. M. Brink and C. V. Sukumar, "Majorana spin-flip transitions in a magnetic trap," *Phys. Rev. A* **74**, 035401 (2006).
- [133] M.-O. Mewes, M. R. Andrews, D. M. Kurn, D. S. Durfee, C. G. Townsend, and W. Ketterle, "Output coupler for Bose-Einstein condensed atoms," *Phys. Rev. Lett.* **78**, 582 (1997).
- [134] K. M. O'Hara, S. R. Granade, M. E. Gehm, T. A. Savard, S. Bali, C. Freed, and J. E. Thomas, "Ultrastable CO<sub>2</sub> laser trapping of lithium fermions," *Phys. Rev. Lett.* **82**, 4204 (1999).
- [135] D. Guery-Odelin, J. Soeding, P. Desbiolles, and J. Dalibard, "Strong evaporative cooling of a trapped cesium gas," *Opt. Express* **2**, 323 (1998).

- [136] Y. Castin and R. Dum, “Bose-Einstein condensation in time dependent traps,” *Phys. Rev. Lett.* **77**, 5315 (1996).
- [137] S. Chen, X.-J. Zhou, L. X. F. Yang, Y.-Y. Sun, Y.-Q. Wang, and X.-Z. Chen, “Analysis of runaway evaporation and Bose-Einstein condensation by time-of-flight absorption imaging,” *Chin. Phys. Lett.* **21**, 2105 (2004).
- [138] N. Houston, E. Riis, and A. S. Arnold, “Reproducible dynamic dark ring lattices for ultracold atoms,” *J. Phys. B* **41**, 211001 (2008).
- [139] J. F. Clément, J. P. Brantut, R. R. de Saint Vincent, R. A. Nyman, A. Aspect, T. Bourdel, and P. Bouyer, “All-optical runaway evaporation to Bose-Einstein condensation,” *Phys. Rev. A* **79**, 061406 (2009).
- [140] A. Ashkin, “Application of laser radiation pressure,” *Science* **210**, 1081 (1980).
- [141] J. J. Chang and P. Engels, “Far-off-resonance optical trapping of atoms,” *Phys. Rev. A* **47**, 4567 (1993).
- [142] I. Shomroni, E. Lahoud, S. Levy, and J. Steinhauer, “Density engineering of an oscillating soliton/vortex ring in a Bose-Einstein condensate,” *Nature Physics* **5**, 193 (2009).
- [143] P. Engels and C. Atherton, “Formation of dispersive shock waves by merging and splitting Bose-Einstein condensates,” *Phys. Rev. Lett.* **101**, 170404 (2008).
- [144] Y. Shin, M. Saba, T. A. Pasquini, W. Ketterle, D. E. Pritchard, and A. E. Leanhardt, “Atom interferometry with Bose-Einstein Condensates in a double-dell potential,” *Phys. Rev. Lett.* **92**, 050405 (2004).
- [145] G.-B. Jo, Y. Shin, S. Will, T. A. Pasquini, M. Saba, W. Ketterle, D. E. Pritchard, M. Vengalattore, and M. Prentiss, “Long phase coherence time and number squeezing of two Bose-Einstein condensates on an atom chip,” *Phys. Rev. Lett.* **98**, 030407 (2007).
- [146] R. Onofrio, D. S. Durfee, C. Raman, M. Köhl, C. E. Kuklewicz, and W. Ketterle, “Surface excitations of a Bose-Einstein condensate,” *Phys. Rev. Lett.* **84**, 810 (2000).

- [147] S. K. Schnelle, E. D. van Ooijen, M. J. Davis, N. R. Heckenberg, and H. Rubinsztein-Dunlop, “Versatile two-dimensional potentials for ultra-cold atoms,” *Opt. Express* **16**, 1405 (2008).
- [148] K. Henderson, C. Ryu, C. MacCormick, and M. G. Boshier, “Experimental demonstration of painting arbitrary and dynamic potentials for Bose-Einstein condensates,” *New J. Phys.* **11**, 043030 (2009).
- [149] *Optics*, E. Hecht, ed., (3rd edition, Addison Wesley Longman, Amsterdam, 1998).
- [150] I. Bloch, M. Köhl, M. Greiner, T. W. Hänsch, and T. Esslinger, “Optics with an atom laser beam,” *Phys. Rev. Lett.* **87**, 030401 (2001).
- [151] T. Schumm, S. Hofferberth, L. M. Andersson, S. Wildermuth, S. Groth, I. Bar-Joseph, J. Schmiedmayer, and P. Krüger, “Matter-wave interferometry in a double well on an atom chip,” *Nature Phys.* **1**, 57 (2005).
- [152] H. Ott, J. Fortágh, S. Kraft, A. Günther, D. Komma, and C. Zimmermann, “Nonlinear Dynamics of a Bose-Einstein Condensate in a Magnetic Waveguide,” *Phys. Rev. Lett.* **91**, 040402 (2003).
- [153] J. Stenger, S. Inouye, A. P. Chikkatur, D. M. Stamper-Kurn, D. E. Pritchard, and W. Ketterle, “Bragg spectroscopy of a Bose-Einstein condensate,” *Phys. Rev. Lett.* **82**, 4569 (1999).
- [154] M. Kozuma, L. Deng, E. W. Hagley, J. Wen, R. Lutwak, K. Helmerson, S. L. Rolston, and W. D. Phillips, “Coherent splitting of Bose-Einstein condensed atoms with optically induced Bragg diffraction,” *Phys. Rev. Lett.* **82**, 871 (1999).
- [155] M. Rab, J. H. Cole, N. G. Parker, A. D. Greentree, L. C. L. Hollenberg, and A. M. Martin, “Spatial coherent transport of interacting dilute Bose gases,” *Phys. Rev. A* **77**, 061602(R) (2008).
- [156] T. H. Bergeman, P. McNicholl, J. Kycia, H. Metcalf, and N. L. Balazs, “Quantized motion of atoms in a quadrupole magnetostatic trap,” *J. Opt. Soc. Am. B.* **6**, 2249 (1989).